Imperial College London

Collisions Between Laser-Cooled Atoms and Molecules

Supervisors:
Prof. Michael R. Tarbutt
Prof. Ben E. Sauer

A Thesis Submitted to the Department of Physics,
Imperial College London
by

Sarunas Jurgilas

In Partial Fulfilment of the Requirements for the Degree of
Doctor of Philosophy

October 26, 2021

Abstract

This thesis describes an experiment to produce the first laser cooled mixtures of atoms and polar molecules in magneto-optical and magnetic quadrupole traps. Inelastic collision processes between $^{40}Ca^{19}F$ molecules and ^{87}Rb atoms are studied in both trapping arrangements. When molecules occupy the first rotationally excited state it is found that loss from either trap occurs at near the universal rate due to collisions with co-trapped atoms. When the molecular sample is transferred to the ground rotational state the loss rate is suppressed by at least an order of magnitude. The experimental results are compared to a quantum scattering model based on quantum defect theory and the results seem to be encouraging for observing a high ratio of elastic to inelastic collision rates in this system. In addition, improvements to the experimental apparatus are presented which led to the first measurements of the elastic cross-section for collisions between CaF and Rb. Although at the currently attainable number densities no thermalization is observed, an upper bound on the value of the cross section is placed.

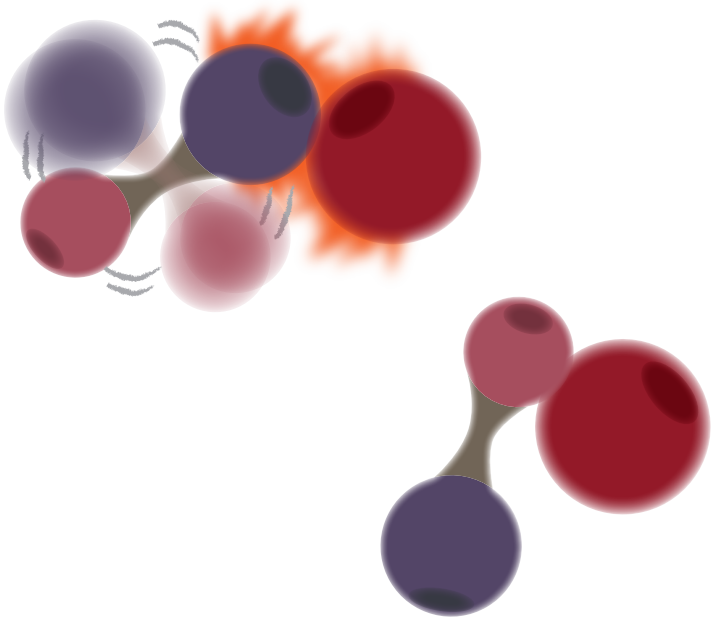

Acknowledgements

Throughout my time as a PhD student at CCM I had the pleasure to work with and learn from many people. First of all, I was lucky to have my supervisors Mike and Ben. They have given me a substantial amount of responsibility and an opportunity to design and build a new experiment. Mike has been a great supervisor who has always found the time to hear me out and has been inspirational due to his rigour and depth of understanding.

I would like to thank Arijit and Caleb for spending long hours together in the lab to help find and solve the various technical problems which would so often prevent us from making the planned measurements. Thanks to Jonas and Bharath who have both helped to improve the experimental apparatus and worked closely in making the often difficult sharing of the experiment more manageable and efficient. Thanks to Noah who has always been there to respond to various technical difficulties in the lab. In the earlier days of the experiment I had the opportunity to work with Thom, Kyle, Hannah and Luke to whom I am also grateful for sharing their experience and time. I met and made friends with many other members of the group who have all made my time as a student much more enjoyable. Hopefully without missing any of these people, thanks to: Sid, Indranil, Xiaxi, Ross, Chris, Simon, Seb, Jongseok.

Thanks to our workshop technicians Jon and Dave who would never say that my amateur designs are unrealistic or not possible to materialize. They have both contributed a lot to making the experiments described in this work possible. Thank you to Miranda and Sanja for helping to navigate through the frequent bureaucracies.

Thanks to my sister Lina and Tim who have looked after me during my PhD and were also the greatest housemates a PhD student in London could ever expect to have. I am grateful for having Kriste who has supported me from the very beginning when I made the decision to start a PhD and all the way throughout it.

Finally, the reason I have managed to come this far is largely due to the support of my parents who have always supported me in whatever passions I had. To them I dedicate this work.

Declaration

I declare that the work presented in this thesis is my own. Any work done by others is declared in the appropriate places and cited.

Contents

List of Figures

1 | Introduction

The advent of laser cooling and trapping of neutral atoms [1, 2, 3] led to a wealth of ground breaking experiments and created vast new areas of research in quantum science. Fundamentally, cooling a physical system towards absolute zero reduces the disorder and reveals the quantum nature of matter and interactions which at room temperature are typically absent. In addition, today it allows experimentalists to manipulate both the internal and external degrees of freedom of single atoms [4]- a feat which for the fathers of modern physics was only ever possible in thought experiments. Amongst the vast range of other achievements that the capability of producing ultracold atomic gases has led to are the creation of Bose-Einstein condensates [5, 6], Fermi degenerate gases [7, 8], platforms for quantum computation [9] and simulation [10], extremely precise atomic clocks [11, 12] and experiments for exploring fundamental physics [13, 14].

Due to their much larger complexity, bringing diatomic molecules into the ultracold regime presents many challenges. On the other hand, these same challenges that make molecules so hard to work with bring exciting new opportunities. Some of the current and future applications of ultracold molecules and the methods of producing them are discussed in some detail throughout this chapter.

1.1 Applications of ultracold molecules

The two key differences between polar molecules and neutral atoms is that molecules have electric dipole moments which may lead to long range interactions and they have a much richer internal structure due to the rotational and vibrational degrees of freedom. These features are compared and discussed below in the context of applications in quantum science and precision measurements.

Quantum simulation

Problems in quantum many body physics are typically prohibitively expensive to solve using classical computers. Instead of writing down and trying to numerically solve the equations which govern the complicated dynamics of such systems, a quantum simulator physically mimics that system and allows to control and observe the specific interactions

of interest. Ultracold atomic gases confined in periodic optical potentials are used today as a platform for exploring various phenomenon in condensed matter and many body quantum physics [15, 16]. For example, fermionic atoms in optical lattices were used to simulate quantum magnetism [17] and show great promise in furthering our understanding of room temperature superconductivity [18]. However, neutral atoms interact only via the short range contact interaction which limits the range of many-body quantum systems that may be simulated. The two exceptions to this are highly magnetic atoms and electronically excited Rydberg atoms. The highly magnetic Cr [19], Dy [20] and Er [21] atoms were successfully cooled to quantum degeneracy and the latter species was used to implement an extended Bose-Hubbard model [22] in a 3D optical lattice. However, even these systems exhibit only relatively short range interactions. For example, a pair of Er atoms separated by 250 nm have an interaction energy of only $V_{\mu\mu} \sim \frac{\mu_0 \mu^2}{4\pi r^3} = (40 \cdot h)$ Hz. On the other hand, Rydberg atoms may be made to interact via the resonant dipole-dipole interaction. For example in [23] interaction energies of $V_{\mathrm{ee}} = (50 \cdot h)$ MHz between a pair of Rydberg atoms separated by 4 μm were demonstrated. Even though Rydberg atoms have typical lifetimes of only a few hundred microseconds and are extremely sensitive to external electric fields their strong and long range interactions make them a very attractive platform for quantum simulation and computation. Today Rydberg atoms are routinely produced in reconfigurable arrays of optical tweezers and are used to probe many body quantum dynamics [24, 25].

When it comes to long range interactions and long coherence times of internal quantum states, diatomic polar molecules offer a very attractive alternative. Polar molecules have an electric dipole moment in their own frame of reference, typically of several Debye (1 Debye $\approx 3.335 \cdot 10^{-30}$ C $\cdot$ m) and exhibit long range electric dipole interactions. For example a pair of CaF molecules with an electric dipole moment of 3.1 Debye and separated by 0.5 μm will have an interaction energy on the order of $V_{\mathrm{dd}} \sim \frac{d^2}{4\pi\epsilon_0 r^3} \approx (12 \cdot h)$ kHz, which is easily resolvable using radio-frequency or microwave spectroscopy. Moreover, these interactions may be tuned by controlling their rotational states, which conveniently have long coherence times. For example, a coherence time of 6.4(8) ms of a transition between two rotational states in CaF was demonstrated [168] and methods to extend it to 1 s were proposed. Quantum simulators with polar molecules are very much within reach and [26, 27] have already detected dipolar spin exchange interactions between KRb molecules in a sparsely filled optical lattice. These types of platforms have been proposed as good candidates for simulating quantum magnetism [28], which is believed to be closely connected with high temperature superconductivity [29]. Moreover, by controlling the spin and rotational degrees of freedom of polar molecules trapped in an optical lattice a complete toolbox for simulating various spin lattice models can be obtained [30]. Such spin models are often used to describe the behaviour of condensed matter systems.

Quantum computation

The quest to find the ideal platform for a universal quantum computer is still ongoing. Amongst the outstanding challenges are the management of decoherence, implementation of effective error correction protocols and scalability of the particular architecture in order to perform useful computations. Polar molecules offer long coherence times and can be made to interact over practical distances- two key building blocks of a quantum gate. The use of polar molecules as quantum bits for an information processing task was first proposed by DeMille [31]. In this seminal proposal, polar molecules are held in a 1D optical lattice in the presence of a spatially varying electric field. The strong electric dipole-dipole interaction induced by the electric field can be used to implement a CNOT gate while molecules at different lattice sites may be addressed individually owing to their different resonance frequencies. Following a more recent proposal [32], the electric dipole interaction may also be induced by the application of a microwave frequency field which couples two rotational states of a molecule. As a particular example, the work showed how to implement a CNOT gate using a pair of CaF molecules trapped in optical tweezers separated by 0.8 μm. It may be possible to couple polar molecules to superconducting quantum devices [33], providing a robust quantum memory for this well established technology. Proposals of quantum error correction codes using the rotational states of molecules [34] now also exist.

Precision measurements

Ultracold atomic gases are used today to build the most precise clocks and test fundamental physics. For example a Sr optical lattice clock with a $5 \cdot 10^{-19}$ measurement stability after 1 hour of integration time has been realized by the JILA group [35] and is amongst the most accurate clocks in the world. Large research collaborations have recently been established [36, 37] to build networks of atom interferometers to detect gravitational waves.

The benefits of molecules for precision measurements stem from their rich internal structure. Vibrational energy levels in a molecule depend on the electron to proton mass ratio which has been probed using ultracold KRb molecules [38]. Optical lattice clocks based on ultracold molecules may be used to probe interatomic forces and test Newtonian gravitation at extremely small length scales [39]. Proposals to use cold molecules for the search of dark matter candidates also exist [40]. In addition, the large internal electric fields present within polar molecules enabled the most precise measurements of the electron's electric dipole moment [41, 42, 43]. The precision of these measurements is limited, amongst other things, by the available coherence time of the internal states being probed in the experiment and by the available number of molecules. Producing cold molecular beams, or even better, large samples of trapped molecules [44] promises

to greatly enhance the sensitivity.

Quantum chemistry and control of chemical reactions

For many years most studies of quantum chemistry and low energy collisions were performed using the molecular beam method [45, 46] (see more about the production of molecular beams in the following section) or in superconducting magnetic traps [47]. Typically, these methods are suitable for studying quantum state resolved collisions in the regime where many partial waves contribute to the scattering process. An exception being the merged molecular beam method [74], which enables the study of collisions at a relative collision energy in the mK regime. On the other hand, when molecules are cooled to ultracold temperatures and the control of internal quantum states is achieved, the steps in a chemical reaction may be monitored [48] and the final outcomes could be controlled [49]. The last couple of decades saw rapid development of methods for producing molecular gases at μK temperatures which have enabled experiments to access this regime.

At first sight it is surprising that a chemical reaction could proceed at temperatures close to absolute zero at all as the available energies are many times lower than typical reaction barriers. Nevertheless, seminal theoretical work by Balakrishnan [50] has shown that chemical reactions may occur between light molecules at considerably high rates even at ultracold temperatures[1]. In this regime, the long collision times and the large de Broglie wavelengths allows tunnelling through potential barriers. In addition, individual partial waves which contribute to the collisional dynamics may be resolved. For example, in the work by the JILA group [51] the reaction rates in a gas of ultracold KRb molecules were controlled by changing the spin state purity of the constituent molecules. Because KRb has total integer spin it obeys Fermi-Dirac statistics and the lowest partial wave (see section 2.3.1) which contributes to the collision is $l = 1$ for a pair of molecules in the same quantum state. Under such conditions the molecules are prevented from reaching short range by a centrifugal barrier. On the other hand, when half of the molecules were transferred to a different spin state head-on collisions ($l = 0$) were allowed which increased the reactivity by two orders of magnitude. The same system was also used to study for the first time the role of dipolar interactions in collisional dynamics [52]. More recently, the group has transferred samples of ultracold KRb molecules to a 2D optical lattice and used external electric fields to tune the electric dipole interaction between colliding molecules [53]. By choosing a precise value and direction of the applied electric field they were able to change the collisional dynamics and shield molecules from unwanted chemical reactions. In another experiment by the Harvard group [54], CaF molecules were shielded

[1]The quantum mechanical tunnelling probability falls of as $\sim \exp(-\sqrt{m})$ thus the discussion in [50] is relevant only for light particles.

from inelastic collisions using off-resonant microwave fields, demonstrating yet another method of controlling collisional processes.

Controlling and understanding the collision dynamics was crucial for the development of experimental methods to produce quantum degenerate gases of a wide range of different atomic species. Although there has recently been some outstanding success in producing a quantum degenerate gas of polar molecules [55], the topic of ultracold molecular collisions is still a very active research area both experimentally and theoretically [56, 57, 58, 59].

1.2 Methods for producing and trapping cold and ultracold molecules

Methods to produce cold and ultracold molecules are typically separated into two different classes depending on whether molecules are cooled directly or assembled out of individual ultracold atoms. While indirect methods are still leading the way in producing the coldest and densest samples of diatomic molecules, the direct class of methods are rapidly catching up. In this section the basic principles that underlie both of these approaches are described.

1.2.1 Indirect methods

The indirect methods for producing ultracold molecules rely on being able to cool the constituent atoms. As mentioned in the above, a wide range of different atomic species with varying physical properties have been cooled all the way down to quantum degeneracy and thus are ideal building blocks of ultracold molecules. Starting from such mixtures of ultracold atoms, diatomic molecules are created using either a magnetic Feshbach resonance [60] or precisely tuned laser light to transfer colliding atoms into a bound state. By coherently transferring these bound pairs to their vibrational ground state, a sample of diatomic molecules with a temperature equal to that of the constituent atoms may be produced.

Magneto-association

The detailed theoretical understanding of quantum scattering in ultracold atomic gases guides experimentalists in designing experimental protocols to produce ultracold diatomic molecules. In particular, the accurate knowledge of interatomic interaction potentials allows very accurate predictions of the locations of magnetic Feshbach resonances. A Feshbach resonance corresponds to the appearance of a closed molecular channel which supports a loosely bound state with an energy close to that of the free atom state. The energy difference between the closed and incoming channels may in some atomic systems

be tuned using an external magnetic field. By sweeping the magnitude of a magnetic field, a pair of atoms may thus be adiabatically transferred into a loosely bound state. From here the loosely bound molecule is coherently transferred using a process known as stimulated Raman adiabatic passage (STIRAP) [61]. The STIRAP method prevents spontaneous emission and thus produces ground-state molecules at the same translational energies as that of the constituent atoms.

The JILA group were the first to successfully use these two methods to produce a sample of KRb molecules at a temperature of 350 nK and a density of 10^{12} cm^{-3}. Following this work several other heteronuclear species were produced at ultracold temperatures and high densities: ^{87}Rb^{133}Cs [62], ^{23}Na^{6}Li [63], ^{23}Na^{87}Rb [64], ^{23}Na^{40}K [65]. Reaching the quantum degenerate regime using this approach is challenging due to the immiscibility of some degenerate atomic gases [66], which depends on the scattering length, and due to light induced or three body losses [67].

Photo-association

Atoms with closed electronic shells are less suitable for magneto-association as they do not have an electronic spin in their ground state. Instead, such atoms could be bound into molecules using photo-association as was recently demonstrated for Cs and Yb atoms [68, 69]. In the photo-association process a colliding atom pair is transferred to a bound state using light which is red-detuned from an electronic transition of an individual atom. The produced electronically excited molecule occupies a high vibrational state and can either dissociate into the constituent atoms or decay to some other vibrational ground electronic state. The relative decay probabilities are given by the overlap of the two wave functions corresponding to the vibrational levels. By carefully selecting the detuning of the photo-association laser, the atoms may be transferred to an electronically excited state which has a large wavefunction overlap with the lowest vibrational level in the ground electronic state thus producing a substantial fraction of ground state molecules. This method was used to produce a number of different molecular species [70, 71, 72]. In the recent work by the Kang-Kuen Ni group [73] NaCs molecules were assembled from single atoms held in optical tweezer traps using photo-association- a fascinating example of the exquisite level of control achieved in state of the art experiments.

1.2.2 Direct cooling methods

The class of direct cooling methods has a longer history and consists of many more different approaches. As the name suggests, a particular cooling method is applied directly to the molecular sample and proceeds after the production of molecules. Some of these methods are described below.

Supersonic expansion

The supersonic molecular beam is amongst the oldest method of producing cold molecules for collisional studies. In this method, a gas held at a pressure of $\sim 10^3$ mbar is suddenly allowed to expand through a nozzle into a much lower pressure region ($\sim 10^{-7}$ mbar). This isentropic expansion converts energy corresponding to random translational motion into kinetic energy corresponding to the forward motion of the molecular beam. The temperature of the gas is thus reduced at the expense of an increased forward velocity, producing a narrow velocity distribution with a supersonic mean velocity. Moreover, the internal degrees of freedom of the constituent molecules are also cooled via molecule-molecule collisions near the exit aperture. In contrast, effusive beams are formed when the mean free path of a molecule is larger than the size of the exit aperture of the nozzle so that no collisions occur before it is extracted into a beam. This method produces a much broader distribution of velocities and internal states.

By merging two supersonic beams, the narrow velocity distributions enable precise control of the relative collision energies simply by controlling the angle between the two beams. The level of control of this angle determines the obtainable energy resolution in collisional studies [74]. In addition, using external fields specific internal states could be selected [75].

Buffer gas cooling

Buffer gas cooling of a particular molecular species relies on elastic collisions with particles from a much colder gas. The buffer gas must be inert, such as helium or neon, so that it does not react with the target molecules. This technique has been used to cool CaH [76] molecules to millikelvin temperatures and load them into a superconducting magnetic trap. A molecular beam [77] may be produced by mixing the target molecules with the buffer gas in a small cell with an exit aperture. Provided that molecules have sufficient time to collide with the buffer gas, the spread in the velocity distribution will be reduced and a cold and slow molecular beam will form. Buffer gas beams have a similar intensity as those produced by supersonic expansion but have a substantially lower forward velocity which makes them an ideal starting point for further deceleration and cooling.

Deceleration using the Zeeman and Stark effects

Molecules may be decelerated by making use of either the Stark or Zeeman effects. In an external field the internal energy of a molecule will be shifted by an amount which depends on both the magnitude of the field and the internal state of the molecule. By applying a periodic spatially varying magnetic field, a moving molecule may be forced to climb potential hills and each time lose kinetic energy. Provided the external field is

switched on and off so that the molecules only ever climb hills in potential energy, a beam of molecules can be brought to a standstill. The first decelerator using the Stark effect was demonstrated by [78] to decelerate CO molecules from an initial velocity of 225 m/s to 98 m/s. Recently, the Narevicius group [79] has demonstrated deceleration of oxygen molecules using a travelling magnetic trap and subsequent loading into a superconducting magnetic trap at a density of 10^{10} cm^{-3}. These methods have a large appeal in that they only require the molecules to have a non-zero interaction energy with applied electric and magnetic fields. An interesting approach to produce ultracold trapped molecules would be to use the magnetic decelerator to load a magnetic trap together with a sample of laser cooled atoms. The atoms could then be used to cool molecules via elastic collisions.

Laser cooling

Laser cooling is the method used in this work to produce ultracold samples of molecules and atoms. It will be described in detail throughout the rest of this work and only a brief introduction is given here. Laser cooling relies on continuous scattering of laser light to remove kinetic energy from atoms or molecules. Thus the basic requirement for this method to work is to find sufficiently closed optical transitions- a daunting challenge for diatomic molecules. Nevertheless, the work by Di Rosa [80] identified certain molecules which have closed optical transitions and are thus amenable to laser cooling. In 2010 the group of DeMille demonstrated laser cooling of a beam of SrF molecules. Today several different molecular species have been laser cooled and captured into conservative traps (much more on this in the following chapter) although with number densities still several orders of magnitude below those obtained using the indirect class of methods. On the other hand, there is no physical reason why densities of laser cooled molecules could not be increased and there already exists a number of proposals of how this could be achieved. Some of these will be described and investigated in this work.

Sympathetic cooling

The sympathetic cooling method uses elastic collisions between two ultracold species to cool another, warmer species. It has been already applied to reduce the temperature of laser cooled atoms, especially in situations when the collisional properties of one species are not suitable for evaporative cooling [81]. For example, fermionic atoms can not undergo s-wave collisions in the ultracold regime due to the Pauli exclusion principle and thus can not be evaporatively cooled to quantum degeneracy. A successful route around this obstacle is to use co-trapped bosonic atoms as a coolant for the fermionic species [82]. Because laser cooled molecules are currently produced at densities which are too low for collisional cooling, co-trapping them with substantially denser and colder samples of atoms offers an alternative route to drive down the temperature further.

1.3 This thesis

In this work, a new experimental apparatus for studying collisions between laser cooled samples of molecules and atoms was built. The long term goal is to use this system for identifying the conditions under which sympathetic cooling of molecules using atoms as a coolant is feasible. In this work the first steps towards this goal are taken. A dual species magneto-optical trap of Rb atoms and CaF molecules is built, which traps and cools both species to milikelvin temperatures. Atom-induced losses of molecules from this trap are studied in detail and the underlying mechanisms are determined. Next, the mixture is transferred to a magnetic trap where sympathetic cooling could proceed. By controlling the quantum states of both atoms and molecules, state dependent inelastic collision processes are investigated empirically.

This thesis is structured as follows. In chapter 2 some of the basic theory related to atomic and molecular structure, light-matter interactions and quantum scattering is presented. Chapter 3 details the construction and characterization of the experimental apparatus. In chapter 4 characteristics of magneto-optical traps of atoms and molecules are presented. Chapter 5 contains the results of inelastic collision measurements in the dual species magneto-optical trap of atoms and molecules. Chapter 6 describes how both species are prepared in pure quantum states and are used to study collisions in a magnetic trap. Transverse cooling of the molecular beam is explored in chapter 7 and finally in chapter 8 the results of the first attempt to observe elastic atom-molecule collisions in this system are presented.

1.3.1 Publications

Some of the work presented in this thesis has been reported in the following journal publications:

- S Jurgilas, A Chakraborty, C J H Rich, L Caldwell, H J Williams, N J Fitch, B E Sauer, Matthew D Frye, Jeremy M Hutson and M R Tarbutt. Collisions between ultracold molecules and atoms in a magnetic trap. *Physical Review Letters*, 126(15):153401, 2021.

- Sarunas Jurgilas, Arijit Chakraborty, Caleb Rich, Ben E Sauer, Matthew David Frye, Jeremy M Hutson, and Mike R Tarbutt. Collisions in a dual-species magneto-optical trap of molecules and atoms. *New Journal of Physics*, 2021.

2 | Background theory

In this chapter the basic theory required to understand some of the experimental results presented in this work is laid out. First, the energy level structures of an alkali atom and a diatomic molecule are reviewed and the spectroscopic notation used to label the different energy levels is introduced. The details of the ^{87}Rb atom and ^{40}Ca^{19}F molecule energy level structures are provided. Then, the interaction of a two-level atom with a monochromatic light field is discussed and applied in deriving the radiation pressure and dipole forces which are used to cool and manipulate atoms and molecules. In addition, these results come in handy when describing absorption imaging and coherent control of internal quantum states. Finally, basic concepts in quantum scattering and their relevance to describing collisions at very low temperatures are introduced.

2.1 Atomic and molecular structure

An atomic or molecular species is considered to be amenable to laser cooling if it has a sufficiently closed optical transition. Finding such species is not a simple task, especially when it comes to diatomic molecules due to their internal complexity. In addition, it is important to consider practical aspects such as the availability of a monochromatic source to be used to address the internal structure. In this work ^{87}Rb atoms and CaF molecules are chosen primarily due to their suitability for laser cooling. Here the energy level structures of the two species are presented. Selection rules for electric dipole transitions are stated with a more detailed discussion of the light-matter interaction postponed to section 2.2.

2.1.1 Alkali atoms

The outermost electronic shells of alkali metal atoms are occupied by a single electron. This makes the internal energy structure of an alkali very similar to that of a hydrogen atom- the outermost electron orbits an effective positively charged nucleus which is composed of the protons and neutrons at the core shielded by electrons from the inner shells. The reduced complexity makes alkali atoms particularly suitable for manipulating them using laser light. Just a pair of different laser frequencies are required to achieve

continuous optical cycling which is necessary for applying laser cooling. Indeed, the first demonstrations of deceleration of an atomic beam [83] and slightly later cooling in an optical molasses [84] were performed using Na atoms. Today laser light is used to manipulate and cool atoms with more complex internal structures such as Yb [85], Er [86], Dy [87]- all of which have a pair of electrons in the outermost shells and thus a substantially more complicated internal energy level structure.

In alkali atoms, the relevant angular momentum operators are the total orbital angular momentum $\hat{\mathbf{L}}$ [1], the total electron spin $\hat{\mathbf{S}}$, and the nuclear spin $\hat{\mathbf{I}}$. It's also convenient to introduce the sums $\hat{\mathbf{J}} = \hat{\mathbf{L}} + \hat{\mathbf{S}}$ and $\hat{\mathbf{F}} = \hat{\mathbf{J}} + \hat{\mathbf{I}}$. The magnetic moment associated with the electron spin $\hat{\mathbf{S}}$ interacts with the magnetic field produced by the motion of the electron through the electric field of the atom. This coupling splits the energy levels by an amount which depends on $\hat{\mathbf{J}}$, which takes values in the range of $|L - S| \leq J \leq |L + S|$. Due to the spherical symmetry of the interaction potential all three operators introduced above commute with each other and with the total electronic Hamiltonian for the atom[2]. Each combination of $\hat{\mathbf{L}}$ and $\hat{\mathbf{S}}$ corresponds to a unique level which by convention is written using the term symbol

$$\mathrm{n}^{2S+1}L_J \ , \tag{2.1}$$

where n is the principal quantum number which indicates the electron shell and $2S + 1$ is the spin multiplicity. The angular momentum quantum numbers are assigned letters {S,P,D,F...} depending on their magnitude $\{0, 1, 2, 3...\}$.

In atoms which have a non zero total nuclear spin $\hat{\mathbf{I}}$ the interaction with the electrons spin leads to the hyperfine structure- each level is further split into components determined by $\hat{\mathbf{F}}$, which takes values in the range $|J - I| \leq F \leq |J + I|$.

Structure of ^{87}Rb and optical transitions

The fine and hyperfine structures of ^{87}Rb are shown in figure 2.1. The P state is split into a pair of levels: transitions to $5^2\mathrm{P}_{1/2}$ are known as the D_1 line while transitions to $5^2\mathrm{P}_{3/2}$ are known as the D_2 line. The total nuclear spin is $I = 3/2$ and the energy levels are further shifted by an amount which depends on F.

Optical transitions on the D_1 line may be driven using 795 nm light while the D_2 line corresponds to a wavelength of 780 nm. Selection rules which govern the allowed electric dipole transitions are $\Delta F = 0, -1, +1$. From these it is evident that the $5^2\mathrm{S}_{1/2}(F = 2) \rightarrow 5^2\mathrm{P}_{3/2}(F = 3)$ transition is closed and thus meets the fundamental requirement of laser cooling. In practice, the laser light addressing the closed hyperfine transition may

[1] Here and in what follows $\hat{\mathbf{L}}$, $\hat{\mathbf{S}}$ and $\hat{\mathbf{J}}$ are vector operators. The eigenvalues of $\hat{\mathbf{L}}^2$, $\hat{\mathbf{S}}^2$ and $\hat{\mathbf{J}}^2$ are $\hbar^2 L(L+1)$, $\hbar^2 S(S+1)$ and $\hbar^2 J(J+1)$ respectively.

[2] As will be discussed below, diatomic molecules have cylindrical symmetry and the set of commuting operators are not always straightforward to identify.

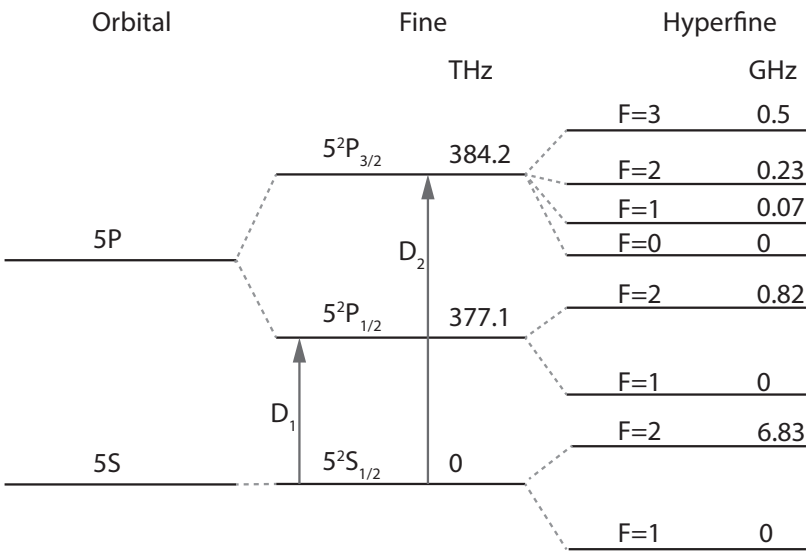

Figure 2.1: Energy level diagram of ^{87}Rb indicating the structure which is arises due to the fine and hyperfine interactions. The splitting energies are from [88] and the hyperfine splittings are given relative to the lowest hyperfine level in a given fine structure level.

off-resonantly drive atoms to $F = 2$ which can then decay to the $F = 1$ level in the ground state. This leak rate is typically quite small but requires an additional light component tuned to drive the $5^2\mathrm{S}_{1/2}(F = 1) \rightarrow 5^2\mathrm{P}_{3/2}(F = 2)$ transition.

In an external magnetic field the hyperfine levels are further split into $2F+1$ levels due to the Zeeman effect. Each magnetic sub-level is labelled as m_F and the electric dipole selection rules between these sub-levels are $\Delta m_F = 0, -1, +1$. The ground electronic state has a substantial magnetic moment, so atoms can be trapped magnetically in certain m_F states.

2.1.2 Diatomic molecules

In addition to the electronic energy level structure found in an atom, a diatomic molecule has the additional degrees of freedom corresponding to vibrations and rotations of the two nuclei. Using the Born-Oppenheimer approximation[3] the dynamics corresponding to each of these three degrees of freedom may be considered separately and the total energy is

$$E_{\mathrm{Tot}} = E_e + E_\nu + E_{\mathrm{Rot}} \ , \tag{2.2}$$

with E_e, E_ν and E_{Rot} the electronic, vibrational and rotational energies respectively. Electronic energies are typically $E_e/h \sim 500$ THz, vibrational energies $E_\nu/h \sim 10$ THz and rotational energies $E_{\mathrm{Rot}}/h \sim 10$ GHz. These three energy scales are discussed in more detail below.

[3]The main assumption of the Born-Oppenheimer approximation is that the motion of the electrons is much faster than the motion of the two nuclei. The electronic wavefunction may be parametrised and the Schrödinger equation solved to find the electronic energies for a set of different inter-nuclear separations.

Electronic structure

In a diatomic molecule the pair of nuclei enforce cylindrical symmetry around the internuclear axis. The total angular momentum operator defined for an alkali atom no longer commutes with the total electronic Hamiltonian and instead the projections of angular momentum onto the internuclear axis z are used to label different levels. The term symbol defined for atoms is replaced with a similar one of the following form

$$[\text{letter}]^{2S+1}\Lambda_{\Omega}^{(+/-)} \ . \tag{2.3}$$

Here the letter in front denotes the electronic state of the molecule and typically follows the convention of using letters {X, A, B, C,...} to label the {ground, second, third, fourth,...} electronic levels. The quantum number Λ is the projection of the angular momentum onto the internuclear axis and is labelled using capital Greek letters $\{\Sigma, \Pi, \Delta, ...\}$ which correspond to absolute values of the angular momentum projections $\{0, 1, 2, ...\}$. The quantum number Ω is the projection of the total angular momentum and finally the symbol $(+/-)$ is used to indicate the sign of the electronic wavefunction under reflection relative to a plane which contains the internuclear axis.

Vibrational structure

The second largest energy scale in a diatomic molecule corresponds to vibrations of the two nuclei relative to an equilibrium internuclear separation R_0. Up to first order, the internuclear potential is harmonic and the vibrational energies correspond to the eigenenergies of the quantum harmonic oscillator

$$E_\nu = \omega_e \left(\nu + \frac{1}{2}\right) \ , \tag{2.4}$$

where $\omega_e = \hbar\sqrt{k/m_{\text{R}}}$ is the vibrational constant[4] and ν is the vibrational quantum number. The harmonic approximation holds for internuclear separations close to R_0. As the vibrational energy is increased the two nuclei explore increasingly more of the in general anharmonic potential. For higher vibrational levels a better approximation to the vibrational energies is given by

$$E_\nu = \omega_e \left(\nu + \frac{1}{2}\right) - \omega_e x_e \left(\nu + \frac{1}{2}\right)^2 + \omega_e y_e \left(\nu + \frac{1}{2}\right)^3 - ... \ , \tag{2.5}$$

with $x_e, y_e, ...$ the anharmonicity constants. The constants of the first couple of terms in the above expansion for the X, A and B states of CaF may be found in [89].

[4] With k and m_{R} the nuclear spring constant and reduced mass of the nuclei respectively

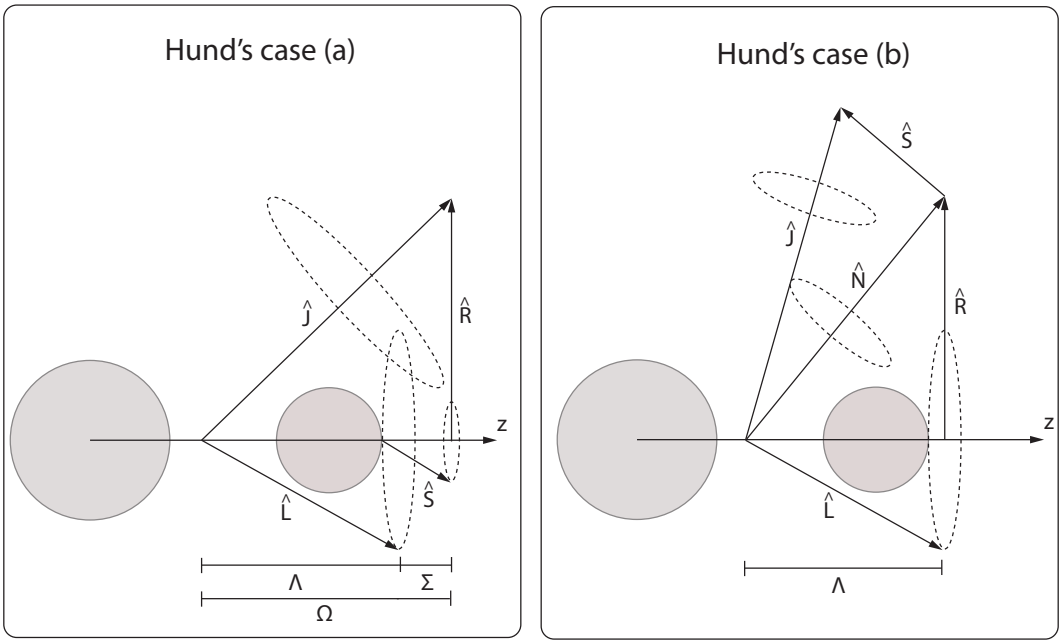

Figure 2.2: Hund's cases (a) and (b) described in more detail in the main text.

Rotational structure

Last but not least is the energy scale corresponding to rotations of the pair of nuclei around their centre of mass. As a first approximation the rotational motion is described well using the quantum rigid rotor model. The energy of a rigid rotor with moment of inertia I is given by

$$E_{\mathrm{Rot}} = BR(R+1) \ , \tag{2.6}$$

where $B = \hbar^2/2I$ is known as the rotational constant and R is the rotational quantum number. Again, in reality the situation is more complicated. Because of the vibrational motion of the nuclei the bond length is not fixed and this affects the moment of inertia. The rotational energy is better approximated by

$$E_{\mathrm{Rot}} = B_\nu R(R+1) - D_\nu R^2(R+1)^2 + ... \ , \tag{2.7}$$

where D_ν is the centrifugal distortion constant and the subscripts ν indicate that the constants depend on the vibrational quantum number.

Angular momentum structure

The various ways angular momenta and the rotation of the nuclei may couple lead to additional electronic structure that spans energies in the range of $E/h \sim 10^6 - 10^{12}$ Hz. These different coupling modes are typically described using a set of five rules known as Hund's coupling cases. The structure of most diatomic molecules including that of CaF is described well using Hund's cases (a) and (b).

Hund's case (a) is depicted in figure 2.2. The angular momentum $\hat{\mathbf{L}}$ strongly couples to the electron spin $\hat{\mathbf{S}}$ via the spin-orbit interaction, which is much larger than the rotational energy. In this case $\hat{\mathbf{L}}$ and $\hat{\mathbf{S}}$ couple to the internuclear axis due to the electrostatic interaction of the chemical bond and together with the total angular momentum $\hat{\mathbf{J}} = \hat{\mathbf{L}} + \hat{\mathbf{S}} + \hat{\mathbf{R}}$ have well defined projections labelled by the quantum numbers Λ, Σ and Ω respectively. More formally the good quantum numbers for this case are defined by the following equations

$$\hat{\mathbf{L}}_z \left|\Lambda\right\rangle = \hbar\Lambda \left|\Lambda\right\rangle \ , \tag{2.8}$$

$$\hat{\mathbf{S}}^2 \left|S, \Sigma\right\rangle = \hbar^2 S(S+1) \left|S, \Sigma\right\rangle \ , \tag{2.9}$$

$$\hat{\mathbf{S}}_z \left|S, \Sigma\right\rangle = \hbar\Sigma \left|S, \Sigma\right\rangle \ , \tag{2.10}$$

$$\hat{\mathbf{J}}^2 \left|J, \Omega\right\rangle = \hbar^2 J(J+1) \left|J, \Omega\right\rangle \ , \tag{2.11}$$

$$\hat{\mathbf{J}}_z \left|J, \Omega\right\rangle = \hbar\Omega \left|J, \Omega\right\rangle \ . \tag{2.12}$$

Here $\hat{\mathbf{L}}_z$, $\hat{\mathbf{S}}_z$ and $\hat{\mathbf{J}}_z$ are the operators which project the momenta onto the internuclear axis z.

In Hund's case (b) the coupling between $\hat{\mathbf{L}}$ and $\hat{\mathbf{S}}$ is very weak or vanishes completely for Σ state molecules. In this case the rotational angular momentum $\hat{\mathbf{R}}$ first couples to $\hat{\mathbf{L}}$ to form $\hat{\mathbf{N}} = \hat{\mathbf{R}} + \hat{\mathbf{L}}$ which then interacts with the electrons spin $\hat{\mathbf{S}}$ to form the total angular momentum $\hat{\mathbf{J}}$. For this case the good quantum numbers are defined by

$$\hat{\mathbf{L}}_z \left|\Lambda\right\rangle = \hbar\Lambda \left|\Lambda\right\rangle \ , \tag{2.13}$$

$$\hat{\mathbf{N}}^2 \left|(N, S), J\right\rangle = \hbar^2 N(N+1) \left|(N, S), J\right\rangle \ , \tag{2.14}$$

$$\hat{\mathbf{S}}^2 \left|(N, S), J\right\rangle = \hbar^2 S(S+1) \left|(N, S), J\right\rangle \ , \tag{2.15}$$

$$\hat{\mathbf{J}}^2 \left|(N, S), J\right\rangle = \hbar^2 J(J+1) \left|(N, S), J\right\rangle \ . \tag{2.16}$$

2.1.3 Structure of CaF

The CaF molecule has an ionic bond: a ^{40}Ca atom gives away one of its outer shell electrons to a ^{19}F atom with the remaining unpaired electron mostly localised around the Ca atom. The unpaired electron thus does not contribute to the bond. As will be discussed in section 2.1.4 this fact is responsible for the desirable property of CaF that after electronic excitation the molecule relaxes to the same vibrational level most of the time. The molecule has a nuclear spin of $I = 1/2$ due to the fluorine atom which gives rise to hyperfine structure in the ground and excited electronic states. Figure 2.3 shows a diagram of the relevant energy levels of CaF. Below is a description of each of these electronic states and the interactions which lead to the various energy splittings.

The $X^2\Sigma^+$ state

The ground electronic state of CaF is described by the term symbol $X^2\Sigma^+$ and is usually called a doublet-sigma state. It has an electron spin of $S = 1/2$ while the projection of the angular momentum onto z is zero. This state is best described using Hund's case (b) as the spin-orbit interaction completely vanishes. The total angular momentum is $\hat{\mathbf{J}} = \hat{\mathbf{S}} + \hat{\mathbf{R}}$ and each rotational level, except $N = 0$, is split into two with quantum numbers[5] $J = N \pm 1/2$ due to the spin-rotation interaction. Each of these pairs of states couples to the nuclear spin and give rise to the hyperfine structure with $F = N + 1, N^+, N^-, N - 1$ levels. The hyperfine interaction mixes the two states that have $F = N$ so that they are each a mixture of the $J = 1/2$ and $J = 3/2$ levels. Because the spin-rotation and hyperfine interactions are of similar strength the different levels which arise due to both of these interactions are typically thought to all be a part of the same hyperfine manifold. To distinguish between the levels with equal F the superscripts +/- are used, with the + state being the higher energy one. The electronic ground state has a substantial magnetic moment which can be used to trap the molecule magnetically. The parity of the rotational states alternates: $N = 0$ is even, $N = 1$ is odd, and so on.

The $A^2\Pi_{1/2}$ state

The first excited electronic state in CaF is $A^2\Pi_{1/2}$. Because this state has a non-zero angular momentum the spin-orbit interaction dominates over the rotational energy and Hund's case (a) is best suited for describing how the momenta couple. The spin-orbit interaction splits the electronic states into a pair of levels corresponding to projections of the total angular momentum of $\Omega = 1/2$ and $\Omega = 3/2$. These pair of states couple to the rotation which splits the levels into components with $\hat{\mathbf{J}} = \hat{\mathbf{\Omega}} + \hat{\mathbf{R}}$. Opposite parity states can be formed from the different angular momentum projection states $|\pm\rangle = |\Lambda = 1\rangle \pm |\Lambda = -1\rangle$. In the absence of any other interactions the opposite parity states are degenerate but here the Π states is mixed with the second electronically excited state $B^2\Sigma^+$ to remove the degeneracy. This effect is known as Λ-doubling and for the term $\Omega + R = 1/2$ leads to the pair of states labelled here as $J = 1/2, -$ and $J = 1/2, +$. In this work the positive parity state which lies 1.36 GHz above the negative parity state is addressed with a laser. Finally, the $J = 1/2, +$ level is further split due to the interaction between the electron and nuclear spins which gives rise to the pair of hyperfine levels $F = 0, 1$ separated by around 5 MHz.

[5] Because the electron orbital angular momentum is zero, $\hat{\mathbf{N}} = \hat{\mathbf{R}}$.

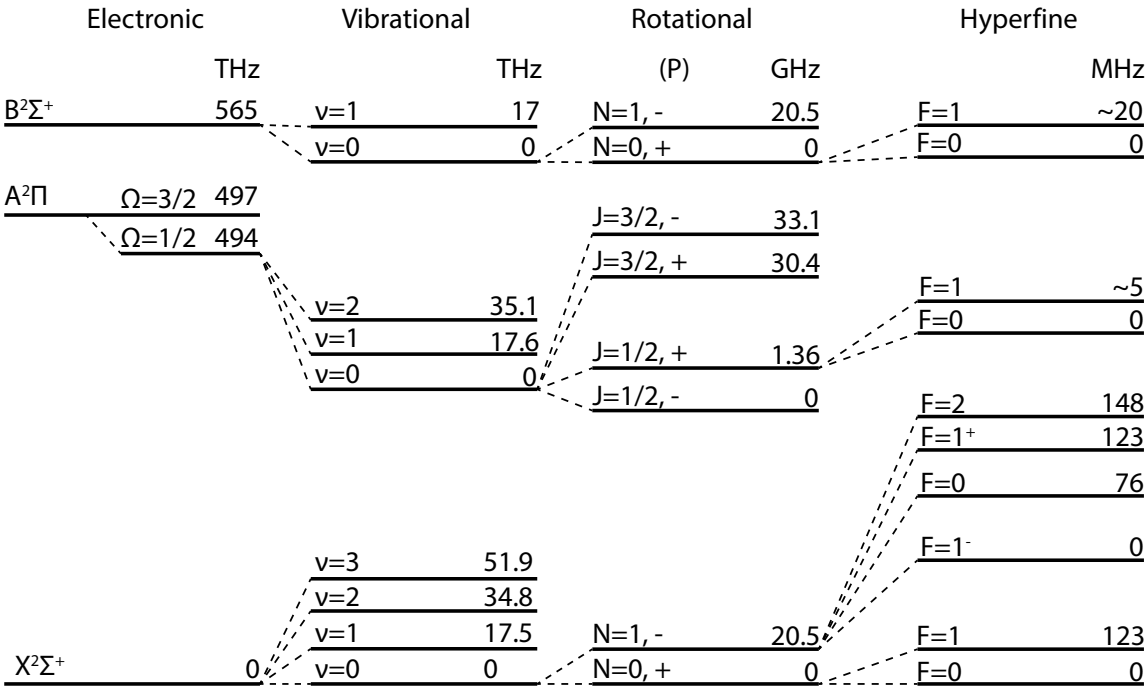

Figure 2.3: Energy level structure of the X, A, B electronic states of CaF relevant for work described in this thesis. The different energy scales corresponding to electronic, vibrational, rotational and hyperfine levels are separated out into different panels. All energies are expressed in frequency units and are indicated relative to the lowest lying level in each of the manifolds.

The $B^2\Sigma^+$ state

The second electronically excited state in CaF is $B^2\Sigma^+$ and has a similar structure to the X state described above. For this state Hund's case (b) can be used to describe the angular momentum structure. In this work only the $N = 0$ rotational level is addressed which is split by the hyperfine interaction into a pair of levels separated by around 20 MHz.

2.1.4 Transitions in CaF

With the detailed energy level structure of the CaF molecule at hand methods of accessing the different quantum states will be looked at here.

Optical transitions and rotational branching

The CaF molecule may be excited to the A and B states by driving electric dipole transitions with laser light at wavelengths of 606 nm and 531 nm respectively. The A state decays to the X state at a rate of $2\pi \times 8.3$ MHz while the B state has a decay rate of $2\pi \times 6.3$ MHz. In addition the B state may decay to the ground state via the A state but the branching ratio for this two-photon route is only around 10^{-5}. Allowed transitions

are given by the electric dipole selection rules

$$\Delta P = \pm 1 \ , \tag{2.17}$$

$$\Delta F = 0, \pm 1 \ (\text{not } F = 0 \rightarrow F' = 0) \ , \tag{2.18}$$

$$\Delta m_F = 0, \pm 1 \ (\text{not } \Delta m_F = 0 \text{ if } \Delta F = 0) \ . \tag{2.19}$$

To sustain optical cycling on any pair of these transitions care must be taken to address the correct rotational/total angular momentum levels. A CaF molecule excited to the $A^2\Pi_{1/2}(\nu' = 0, J = 1/2, +)$ state will only be able to decay to the $X^2\Sigma^+(\nu = 0, N = 1)$ state due to parity and angular momentum ($\Delta J = 0, \pm 1$) selection rules. Thus by tuning the laser frequency to drive the $A^2\Pi_{1/2}(\nu' = 0, J = 1/2, +) \leftarrow X^2\Sigma^+(\nu = 0, N = 1)$ transition rotational branching to states with other values of R is eliminated. Finding such transitions in a diatomic molecule is a key step towards successful application of laser cooling and was first reported in [90]. Similarly, the second electronically exited state is accessed by driving the $B^2\Sigma^+(\nu' = 0, N = 0) \leftarrow X^2\Sigma^+(\nu = 0, N = 1)$ transition.

Vibrational branching

The allowed transitions between different vibrational levels are not restricted by selection rules. Instead, a molecule excited from the ground electronic level with vibrational quantum number ν to some higher electronic level with ν' will decay back to any vibrational level ν'' in the ground state with a probability given by the Franck-Condon (FC) factor

$$P_{\nu',\nu''} = \left| \int f_{X,\nu''}(R) f_{A,\nu'}(R) \ dR \right|^2 \ . \tag{2.20}$$

This quantity corresponds to the square of the overlap between the vibrational wavefunctions of the ground and excited electronic states. To sustain optical cycling when driving a transition between a pair of vibrational levels it is desirable to have $P_{\nu',\nu''} \approx 1$ which means finding a molecule where the matrix of all FC factors is highly diagonal. Physically this implies that excitation of the electron should not affect significantly the internuclear bond length or strength. For the CaF molecule this turns out to be the case: the internuclear potentials for the A and B states have very similar equilibrium bond lengths R_0 and harmonic frequencies ω_e to that of the ground electronic state. The vibrational wavefunctions with ν' in the two excited states have a large overlap with the vibrational functions in the ground state with $\nu'' = \nu'$. The excited electronic states A and B have FC factors $P_{0,0} = 0.97$ and $P_{0,0} = 0.998$ respectively [91] and with the addition of only a few vibrational repumpers allow to scatter many photons.

2.2 Interaction with light

In the previous section the detailed energy level structures of a Rb atom and a CaF molecule were presented. In situations when a laser beam frequency is tuned to interact with only a pair of internal states the complexity reduces to that of a two-level quantum system. Here the attention is focused towards describing how such a system interacts with monochromatic light.

2.2.1 Optical Bloch equations

Consider a two-level atom at position $z = 0$ with ground and excited state energies equal to $E_0 = 0$ and $E_1 = \hbar\omega_1$. The atom interacts with the electric field of a laser beam which is propagating along the z-axis. The field has a frequency ω, an amplitude $\mathcal{E}_0$ and is given by

$$\mathcal{E}(t) = \hat{\epsilon}\mathcal{E}_0 \cos(kz - \omega t) \ , \tag{2.21}$$

with $k = 2\pi/\lambda$ the wave vector and $\hat{\epsilon}$ the polarization of the electric field. The two level atom is described by a 2x2 density matrix $\hat{\rho}$. The diagonal entries ρ_{00} and ρ_{11} correspond to the atomic populations in the ground and excited states respectively while the off-diagonal elements ρ_{01} and ρ_{10} are known as the coherences which describe the interaction with light. The electric field of the laser beam induces an electric dipole moment in the atom which may be written as

$$\langle \hat{d} \rangle = -\mathcal{D}_0(\widetilde{\rho}_{01}e^{-i\omega t} + \widetilde{\rho}_{10}e^{i\omega t}) \ , \tag{2.22}$$

with $\widetilde{\rho}_{01} = \rho_{01}e^{i\Delta t}$ and $\widetilde{\rho}_{10} = \rho_{10}e^{-i\Delta t}$, the frequency detuning $\Delta = \omega - \omega_1$ and the dipole matrix element $\mathcal{D}_0 = \langle 0 | \hat{d} | 1 \rangle$. Here $\hat{d}$ is the electric dipole moment operator. The matrix elements of $\hat{\rho}$ for a two-level system which is damped at a rate Γ are found by solving the optical Bloch equations in the rotating wave approximation:

$$\dot{\rho}_{00} = \Gamma\rho_{11} - i\frac{\Omega}{2}(\widetilde{\rho}_{10} - \widetilde{\rho}_{01}) \ , \tag{2.23}$$

$$\dot{\rho}_{11} = -\Gamma\rho_{11} + i\frac{\Omega}{2}(\widetilde{\rho}_{10} - \widetilde{\rho}_{01}) \ , \tag{2.24}$$

$$\dot{\widetilde{\rho}}_{01} = -\left(\frac{\Gamma}{2} + i\Delta\right)\widetilde{\rho}_{01} + \frac{i\Omega}{2}(\rho_{00} - \rho_{11}) \ , \tag{2.25}$$

$$\dot{\widetilde{\rho}}_{10} = -\left(\frac{\Gamma}{2} - i\Delta\right)\widetilde{\rho}_{10} - \frac{i\Omega}{2}(\rho_{00} - \rho_{11}) \ . \tag{2.26}$$

Here $\Omega = \mathcal{D}_0\mathcal{E}_0/\hbar$ is the Rabi frequency which describes the strength of the interaction between the driving field and the induced dipole moment. It takes a time $\sim 1/\Gamma$ for the system to reach a steady state. By setting the time derivatives to zero and remembering

that $Tr\{\hat{\rho}\} = 1$, the steady state solutions for the density matrix elements are obtained:

$$\rho_{00}^{(s)} = 1 - \rho_{11}^{(s)} \ , \tag{2.27}$$

$$\rho_{11}^{(s)} = \frac{\Omega^2}{\Gamma^2 + 4\Delta^2 + 2\Omega^2} \ , \tag{2.28}$$

$$\widetilde{\rho}_{01}^{(s)} = \frac{i\Omega(\Gamma - 2i\Delta)}{\Gamma^2 + 4\Delta^2 + 2\Omega^2} \ , \tag{2.29}$$

$$\widetilde{\rho}_{10}^{(s)} = \widetilde{\rho}_{01}^{(s)*} \ . \tag{2.30}$$

The star in the last equation above denotes the complex conjugate. The relaxation constant Γ is known as the spontaneous decay rate and is given by

$$\Gamma = \frac{\omega_0^3 |\mathcal{D}_0|^2}{\pi \epsilon_0 \hbar c^3} \ . \tag{2.31}$$

An important observation from the equation above is that the decay rate is a strong function of the resonance frequency ω_0. For closely spaced levels the decay rate of the excited states becomes small and the driving field sustains long periodic oscillations between the ground and excited state populations. The time evolution of the population in the excited state when $\Gamma = 0$ is given by

$$\rho_{11}(t) = \frac{\Omega^2}{\Omega^2 + \Delta^2} \sin^2\left(\frac{\sqrt{\Omega^2 + \Delta^2}\ t}{2}\right) \ . \tag{2.32}$$

This effect is known as Rabi flopping. A resonant laser beam will transfer all of the population into the excited state in a time $t_\pi = \pi/\Omega$ and is commonly called a π pulse. A pulse of duration $t_{\pi/2} = \pi/2\Omega$ will create a coherent superposition of the ground and excited states.

2.2.2 The scattering and dipole forces

It is insightful to decompose the steady state induced dipole moment into parts which oscillate in phase and out of phase with the driving field. Expanding the complex exponentials in eq. 2.22 into their real and imaginary parts gives

$$\langle \hat{d}^{(s)} \rangle = -\mathcal{D}_0 \left[u^{(s)} \cos\omega t + v^{(s)} \sin\omega t \right] \ , \tag{2.33}$$

where

$$u^{(s)} = \widetilde{\rho}_{01}^{(s)} + \widetilde{\rho}_{10}^{(s)} \ , \tag{2.34}$$

$$v^{(s)} = -i(\widetilde{\rho}_{01}^{(s)} - \widetilde{\rho}_{10}^{(s)}) \ , \tag{2.35}$$

are found using the steady state solutions of the optical Bloch equations. The response of a dipole to an electric field $\mathcal{E}$ of a laser beam propagating along the z-axis may be characterized via the linear relation $\langle \hat{d}^{(s)} \rangle = \alpha \mathcal{E}$, where α is called the polarizability. The

induced dipole interacts with the driving field itself [92] and this interaction energy is given by

$$U = -\frac{1}{2}\alpha\mathcal{E}^2 \ . \tag{2.36}$$

Because of this interaction the atom experiences a force along the z-axis given by

$$F_z = -\frac{\partial U}{\partial z} = \langle\hat{d}^{(s)}\rangle\frac{\partial\mathcal{E}}{\partial z} \ . \tag{2.37}$$

Inserting eq. 2.33 into the above and taking the spatial derivative of the electric field, the time averaged force which the atom experiences may be written as

$$\bar{F}_z = -\frac{\mathcal{D}_0}{2}\left(u^{(s)}\frac{\partial\mathcal{E}_0}{\partial z} - v^{(s)}\mathcal{E}_0 k\right) \ . \tag{2.38}$$

In the above the relations $\overline{\cos^2(\omega t)} = \overline{\sin^2(\omega t)} = 1/2$ and $\overline{\cos(\omega t)\sin(\omega t)} = 0$ were used to obtain the average over several periods of the laser field. The total force depends on both the in-phase and out of phase components of the induced dipole. By inserting eqs. 2.34 and 2.35 into eq. 2.38 and using $\Omega = \mathcal{D}_0\mathcal{E}_0/\hbar$ the force experienced by the atom may be written in a more useful form

$$\bar{F}_z = \hbar k\frac{\Gamma}{2}\frac{\Omega^2/2}{\Delta^2 + \Omega^2/2 + \Gamma^2/4} - \frac{\hbar}{2}\frac{\Delta\Omega}{\Delta^2 + \Omega^2/2 + \Gamma^2/4}\frac{\partial\Omega}{\partial z} \ . \tag{2.39}$$

The first term in the above equation is the force which arises due to the interaction with the out of phase component of the induced dipole and is called the scattering force $F_{\rm sc}$. The scattering force saturates when $\Omega >> \Gamma$ at a value of $F_{\rm sc} = \hbar k\Gamma/2$ and, as will be demonstrated below, may be used to decelerate and cool atoms. On the other hand, the force corresponding to the second term in the equation above does not saturate. It vanishes when $\Delta = 0$ or when the laser field has no spatial variation. This force is commonly known as the dipole force $F_{\rm dip}$ and for $|\Delta| >> \Omega$ may be written as

$$F_{\rm dip} = -\frac{\partial}{\partial z}\left(\frac{\hbar\Omega^2}{4\Delta}\right) \ . \tag{2.40}$$

The term in brackets in the equation above corresponds to a shift in the ground state energy of the atom due to the interaction with the laser field. This change in energy is commonly known as the light or AC Stark shift. For $\Delta < 0$ the dipole force acts in the direction of increasing light shift and since the laser intensity $I \propto \Omega^2$ the dipole force may be used to confine atoms in the focus of an off-resonant laser beam. In addition, as will be discussed below, the light shift plays an important role in laser cooling.

2.2.3 Doppler cooling

Intuitively, the scattering force arises when an atom absorbs and subsequently emits photons. Each absorbed photon imparts a momentum $\hbar k$ along the direction of the laser beam while spontaneously emitted photons propagate along random directions. After

many absorption-emission cycles, the photons transfer a net momentum to the atom along the direction of the laser beam. On the other hand, the net momentum due to spontaneously emitted photons averages out to zero. Thus $F_{\rm sc}$ depends on the photon scattering rate $R_{\rm sc} = \Gamma\rho_{11}^{(s)}$ and may be written as $F_{\rm sc} = \hbar k R_{\rm sc}$. Using eq. 2.39 an atom will scatter photons out of a laser beam with intensity $I = \frac{1}{2}c\epsilon_0\mathcal{E}_0^2$ at a rate of

$$R_{\rm sc} = \frac{\Gamma}{2}\frac{I/I_{\rm sat}}{1 + 4\Delta^2/\Gamma^2 + I/I_{\rm sat}} \ . \tag{2.41}$$

Here $I_{\rm sat}$ is the saturation intensity given by

$$I_{\rm sat} = \frac{\pi hc\Gamma}{3\lambda^3} \ . \tag{2.42}$$

The scattering force may be used to reduce the velocity and ultimately the temperature of a collection of atoms. Consider an atom moving with velocity v along the z-axis and interacting with two counter-propagating laser beams of detuning Δ. In the reference frame of the atom the frequency of the laser beam which is propagating against the direction of the atoms motion is shifted higher by an amount $\Delta_D = kv$ due to the Doppler effect. The frequency of the second beam appears to be smaller in the reference frame of the atom by an amount $-kv$. In the low intensity regime where stimulated emission may be ignored, the total force experience by the two-level atom is given by

$$F_{\rm Tot} = F_{\rm sc}^{(+z)}(\Delta - kv) - F_{\rm sc}^{(-z)}(\Delta + kv) \ . \tag{2.43}$$

For low velocities, the total force may be found by expanding the above expression around $v = 0$ in a Taylor series

$$F_{\rm Tot} = -\beta v \ , \tag{2.44}$$

with the damping constant given by

$$\beta = -\frac{8s\Delta\hbar k^2}{\Gamma(1 + s + 4\Delta^2/\Gamma^2)^2} \ . \tag{2.45}$$

Here $s = I/I_{\rm sat}$ is the saturation parameter. For a negative frequency detuning the total force opposes the motion of the atom and it is cooled towards $v = 0$. A positive frequency detuning results in a total force which pushes the atom along the direction of its velocity and thus results in heating. The damping force arises for $\Delta < 0$ is used to cool atoms and molecules and is, rather intuitively, known as the optical molasses technique. In practice the scheme is extended to 3D by adding two additional pairs of counter-propagating beams along the other pair of orthogonal directions.

Doppler cooling limit

The randomness of momentum kicks imparted to the laser cooled particle due to photon absorption and emission events will increase the average kinetic energy at a rate of

$$P_{\rm heat} = \frac{dE}{dt} = \frac{(\hbar k)^2 R_{\rm sc}}{m} \ , \tag{2.46}$$

where $dE = (\hbar k)^2(R_{\rm sc}dt)/m$ is the kinetic energy gained by a particle in a time dt which scatters photons at a rate $R_{\rm sc}$. On the other hand, the optical molasses cools the particles at a rate of

$$P_{\rm cool} = \frac{-2\beta E}{m} \ , \tag{2.47}$$

with β the damping constant which for the case of a two-level system was defined in eq. 2.45. In the steady state the heating and cooling powers are equal. Assuming the velocities of laser cooled particles are described by a Maxwell-Boltzamann distribution the average kinetic energy may be linked to temperature via the equipartition theorem and the equilibrium temperature may be found by equating eqs. 2.46 and 2.47. This is known as the Doppler temperature

$$T_{\rm D} = \frac{(\hbar k)^2 R_{\rm sc}}{3\beta k_{\rm B}} \ , \tag{2.48}$$

which quantifies the lowest achievable temperature when laser cooling relies only on the scattering force. Using the definitions of the damping constant (eq. 2.45) and the scattering rate (eq. 2.41) the Doppler temperature may be rewritten as

$$T_{\rm D} = -\frac{\hbar\Gamma^2}{8k_{\rm B}\Delta}\left(1 + s + \frac{4\Delta^2}{\Gamma^2}\right) \ , \tag{2.49}$$

with the minimum temperature obtained when using a laser frequency detuning of $\Delta = -\frac{1}{2}(1+s)^{1/2}\Gamma$. In the limit of $s \to 0$, for ^{87}Rb atoms cooled on the D_2 transition $T_{\rm D}^{\rm min} = 145\ \mu$K while for CaF molecules cooled using the A-X transition $T_{\rm D}^{\rm min} = 199\ \mu$K.

2.2.4 Sub-Doppler cooling

Soon after the first laser cooling experiments using Na atoms, temperatures far below the Doppler limit were obtained [93]. The experimental observations suggested the presence of new cooling mechanisms and the first theoretical explanations were provided by Jean Dalibard and Claude Cohen-Tannoudiji [94]. The authors identified two novel laser cooling schemes which do not rely on the scattering force but rather arise in multi-level systems interacting with laser light with spatial polarization gradients.

In the first sub-Doppler scheme an atom with $J = 1/2$ in the ground state and $J' = 3/2$ in the excited state is exposed to a pair of counter-propagating red-detuned laser beams which have orthogonal linear polarizations. The polarization varies spatially from linear to circular with a period of $\lambda/2$. The coupling strength of the laser field to the atom depends on the local polarization and is quantified by the Clebsch-Gordan coefficients. Thus the pair of ground state levels will experience a different (negative) light shift which will oscillate in magnitude as the atom moves through the polarization gradient. Figure 2.4 illustrates this arrangement: the $m_J = +1/2$ magnetic sub-level at a position where the local polarization is σ^+ will have a greater light shift than the $m_J = -1/2$ level. When

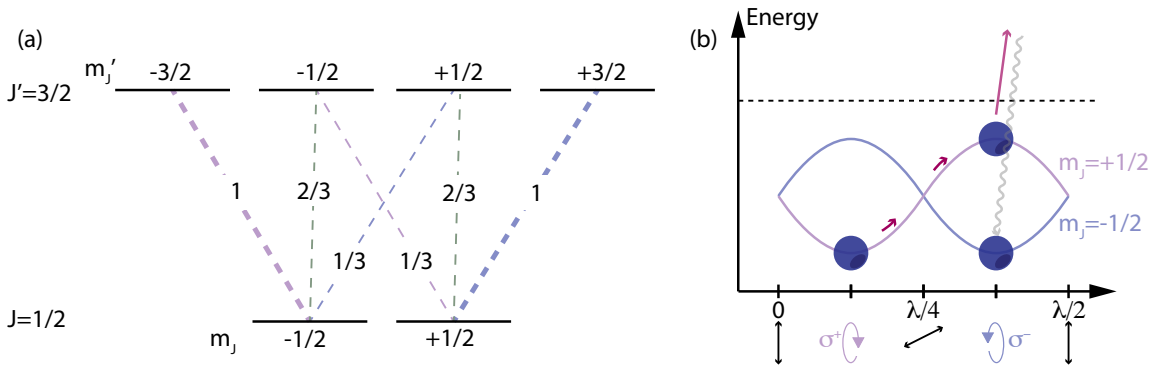

Figure 2.4: Sisyphus cooling mechanism. (a) Energy levels of an atom with $J = 1/2$ in the ground state and $J' = 3/2$ in the excited state. Numbers next to the dashed lines are the relative transition strengths. (b) Polarization dependent light shifts of the ground magnetic sub-levels. The dashed line is the field free energy. An atom climbs a potential hill and close to the top is optically pumped into a state with a more negative light shift.

the atom moves in either direction the kinetic energy is converted into internal energy as the light shift becomes more positive. At the position where the local polarization is reversed to σ^+ the atom may be excited to $m'_J = -1/2$ and due to a higher branching ratio it will be optically pumped into $m_J = -1/2$ where it will again experience a more negative light shift. In this idealised case the atom loses kinetic energy proportional to the light shift $E_\mathrm{k} \propto \hbar\Omega^2/\Delta$. Provided that optical pumping occurs on a similar time scale compared to the motion of the atom through the polarization gradient, the atom will carry on climbing potential hills and thus continue to lose kinetic energy. This mechanism of energy dissipation is widely known as Sisyphus cooling. If the frequency detuning is reversed to positive, the atom will instead go down the potential hills and on average gain kinetic energy.

In the second sub-Doppler cooling scheme the two beams have opposite circular polarizations. It requires at least 3 magnetic sub-levels in the ground state. This situation is encountered more frequently in practice as circularly polarized light is required to form a magneto-optical trap (Chapter 4). In this case the polarization is linear everywhere thus the light shift is the same for all of the ground state sub-levels. An atom at rest will scatter photons at the same rate from each laser beam because the $m_J = -1, +1$ levels are equally populated. On the other hand, an atom moving towards the beam which drives σ^+ transitions will have its population biased towards $m_J = +1$ due to an effect known as motion-induced orientation. Because σ^+ light couples more strongly to an atom in the $m_J = +1$ than the counter-propagating beam which drives σ^- transitions, a net damping force is experienced by the atom.

In practice the temperature of atoms is first reduced with the help of Doppler cooling. When the atom velocity is sufficiently low sub-Doppler mechanisms described above become effective. From eq. 2.39 the scattering force is $F_\mathrm{sc} \propto I/\Delta^2$ for large Δ while

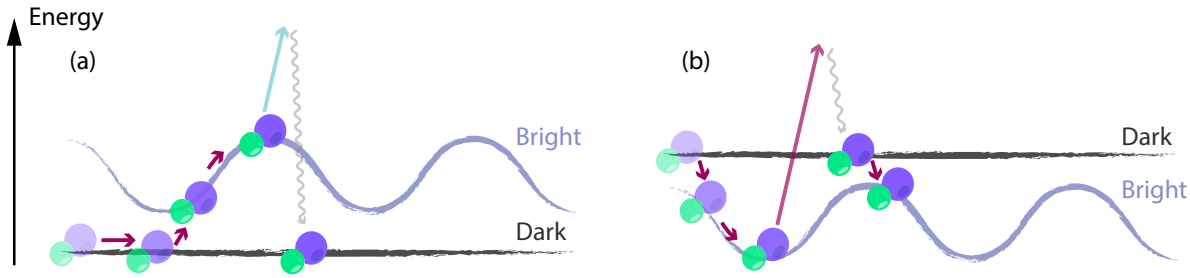

Figure 2.5: Laser cooling in the presence of dark states. (a) The cooling light is blue-detuned so that the light shift is positive for bright states. Molecules make non-adiabatic transitions from dark to bright states where they climb potential hills and lose kinetic energy. Close to the top of the hill a molecule is optically pumped to the dark state. (b) The cooling light is red-detuned. In this case non-adiabatic transitions have a higher probability close to the top of the potential hills and the molecule gains kinetic energy.

the dipole force $F_{\text{dip}} \propto I/\Delta$. Thus after cooling in a regular optical molasses the laser detuning is commonly increased further to the red in order to reduce heating due to spontaneous scattering while still retaining a substantial light shift to sustain sub-Doppler cooling mechanisms.

Sub-Doppler cooling of molecules

In systems with an angular momentum structure $J' \geq J$ there always exist dark states [95]. Dark states are internal states of the molecule which do not couple to the cooling light for a given polarization. As discussed in section 2.1.4, laser cooling of molecules works using transitions which have a larger total angular momentum in the excited state in order to avoid leakage to other rotational states not addressed by the laser light. Because dark states do not experience a light shift it is interesting to consider how sub-Doppler cooling using this type of transition may proceed.

Figure 2.5(a) illustrates the key concept behind sub-Doppler cooling in the presence of a dark state. A pair of counter-propagating laser beams which are now blue-detuned are linearly polarized at an angle ϕ. For $0 < \phi < \pi/2$, both polarization and intensity gradients are present. The bright state couples to the light and due to the intensity gradient experiences a position dependent light shift. Because the polarization varies in space a molecule may make a non-adiabatic transition from a dark to a bright state. It turns out that the probability of these transitions is maximum when the difference in the bright and dark state energies is minimum, which also corresponds to locations where the light shift of the bright state is smallest. A molecule will climb a potential hill before being optically pumped back into the dark state [6]. Provided the motion occurs at a timescale

[6]The molecule is more likely to be optically pumped in regions with high intensity as the scattering rate $R_{\text{sc}} \propto I$.

similar to the time it takes to optically pump the molecule, it will continue to climb potential hills and lose kinetic energy. In figure 2.5(b) the cooling beams are red-detuned and the bright state has a negative light shift. Molecules will on average gain kinetic energy and thus be heated. Laser cooling in the presence of dark states was first demonstrated for atoms [96] and more recently applied to diatomic molecules [97, 98, 99, 100] to obtain temperatures of around 5 μK.

It is worth mentioning here that there exists another scheme which works when the pair of beams have the same polarizations ($\phi = 0$). In this case there is only an intensity gradient and dark states are destabilized using a magnetic field. Choosing a magnetic field such that the precession from a dark to a bright state occurs on the time scale for a molecule to move through half a period of the standing wave again ensures that the molecule continues to climb potential hills and lose kinetic energy. Sub-Doppler cooling mechanisms which rely on a magnetic field to destabilise dark states are known as magnetically assisted Sisyphus cooling [101, 102].

The topic of Doppler and Sisyphus cooling of molecules will be revisited again in Chapter 7 in the context of transverse cooling of a beam of CaF molecules.

Recoil temperature

The sub-Doppler cooling mechanisms described above do not rely on the scattering force; thus, a different limit may be placed on the minimum achievable temperatures using laser cooling. It corresponds to the energy gained by an atom when it spontaneously emits a photon and is known as the recoil temperature

$$T_{\mathrm{r}} = \frac{\hbar^2 k^2}{2 m k_{\mathrm{B}}} \, . \tag{2.50}$$

For ^{87}Rb atoms cooled on the D_2 line, $T_{\mathrm{r}} = 181$ nK while for CaF molecules cooled using the A-X transition $T_{\mathrm{r}} = 442$ nK.

2.2.5 Scattering rate for a multi-level system

A system with multiple ground states will require more than one laser frequency to keep on cycling photons. For a number f_g of ground states coupled to f_e excited states the total scattering rate is given by[7] [103]

$$R_{\mathrm{sc}} = \Gamma \frac{f_e}{(f_g + f_e) + \sum_{j=1}^{f_g} \left(1 + \frac{4\Delta_j^2}{\Gamma^2}\right) \frac{I_{s,j}}{I_j}} \, , \tag{2.51}$$

where the indices j indicate the transition which is being driven by the laser component with intensity I_j and detuning Δ_j. The saturation intensities for each individual transition

[7] This result is derived by solving a set of rate equations which do not include quantum mechanical coherences.

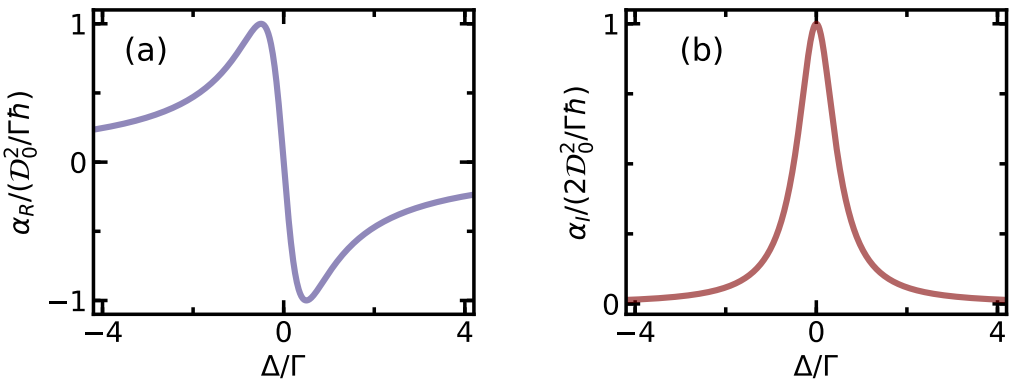

Figure 2.6: Real(a) and imaginary(b) parts of the complex polarizability of a two-level atom plotted as a function of laser frequency detuning Δ.

are labelled as $I_{s,j}$. In the case where each laser component has the same intensity I and detuning Δ the scattering rate may be written in the same form as for the two-level system

$$R_{\rm sc} = \frac{\Gamma_{\rm eff}}{2}\frac{s_{\rm eff}}{1+s_{\rm eff}+\frac{4\Delta^2}{\Gamma^2}}\ , \tag{2.52}$$

with the effective decay rate $\Gamma_{\rm eff} = 2\Gamma f_e/(f_g+f_e)$ and the effective saturation parameter $s_{\rm eff} = 2I(f_g+f_e)/I_s f_g^2$. Thus a multi-level system will have a scattering rate which is lower than for a two-level system and will typically require a larger laser intensity to saturate $R_{\rm sc}$.

2.2.6 Light absorption and refractive index

A laser beam propagating through a gas will induce dipole moments in the constituent particles. These dipoles oscillate at the same frequency as the driving field and contribute to the excitation field with a frequency detuning dependent phase. When working with multiple waves it is easier to use complex notation and it is common to define a complex polarizability. For low laser light intensities when $\Omega << \Gamma$ it may be written as

$$\alpha = -\frac{\mathcal{D}_0^2}{\hbar}\frac{1}{\Delta+i\Gamma/2}\ . \tag{2.53}$$

The induced dipole moment $\langle\hat{d}^{(s)}\rangle = \alpha\mathcal{E}_0$ is then a complex quantity. The real and imaginary parts of the polarizability are given by

$$\alpha_R = -\frac{\mathcal{D}_0^2}{\hbar}\frac{\Delta}{\Delta^2+(\Gamma/2)^2}\ , \tag{2.54}$$

$$\alpha_I = \frac{\mathcal{D}_0^2}{\hbar}\frac{\Gamma/2}{\Delta^2+(\Gamma/2)^2}\ . \tag{2.55}$$

To understand how the induced dipole moments affect the incident field consider a plane wave $\mathcal{E}_0 e^{i(kz-\omega t)}$ propagating through a medium with an atom number density of

$N(x,y,z)$. It may be shown [104] that the total field (incident plus the field due to the induced dipoles) is given by

$$\mathcal{E}(x,y,z) = \mathcal{E}_0 \exp\left(i\int_{-\infty}^{z}\left(1+\frac{1}{2}\chi_R\right)k\ dz'\right)\exp\left(-\frac{1}{2}\int_{-\infty}^{z}\chi_I k\ dz'\right)\ , \tag{2.56}$$

with χ_R and χ_I the real and imaginary parts of the complex susceptibility defined as

$$\chi(x,y,z) = \frac{N(x,y,z)}{\epsilon_0}\left(\alpha_R + i\alpha_I\right)\ . \tag{2.57}$$

Two important observations can be made from eq. 2.56. Firstly, the electric field of the propagating wave is attenuated at a rate proportional to $\chi_I k$, also known as the extinction coefficient. Secondly, the wave accumulates a total phase given by

$$\phi(x,y,z) = \left(\int_{-\infty}^{z}\left(1+\frac{1}{2}\chi_R\right)\ dz'\right)k\ , \tag{2.58}$$

which allows to define the refractive index of the medium as

$$n = 1+\frac{1}{2}\chi_R\ . \tag{2.59}$$

Thus the imaginary part of α is responsible for attenuation of the beam while the real part is responsible for refraction. For $\Delta = 0$ the phase of the input wave is left unchanged (except for the propagation phase e^{ikz}). In figure 2.6 the real and imaginary parts of the polarizability are plotted as a function of laser detuning.

2.3 Scattering theory

The collisional properties between atoms and molecules at low temperatures are important in understanding the limitations of sympathetic and evaporative cooling. For collisional cooling to be efficient, the rate of elastic collisions must be much larger than the rate of inelastic collisions. In this section some basic concepts relevant to elastic scattering at low temperatures are briefly described. The single-channel loss model [105] is introduced, which is used later in this work to describe the inelastic scattering properties of the CaF-Rb system.

2.3.1 Elastic scattering: partial waves and s-wave regime

Consider two structureless particles with masses m_1 and m_2 interacting via a potential $V(r)$. In practice, the internal structure may be ignored when the colliding particles are in their ground states and the collision happens at ultralow temperatures. An inelastic process which excites a particle is then energetically forbidden[8]. The relative motion between the two particles is described by the time-independent Schrödinger equation

$$\left(\frac{p^2}{2m_r}+V(\vec{r})\right)\psi_k(\vec{r}) = E_k\psi_k(\vec{r})\ , \tag{2.60}$$

[8]Exothermic chemical reactions may still occur.

where $m_r = (m_1 m_2)/(m_1 + m_2)$ is the reduced mass, $E = \hbar^2 k^2 / 2m_r$ is the energy of the relative motion and k the wave number of the incident wave. Because the collision is elastic, the magnitude of k is a conserved quantity. For an isotropic potential, the radial and angular motion may be separated and the wavefunction written as

$$\psi(\vec{r}) = R_l(r) Y_l^m(\theta, \phi) \ , \tag{2.61}$$

where $R_l(r)$ is the radial wavefunction and $Y_l^m(\theta, \phi)$ are the spherical harmonics. This reduces the 3D problem to 1D

$$\left(\frac{p^2}{2m_r} + V_{\text{eff}}(r) \right) R_l(r) = E R_l(r) \ , \tag{2.62}$$

with the effective interaction potential

$$V_{\text{eff}} = \left(V(r) + \frac{\hbar^2 l(l+1)}{2m_r r^2} \right) \ . \tag{2.63}$$

The consequence of the separation of variables is to introduce a centrifugal barrier which is added onto the interaction potential as shown in figure 2.7(a).

In general, the wavefunction $\psi_k(\vec{r})$ is a superposition of solutions with different values of l. The physical quantity of interest, which determines the rate of elastic collisions is the elastic cross-section

$$\sigma_{\text{el}} = \frac{4\pi}{k^2} \sum_l (2l+1) \sin^2(\delta_l(k)) \ , \tag{2.64}$$

with $\delta_l(k)$ the phase shift between the incoming and scattered waves. The equation above is the result of the so called partial wave expansion of $\psi_k(\vec{r})$.

The partial waves involved in a collision are determined by the relative energy of the colliding pair. Partial waves for which the barrier height is larger than the relative energy will not penetrate sufficiently close to experience the interaction potential. For a van der Waals interaction potential, the barrier occurs at an internuclear separation of

$$R_b = \left(\frac{6 C_6 m_r}{l(l+1)} \right)^{1/4} \ , \tag{2.65}$$

which corresponds to a barrier height of

$$T_b = \frac{2}{k_{\text{B}} C_6^{1/2}} \left(\frac{\hbar^2 l(l+1)}{6 m_r} \right)^{3/2} \ , \tag{2.66}$$

in temperature units. At long range the interaction between a Rb atom and a CaF molecule may be approximated by a van der Waals potential. Using the value[9] $C_6 = 3084 E_{\text{h}} a_0^6$ estimated in [106], the p-wave barrier, which is the lowest non-zero partial wave, corresponds to a temperature of 134 μK. For substantially lower temperatures,

[9] Here E_{h} is 1 Hartree and a_0 is the Bohr radius.

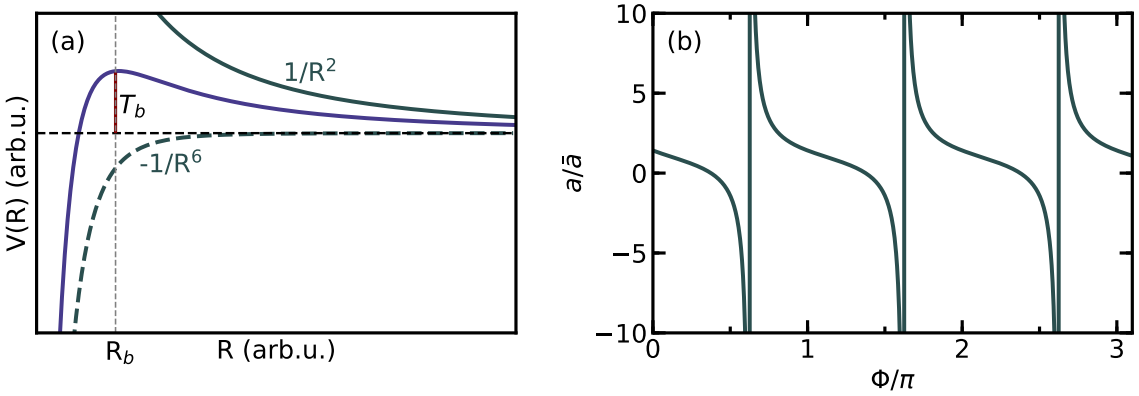

Figure 2.7: (a) Sketch of van der Waals $\sim -1/R^6$ and centrifugal $\sim 1/R^2$ potentials. The sum of the two lead to an attractive potential with a repulsive barrier of height T_b. (b) The scattering length as a function of the phase integral Φ.

when the p-wave barrier is much greater than the collision energy, the scattering cross-section reduces to

$$\sigma_{\text{el}} = 4\pi a^2 \ , \tag{2.67}$$

where the parameter a is known as the scattering length and is related to the phase shift by $\delta_0(k) = -ka$. It has units of length and the result is equivalent to the one found for scattering off a hard sphere potential. The scattering length has the following [107] definition

$$a \equiv -\lim_{k\to 0} \frac{\tan(\delta_0(k))}{k} \ . \tag{2.68}$$

The value of a depends on the interaction potential. For the case of a van der Waals potential [108], it is given by

$$a = \bar{a}\left(1 - \tan\left(\Phi - \frac{\pi}{8}\right)\right) \ , \tag{2.69}$$

with $\bar{a} = 0.477988...(2m_r C_6/\hbar^2)^{1/4}$ the mean scattering length [109]. For the CaF-Rb system using the value of C_6 from above it is equal to $\bar{a} = 35.7$ Å. The phase Φ is given by the WKB integral

$$\Phi = \int_{R_0}^{\infty} \sqrt{\frac{2m_r}{\hbar^2} V(R)}\, dR \ , \tag{2.70}$$

where the integration is carried out between the classical turning point R_0 and infinity. Figure 2.7(b) shows how the scattering length varies as a function of the phase integral. It is clear that a is very sensitive to the shape of the potential. Calculating the anisotropic interaction potential for a molecule-atom collisions is complicated and it is this fact that makes theoretical calculations of the elastic cross-section very challenging. For simple atom-atom collisions accurate interaction potentials are in some cases possible to be determined from first principles [110] although in general experimental data is frequently required to guide these theoretical calculations.

2.3.2 Inelastic collisions

In an inelastic collision, the colliding particles may undergo a chemical reaction or a change of the internal state. In either scenario, energy may be released which can lead to heating. For state sensitive traps a collision which alters the quantum states may eject the particles out of the trap. To check whether a chemical reaction of the form $AB + C \rightarrow CB + A$ is allowed it is sufficient to compare the bond dissociation energies of AB and CB. At ultracold temperatures the relative kinetic energy is negligible compared to the bond strengths so that only exothermic reactions are allowed. The reaction CaF + Rb $\rightarrow$ RbF + Ca is endothermic by 0.53 eV [111] and the reaction CaF + Rb $\rightarrow$ RbCa + F is endothermic by 5.32 eV [112]. Thus two-body Rb-CaF collisions are chemically stable.

2.3.3 Single-channel loss model

To answer whether a collision which changes the internal state is likely, quantum scattering calculations are required. As mentioned above, these are challenging for a system such as Rb-CaF. Instead, a single-channel loss model based on quantum defect theory (QDT) [105, 113] is used. A more familiar application of QDT is in determining the energy levels of multi-electron atoms. In the case of alkalis, the single outer electron experiences an effective Coulomb potential. For higher electron orbitals, the potential is very similar to a hydrogen atom. For lower orbitals, interactions with other electrons become significant. Instead of analysing the complicated interaction potential explicitly, the energy dependence is parametrized using a single quantity known as the quantum defect. In this particular example, the quantum defect is subtracted from the principal quantum number. In a similar fashion, this method may also be applied to a quantum scattering problem where a complicated interaction potential is involved.

For a molecule-atom collision the long range interaction potential is modelled by $-C_6/R^6$. At low energies, a large flux of incoming particles may be reflected by the long range potential and never reach short range where the interaction becomes much more complicated. The scattering of particles which do reach short range are characterized using two parameters, y and δ^{S}. The parameter y is the loss parameter which may vary between 0 (no loss) and 1 (complete loss) and δ^S is the scattering phase shift at short range. The phase shift may be related to the scattering length by

$$\frac{a}{\bar{a}} = 1 + \cot\left(\delta^{\mathrm{S}} - \frac{\pi}{8}\right) \ , \tag{2.71}$$

The loss parameter is related to the probability of loss at short range by

$$p_{\mathrm{loss}} = \frac{4y}{(1+y)^2} \ . \tag{2.72}$$

In the limiting case when $y \rightarrow 1$ the probability of loss $p_{\mathrm{loss}} \rightarrow 1$ and there is no dependence of p_{loss} on δ^{S}. This is known as the universal loss regime. If $y << 1$, the loss depends

strongly on the scattering length and is not universal. At zero temperature, in the limit of universal loss, the loss rate coefficient is given by [113]

$$k_2^{\mathrm{Univ}}(T=0) = \frac{2gh\bar{a}}{m_r} \ , \tag{2.73}$$

where $g = 1$ for distinguishable particles and $g = 2$ for indistinguishable particles. For the Rb-CaF system, $k_2^{\mathrm{Univ}}(T=0) = 8.11 \cdot 10^{-11}$ cm$^3 \cdot$ s^{-1}. Away from this zero energy limit higher partial waves begin to contribute and lead to a strong energy dependence.

In this thesis, the single-channel loss model is used to help interpret the experimental results obtained for Rb-CaF collisions, both in the magneto-optical and the magnetic quadrupole traps.

3 | Setting up the experiment

The first generation apparatus for making a molecular MOT in our group was built to demonstrate and investigate direct laser cooling of CaF. The final outcome of this work was a sample of molecules cooled to below 10 μK [98] and subsequently transferred into a magnetic quadrupole trap [114]. Implementing a dual atom-molecule MOT and transferring both species into a conservative trap to study atom-molecule collisions required the addition of a cold atom source. The key requirement was to create a high number density atomic sample with a good spatial overlap with the molecular cloud. Large atomic MOTs are typically realized by loading the trap from a slowed atomic beam or a pre-cooled cloud of atoms. Due to the experimentally demonstrated performance [115, 116] and simplicity a 2D MOT of ^{87}Rb was chosen as the source of cold atoms for experiments described here. In addition, earlier theoretical work [106] has investigated sympathetic cooling of CaF using Rb atoms and found that Rb has promising collisional properties as a potential coolant for molecules. Moreover, this particular isotope of Rb may be cooled evaporatively without substantial obstacles in reaching quantum degeneracy and today many cold atom experiments choose to work with it for this reason. Indeed, record low temperatures of around 50 pK were obtained [117] by evaporatively cooling a gas of ^{87}Rb atoms. Furthermore, with both species having similar masses is beneficial for two reasons. First, it helps to improve the spatial overlap in conservative traps where the gravitational pull is significant. Second, it requires a lesser number of elastic collisions for the two gases to thermalize (more on this could be found in chapter 8).

To implement the cold atom source a new vacuum system had to be installed in place of the original one to extend the available optical and mechanical access. In addition, a laser system to trap Rb atoms had to be integrated together with the diagnostic tools used to characterize the atom and molecule clouds. These new additions and other essentials bits of the experimental hardware are described in this chapter.

3.1 Overview of apparatus

Figure 3.1 gives an overview of the apparatus. Each part of the experiment will be described in more detail in the sections that follow. A pulsed beam of CaF molecules is produced by a cryogenic buffer gas source. The molecules exiting this source typically

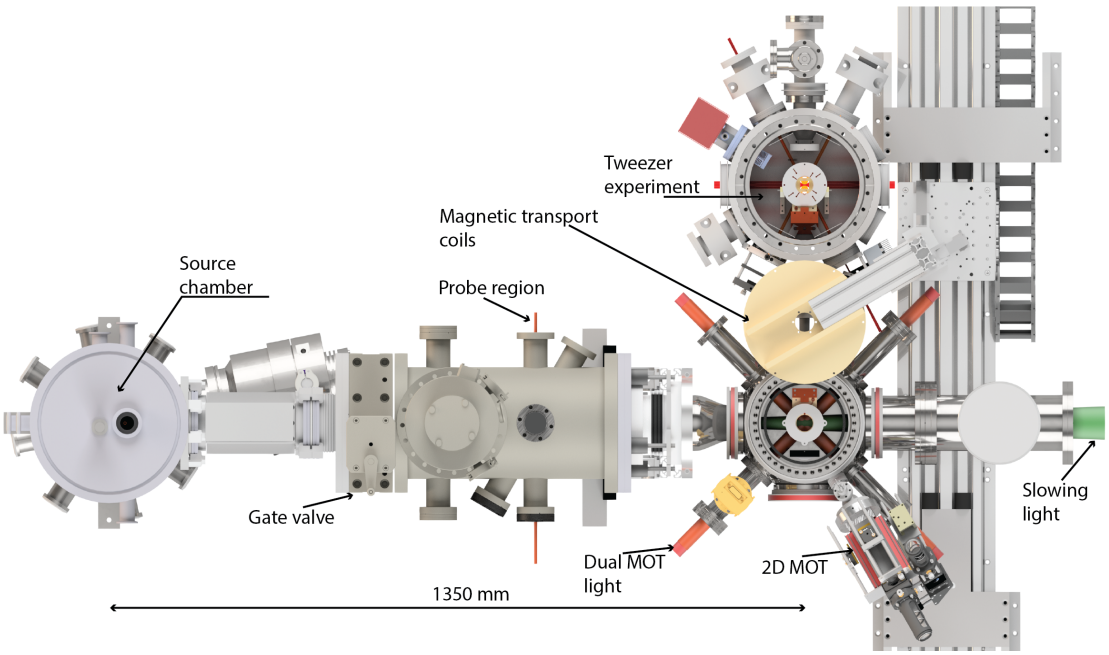

Figure 3.1: Overview of the experimental apparatus used to load a dual species MOT of atoms and molecules. The vacuum chamber at the top right corner is for the optical tweezer experiment which is not described in this thesis.

have a mean speed of about 160 m/s. They are slowed to about 10 m/s by frequency chirped radiation pressure slowing using a counter-propagating laser beam that primarily addresses the $B^2\Sigma^+ - X^2\Sigma^+$ transition of the molecule. They are captured in the 3D magneto-optical trap using laser light that addresses the $A^2\Pi_{1/2} - X^2\Sigma^+$ transition. A cold beam of Rb atoms is extracted from a 2D MOT and captured into the 3D MOT located at the same position as the molecular MOT. To detect both species, the fluorescence from the atomic and molecular MOTs is imaged onto a CCD camera. The atoms can also be detected by absorption imaging. The MOT chamber is connected to a second chamber and the atoms and molecules can be transported to this second chamber using a translatable magnetic trap. The second chamber houses an experiment for capturing molecules in optical tweezer traps; this experiment is not described in this thesis.

3.2 Science chamber assembly

The science chamber together with all the key components are shown in figure 3.2. The chamber was designed in house and was machined by *Kimball Physics*. It is made out of stainless steel with electro-polished walls to reduce adsorption of background gasses and thus the load on the pumping system.

In-vacuum coils are used to generate the magnetic quadrupole field for trapping molecules and atoms in the dual species magneto-optical and magnetic quadrupole traps. The current to the coils is delivered using a pair of high current (up to 30 A) electrical

vacuum feedthroughs connected to the chamber via two DN16 ports. A set of 3 pairs of coils are used to control the magnetic field important for cooling atoms and molecules to the lowest temperatures and the quantum state preparation steps.

A turbomolecular pump is connected to the system away from the main body of the chamber to reduce the vertical extent of the chamber assembly. This provides with space for a set of coils (not shown here) used to magnetically transport molecules to another chamber where the optical tweezer experiment will take place. No other details of this experiment will be provided in the rest of this thesis.

For fluorescence imaging, a high numerical aperture lens is mounted inside a custom made lens holder clamped down to the bottom flange of the chamber. Having the lens inside the chamber increases the light collection efficiency by at least a factor of 4 compared to a lens with the same size aperture placed outside the chamber at the closest possible position from the region where the molecules are trapped.

A cylindrical aluminium shield is clamped down to the bottom flange and serves as a light baffle that helps to reduce background and scattered light reaching the detection system. Most of the in-vacuum components are covered in black paint to further reduce light scatter as will be described in some detail below. Optical access through the light baffle is provided for all the CF16, CF40 and the CF63 ports as well as along the extension tee where the molecule slowing laser light propagates.

A separate and modular assembly to create a 2D MOT of Rb atoms is connected to the chamber using one of the CF16 ports. The atom trap is formed in a glass cell connected to the science chamber via a differential pumping stage. An aluminium cage protects the fragile glass cell and holds the 2D magnetic quadrupole coils. The optical assembly to deliver the trap light attaches to this aluminium cage.

3.2.1 Magnetic quadrupole coils

The magnetic field required to capture the molecules and atoms in a MOT and later in a magnetic quadrupole trap is generated by a set of coils inside the vacuum chamber. In the first iteration of the CaF MOT experiment it was found that having large coils outside the vacuum chamber produces a fringing magnetic field at the region of the incoming molecular beam which significantly impedes the laser slowing and thus the obtainable flux of molecules below the capture velocity of the MOT. Since rapid current switching of coils with a large inductance is technically challenging [118] it was decided to install smaller coils inside the vacuum chamber. The reduced size of the coils eliminates the large fringing field, enables fast switching of current and minimizes the eddy currents induced on the surfaces of the chamber. The challenge then becomes to design these coils such that they are UHV compatible when in operation with currents required for the MOT and magnetic trap.

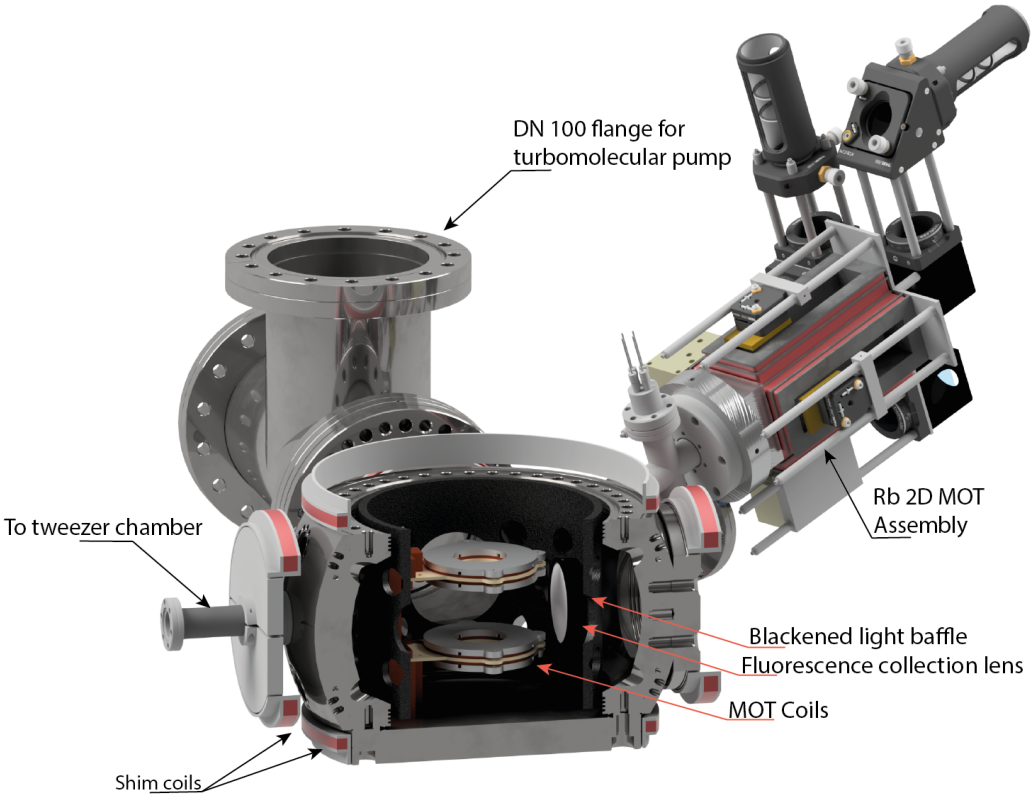

Figure 3.2: The science chamber assembly. In-vacuum coils generate the magnetic quadrupole field and a set of 3 coil pairs outside the chamber are used to cancel the background magnetic field and apply small, well-controlled fields. A high NA lens inside the chamber collects the light induced fluorescence from the trapped molecules. A cylindrical light baffle reduces the amount of background and scattered light reaching the fluorescence detection system. The assembly to create a 2D MOT of atoms is attached to the main chamber via a differential pumping stage.

Figure 3.3 shows the in-vacuum coil assembly. Two pairs of copper spirals are laser cut out of 2 mm thick copper sheets and act as the electromagnets. Each spiral has 14 turns with a wire thickness of 0.8 mm. The spacing between each turn is only 0.4 mm. While the spirals are being laser cut thin bridges of material must be left between the adjacent turns so that the spiral does not spring out. These bridges have to then be carefully removed to ensure that consecutive windings of the spiral are not in electrical contact with each other. As the number of turns increases it becomes significantly harder to maintain the original shape of the spiral once the retaining bridges are removed. Laser cut steel combs (with 0.4 mm width teeth) are used to aid the assembly of the coils and to prevent the spirals from deforming while the retaining bridges are being removed. The clamping alumina plates have small slits so that the spiral may be secured in place without first removing the steel combs. To remove the retaining copper bridges a scalpel knife is used. In the future this process may potentially be simplified by annealing the copper sheets before the spirals are cut. This would reduce the stress in the copper sheets while

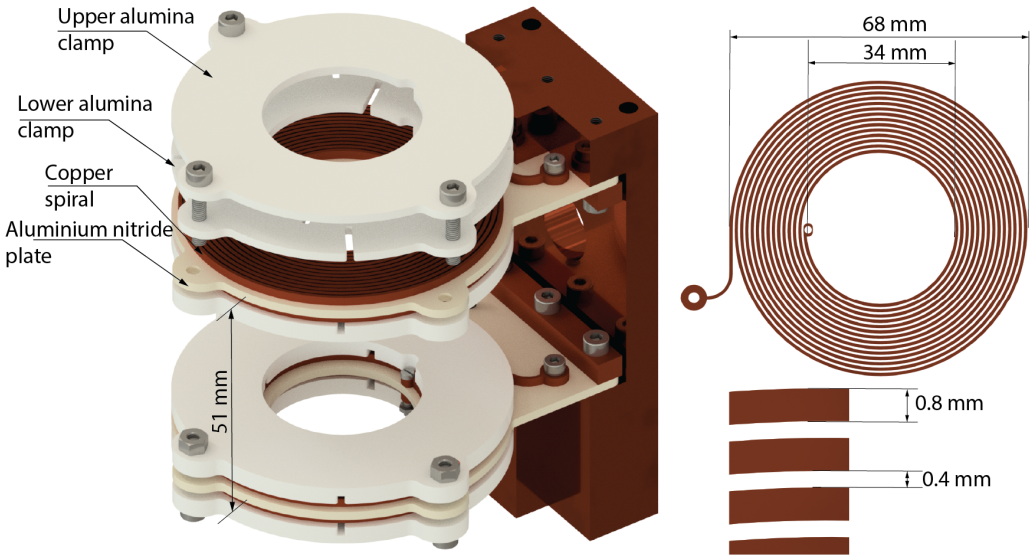

Figure 3.3: The in-vacuum MOT coils consist of two pairs of copper spirals each with 14 turns. The spirals are clamped between alumina and aluminium nitride plates both of which are bolted onto a copper spacer. Spirals in each pair are interconnected.

it is shaped into a spiral.

Aluminium nitride is used for the base plates since it has a high thermal conductivity, is UHV compatible and is reasonably rigid. Aluminium nitride can not be laser cut and may only be machined using specialized tooling. For this reason these were subcontracted to an external company (Precision Ceramics) while the rest of the coil assembly was made in house. The clamping plates are laser cut out of 2 mm thick alumina (aluminium oxide) sheets. Each spiral pair is connected in series with small screws and then secured on the aluminium nitride base plates by sandwiching them between the alumina clamps. Because alumina is brittle and breaks easily under mechanical stress each spiral is held down using a pair of alumina clamps. The connections to the electric current vacuum feedthroughs are made using a UHV compatible electrically insulated copper wire.

Field gradient and switching time

When the coils are operated in an anti-Helmholtz configuration they produce a magnetic field gradient of 3 $G \cdot cm^{-1} \cdot A^{-1}$ in the axial direction. The magnetic field is mapped out using a Hall probe prior to installing the coils into the science chamber. The gradient is found to be uniform over a region of at least 20 mm in the axial and radial directions.

The typical current used for creating a dual species MOT is 10 A. Given that a single copper spiral is 2.26 m long the total dissipated power at this current is around 9.5 W. Although the temperature of the coil assembly in UHV conditions is not measured separately it is found that for a current of 15 A the background pressure in the science chamber jumps up by more than an order of magnitude 10-20 s after switching on the

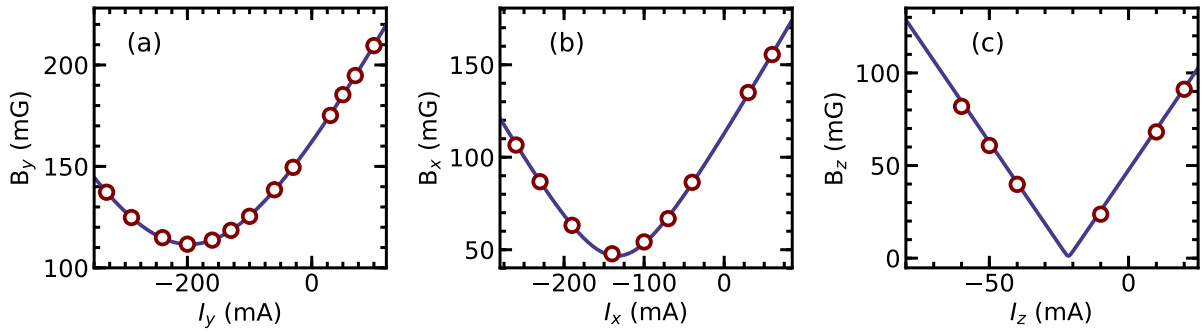

Figure 3.4: Calibration of the three pairs of shim coils by driving a magnetically sensitive transition in CaF. (a) Along the y-axis; (b) along the x-axis; and (c) along the z-axis. The measured shift in transition frequency is converted to an absolute value of the magnetic field.

coils. This is most likely due to the paint which covers the coil assembly (section 3.2.3) heating up and beginning to outgas. Luckily, at a current of 10 A no change in background pressure is observed over an hour of continuous operation.

A power supply delivers up to 35 A of current to the MOT coils. To control and rapidly switch the current flow a feedback circuit is used. The 1/e current rise/fall time is measured to be around 500 μs.

3.2.2 Shim coils

Three pairs of coils set up in Helmholtz configuration are used to control the magnetic field at the centre of the science chamber. To calibrate the coils the $|N = 1, F = 0, M_F = 0\rangle \rightarrow |N = 0, F = 1, M_F = +1\rangle$ rotational transition in CaF is driven and the resonance frequency is measured[1]. The total magnetic field at the position of molecules is given by

$$B_{\text{Tot}} = \sqrt{(B_x^s + b_{0x})^2 + (B_y^s + b_{0y})^2 + (B_z^s + b_{0z})^2}\ , \tag{3.1}$$

with $\{B_x^s, B_y^s, \mathrm{B}_z^s\}$ the applied magnetic field components along the three orthogonal directions and $\{b_{0x}, b_{0y}, b_{0z}\}$ the stray magnetic field components along the same directions. Due to the Zeeman effect the transition frequency is shifted by an amount $f = \mu_{\text{B}} B_{\text{Tot}}/h$. Starting with the shim coils along the y-axis, the magnetic field is varied along all three orthogonal directions independently and the transition frequencies are measured. The magnetic field generated by each set of shim coils is proportional to the current and may be expressed as $B_{\text{Tot}} = \beta_i I_i$, with $i \in \{x, y, z\}$.

Figure 3.4 shows the calibration curves for all three shim coil pairs. The measured transition frequencies are converted to the absolute value of the magnetic field B_{Tot} at the position of the molecule cloud. When the applied field from one coil is small compared to

[1]The experimental sequence used to drive microwave transitions in CaF is described in detail in section 6.3.

the background in the orthogonal directions, the total field varies quadratically with the applied field. Once the applied field is much larger than the background in the orthogonal direction, the scaling becomes linear. In these experiments, the x and y backgrounds were zeroed first. The field then scales linearly with the current applied to the coils in the z-direction. Fits to these data give the following calibration coefficients β_x=599(1) mG/A, β_y=766(1) mG/A and β_z=2202(22) mG/A.

3.2.3 Reducing light scatter

Capturing large numbers of molecules in a MOT is not yet possible. Typically up to $2 \cdot 10^4$ molecules may be captured into the MOT and significantly less than that before the alignment of the trap beams and laser frequencies are fully optimized. Because CaF molecules are detected by collecting their light induced fluorescence by the main cooling light the smallest detectable signal is usually limited by the background scatter of these laser beams. For a 100 mW trap beam traversing an AR coated viewport with 99.9 % transmission roughly 10^{11} photons may be scattered by the viewport surface in 1 ms. By comparison, with a detection efficiency of 1 % and a scattering rate of 2 MHz a thousand molecules would give a signal which corresponds to only $2 \cdot 10^4$ photons. Thus even a small fraction of the scattered laser light reaching the detector could be comparable or far larger than the detected signal from fluorescing molecules.

There are two ways in which the background scatter may obscure or limit the detectable signal from fluorescing molecules. Firstly, for extremely small signals an excessively large background may simply saturate the detection instrument due to its finite dynamic range and thus make the discrimination of the signal from the background impossible. Secondly, even if the background level is comparable or smaller than the signal from molecules, the shot noise will enforce a limit on the smallest detectable signal. For low light applications in microscopy an effective and commonly used tool for increasing the signal-to-noise ratio is to spatially filter out the background light with the aid of a small aperture placed at the Fourier plane of a $4f$ imaging system. To image CaF molecules a field of view of around 1 cm is required due to the rather large size of the cloud, making spatial filtering ineffective.

To reduce light scatter reaching the CCD camera the cylindrical light baffle and all other parts within the science chamber are coated with a vacuum compatible black paint MH2200 from *Alion Science*. This paint should absorb >98 % of visible light. To ensure the paint will not compromise the vacuum all coating and paint curing procedures must be followed carefully. Two layers of paint are applied immediately one after the other using a spray gun. The paint is then allowed to dry in air for 72 hours. The parts are then baked in an oven at a 200 °C temperature for 8 hours. Once cooled down the quality of the coating is tested under UHV conditions at a temperature of 150 °C. A

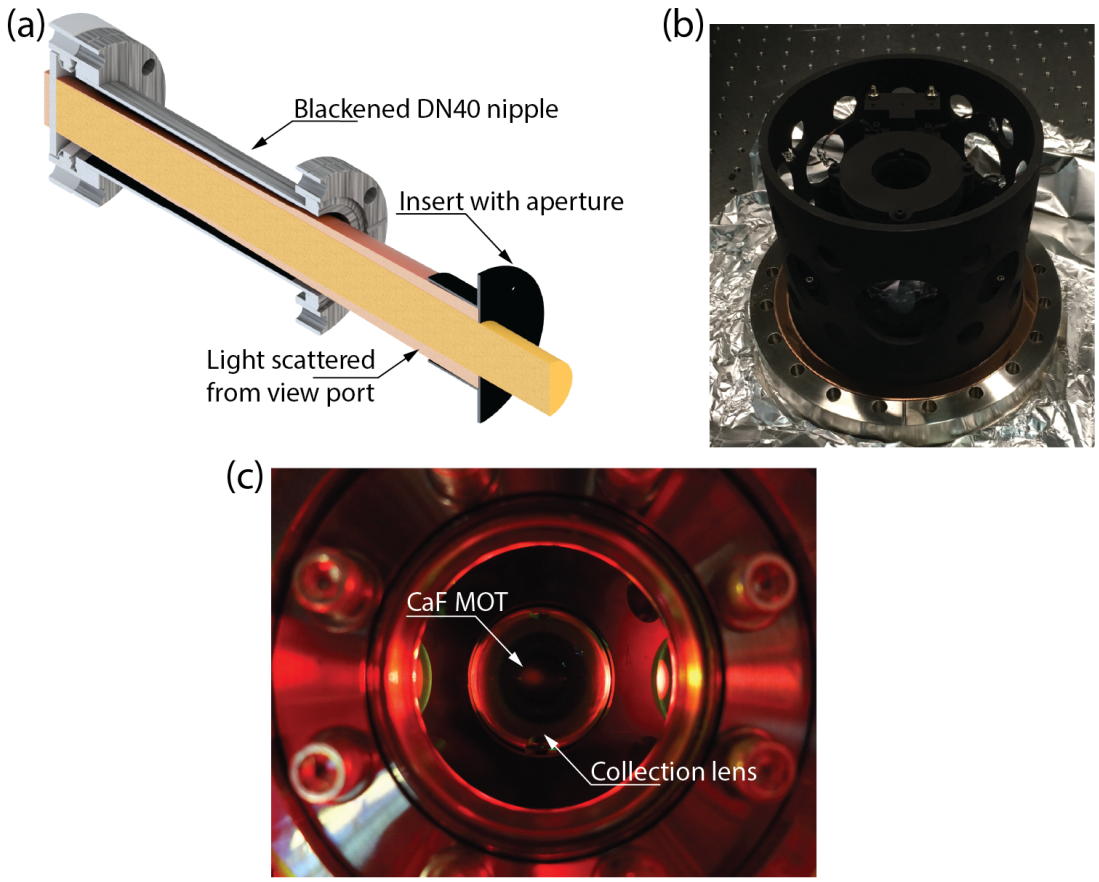

Figure 3.5: Reducing scattered trap light from AR coated view ports using (a) apertures of 23 mm diameter inserted into the chamber ports. In (b) the blackened science chamber assembly is shown. (c) An image of the CaF MOT through the in-vacuum collection lens and the CF63 detection view port taken with an amateur camera.

separate chamber is used for this purpose where a pressure of 10^{-7} mbar is maintained by a turbomolecular pump while the chamber is hot. A dummy glass view port is attached to this chamber and thoroughly investigated for any suspicious deposits after baking the parts over night. Using this procedure, one can asses whether the paint cured properly and all coated components can safely be installed into the science chamber. The base solvent of this paint is xylene so it may be used to wipe off erroneously coated spots although it becomes ineffective after the paint has been cured. For multiple uses of the paint it must be kept refrigerated. In the first iteration of the spray painting procedure a batch of paint close to its expiry date and kept at room temperature for several months was used. After curing the paint large parts of it peeled off while others where hard to remove intentionally. This, of course, required to repeat the procedure from the start.

The cylindrical light baffle primarily helps to reduce the background lab light that enters the chamber through all of its viewports and reflects off its shiny concave walls. The viewports themselves are indeed found to scatter a significant amount of the trap light into the detection system and are the dominant source of unwanted background signal. To mitigate this, the 4 viewports in the horizontal plane are connected to the science

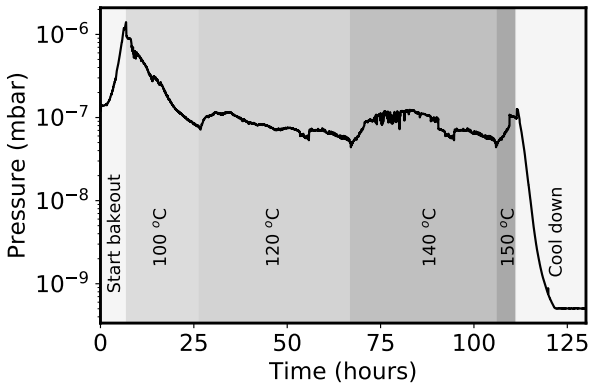

Figure 3.6: Evolution of the background pressure in the science chamber during bakeout. A maximum temperature of 150 °C is obtained. Once cooled down the pressure in the chamber falls to below $5 \cdot 10^{-10}$ mbar.

chamber via extension pieces which increase the distance from the detection optics. To block light scattered from the viewports apertures coated with MH2200 are inserted into the chamber ports as shown in figure 3.5(a). The complete blackened assembly is shown in figure 3.5(b) with an image of molecules fluorescing in the MOT shown in figure 3.5(c). Quantitative measurements of the background scatter and the achieved signal to noise ratio are postponed to section 3.7.2.

3.2.4 Reaching and maintaining UHV

UHV conditions in the science chamber are reached and maintained using a turbomolecular pump (*Twiss Torr 304 FS*) with a pumping speed of 240 l/s. The backing pressure for this pump is maintained at $5 \cdot 10^{-3}$ mbar using a *Leybold ScrollVac Plus* scroll pump. At this pressure the compression ratio for pumping all gases is completely saturated[2]. After assembly, the chamber is leak checked using a helium leak checker and a leak rate of below 10^{-10} mbar·l/s is found.

Figure 3.6 shows the evolution of the background pressure in the science chamber measured using a *Leybold IONIVAC* ITR 90 ion gauge. After a day of pumping a pressure of roughly 10^{-7} mbar is reached. At this point the chamber is heated up to 100 °C over the course of several hours. The temperature is increased further up to a maximum of 150 °C. Subsequently, over about 90 hours, the temperature of the glass cell is monitored in several different locations and ensured to be uniform during the bakeout within a few degrees. This is important for avoiding temperature gradients which, due to different thermal expansions of steel and glass, could damage the cell. Heating of the chamber speeds up the removal of gases adsorbed by the chamber walls and other vacuum parts.

[2]The mean free path of air molecules is larger than the distance between the pump blades so that there is no back flow of gas towards the UHV side. In this regime, the compression ratio depends only on the blade rotation speed and the mass of molecules being pumped.

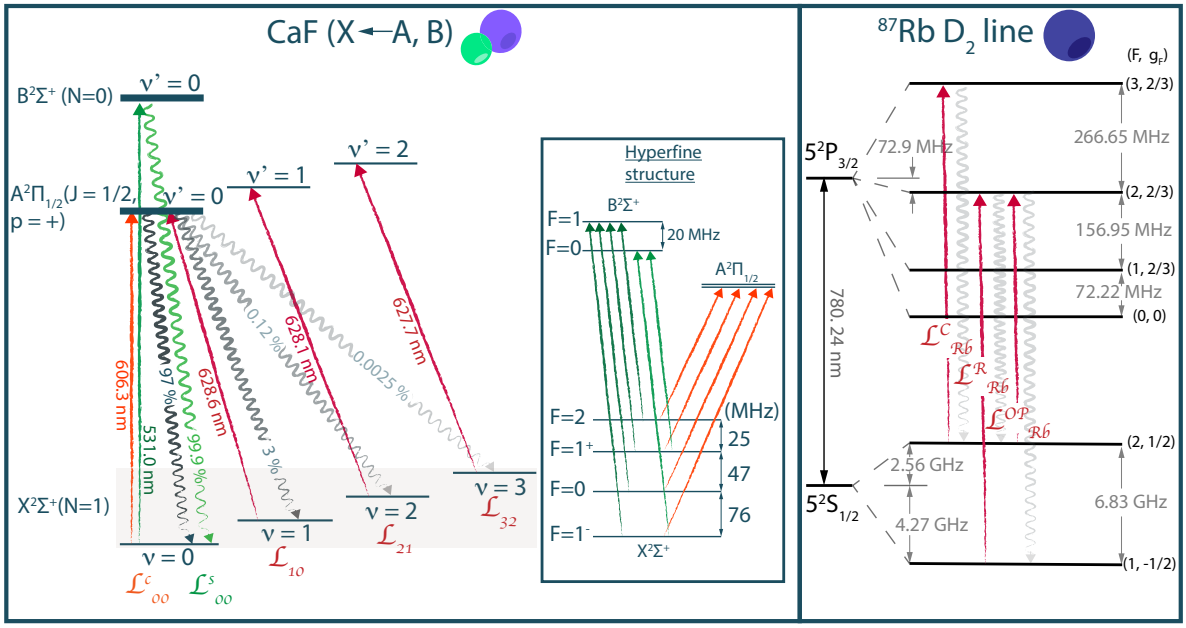

Figure 3.7: The energy level structures relevant for laser cooling of CaF molecules and ^{87}Rb atoms. Light used to slow the molecule beam is denoted as $\mathcal{L}^s_{00}$ and is tuned to drive the $B^2\Sigma^+(\nu' = 0, N = 0) \leftarrow X^2\Sigma^+(\nu = 0, N = 1)$ transition. The MOT and cooling light, denoted as $\mathcal{L}^C_{00}$, is tuned around the $A^2\Pi_{1/2}(\nu' = 0, J = 1/2, +) \leftarrow X^2\Sigma^+(\nu = 1, N = 1)$ transition. In total 3 vibrational repumpers are used to maintain molecules in the cooling cycle and these are labelled as $\mathcal{L}_{10}$, $\mathcal{L}_{21}$, $\mathcal{L}_{32}$. All these frequency components have sidebands added to them to address the 4 hyperfine levels in each of the ground electronic state vibrational levels. To cool ^{87}Rb atoms the F = 2 $\rightarrow F' = 3$ transition is used, atoms that leak into $F = 1$ are brought back to the cooling cycle with light tuned to drive the $F = 1 \rightarrow F' = 2$ transition. These lasers are labelled as $\mathcal{L}^C_{Rb}$ and $\mathcal{L}^R_{Rb}$ respectively. Light tuned to drive $F = 2 \rightarrow F' = 2$ is used to optically pump atoms and is denoted as $\mathcal{L}^{OP}_{Rb}$. The wavy arrows indicate spontaneous decay channels. The decay probabilities from $\nu' = 0$ to $\nu = 0, 1, 2, 3$ vibrational levels are also shown.

Once cooled down, a pressure below $5 \cdot 10^{-10}$ mbar is reached, which is the lowest value the ion gauge can register.

3.3 Laser systems

A total of 8 narrow linewidth laser systems are used in this work. Laser slowing and cooling of CaF molecules requires 5 different wavelengths while to cool and trap Rb atoms only two wavelengths are needed. The last laser is used as a frequency reference. Towards the end of my work in the lab an additional laser was added for transverse cooling of the molecular beam as described in chapter 7.

Relevant CaF structure

The energy level structures of CaF and Rb relevant for laser cooling are shown in figure 3.7. Light used to decelerate the molecular beam ($\mathcal{L}_{00}^{s}$) is tuned to drive the $B^2\Sigma^+(\nu'=0, N=0) \leftarrow X^2\Sigma^+(\nu=0, N=1)$ transition. A molecule excited to $B^2\Sigma^+(\nu'=0, N=0)$ will decay back to $\nu=0$ with a 0.999 probability so that roughly 1000 photons will be scattered before the molecule decays to another vibrational level and is lost. The laser ($\mathcal{L}_{10}^{s}$) which returns the population leaked to $\nu=1$ back into the cooling cycle is tuned to the $A^2\Pi_{1/2}(\nu'=0, N=0) \leftarrow X^2\Sigma^+(\nu=1, N=1)$ transition and increases the number of scattered photons up to $\sim 3\cdot 10^4$ [119]. The CaF MOT and cooling light ($\mathcal{L}_{00}^{c}$) is tuned around the $A^2\Pi_{1/2}(\nu'=0, J=1/2, +) \leftarrow X^2\Sigma^+(\nu=0, N=1)$ transition. The Franck-Condon matrix for this transition is not as diagonal as the one used to slow the molecular beam thus a total of three repump lasers ($\mathcal{L}_{10}$, $\mathcal{L}_{21}$ and $\mathcal{L}_{32}$) are required to retain molecules within the cooling cycle. Only the $\mathcal{L}_{10}$ laser is used to repump molecules via $\nu'=0$ while the repumpers for retrieving population from $\nu=2$ and $\nu=3$ do not use the $\nu'=0$ state. This allows to substantially increase the scattering rate [119]. The $A^2\Pi_{1/2}$ and $B^2\Sigma^+$ excited states have decay rates of $\Gamma = 2\pi \times 8.3$ MHz and $\Gamma = 2\pi \times 6.3$ MHz respectively. Each vibrational level in the ground state is split into 4 hyperfine levels. The frequency components required to address these are generated using electro-optic modulators (EOM's) and the necessary sidebands are added onto all 5 laser frequencies.

Relevant Rb structure

Atoms are trapped and cooled on the D_2 line of ^{87}Rb. Trapping and cooling light is tuned around the $F=2 \rightarrow F'=3$ transition and is denoted as $\mathcal{L}_{Rb}^{C}$. This is also the transition used to image the atoms. For a typical light intensity and detuning used to create a MOT the $\mathcal{L}_{Rb}^{C}$ light will off-resonantly excite the $F=2 \rightarrow F'=2$ transition at a rate of roughly 30 kHz. From there the decay channel to $F=1$ is open and thus all of the atoms will quickly be pumped into a state not addressed by the cooling light. To circumvent this a repumping laser ($\mathcal{L}_{Rb}^{R}$) drives the $F=1 \rightarrow F'=2$ transition and ensures that the cooling transition may always be driven. The $F=2 \rightarrow F'=2$ transition is used to optically pump atoms into a dark state and spin polarize the atom cloud for magnetic trapping.

3.3.1 CaF laser system

Light at 606.3 nm , labelled as $\mathcal{L}_{00}^{C}$, and 628.6 nm, labelled as $\mathcal{L}_{10}$, are derived from two very similar systems: the output of an infra-red laser diode (*Toptica DL PRO*) is amplified by a Raman fibre amplifier (*MPB* VRFA-P) and then frequency doubled in a non-linear crystal to produce the desired frequency. The two laser diodes produce light at wavelengths of 1212 nm and 1256 nm. After amplification and frequency doubling, the

available $\mathcal{L}_{00}^{C}$ and $\mathcal{L}_{10}$ laser powers are 1.0 W and 1.8 W respectively. The frequencies of these lasers are tuned by varying the angle of the feedback diffraction grating in the master lasers. Slowing light at 531 nm $\mathcal{L}_{00}^{S}$ is generated by amplifying the output of a distributed feedback (DFB) laser (Koheras from *NKT Photonics*) which is then frequency doubled in a non-linear crystal. The output frequency may be tuned by varying the length of the DFB fibre in the seed laser. This laser system produces a maximum of 1 W of laser power[3] at 531 nm.

To repump molecules from the $\nu = 2$ and $\nu = 3$ vibrational levels a pair of lasers, labelled as $\mathcal{L}_{21}$ and $\mathcal{L}_{32}$, at wavelenghts of 628.1 nm and 627.7 nm are used. In the MOT, populations of molecules in these two levels are low. It is found empirically that peak laser intensities of 30 mW·cm^{-2} for repumping from $\nu = 2$ and 2 mW·cm^{-2} for repumping from $\nu = 3$ are sufficient. A distributed Bragg reflector (DBR) laser diode (Ferdinand Braun Institute) with an output power of around 5-7 mW is used to seed a free-running higher output power laser diode (Ushio HL63263DG or HL63163DG). The output power of the bare DBR would not be sufficient, especially when losses through the optical setup are taken into account. The output frequency of the DBR laser may conveniently be tuned by varying the current and temperature of the diode with an in-built Peltier element. The diode is thermally connected to a two-stage water and electrically cooled platform housed in a home-built enclosure. The diodes are operated below the dew point of air at atmospheric pressure to obtain the desired lasing wavelength. Because of this, the enclosures are maintained at rough vacuum to avoid condensation of water vapour. The output of the DBR laser diode is fed into the higher output power diode operated with a current of around 100 mA. The specified output wavelengths for the HL63263DG and HL63163DG diodes are 638 nm and 633 nm respectively at room temperature. To shift the laser gain profiles towards the required wavelengths the diodes are cooled down. The HL63263DG laser diode is used to amplify $\mathcal{L}_{21}$ light and is cooled down to around -20 °C while the HL63163DG diode is used to amplify the $\mathcal{L}_{32}$ light and is cooled down to around -5 °C. In practice any of the two models may be used to produce the desired wavelength though the particular mentioned order leads to a longer life span of the diodes. Provided that the operating current does not significantly exceed 100 mA the average life span is around 3-6 months. The DBR laser diodes last much longer and do not have to be replaced over a couple of years of continuous operation.

Figure 3.8 shows a simplified schematic of the CaF laser system. A small fraction of the output of each laser is used to monitor the frequency using a wavemeter. The wavemeter has an accuracy of only 100 MHz so it is used for coarse adjustment of the

[3]In practice a maximum of 0.7 W is used in the experiment. This is because the light inside the fibre amplifier creates an effective grating and when the seed frequency is changed rapidly the amount of back reflection from this effective grating increases. Luckily, the laser unit detects this back reflection and automatically switches off the amplifier to prevent damage.

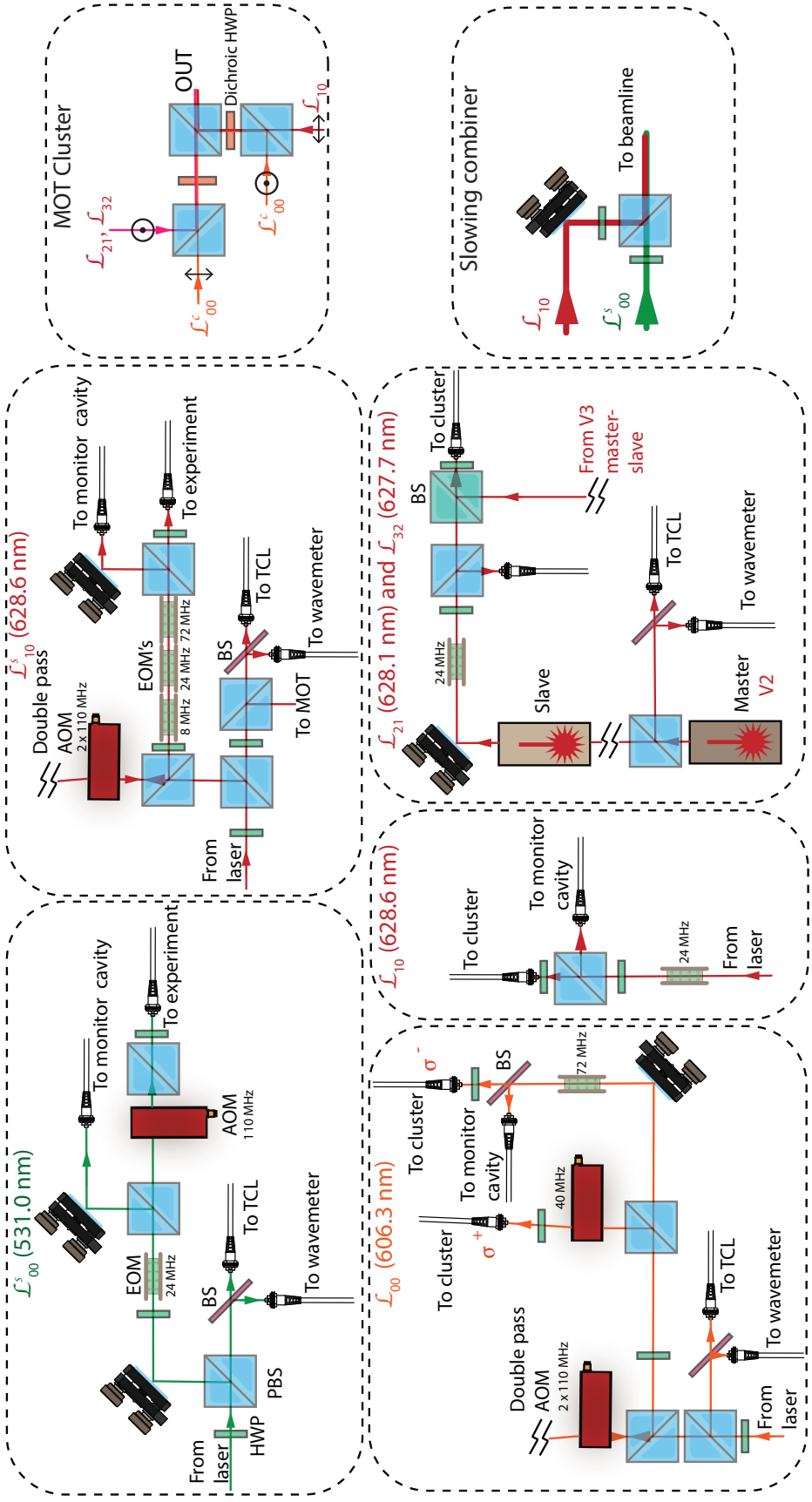

Figure 3.8: The CaF light distribution system. Each panel shows a simplified schematic of the optical setup used to prepare each colour of light required to slow and cool molecules. The method of producing $\mathcal{L}_{32}$ light is identical to the way $\mathcal{L}_{21}$ is produced thus only $\mathcal{L}_{21}$ is shown here. The vibrational repumpers $\mathcal{L}_{10}$, $\mathcal{L}_{21}$, $\mathcal{L}_{32}$ are combined with the main cooling light $\mathcal{L}_{00}^{C}$ in the MOT cluster and delivered to the experiment in a single fibre. The slowing light $\mathcal{L}_{00}^{S}$ is combined with the vibrational repumper $\mathcal{L}_{10}^{S}$ into a single beam in free space just before the beam enters the slowing chamber.

laser frequencies. The different wavelengths required to make the MOT are combined in a fibre cluster (Schäfter and Kirchhoff) which has a single fibre as its output. The $\mathcal{L}_{21}$, $\mathcal{L}_{32}$ components must have the same polarization due to the optical layout of the cluster and are thus combined into a single input fibre using a 90:10 beam splitter. Since less $\mathcal{L}_{32}$ optical power is required most of the power at this frequency is sacrificed on the beam splitter. There is a dedicated input fibre for all other wavelengths and a typical coupling efficiency of 70 % is obtained in each port.

Frequency components to address the hyperfine levels in each of the vibrational levels of the ground electronic state are generated using home built EOM's. An EOM driven at 72 MHz modulates $\mathcal{L}_{00}^{C}$ to generate sidebands which address the F=1^-, 0, 2 hyperfine components while an AOM is used to obtain the frequency to address the F=1^+ component. The $\mathcal{L}_{00}^{s}$, $\mathcal{L}_{10}$, $\mathcal{L}_{21}$, $\mathcal{L}_{32}$ beams are modulated using EOM's driven at 24 MHz. The drive amplitudes are chosen to extinguish the 1st order sidebands and to create 2nd and 3rd order sidebands. This addresses all of the hyperfine components. A chain of three EOM's driven at 8 MHz, 24 MHz and 72 MHz is used to frequency broaden the $\mathcal{L}_{10}^{s}$ light so that it addresses a wide range of molecule velocities. The sideband structures generated by each EOM are monitored with a pair of dedicated Fabry-Perot cavities.

The CaF MOT requires two orthogonal circular polarizations. To produce these, two separate fibre inputs into the fibre cluster are used. Fine control of the $\mathcal{L}_{00}$ frequency is obtained using a double-pass AOM which simultaneously shifts the detuning of all 4 sidebands.

3.3.2 Rb laser system

The main atom cooling light $\mathcal{L}_{Rb}^{C}$ and hyperfine repumper $\mathcal{L}_{Rb}^{R}$ are derived from two separate commercial tapered amplifier systems from *Toptica*. Each laser can produce up to 3 W of output power although only around 60 % of the available power may be coupled into a single mode fibre. Both lasers are kept on a separate optical table. The $\mathcal{L}_{Rb}^{C}$ light is delivered to the light distribution system with a pair of optical fibres while $\mathcal{L}_{Rb}^{R}$ is delivered with a single fibre. The larger fraction of the cooling light is used for the 3D MOT, push beam and absorption imaging while the smaller fraction is used for the 2D MOT and optical pumping. The frequencies of these components are finely tuned using AOM's. The repumper light is combined both with the 2D and 3D cooling light into single beams before being coupled to the optical fibres which deliver the light to the experiment. A pair of 1-3 fibre splitters from *Evanescent Optics* are used to deliver the trap light to the science chamber and make a six beam 3D MOT. The splitting ratio is balanced to within a few percent.

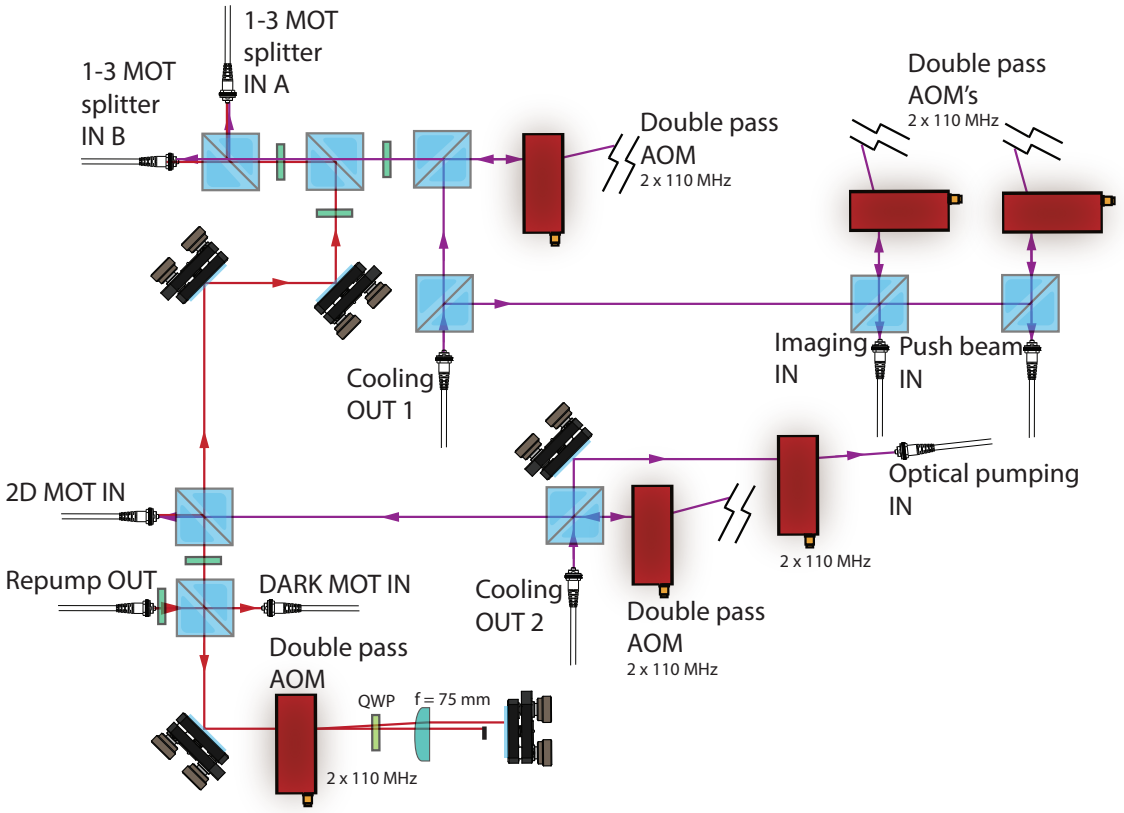

Figure 3.9: Simplified schematic of the Rb light distribution system. The hyperfine repumper, 2D and 3D MOT cooling, absorption imaging, push beam and optical pumping component frequencies are controlled independently using AOM's.

3.3.3 Frequency stabilization

The reference laser is locked to the $F = 2 \rightarrow F' = 2, 3$ cross-over feature of the ^{87}Rb D_2 line produced using Doppler-free saturated absorption spectroscopy. The stability of this laser is transferred to all of the laser systems used in this work as described below.

Frequency offset lock

The Rb cooling and repump lasers are stabilized using electronic offset locks. Figure 3.10 shows a schematic of the offset lock setup. Laser beams from the laser to be stabilized (slave) and the reference (master) are combined onto a beam splitter and coupled into a single PM optical fibre ensuring that both polarizations are aligned along a common axis. The fibre delivers the combined light (roughly 200 μW of optical power for each frequency component) onto a fast photodiode (*Hamamatsu G4176-03*) that produces a signal at a frequency equal to the difference between the master and slave (beat note). The signal is first amplified and then mixed with the output of a frequency tunable local oscillator. The mixed down signal is equally divided into two and fed into the error signal circuit. The first part passes a low-pass frequency filter and a passive -3 dB attenuator. The second branch is used as a reference and is attenuated by -6 dB. Both signals are then

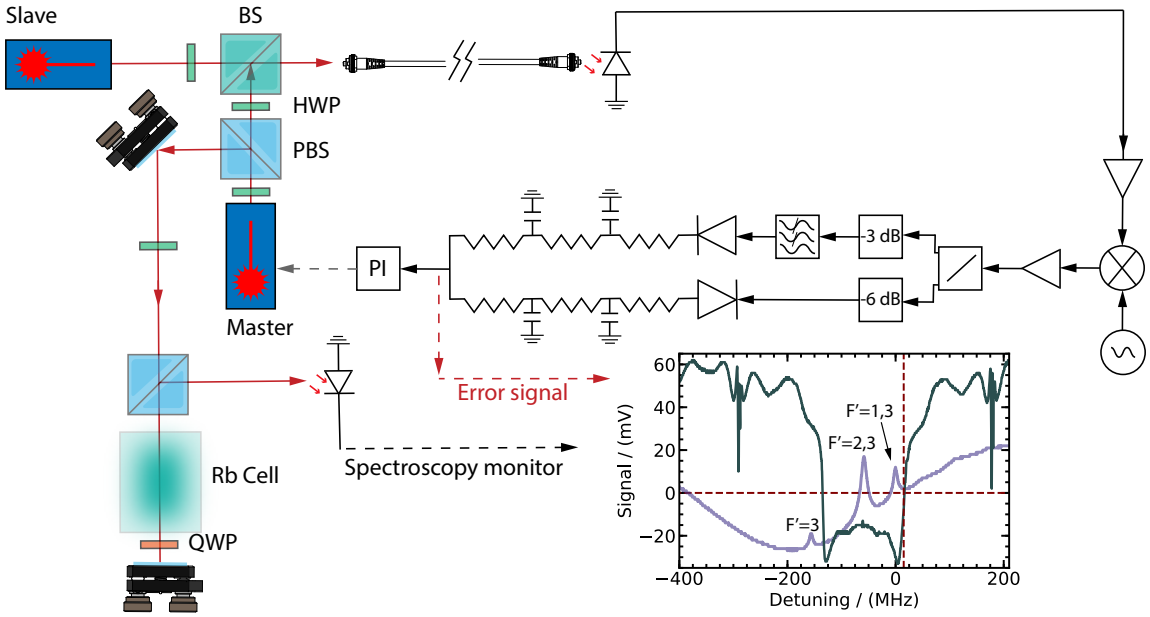

Figure 3.10: The Rb frequency offset lock setup described in detail in the main text. The graph shows traces of the saturated absorption spectrum corresponding to transitions from F=2 in purple and the error signal used to lock the cooling laser in grey.

rectified to produce a DC signal, the reference is inverted and finally added to produce an output voltage proportional to the frequency of the input signal. When the frequency of the input signal coincides with the -3 dB point of the low-pass filter the two input branches will have equal powers thus producing 0 V at the output of the error signal circuit which serves as the laser frequency lock point. The power ratio of the two signals may be changed by using different attenuators to adjust the zero-crossing of the error signal. To change the lock point, the frequency of the tunable local oscillator is varied.

The error signal is fed into a proportional-integral controller which servos the slave laser frequency around the 0 V set point. Figure 3.10 shows the offset lock error signal used to stabilize the cooling laser as it is scanned through the $F = 2$ transitions. Two symmetric features are produced corresponding to the same absolute value of the frequency difference between the optical beat note and the local oscillator. Either one of the features may be chosen as the lock point by simply switching the sign of the gain on the PI controller.

Transfer cavity lock

Light from each of the CaF lasers is coupled into one of a pair of scanning Fabry-Perot cavities. The transmission of each component through these cavities is monitored by a computer programme which fits a Lorentzian function to the transmission peak and determines its location on the voltage ramp supplied to the cavity. The length of both cavities are locked to the reference laser: the offset ramp voltage is actively adjusted to

maintain a constant position of the reference peak on the voltage ramp. The error signal used to lock the experiment laser is thus generated by measuring the difference between the reference and slave laser transmission peaks. When locked the $\mathcal{L}_{00}^{C}$, $\mathcal{L}_{00}^{S}$, $\mathcal{L}_{01}$ lasers have an RMS frequency noise of around 1 MHz while the noise of the $\mathcal{L}_{12}$ and $\mathcal{L}_{23}$ lasers is in the range of 2-3 MHz.

3.4 The 2D MOT assembly

The 2D MOT chamber assembly is shown in figure 3.11(a). The glass cell is from *Triad Technologies* and is made out of Pyrex. The cell has no AR coating. It is bonded onto a CF40 flange and has dimensions of (30x30x100) mm. A hollow steel tube of 125 mm length and an inner diameter of 8 mm connects the glass cell and science chambers via a custom 4-way CF cross. The end of this tube facing the glass cell has a thin facet welded onto it and a 2 mm diameter hole drilled through it. The total conductance of the differential pumping stage is given by

$$\frac{1}{C_{\text{Tot}}} = \frac{1}{C_{\text{Aperture}}} + \frac{1}{C_{\text{Tube}}} \ , \tag{3.2}$$

with the conductances of the aperture and tube given by

$$C_{\text{Aperture}} = \frac{\pi d^2 v_{\text{th}}}{4} \tag{3.3}$$

$$C_{\text{Tube}} = \frac{\pi v_{\text{th}} D^3}{12 l} \ . \tag{3.4}$$

Here d is the diameter of the aperture, D is the diameter of the tube and l is the length. The mean thermal velocity of atoms is given by

$$v_{\text{th}} = \sqrt{\frac{8 k_B T}{\pi m}} \ , \tag{3.5}$$

with T the temperature of the gas and m the mass of the constituent atoms or molecules. From the above equations, the total conductance is equal to 0.12 l/s for Rb vapour at room temperature. The turbomolecular pump which maintains UHV in the science chamber has a pumping speed of 250 l/s thus the pressure will drop by more than three orders of magnitude between the glass cell and science chambers. The Rb vapour pressure in the glass cell does not exceed 10^{-6} mbar so that a pressure of around $5 \cdot 10^{-10}$ mbar in the science chamber should be possible to maintain. The tube length is chosen so that the 2D MOT may be formed next to the exit aperture. This reduces the amount of time a laser cooled atom must travel from the cooling region to the exit aperture and minimizes losses due to divergence of the atom trajectories and collisions with background gas.

A pair of current feedthroughs on each side of the 4-way cross are used to deliver electrical current to the Rb dispensers. In total 4 Rb dispensers are installed. Each

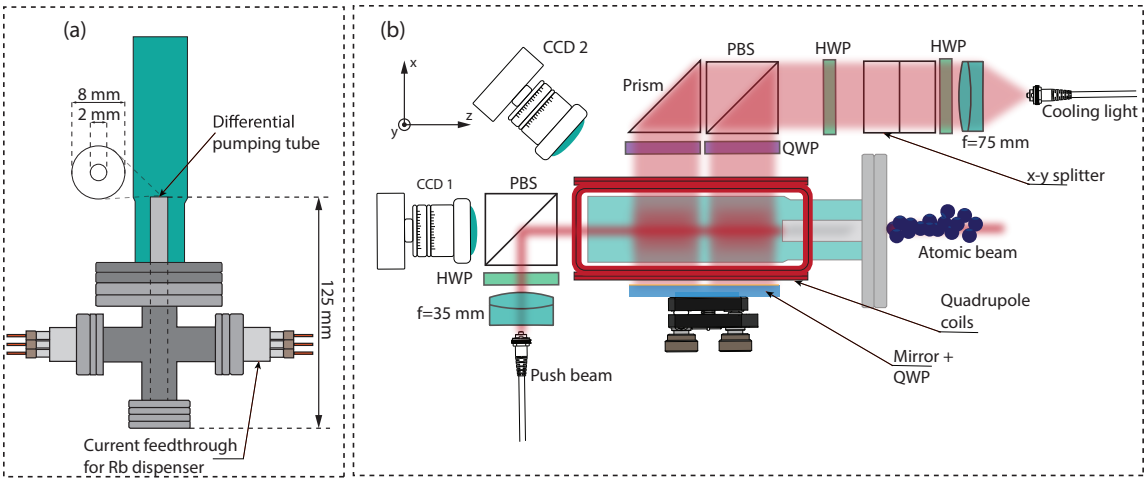

Figure 3.11: (a) Glass cell and differential pumping arm assembly. (b) The setup to make a 2D MOT of atoms. The cooling and repumper light are combined into a single beam which is split into two and wrapped around the cell. Two CCD cameras are used to observe the 2D MOT.

dispenser resides within the tube of the 4-way cross so most of the active surface area does not have a direct line of sight to the trap region and a large fraction of the dispensed atoms may stick onto the surrounding walls. Ideally these should be closer to the trap region which would enable to use lower current to obtain the same Rb vapour pressure in the glass cell.

Optics assembly

A schematic of the setup used to deliver the cooling light to the glass cell and form a 2D MOT is shown in figure 3.11(b). Two pairs of rectangular coils in anti-Helmholtz configuration produce a magnetic quadrupole field: the field is zero along the z-axis and varies linearly in x-y plane. A single beam with a $1/e^2$ radius of 7 mm contains the cooling and repumper light. The beam is split into two on a PBS cube to address the x and y trap axes. Each beam is then again split into two beams of equal intensity using a PBS cube and prism pair. Before entering the chamber both beams are circularly polarized using a pair of quarter wave plates. Finally, after passing the cell both beams are retroreflected with a mirror which has a $\lambda/4$ phase retarder integrated onto its surface. Because of the small gap between the pairs of beams traversing the glass cell two distinct trap regions are formed. A push beam with a $1/e^2$ radius of 3 mm propagates along the z-axis and is used to accelerate the cooled atoms out of the glass cell. Two CCD cameras are used to observe the 2D MOT and aid the initial alignment of trap light.

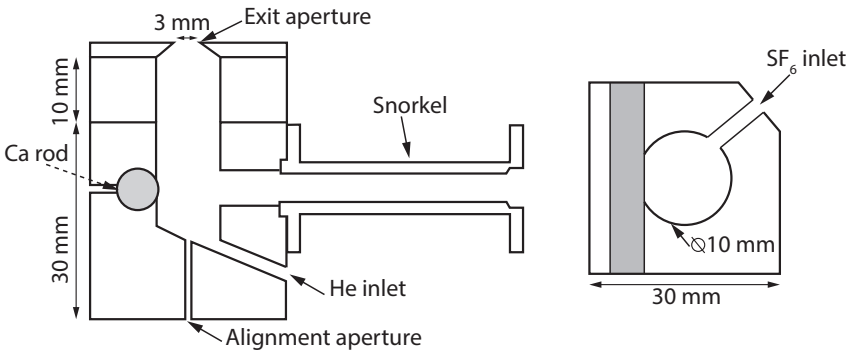

Figure 3.12: Schematic cross-sections of the buffer gas cell used to produce cold CaF molecules.

3.5 Molecule source

The design and characteristics of the buffer gas source of CaF molecules are described in detail in [120] and here only a brief review is given. Based on some of the rather painful experiences while working with this source a new cell was designed (but not yet tested). The new design is presented in appendix B.

A schematic cross-section of the buffer gas cell used in this experiment is shown in figure 3.12. It is machined out of deoxygenated copper and has dimensions of 30x30x40 mm and an inner bore diameter of 10 mm. The cell is bolted down to a cryostat cooled to a temperature of 4 K using a cryocooler. A laser pulse with an energy in the range of 5-10 mJ and a spot size of roughly 1 mm ablates a solid Ca rod inside the cell. New areas of the rod may be exposed to the ablation laser by rotating and advancing it via a vacuum feedthrough. The ablated Ca atoms react with SF_6 to produce CaF which then thermalise with the cold He atoms via elastic collisions. The flow of He and SF_6 gas into the buffer gas cell is controlled using a pair of mass flow controllers. Flow rates of 0.3 sccm and 0.05 sccm are found to work best in terms of the long term consistency in the number of molecules captured into the MOT. A beam of cold CaF molecules is extracted out of the cell through a 3 mm diameter aperture and propagates towards the science chamber.

A copper cylindrical shield with its inner surfaces delicately coated with coconut charcoal is bolted down to the cold head and also cools to around 4 K. At temperatures below 8 K charcoal starts to absorb He gas efficiently [121] and thus reduces the background pressure in the vicinity of the buffer gas cell. When the source is running the background pressure rises from around $3 \cdot 10^{-8}$ mbar to 1-2$\cdot 10^{-7}$ mbar.

After a day of running the source, the He compressor is switched off, after which the background pressure spikes up to 10^{-1} mbar and quickly falls back down. This large spike in pressure happens when the charcoal temperature rises by a few Kelvin and the absorbed He gas is suddenly released. It is found that a warm up and subsequent cool down cycle over the night helps to maintain more consistent performance of the source.

This may be due to SF_6 gas freezing[4] on the cell walls and affecting the thermalization process.

The source used to produce up to $5{\cdot}10^{10}$ molecules/steradian in the $\nu = 0$, $N = 1$ state with a mean pulse velocity of roughly 160 m/s though since its inception the performance has degraded substantially. Amongst the many small changes made to this source the two which made the biggest improvement were: (i) renewing the charcoal shields and (ii) swapping out the Ca rod with a new one. When the new Ca rod was installed it was slightly too large and when the cell was cooled to 4 K it would get jammed. Under such circumstances the molecular beam had a 20-30 % lower forward velocity and a substantial increase in the number of molecules captured into the MOT was observed. Again, one can only speculate about the reasons for this improvement but this would intuitively suggest that a better thermal contact of the Ca rod with the cell improved the source performance. After various such small changes throughout a couple of years the source now allows to capture 50-60 % of the previously recorded numbers of molecules into the MOT.

3.6 Science chamber optical setup

The complete optical setup around the science chamber is shown in figure 3.13. The CaF MOT vibrational repumpers $\mathcal{L}_{10}$, $\mathcal{L}_{21}$, $\mathcal{L}_{32}$ are combined with the CaF cooling light $\mathcal{L}_{00}^{\mathrm{C}}$ into a single beam. The available laser powers for $\mathcal{L}_{10}$ and $\mathcal{L}_{00}^{\mathrm{C}}$ light are not sufficient[5] to make a molecule MOT using three independent beams thus the optical power is recycled by wrapping a single beam around the chamber. At the output of the collimator, the CaF trap beam has a $1/e^2$ radius of 8.2 mm. Losses in optical power as the beam traverses the various optical components causes a significant intensity imbalance in the counter-propagating beam pairs. The loss in power is compensated to some extent by slightly focusing the beam.

The Rb MOT is made using six independent laser beams. Each beam contains up to 20 mW of cooling and around 3 mW of repump power. The beams are collimated to a $1/e^2$ radius of 10 mm and may each be steered using dedicated mirrors. The CaF and Rb beams are combined on dichroic mirrors: the CaF light is reflected while the Rb light is transmitted. Before entering the chamber both beams are circularly polarized with the appropriate handedness using dichroic quarter wave plates. For certain linear polarization orientations it was found that the dichroic mirrors may act as quarter wave retarders for the Rb light in transmission, producing circularly polarized light. In general, a laser beam

[4] The melting point of SF_6 is at 209 K

[5] The maximum output power of the $\mathcal{L}_{00}^{\mathrm{C}}$ used to be 600 mW throughout most of my PhD although the laser was specified for 1 W of output power. This turned out to be due to a laser controller software issue which was recently fixed enabling to run the laser at full power. Making a three beam MOT which captures the same number of molecules as the single beam MOT may now be possible.

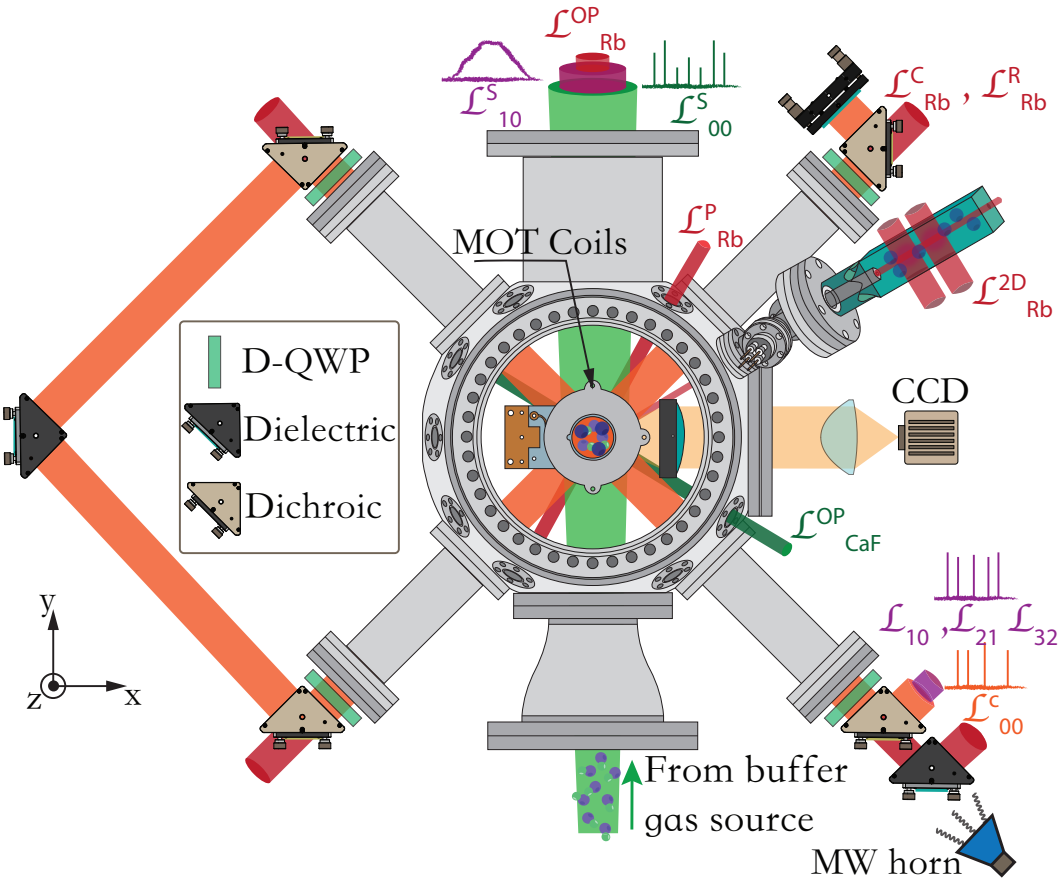

Figure 3.13: Science chamber optical setup. The various beams are indicated using the following notation. $\mathcal{L}^{C}_{Rb}$: Rb 3D MOT cooling; $\mathcal{L}^{R}_{Rb}$: Rb 3D MOT repump; $\mathcal{L}^{2D}_{Rb}$: Rb 2D MOT; $\mathcal{L}^{P}_{Rb}$: Rb absorption imaging probe beam; $\mathcal{L}^{OP}_{Rb}$: Rb optical pumping beam; $\mathcal{L}^{C}_{00}$: CaF MOT cooling; $\mathcal{L}_{10}$, $\mathcal{L}_{21}$, $\mathcal{L}_{32}$: CaF MOT repumps; $\mathcal{L}^{S}_{00}$: CaF slowing; $\mathcal{L}^{S}_{10}$: CaF slowing repump; $\mathcal{L}^{OP}_{CaF}$: CaF B-X optical pumping beam. For clarity, the vertical trap beams are not. Also indicated are the frequency spectra of the lasers for CaF. A microwave horn is used to couple 20 GHz microwaves into the science chamber.

which is not polarized either parallel or orthogonal with respect to the plane of incidence will have its polarization altered. For this reason half wave plates are used to set the linear polarization of the Rb beams before they go through the dichroic mirrors.

The weakest point of the current setup is the way the CaF trap light is coupled into the science chamber. The beam traverses a total distance of 6-7 m which makes it particularly sensitive to small mirror misalignments. In practice it is found that the first and retro-reflecting mirrors need to by adjusted very slightly every several days to maintain a similar molecule MOT performance. The standard procedure is to align the beam through the centre of each of the vacuum view-ports which typically produces a somewhat distorted cloud shape. Small adjustments are then made to the first and last mirror while observing the shape and brightness of the trapped cloud. In the future the plan is to try a three beam MOT which would make the standard alignment procedure more reproducible and

would enable better control of the trap beams.

The CaF slowing light $\mathcal{L}_{00}^{\mathrm{S}}$ is combined with a frequency broadened vibrational repump $\mathcal{L}_{10}$ into a single beam and is coupled through the science chamber along the molecule beam line. The beam is slightly focused in order to provide some cooling force to the molecules along the transverse direction.

The optical pumping beam $\mathcal{L}_{\mathrm{Rb}}^{\mathrm{OP}}$ used to prepare atoms in a single quantum state is combined with the slowing light on a dichroic mirror. The B-X optical pumping beam $\mathcal{L}_{CaF}^{\mathrm{OP}}$ used to pump molecules into the spin stretched state is coupled into the chamber using a CF16 viewport. Finally, a microwave horn is used to couple 20 GHz microwaves into the science chamber.

3.7 Fluorescence imaging

The molecule cloud is imaged by collecting the light induced fluorescence (LIF) by the $\mathcal{L}_{00}^{C}$ trap beams[6]. Figure 3.14 shows the fluorescence imaging setup. A plano-convex lens with a back focal length of 50 mm and a clear aperture of 50.8 mm is situated inside the science chamber. The lens is positioned such that the collected LIF is focused to infinity. An aspheric lens outside the chamber images the collected light onto an interline transfer CCD camera (Hamamatsu *Orca R2*). Background and laser light from the vibrational repumpers is blocked by a band-pass interference filter centred around 605 nm with a bandwidth of 4 nm. When using the fluorescence imaging system to image the atom cloud the interference filter is swapped for a neutral density filter.

The total magnification of the imaging system is measured by releasing a molecule cloud from an optical molasses and allowing it to drop freely under gravity. By tracking the position of the cloud as a function of time and using the pixel size of the CCD array it is possible to estimate the magnification. For this fluorescence imaging system the magnification is found to be 0.47, which is very close to the design value of 0.5.

3.7.1 Imaging molecules

The geometrical light collection efficiency of the imaging system is found using numerical optical ray tracing. The mathematics of ray tracing is described in detail in appendix A. The molecule cloud is modeled by a Gaussian spatial distribution of 1.2 mm radius in all three dimensions. In total 2000 particles are used in the simulation. A bundle of optical rays sampled from a uniform spherical distribution of angles represents the photons a molecule scatters in random directions. These rays are propagated through the optical system and the fraction of rays hitting the detector of a given size is calculated.

[6]Note that the $\mathcal{L}_{10}$ light also causes the molecules to fluoresce.

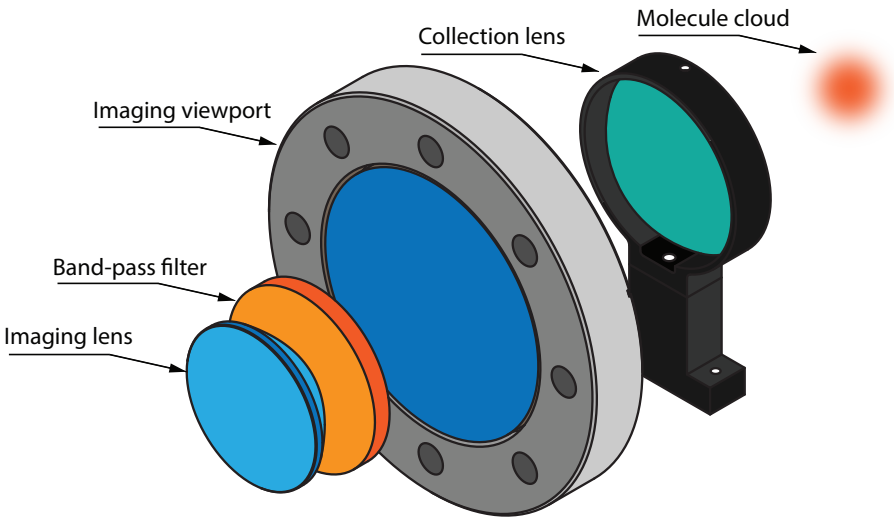

Figure 3.14: Fluorescence imaging setup. An in-vacuum high numerical aperture lens collects the LIF from the molecules. The light is focused to infinity and coupled out through an AR coated CF63 vacuum view port. An aspheric lens is used to image the LIF onto an interline CCD camera. A band-pass interference filter blocks background and vibrational repumper light.

In figure 3.15(a) the fraction of rays η_{G} imaged onto a square detector of length $\mathrm{d}_{\mathrm{det}}$ is plotted. It is evident that the collection efficiency saturates at around $\eta_{\mathrm{G}} = 0.02$ for a detector size of 6x6 mm^2. The rather slow convergence of the collection efficiency is due the large amount of spherical aberrations present in this optical system. Because the exact shape of the imaging lens is not specified by the manufacturer in the simulation it is replaced by a plano-convex lens with an equivalent focal length and clear aperture. An aspheric lens reduces the amount of spherical aberrations thus the result of the simulation gives a conservative estimate of the detection efficiency and in reality it may be somewhat larger.

A charge amplifier in the readout register of the CCD camera converts the electrons generated in each pixel into an analogue voltage. Then, a digital-to-analogue converter converts the voltage associated to a specific pixel into an integer pixel count number $\mathcal{N}$. The number of photons corresponding to $\mathcal{N}$ may be found from

$$\mathcal{N}_p = \frac{(\mathcal{N} - b)\chi}{\mathcal{N}^{\mathrm{Max}} G \eta_{\mathrm{QE}}} \,, \tag{3.6}$$

where b, χ, $\mathcal{N}^{\mathrm{Max}}$, G, η_{QE} are the electronic camera offset, full well capacity, pixel bit depth, readout amplifier gain and quantum efficiency respectively. Within an exposure time t_{exp}, a molecule will scatter $R_{\mathrm{s}} t_{\mathrm{exp}}$ photons of which a fraction $\eta_{\mathrm{T}}\eta_{\mathrm{G}}$ will be imaged onto the CCD. Here R_{s} is the scattering rate which is a function of the laser intensity and detuning and η_{T} is the transmission of the LIF through the various optical components. In terms of these and previously defined quantities the total number of molecules is given

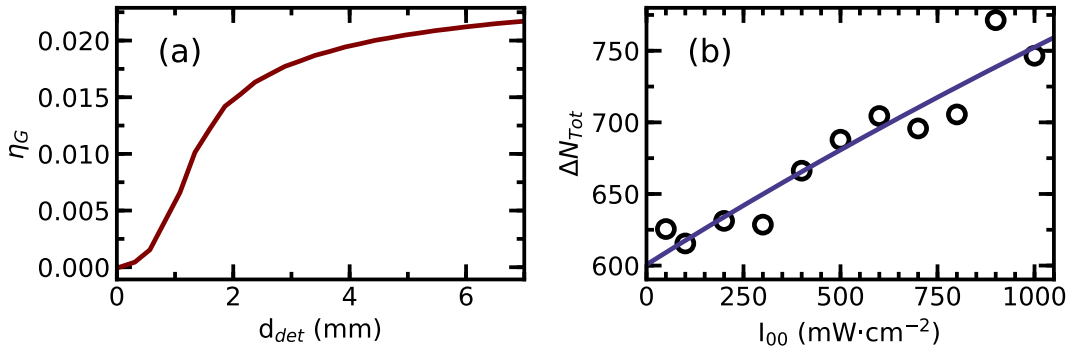

Figure 3.15: (a) Results of numerical ray tracing through the fluorescence detection setup. The detection efficiency η_{G} is plotted as a function of a square detector size of length $\mathrm{d_{det}}$. (b) Measured total camera detection noise for variable background levels. The background is varied by changing the trap light intensity I_{00}. The line is a fit to the model described in the main text.

by

$$\mathcal{N}_{\mathrm{mol}} = \frac{\chi}{\mathcal{N}^{\mathrm{Max}} G \eta_{\mathrm{QE}} \eta_{\mathrm{T}} \eta_{\mathrm{G}} R_{\mathrm{s}} t_{\mathrm{exp}}} \sum_{i,j} (\mathcal{N}^{\mathrm{s}}_{i,j} - \mathcal{N}^{\mathrm{bg}}_{i,j}) \ , \tag{3.7}$$

with $\mathcal{N}^{e,\mathrm{s}}_{i,j}$ and $\mathcal{N}^{\mathrm{bg}}_{i,j}$ the counts in pixel i,j due to the LIF from the molecules and laser scatter respectively. The sum runs over the entire array of pixels.

3.7.2 Smallest detectable signal

The smallest detectable signal will be limited by the detection noise which has three independent contributions: the detection shot noise from counting both the signal and background photons, the camera readout and thermal noise. To measure the total noise, the camera is exposed for 10 ms to a variable intensity background. The background level is varied by simply changing the $\mathcal{L}_{00}$ intensity. For each background level 524 images are recorded and the standard deviation of the total pixel counts within a region of interest corresponding to where the molecule cloud is trapped is computed. For these measurements a 10 ms exposure time is used.

Figure 3.15(b) shows how the total detection noise varies with the background light level. The noise added by the laser scatter is small compared to the readout noise, even at the highest laser intensity used, so the smallest detectable signal is limited by the readout noise. Fitting this data to the following model

$$\Delta\mathcal{N}_{\mathrm{Tot}} = \sqrt{\alpha I_{00} + \Delta\mathcal{N}_{\mathrm{r}} + D t_{\mathrm{exp}}} \ , \tag{3.8}$$

with $\Delta\mathcal{N}_{\mathrm{r}}$ and Dt_{exp} the readout and dark noise respectively, and extrapolating to zero intensity gives a detection noise of 600 pixel counts. This corresponds to the signal generated by roughly 20 molecules. At full intensity, the detection noise is 750 pixel

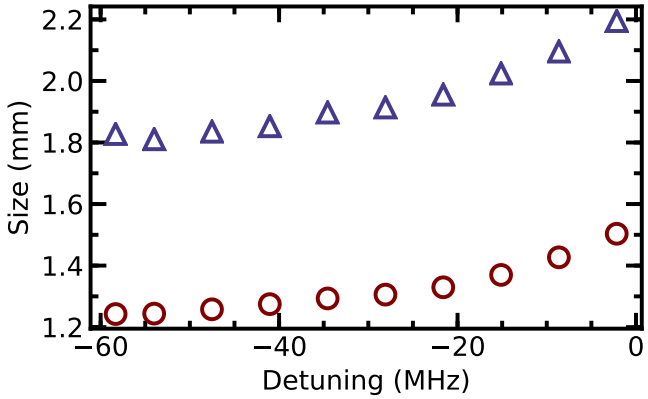

Figure 3.16: The apparent size of a cloud of atoms acquired using fluorescence imaging. Images are acquired using a variable detuning of the trap beams which illuminate the atom cloud.

counts which corresponds to 25 molecules- the smallest number of molecules that may be detected within a single image of a 10 ms exposure time.

3.7.3 Imaging atoms

In some of the experiments described in this work it was necessary to know accurately the relative positions of the trapped molecule and atom clouds; thus the fluorescence imaging system described above was also used to image atoms. Fluorescence imaging of large and optically thick atom clouds presents several challenges. First, the laser beams (typically the trap beams) will be attenuated as they penetrate through the cloud of atoms. Atoms further away from the cloud centre will interact with more intense light and thus scatter more photons in a given time compared to atoms near the dense core which will scatter photons from an attenuated laser beam. The cloud will thus appear larger than it actually is and this effect will be exacerbated for light with a frequency closer to the atomic resonance. This effect is investigated empirically: atoms are imaged for 100 μs by illuminating them with all 6 MOT beams detuned from resonance by a different amount. Figure 3.16 shows how the apparent size of an atom cloud varies with the trap light detuning. As expected, the cloud appears to be larger when atoms are illuminated with laser light closer to the resonance frequency. For laser detunings below -60 MHz the apparent cloud size becomes roughly constant because the attenuation of the trap laser beams is reduced. When using fluorescence imaging to get the atom cloud size a detuning of -60 MHz is used.

Secondly, photons may be rescattered multiple times within the cloud. This will again effect the apparent size of the cloud and in addition make it complicated to determine the atom number. For this reason the fluorescence imaging system is employed only to determine the atom cloud size using far red-detuned trap beams while the atom number

is found using absorption imaging as described below.

3.8 Absorption imaging

The number of atoms in a cloud is determined using absorption imaging. The absorption of a weak probe beam was discussed in section 2.2.6. The change in intensity of the probe beam as it propagates through a cloud of atoms with a spatially varying number density $N(x, y, z)$ is commonly written as

$$I(x, y) = I_0(x, y) \exp\left(-\sigma(\Delta) \int_{-\infty}^{+\infty} N(x, y, z) dz\right) , \tag{3.9}$$

where $I_0(x, y)$ is the incident beam intensity, Δ is the frequency detuning and $\sigma(\Delta)$ is known as the absorption[7] cross section. The integration bounds are chosen assuming that the extent of the laser beam is much larger than the size of the atom cloud.

The probe beam is typically set up in a way so that it drives a closed transition reducing the complexity of the atom to a two-level system. In this case the absorption cross section has the simple form

$$\sigma(\Delta) = \frac{\sigma_0}{1 + 4\frac{\Delta^2}{\Gamma^2}} , \tag{3.10}$$

with Γ the spontaneous decay rate. The resonant absorption cross-section is given by

$$\sigma_0 = \frac{3\lambda^2}{2\pi} , \tag{3.11}$$

with λ the transition wavelength. For a real atom the scattering cross-section will depend on the initial state distribution, magnetic field and the imaging light parameters. All of these parameters must therefore be carefully controlled and calibrated in order to obtain a reliable estimate of the number of atoms.

The atom column density defined as

$$N_{\mathrm{Cl}}(x, y) = \int_{-\infty}^{+\infty} N(x, y, z)\ dz , \tag{3.12}$$

is determined by measuring the amount by which the probe laser beam is attenuated

$$N_{\mathrm{Cl}}(x, y) = \frac{1}{\sigma(\Delta)} \ln\left(\frac{I_0(x, y)}{I(x, y)}\right) . \tag{3.13}$$

The logarithm of intensities in the above expression is commonly called the optical depth. The total number of atoms is found by integrating the column density

$$\mathcal{N}_{\mathrm{At}} = \int_{-\infty}^{+\infty} \int_{-\infty}^{+\infty} N_{\mathrm{Cl}}(x, y)\ dx\ dy . \tag{3.14}$$

[7] Strictly speaking this is a scattering cross section because photons are removed from the probe beam due to spontaneous scattering of the probe beam photons. In an experiment the attenuation of the laser beam is measured which leads to the more intuitive notion of absorption.

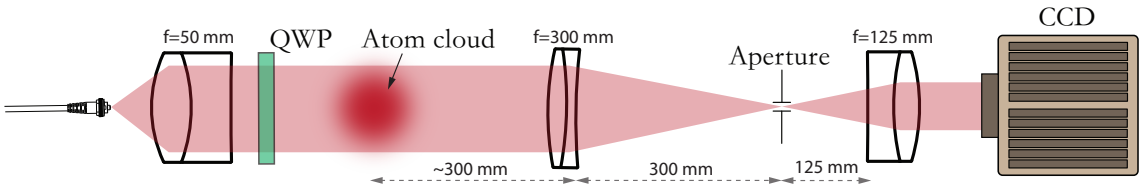

Figure 3.17: Absorption imaging system. Light emerging from a single mode polarization maintaining fibre is collimated using a 50 mm focal length doublet lens to a waist radius of 5 mm. Before entering the science chamber the beam is circularly polarized using a quarter wave plate. The shadow cast by the cloud of atoms in the path of the beam is imaged onto a CCD camera using a 4-f optical relay composed of 300 mm and 125 mm focal length doublet lenses. An aperture placed in the Fourier plane (in between the two lenses) blocks most of the fluorescence light from the atoms.

If the density distribution of the cloud is known the measured distribution of the column density may be used to extract directly both the size of the cloud and the atom number. To measure the column density distribution the shadow cast by the atom cloud is imaged onto a CCD camera and compared to the probe intensity in the absence of atoms. For an arbitrary density distribution the integral of eq. 3.14 may be replaced by a discrete sum

$$\mathcal{N}_{\mathrm{At}} = \frac{A}{\sigma(\Delta)} \sum_{i,j} \ln\left(\frac{I_0^{i,j}}{I^{i,j}}\right) \ , \tag{3.15}$$

with A the area in the object plane represented by one pixel. Here $I_0^{i,j}$ and $I^{i,j}$ are the measured probe intensities in pixel i, j in the absence and presence of atoms respectively. Atom numbers in this work are found by evaluating the sum in eq. 3.15 as it is simpler to compute for any arbitrary density distribution.

3.8.1 Imaging system

The absorption imaging system is shown in figure 3.17. The shadow cast by atoms in the path of a probe beam with a $1/e^2$ radius of 5 mm is imaged using a 4-f optical relay onto a CCD camera. A pair of doublet lenses form the optical relay system with a magnification of $f_2/f_1 = 0.42$, which is confirmed empirically by dropping the atom cloud released from the MOT and measuring the rate of change in its position. In situations where the cloud contains many atoms the bright fluorescence may saturate the CCD camera and produce unwanted artefacts in an absorption image. This is because the camera may not be able to clear the excess charge accumulated due to the bright fluorescence light impinging on the camera before the trap beams are turned off and an absorption image is acquired. This effect is observed when imaging large clouds right after releasing from the MOT and is eliminated by placing an aperture in the Fourier plane of the $4f$ optical relay.

To extract information about the atom cloud a set of three images in quick succession

is acquired: probe images in the presence and absence of atoms and a background image with the probe switched off. Each image is acquired by turning on the absorption probe beam using an AOM for 100 μs and simultaneously triggering the CCD camera. The intensity of the probe beam is $0.02 I_{\mathrm{Sat}}$.

Probe polarization

The probe beam is circularly polarized and propagates along the direction of a uniform magnetic field of 400 mG. For a right-hand circular polarization of the probe only transitions which change the Zeeman level by $\Delta m_F = +1$ are driven (σ^+ transitions). Equation 3.10 for the absorption cross-section becomes valid when atoms populate the $|F = 2, M_F = +2\rangle$ state as the probe beam then connects only to the $|F' = 3, M_{F'} = +3\rangle$ state. The coupling between these two states is strongest and so the absorption cross-section is maximized.

To confirm that the probe beam drives only σ^+ transitions a spin polarized cloud of atoms released from a magnetic quadrupole trap (described in detail in chapter 6) is imaged using a variable resonant probe beam polarization. Imaging atoms released from the magnetic trap eliminates the uncertainty of the initial state distribution[8] and enables a comparison of the measured probe beam absorption with a rate equation model which describes the interaction of light with the multi-level atom. In this experiment the angle of the QWP fast axis relative to the direction of the input linear polarization is varied. Figure 3.18 shows how the total relative absorption varies with the QWP angle. When the angle is at 45° the probe beam is circularly polarized to drive σ^+ transitions and the absorption is maximum. At QWP angles of -45° and 135° the probe is polarized to drive σ^- transitions. For this polarization it takes a finite amount of time for atoms to be pumped into the $|F = 2, M_F = -2\rangle$ state where the absorption is again maximized. Thus the time averaged absorption cross-section will be smaller. For wave plate angles of 0° and 90° both σ^+ and σ^- transitions are driven with an equal intensity.

The solid line in figure 3.18 is the solution to a rate equation model which describes the interaction of the probe with atoms prepared in the $|F = 2, M_F = +2\rangle$ state. The model accurately predicts the contrast in absorption between the two extreme polarizations and matches the measured variation with the QWP angle reasonably well. Deviations from the model may be explained by imperfect intermediate polarizations produced using the QWP.

[8]The magnetic field gradient for the trap is chosen such that only atoms in the $|F = 2, M_F = +2\rangle$ state are levitated against gravity.

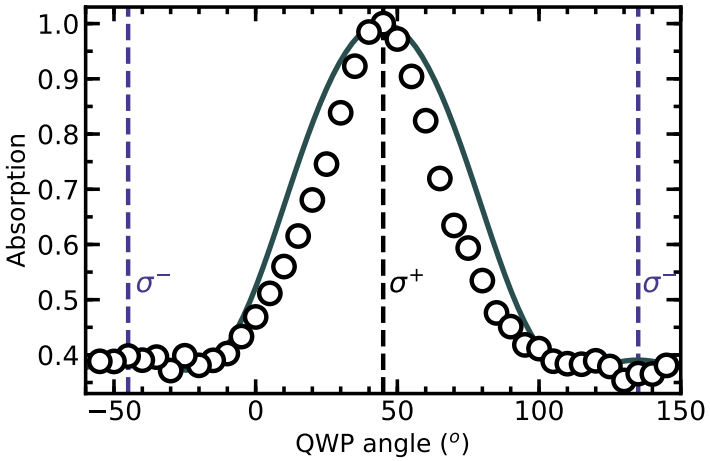

Figure 3.18: Absorption of a resonant probe beam as a function of the QWP angle which sets the polarization of the beam. The absorption is plotted relative to the peak absorption for light polarized to drive the $|F = 2, M_F = +2\rangle \rightarrow |F' = 3, M_{F'} = +3\rangle$ transition. The solid line is obtained by solving the system of rate equations which describes the time dependence of atomic populations for a variable probe polarization.

Probe detuning

To find the resonance frequency, the probe frequency is scanned and the absorption by a small cloud of atoms released from the magnetic trap is measured. Figure 3.19(a) shows how the relative probe absorption varies with detuning. Because the cooling, push beam and optical pumping light are derived from the same laser and shifted in frequency using dedicated AOM's the absorption profile is also used to accurately determine the frequency detuning of all these light components. The absorption profile will be a convolution of the natural transition line shape and a Gaussian distribution which takes into account the broadening due to the finite laser line width and the stability of the frequency offset lock. The natural line width is described by a Lorentzian function so that the absorption profile will be described by a Voigt profile. The data is fitted to a Voigt profile with the transition line width set to $\Gamma = 6.065$ MHz. The fit gives a Gaussian width of 1.08(7) MHz. At a temperature of 300 μK, the transition is Doppler broadened by 300 kHz, which adds in quadrature with the frequency noise of the laser.

Due to the limited dynamic range of a CCD camera there will be a maximum number of atoms that may be measured by recording an absorption image. The dynamic range of the camera is defined as the ratio of the maximum number of photo-electrons that may be accumulated within a single pixel and the readout noise. The CCD camera used in this work has a dynamic range of 3000 and thus a maximum optical depth of $\ln(3000) \approx 8$ may be measured. A spherically symmetric cloud of radius 0.22 mm and a peak number density of $5 \cdot 10^{10}$ cm^{-3}, typical for atomic MOT's, contains roughly 10^7 atoms. Probing such a cloud with resonant light would lead to a peak optical depth of around 8, which

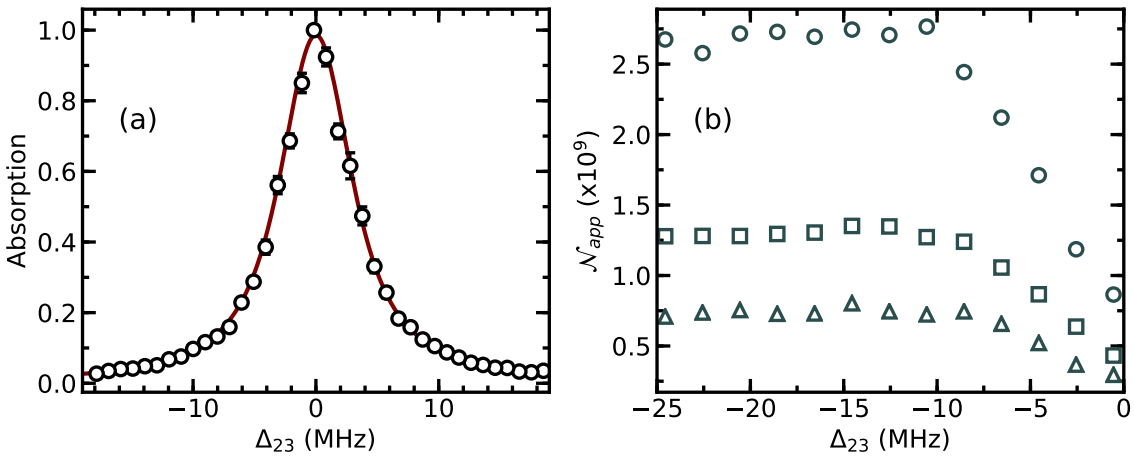

Figure 3.19: (a) Absorption of the probe beam by a small cloud of atoms as a function of laser frequency detuning. The line is a fit to a Voigt profile. (b) Apparent number of atoms $\mathcal{N}_{app}$ as a function of the probe beam frequency detuning Δ_{23} for clouds containing three different atom numbers.

is the maximum the CCD camera can measure. In this work atom clouds containing more than 10^9 atoms are routinely produced. In order to image these clouds the probe frequency is detuned so that the absorption is reduced.

The optical depth saturation effect in absorption imaging is demonstrated experimentally by imaging clouds containing different atom numbers using a variable probe detuning. Figure 3.19(b) shows how the apparent number of atoms varies with probe detuning for three clouds containing a different number of atoms. Atom numbers are computed using eq. 3.15 and the two-level absorption cross section adjusted for the different probe detunings. As the absolute value of the detuning is increased there appears to be more atoms. For a sufficiently large detuning the apparent atom number becomes constant and at this point the true value is revealed. Clouds with a larger spatial extent and containing more atoms at a fixed peak number density will lead to a higher peak optical depth. For this reason the apparent atom number saturates at a larger frequency detuning as is evident from the figure. In this work a detuning of -14.2 MHz is typically used to image the atom clouds. Depending on the size of the cloud, the peak optical depth varies in the range of 1-3.

3.8.2 Systematic errors in absorption imaging

A total of three sources of systematic error are identified when inferring properties of the cloud from an absorption image. The first two affect the atom number estimates while the last one affects estimates of cloud size as described below.

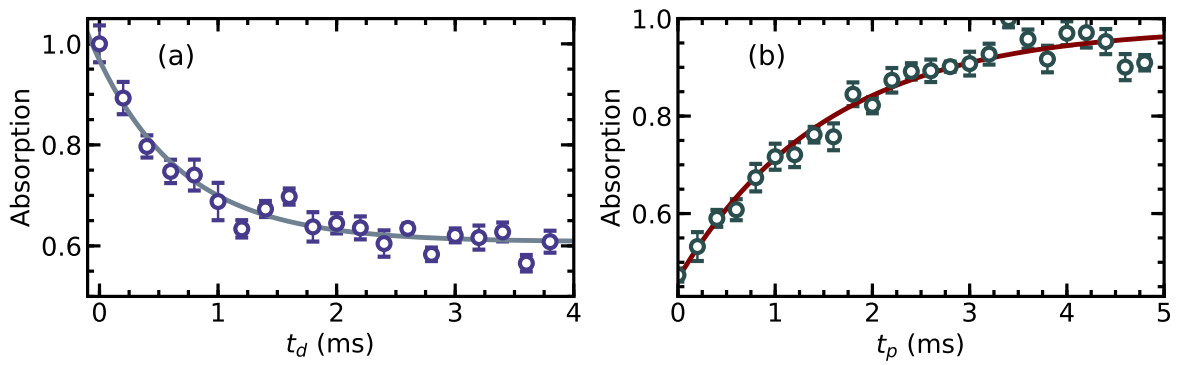

Figure 3.20: Sources of systematic error in absorption imaging. (a) Absorption images are acquired after a delay time t_d after switching off the MOT coils. (b) Atoms are pumped for a duration t_p using the probe beam before the absorption is measured. The solid lines are fits to a single exponential decay model.

Decaying magnetic field

The scattering cross section is sensitive to the direction and magnitude of the magnetic field at the position of atoms relative to the probe beam propagation direction and its polarization. The field direction will determine the allowed transitions that the probe may drive while a large field magnitude may significantly shift the transition frequency due to the Zeeman interaction. It takes a finite time for the current flowing through the MOT coils to be switched off. In addition, rapid switching of current induces time varying Eddy currents in the surrounding electrically conducting surfaces. These in turn produce a time varying magnetic field at the position of the atom cloud. The additional contributions to the applied bias field along the probe beam lead to a poorly defined total magnetic field direction and magnitude shortly after switching off the MOT coils.

This effect is investigated empirically by imaging atoms released from the MOT for 100 μs after a variable delay time t_d after the coils are triggered to switch off. Figure 3.20(a) shows how the total absorption of the probe beam varies with t_d. At $t_d = 0$ the absorption is highest because the MOT magnetic field tends to shift the atoms closer to resonance with the light. An exponential decay fit to these data gives a decay time constant of 0.73(9) ms. Imaging of atoms is performed with $t_d = 1$ ms where the cross section is about 19 % smaller than its value at zero field. This reduced cross section is used when estimating the number of atoms.

Initial state distribution

Because atoms in the MOT are distributed across all the Zeeman sub-levels in the F=2 state and the probe beam perturbs this distribution very weakly it will take a finite amount of time for the absorption cross section to reach a steady state. For the chosen probe polarization the steady state corresponds to cycling photons between the spin stretched

states $|F = 2, M_F = +2\rangle \rightarrow |F' = 3, M'_F = +3\rangle$ and the resonant absorption cross-section in this case is $\sigma_0 = 3\lambda^2/2\pi$.

To find the initial MOT state distribution and how it affects the absorption of the probe beam the following experiment is performed. The probe beam is turned on 1 ms after switching off the MOT coils for a variable amount of time t_p before the CCD camera is triggered to acquire the absorption image. Figure 3.20(b) shows how the total absorption of the probe beam varies with t_p. Fitting the data to an exponential model gives an optical pumping time constant of 1.54(13) ms. By solving rate equations describing the light-atom interaction we find a similar time scale of around 1 ms for the atom population to reach a steady state. The discrepancy may be explained by the increasing Doppler shift. As the atoms interact with the probe beam they are being pushed by it which gradually shifts them further from resonance and thus reduces the amount of absorption.

The instantaneous absorption cross-section for atoms distributed equally over the 5 ground states Zeeman-levels is equal to $7\sigma_0/15$ if only σ^+ transitions are driven. From the fit to the data in figure 3.20(b) it is found that at $t_p \rightarrow \infty$ the absorption of the probe light is a factor of 2.10(4) higher than at $t_p = 0$. This result is consistent with an initial equal distribution of atoms over the ground state sub-levels. Since the absorption image is acquired with $t_p = 0$ the number of atoms will be underestimated by a factor of 15/7. This correction is applied to all atom number estimates when imaging clouds released from the MOT. Atoms in a magnetic trap are all in the $|F = 2, M_F = +2\rangle$ state thus this effect is absent.

Lensing effect

For a frequency detuned probe beam the real part of the complex susceptibility $\chi_R \neq 0$. The refractive index defined in eq. 2.59 is $n > 1$ for a negative detuning and $n < 1$ for a positive detuning. Thus an atom cloud behaves as either a diverging ($\Delta > 0$) or converging lens ($\Delta < 0$) with a focal length f_A which is derived below.

Using eqs. 2.54 and 2.54, the real and imaginary parts of the complex susceptibility are related as

$$\chi_R = -\frac{2\Delta}{\Gamma}\chi_I \ . \tag{3.16}$$

Using eq.2.56 the intensity of a laser beam will be attenuated as

$$I(x, y) = I_0(x, y) \exp\left(\int_{-\infty}^{+\infty} \chi_I(x, y, z)k \ dz\right) \ . \tag{3.17}$$

By comparing the equation above with eq. 3.9 it is evident that the integral in the exponent is simply the optical depth measured in an absorption image

$$O.D.(x, y) = \left(\int_{-\infty}^{+\infty} \chi_I(x, y, z)k \ dz\right) \ . \tag{3.18}$$

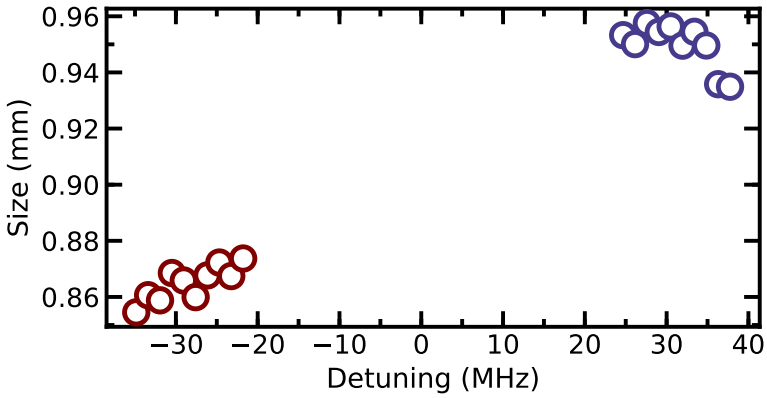

Figure 3.21: Lensing effect of the atom cloud. The cloud appears to be smaller for a red detuned probe compared to a blue detuned probe.

The field corresponding to the laser beam traversing the cloud accumulates a total phase, which using eqs. 3.16 and 3.18 is given by

$$\begin{aligned}\phi(x,y) &= \int_{-\infty}^{+\infty} \left(1 - \frac{\Delta}{\Gamma}\chi_I(x,y,z)\right) k \; dz \\ &= \phi_0 - \frac{\Delta}{\Gamma} O.D.(x,y) \; ,\end{aligned} \tag{3.19}$$

where ϕ_0 is a propagation phase. The cloud typically has a Gaussian spatial distribution and so the optical depth also takes the form of a Gaussian. Up to 2^{nd} order, the optical depth is given by

$$O.D.(x,y) \approx \tau \left(1 - \frac{x^2}{2\sigma_x^2} - \frac{y^2}{2\sigma_y^2}\right) \; , \tag{3.20}$$

with σ_x and σ_y the $1/e^2$ radii of the cloud along x and y directions and τ the peak optical depth

It may be shown [122] that a thin lens with focal length f will impart a phase given by

$$\phi_f(x,y) = -\frac{k\,(x^2+y^2)}{2f} \; . \tag{3.21}$$

By comparing this result with eq. 3.19, and using the approximation of eq. 3.20, the effective focal length of an atom cloud may be written as

$$f_{\mathrm{A}} = -\frac{2\pi\Gamma\sigma^2}{\Delta\lambda\tau} \; . \tag{3.22}$$

Using optical ray transfer matrices, the total magnification of the absorption imaging system, including the atom acting as a thin lens, is given by

$$M = \frac{\delta l_2 f_1}{f_2 f_A} + \frac{f_2(\delta l_1 - f_A)}{f_1 f_A} \; , \tag{3.23}$$

with δl_1 and δl_2 the positioning errors of the two lenses. For a perfectly aligned optical system the total magnification is $M = f_1/f_2$ and the refractive index of the atom cloud does not affect the apparent size. On the other hand, for a resonant probe $f_A \to \infty$,

and the total magnification is robust to misalignments. Because atom clouds are probed using $\Delta < 0$ it is important to consider potential misalignments. For this purpose, the atom cloud is imaged using a range of positive and negative detunings and the sizes at both ends are compared. Figure 3.21 shows the measured cloud size as a function of probe detuning. This cloud contains $1.5 \cdot 10^9$ atoms. As expected from eq. 3.23, the cloud appears to be smaller for a red detuning and a measurement here underestimates the size by 5%. For the smallest clouds used in magnetic trapping experiments, this systematic error is around 3%.

3.8.3 Temperature measurements

The temperature of a cloud of atoms or molecules is measured via ballistic expansion. A cloud which is in thermal equilibrium will have a Gaussian spatial distribution with radius σ_0 in the trap. As the trap is turned off and the cloud is allowed to freely expand its size will change as

$$\sigma(t) = \sqrt{\sigma_0^2 + \frac{k_\mathrm{B} T}{m} t^2} \,, \tag{3.24}$$

with T the temperature and m the mass of the constituent particles. A series of absorption or fluorescence images are recorded at variable free expansion times to find the rate of expansion and thus the temperature of the cloud.

4 | Magneto-optical trapping of Rb and CaF

This chapter introduces the basic working principle of the magneto-optical trap (MOT) and the characteristics of the Rb and CaF MOT's produced in this work. Experimental procedures used to load both species into the trap are described in some detail together with the optimization of key experimental parameters.

4.1 Basics of magneto-optical trapping

The optical molasses technique damps the motion of atoms or molecules but does not spatially confine them. Particles with sufficiently low initial velocities accumulate around the intersection region of the cooling laser beams and slowly diffuse out with typical diffusion times of around a second. On the other hand in a MOT atoms or molecules experience both cooling and trapping forces, which create dense and cold clouds. Atomic MOTs today are the starting point of probably any ultracold atom experiment. On the other hand MOT's for diatomic molecules are still a novelty and confinement in all 3 dimensions was thus far been demonstrated for only 3 different species: SrF at Yale [123], CaF here at Imperial College [97] and Harvard [124], and YO at JILA [125]. More recently the magneto optical force was used to compress in 1D a beam of polyatomic molecules [126].

4.1.1 MOT force in 1D

To understand how the magneto-optical force arises consider a toy 2-level atom in a spatially varying magnetic field in 1-D depicted in figure 4.1. For simplicity $F = 0$, $F' = 1$ and the Landé g-factor is $g_{F'} = 1$. The magnetic field points along the z-axis for $z > 0$ and in the opposite direction for $z < 0$. The magnitude of the field increases linearly from $z = 0$ along both directions with a gradient b_z and shifts the transition frequency of the atom by an amount $m_F \mu_B b_z z/\hbar$ due to the Zeeman effect. A pair of counter-propagating right-hand circular polarized laser beams detuned to the red from the zero field resonance by an amount Δ interact with the atom. An atom which scatters photons from the beam

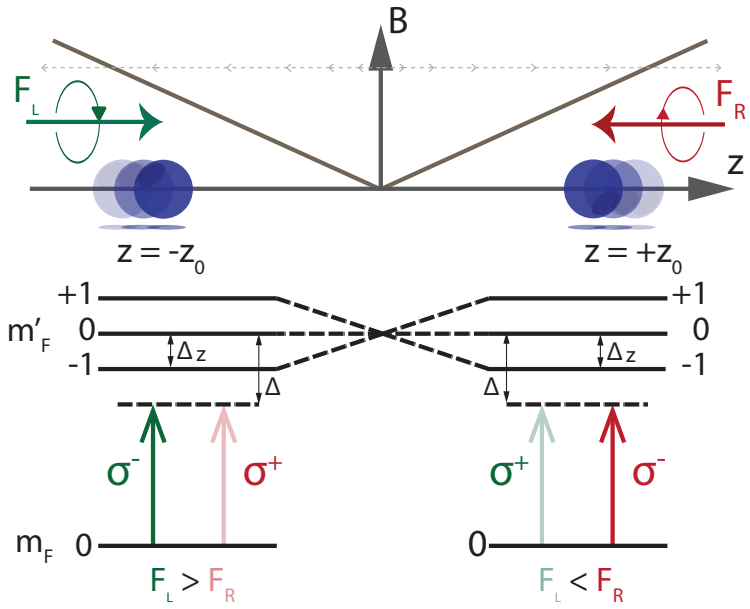

Figure 4.1: Operating principle of a MOT. Top: an atom moving in a spatially varying magnetic field interacts with a pair of counter-propagating laser beams detuned to the red by an amount Δ. The beams are left-hand circularly polarized. Bottom: an atom with a non-zero magnetic moment has its energy levels shifted by an amount Δ_z due to the Zeeman effect. Each beam drives transitions for which the change in magnetic quantum number is $\Delta m_F = \pm 1$, denoted as σ^+/σ^-. Depending on the position of the atom the radiation pressure force F_L arising from the beam propagating from the left will be smaller or larger than the force F_R exerted by the beam propagating from the right. A net restoring force is thus exerted on the atom which pushes it towards the field zero. See main text for a more detailed discussion.

propagating from left to right experiences a force F_L along the direction of propagation of the beam. Similarly, an atom which scatters photons from the counter-propagating beam experiences a force F_R in the opposite direction. The scattering rate and thus the force depends on the position of the atom. Consider, for example, an atom displaced to the left, at $z = -z_0$. Setting the local direction of the magnetic field as the quantization axis of the atom it is evident that the left beam will drive transitions for which $\Delta m_F = -1$ (σ^- transitions) while the right beam will drive transitions for which $\Delta m_F = +1$ (σ^+ transitions). Because of the Zeeman shift the σ^- transitions will be closer to the laser frequency and the atom will scatter mostly from the left beam which will push it towards the field zero. The same arguments apply for an atom at $z = +z_0$ and a net restoring force on the atom is produced. In experiments, this scheme is extended to 3-D by using anti-Helmholtz coils to generate the quadrupole field and 3 pairs of circularly polarized laser beams.

The simple equation used to describe the damping force produced in the optical molasses can be extended to describe the MOT. The total force experienced by the atom in

a 1-D MOT may be written as[1]

$$\mathrm{F}_{\mathrm{Tot}}^{\mathrm{MOT}} = F_s(\Delta - \Delta_Z) - F_s(\Delta + \Delta_Z) \ , \tag{4.1}$$

where $\Delta_Z = \mathrm{m_F}\mu_B b_z z/\hbar$ is the Zeeman shift at position z. For small displacements from the field zero the force may be approximated using a Taylor series expansion up to first order. The total magneto-optical force is then

$$\mathrm{F}_{\mathrm{Tot}}^{\mathrm{MOT}} = 4k\mu_{\mathrm{B}} b_z s \frac{2\Delta/\Gamma}{(1 + s + 4\Delta^2/\Gamma^2)^2} z \ , \tag{4.2}$$

and for $\Delta < 0$ is indeed a restoring force. Combining this result with the radiation damping force gives the total force experienced by an atom in the MOT

$$\mathrm{F}_{\mathrm{Tot}} = -\beta v - \kappa z \ , \tag{4.3}$$

with the damping constant β defined in eq. 2.44 and the MOT spring constant given by

$$\kappa = -4k\mu_{\mathrm{B}} b_z s \frac{2\Delta/\Gamma}{(1 + s + 4\Delta^2/\Gamma^2)^2} \ . \tag{4.4}$$

In the MOT the presence of a spatially varying magnetic field disturbs sub-Doppler cooling and precludes obtaining the lowest temperatures. Thus in practice, after loading the MOT with atoms or molecules, the magnetic field is switched off to initiate the stronger sub-Doppler forces and achieve lower temperatures.

4.1.2 Type I and II MOT's

It is common to classify MOT's into two different types depending on the angular momentum structure of the ground and electronic states addressed by the trapping light. The trap described above and illustrated in figure 4.1 employs the transition for which $F > F'$ and is classed as a type-I MOT. Almost all atomic MOT's are formed using the type-I transition.

Confining molecules using a rotationally closed transition requires states where $F \leq F'$. This is classed as a type-II MOT and in general may lead to dark states and no net trapping force. To understand the complications of a MOT formed using a type-II transition consider a molecule with $F = 1$ and $F' = 0$ interacting with two counter-propagating laser beams depicted in figure 4.2(a). A molecule which is displaced to the right (magnetic field points along the $z-$axis) and starts in the state $m_F = +1$ will scatter a photon from the right beam. After only a few scattering events the molecule will decay to the $m_F = -1$ state which is dark to the right beam. On the other hand, the left beam will eventually drive the transition and push the molecule away from the field zero. In this case no net restoring force is exerted on the molecule.

[1]Note that here the Doppler shift and effects due to stimulated absorption are ignored.

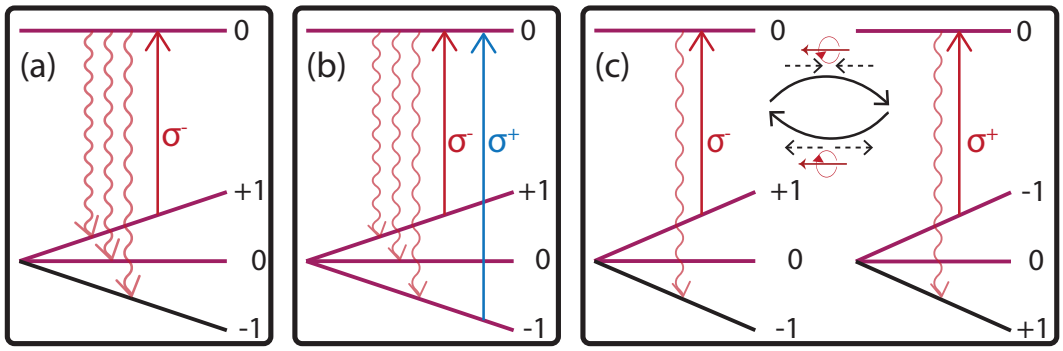

Figure 4.2: (a) In a type-II MOT there are states which are dark to the restoring laser beams and no net confining force is generated using the trapping scheme of the type-I MOT. (b) A dual-frequency MOT with two different laser frequencies which have opposite handedness polarizations generates a net restoring force. (c) In an RF-MOT the trap laser polarization and magnetic field direction are switched rapidly to create a net restoring force. See main text for a detailed explanation of the schemes in (b) and (c). Solid arrows indicate the laser frequencies of laser beam propagating from the right together with the transition types. Wavy arrows indicate the decay of the molecule after excitation. Energy levels indicated by purple lines are bright to the trap light while black lines indicate states which are dark to the trap light. Note that the $m_F = 0$ state is also dark to the trap light for this particular choice of ground and excited state hyperfine structures although molecules will be pumped out from this state by the orthogonal beams in a 3D MOT.

Two methods exist to get around the problem of optical pumping into dark states using the type-II transition. The first method uses two different laser frequencies with opposite circular polarizations to form the trap. This scheme is depicted in figure 4.2(b). Continuing with the example above, an additional blue-detuned component which propagates along the same direction as a red detuned component with opposite polarization will push a molecule which decays to $m_F = -1$ towards the trap centre. A net restoring force is exerted on the molecule and this scheme is know as the dual-frequency MOT. The second method uses only a single laser frequency but the polarization of the beams together with the field direction are rapidly reversed to maintain photon cycling. This scheme is depicted in figure 4.2(c). When a molecule decays to the state $m_F = -1$ the direction of the field is reversed so that the Zeeman shift changes sign and the $m_F = -1$ state is now closer to resonance. In addition the polarization is reversed to an opposite handedness- the molecule will scatter a photon from the right beam which pushes it towards the trap centre. By switching the polarization and field direction at a rate similar to the time it takes to pump the molecule into a dark state a net trapping force is exerted. This scheme is known as the RF-MOT and was employed to create MOT's of SrF [127] and CaF [124].

In this work the type-I transition is used to trap ^{87}Rb atoms while the difficulties of using the type-II transition to confine CaF molecules are circumvented using the dual-

frequency MOT.

4.2 The Rb MOT

The Rb 3D MOT is formed using 6 independent laser beams. To obtain a high loading rate without compromising the background pressure in the experiment chamber, a 2D MOT is formed in a glass cell attached to the main chamber via a differential pumping stage. A high vapour pressure of Rb can be maintained in the glass cell where the 2D MOT produces a beam of transversally cold and longitudinally slow atoms which is then captured into the 3D MOT. The design of both traps was described in chapter 3 and this section is devoted to the characteristics of the 2D-3D MOT system realized in this work.

4.2.1 Operating principle of the 2D MOT

A 2D MOT is formed using two pairs of counter-propagating laser beams in the x-y plane which intersect at right angles. Atoms traversing the intersection region of these beams are cooled towards the z-axis. An exit aperture with a diameter similar to that of the trap ensures that only transversally cooled atoms are extracted into a beam. In addition, the finite amount of time it takes to transversally cool an atom restricts the range of forward velocities v_z in the atomic beam.

To understand how the 2D MOT filters the longitudinal velocities, consider the case of an atom with longitudinal and transversal velocities v_z and v_{tr} entering the trap volume a distance Δz from the exit aperture. The edge of the trap coincides with the position of the exit aperture. This atom will spend a time $\tau_l = \Delta\mathrm{z}/v_z$ in the cooling region. The time it takes to transversally cool an atom towards zero velocity is $\tau_{\mathrm{tr}} = v_{\mathrm{tr}}/a$ with a the deceleration of the atom due to the strong laser cooling force. For an atom to contribute to the atomic beam it must spend a sufficient time in the cooling region so that its transversal velocity is reduced to close to zero. This means that $\tau_l > \tau_{\mathrm{tr}}$ which limits the longitudinal velocity to $v_z < \Delta\mathrm{z}/\tau_{\mathrm{tr}}$. Setting Δz equal to the trap length, which in this experiment is around 3 cm and taking an average transversal cooling time of 1 ms, the average longitudinal mean velocity is very roughly equal to 30 m/s. This is much smaller than the mean velocity of a thermal vapor at room temperature and is below the capture velocity of a 3D MOT.

The 2D MOT thus provides a bright beam of atoms which may be loaded into the 3D MOT. It is rather simple to construct and is very compact compared to, for example, a Zeeman slower. Also, it does not require a resonant laser beam to decelerate atoms to below the capture velocity of a 3D MOT which may affect the trap itself.

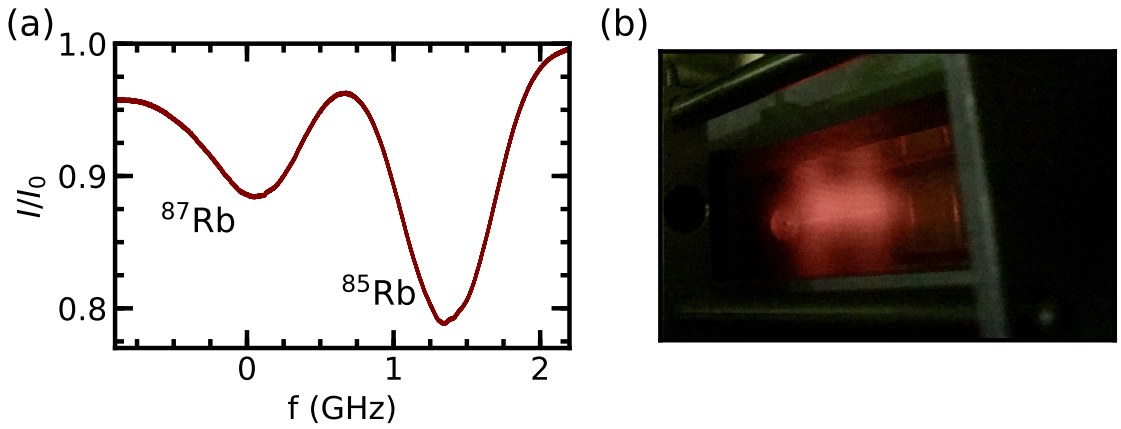

Figure 4.3: (a) The absorption of a 5 μW probe beam traversing the 2D MOT cell as its frequency is scanned. The transmitted intensity is normalized to the intensity of the beam before it enters the cell. The dispenser current is 3.2 A. (b) Image of the 2D MOT with a phone camera. A pair of brighter strings are just about visible and correspond to the two intersection regions of the trap beams where the atoms accumulate.

4.2.2 First signal from the 2D-3D MOT's

Because of the high differential pumping, the Rb vapour pressure will be very low in the experiment chamber and very little signal is expected from a 3D MOT loaded from this background vapour. For this reason the basic optimization begins from the 2D MOT. Once the 2D MOT is detected the loading rate of the 3D MOT is used as a diagnostic for further fine tuning. Methods for characterizing the flux of the atomic beam as a function of v_z extracted from a 2D MOT may be found in other work [115, 116].

Detecting Rb in the glass cell

Before starting to look for a MOT it is important to check whether Rb atoms are present in the cell when electrical current is flowing through the metal dispenser. A weak probe beam is directed through the glass cell onto a photo-diode positioned on the other side. The frequency of this probe is continuously scanned. Provided that atoms are being dispensed, the probe beam traversing the cell will be attenuated by an amount which depends on the laser frequency. Because the amount of absorption will be low for typical Rb vapour pressures, it is important to use a probe intensity which is much smaller than I_s. For high probe intensities the absorption signal may easily be obscured by the intensity noise of the laser or the shot noise. Figure 4.3(a) shows the recorded absorption of a probe beam traversing the glass cell as its frequency is scanned.

Another simple method to detect the presence of Rb is by viewing the traversing probe beam with an IR viewer. With a sufficiently slow frequency scan the path of the probe will light up periodically provided Rb is being dispensed.

Initial alignment

First, the beams to form the 2D MOT are aligned through the glass cell and made to intersect at right angles. A CCD camera is positioned close to the face of the glass cell and pointed at the position where the trap beams intersect. A zoom lens attached to the camera is used to focus this intersection region on the CCD sensor. Provided the trap beams have the correct polarization for the chosen direction of the magnetic quadrupole field and are detuned by roughly $\Delta = -2\Gamma$, a bright string of fluorescing atoms becomes visible. For higher Rb vapor pressures in the cell, fluorescence from the trapped atoms may be obscured by the fluorescing background atoms as may be seen in figure 4.3(b). A simple and effective method to check whether the observed brighter region is indeed a 2D MOT rather than light scattered from the face of the cell is to reverse the direction of the quadrupole field. Provided the localized fluorescence disappears the presence of the 2D MOT may be confirmed with confidence.

Next, the six beams which form the 3D MOT are aligned through the centre of the main chamber. The same laser detuning is chosen. A lens is used to collect light from the centre of the chamber which is then focused onto a photo-diode. After turning on the 2D MOT, the signal recorded by the photo-diode will increase provided the atoms cooled and confined in the 2D MOT are efficiently extracted towards the 3D MOT. Tight mechanical constraints of the glass cell assembly and the MOT optics ensures that this is the case. Once the signal is visible on the photo-diode it is useful to repeatedly load the 3D MOT for a second or so and make fine adjustments to the 2D MOT beam alignment and intensity balance. By maximizing the fluorescence, the alignment of the 2D MOT beams may be optimized. The fine tuning of the laser detunings and the magnetic field are done by acquiring absorption images of the 3D MOT as described below.

4.2.3 Rb dispenser

The Rb vapor pressure in the glass cell is controlled by adjusting the current through the dispenser. Figure 4.4 shows how the number of atoms loaded into an optimized 3D MOT varies with dispenser current. At a threshold current of about 3 A, the number starts to rise rapidly as more and more atoms are available to be cooled by the 2D MOT and extracted into the beam. The number of atoms loaded into the 3D MOT starts to saturate for a current of 4 A. For even higher currents the mean free path of an atom becomes comparable or smaller than the length of the cooling region and atoms are knocked out from the trap due to collisions with hot atoms in the background vapour.

These characteristic currents will be different depending on the positioning of the metal dispenser relative to the trapping region. In this setup most of the active length of the dispenser resides within the tube of the 4-way cross. Because Rb sticks to walls very easily, a higher dispensing rate will be required to reach a sufficiently high number density

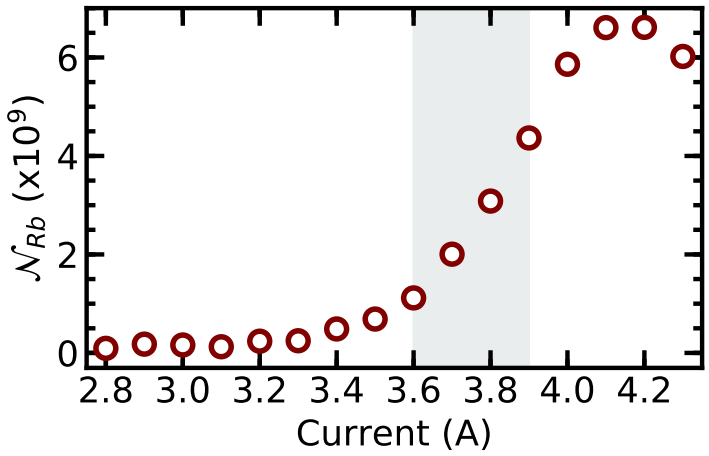

Figure 4.4: Number of atoms loaded into a 3D MOT for a fully optimized system using different Rb dispenser currents. The measurement is performed starting with the lowest current. Roughly 10 minutes are allowed before measuring the number of atoms at a higher current using absorption imaging. The shaded region corresponds to the range of currents typically used in the experiment.

of atoms at the position of the trap. For example, in a 2D MOT formed in a glass cell from *Cold Quanta*, the dispenser is positioned right in front of the trapping region. The current at which the loading rate saturates for such a geometry is only 2.8 A as measured in [128].

Running the dispenser with currents in the range of 3.5-3.8 A shows no apparent deterioration in the number of atoms captured into the MOT over a year of daily operation. To maintain the longevity of the dispenser the current is turned off for the night or over the weekends when not in use. It takes about 10-15 minutes for the dispenser to warm up and produce a steady flux of atoms after the current is turned on. If an activated dispenser is exposed to air, for example when breaking vacuum, it is considered unusable and is replaced.

Over the range of electrical currents explored in figure 4.4, the pressure in the experiment chamber remains at $5 \cdot 10^{-10}$ mbar, which is the lower limit of the ion gauge used to monitor the pressure.

4.2.4 Basic characteristics of the 2D MOT

A CCD camera is positioned by the side of the glass cell and is used to image the 2D MOT. The camera axis is at an angle of roughly 45^o relative to the axis of the atomic beam and thus affects the apparent length of the trapped cloud. As is visible from figure 4.3(b) two separate traps are formed of similar dimensions due to the geometry of the trap beams. The camera is focused on to one of these traps and is used to extract information about the cloud size and the loading time. These images are acquired in the absence of the push

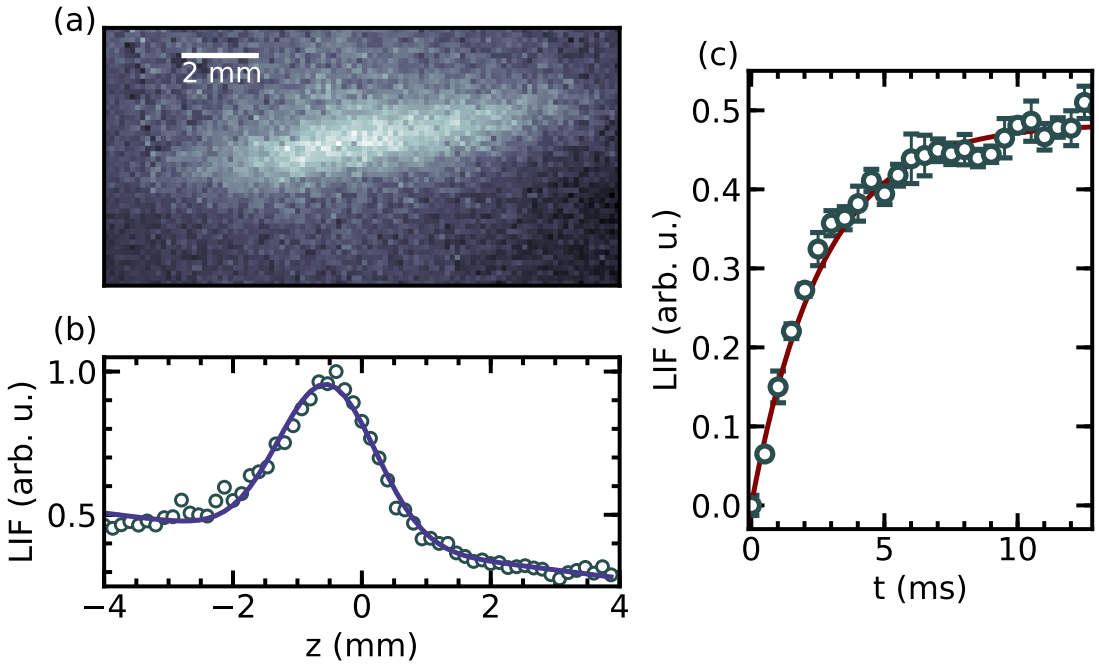

Figure 4.5: (a) Fluorescence image of one of the two 2D traps formed in the glass cell. (b) The cross-section of the cloud along the trapped axis, the line is a fit to a sloping Gaussian function. (c) The light induced fluorescence from the 2D MOT region detected at variable times after turning on the trap light. Points are averages of 6 experiments and error bars are the standard errors. The line is a fit to an exponential model. These data corresponds to the fully optimized double MOT system which produces a loading rate of $3 \cdot 10^9$ atoms/s at a dispenser current of 3.8 A.

beam.

Figure 4.5(a) shows a fluorescence image of atoms trapped in the 2D MOT. The trap extends by roughly 10 mm. In (b), the cross-section along the confined axis of the trap is shown together with a fit to a sloping Gaussian function. The fit gives an RMS radius of 0.76 mm. Because the exit aperture diameter is 2 mm, most trapped atoms should be extracted out of the cell. There is a large offset in these images due to the fluorescing Rb background vapour.

Figure 4.5(c) shows the loading of the 2D MOT. The CCD camera is exposed for 100 μs at variable times after the 2D MOT light is turned on to detect the light induced fluorescence. A fit to an exponential function gives a loading time of 2.68(9) ms, which is 3 orders of magnitude shorter than the time it takes to load the 3D MOT.

4.2.5 Optimum 2D MOT parameters

The powers and detunings of the cooling and push beam lasers are optimized by maximizing the number of atoms loaded into the 3D MOT in 1 s. Absorption imaging is used to determine the number of atoms $\mathcal{N}_{\mathrm{Rb}}$.

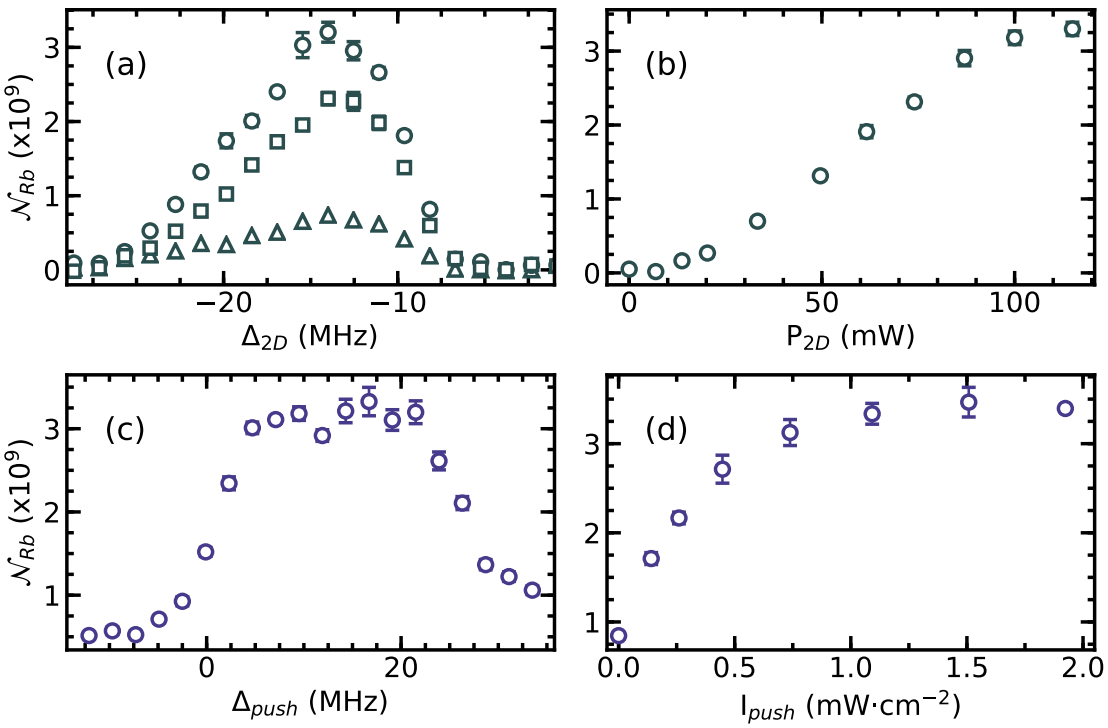

Figure 4.6: Optimum 2D MOT parameters using the number of atoms $\mathcal{N}_{\mathrm{Rb}}$ loaded into an optimized 3D MOT in 1 s. (a) $\mathcal{N}_{\mathrm{Rb}}$ for different 2D MOT cooling light detunings Δ_{2D} at 2D MOT magnetic quadrupole field gradients of 11.6 G/cm (△), 23.2 G/cm (□) and 34.8 G/cm (○). (b) $\mathcal{N}_{\mathrm{Rb}}$ for different 2D MOT cooling light powers P_{2D}. (c) $\mathcal{N}_{\mathrm{Rb}}$ for different push beam detunings Δ_{push} and (d) beam intensities I_{push}. Data in (a) and (b) are recorded using an optimized push beam.

Cooling light

Figure 4.6(a) shows how $\mathcal{N}_{\mathrm{Rb}}$ varies with the 2D MOT cooling light detuning Δ_{2D} for a set of three different 2D magnetic quadrupole gradients. The highest loading rate is obtained using $\Delta_{2D} = -14$ MHz at a field gradient of 23.2 G/cm. Figure 4.6(b) shows how $\mathcal{N}_{\mathrm{Rb}}$ varies with the total cooling light power for $\Delta_{2D} = -14$ MHz. A power of 100 mW saturates the loading rate. The true power at the position of atoms is 20-30 % lower due to losses on the various optical components and the non AR coated walls of the glass cell.

Push beam

Figures 4.6(c)-(d) show how $\mathcal{N}_{\mathrm{Rb}}$ varies with the push beam detuning Δ_{push} and intensity I_{push} respectively. In (c) Δ_{push} is varied at a push beam intensity of 2 mW·cm^{-2}. The initial expectation was that a red detuned push beam will increase the 3D MOT loading rate as it will turn around the trajectories of the atoms cooled in the 2D MOT which move away from the 3D MOT. For the push beam intensities explored here no effect on the loading rate was observed using a red detuned push beam. As may be seen in

figure 4.6(c) the loading rate is maximized for a blue detuned push beam which could be explained with the following argument. The mean longitudinal velocity of the atomic beam emerging from the glass cell is small enough so that the transverse divergence of the beam is important. Since a blue detuned push beam interacts with atoms which are already moving towards the 3D MOT it gives them an additional push, shifting the mean longitudinal velocity to a higher value. This then reduces the loss due to beam divergence and increases the flux of atoms passing the capture volume of the 3D MOT.

The measured dependence of the loading rate with Δ_{push} may be used to make a rough inference about the properties of the longitudinal velocity distribution. Assuming that the mean longitudinal velocity of the atomic beam (without the push beam) is significantly lower than the capture velocity of the 3D MOT, the push beam will have the largest effect on the loading rate when it is tuned to interact with this velocity class. For a fixed value of Δ_{push}, atoms resonant with the beam will be rapidly accelerated and shifted away from resonance. The highest loading rate is achieved with $\Delta_{\text{push}} \approx 16$ MHz. This corresponds to a velocity of 12.5 m/s at which the atoms are resonant with the beam. The range of Δ_{push} values for which the loading rate is increased is roughly ± 15 MHz which corresponds to a range of velocities of roughly ± 12 m/s, assuming the longitudinal velocity distribution is symmetric. These values compare very well with more rigorous measurements [116] of the longitudinal velocity distributions of an atomic beam produced using a 2D MOT of ^{87}Rb atoms.

4.2.6 Optimum 3D MOT parameters

There are two main requirements for the 3D MOT of atoms: (i) the cloud should both be large and have a high number density so that the spatial overlap with the molecule cloud is as large as possible and (ii) the trap has to work well with an axial magnetic field gradient of around 30 G/cm, which turns out to be the optimum value for the molecule trap.

Cooling and repump light

Figure 4.7(a) shows how the number of atoms loaded into the 3D MOT varies with the cooling light detuning $\Delta_{2\to3}$. Here, the 2D MOT is fully optimized to give the largest loading rate and a total cooling light intensity of $21 I_{sat}$ is used (with $I_{sat} = 3.6$ mW·cm^{-2}). Each trap beam also contains around 3 mW of repump light. The frequency of the repump is tuned to be resonant with the $F = 1 \rightarrow\ F' = 2$ transition. For $\Delta_{2\to3} = -10$ MHz the MOT loading becomes unstable and for $\Delta_{2\to3} = 0$ MHz no atoms are loaded as there is no net trapping force. The 3D MOT is robust to both the frequency and the magnetic field gradient and accumulates a similar number of atoms using a wide range of different parameters.

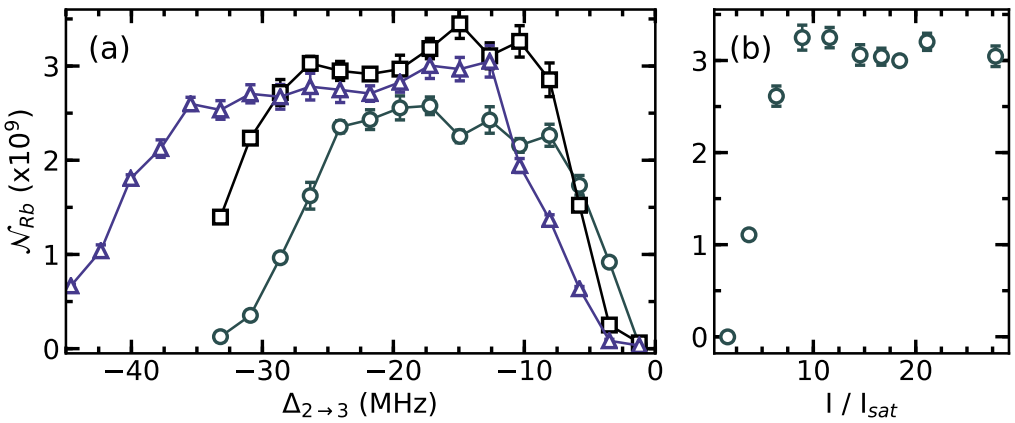

Figure 4.7: (a) Atom number $\mathcal{N}_{\mathrm{Rb}}$ in the 3D MOT versus the detuning of cooling light $\Delta_{2\to3}$ from the $F = 2 \to F' = 3$ transition for axial magnetic field gradients of 5 G/cm (○), 15 G/cm (□) and 30 G/cm (△). (b) $\mathcal{N}_{\mathrm{Rb}}$ for different total cooling light peak intensities with $\Delta_{2\to3} = -26$ MHz and an axial field gradient of 30 G/cm.

In figure 4.7(b) the total intensity of the cooling light is varied. The number of atoms captured into the trap saturates for intensities greater than $7I_{sat}$. Although the number of atoms loaded into the 3D MOT within 1 s saturates well below the available laser intensity in this experiment, using a higher intensity trap accumulates more atoms in a stable MOT loaded for longer durations.

Trap loading and stability

The loading of the 3D MOT is investigated by recording the trap beam LIF with a photodiode. Figure 4.8(a) shows loading curves of the 3D MOT using a set of four trap beam intensities. For $s = 6.8$ the trap loading becomes unstable beyond loading times of $t = 8$ s. This kind of unstable MOT behaviour was observed in other experiments [129, 130] and attributed to the interplay between the confining MOT force and the repulsive force due to photon rescattering. As more atoms are loaded into the trap, the radiation pressure force due to rescattered photons increases and at some point become comparable to the trapping force itself. The sudden drops in LIF for $s = 6.8$ may be attributed to atoms being ejected out of the trap when the repulsive force due to photon rescattering suddenly becomes significantly larger than the trap force. As the trap is loaded continuously from the 2D MOT it is periodically being replenished with new atoms to again reach this critical number where a portion of the atoms are ejected.

For higher trap beam intensities this behaviour disappears and instead a much faster periodic oscillation in the detected LIF becomes clearly visible. Figure 4.8(b) shows a close-up view of the observed oscillation when $s = 21$. The oscillation occurs at a frequency of roughly 50 Hz[2], very similar to the behaviour observed in [129]. It may be

[2]Although this is suspiciously close to the mains frequency, no 50 Hz noise was observed on either the

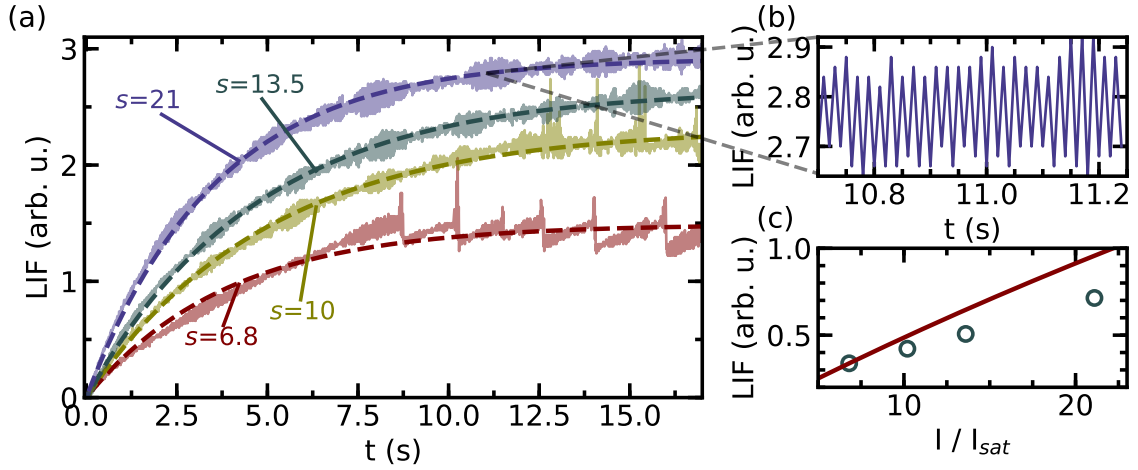

Figure 4.8: (a) Loading curves of the Rb 3D MOT for a set of 4 different peak cooling light intensities. The solid lines are fits to an exponential model. The Rb trap light induced fluorescence is recorded with a photo-diode. For these data $\Delta_{2\to3} = -30$ MHz and the axial field gradient is 30 G/cm. (b) Periodic oscillations in the detected LIF. (c) LIF at $t = 1$ s for the different trap beam intensities. The solid line is the LIF expected from the scattering rate model of a two-level atom. The model is normalized to the detected LIF using an intensity of $6.8I_{\text{sat}}$.

speculated that the observed oscillation of the detected LIF is due to rapid expansions and contractions of the trapped cloud. When the density of the cloud is reduced more photons are able to escape the then less dense cloud. The MOT force then compresses the cloud again and thus leads to a periodic oscillation in the size of the cloud. In this regime the dynamics of the cloud become particularly sensitive to the trap beam alignment and the cooling laser frequency detuning.

Figure 4.8(c) shows the detected LIF after a trap loading time of 1 s using different beam intensities. Because the atom number, measured by absorption imaging, is the same for the intensities used, the LIF should be proportional to the scattering rate and depend only on intensity. The solid line in the figure corresponds to the scattering rate for a two-level atom given by eq. 2.41 normalized to the LIF detected using $6.8I_{\text{sat}}$. The measured fluorescence is below the expected values which may be viewed as an indication of radiation trapping within the atom cloud. This demonstrates why fluorescence imaging of large atom clouds is not suitable when trying to infer the atom number.

The total trap beam intensity is maintained at around $20I_{\text{sat}}$ and makes the cloud shape and centre of mass position less sensitive to drifts in the trap beam polarizations and intensities.

MOT coils current supply or the intensity of the laser. The noise of the laser lock was not investigated.

4.2.7 Size of the Rb 3D MOT

In the absence of inter-atomic interactions the size of the cloud is determined by its temperature. For a damped harmonic trap the size σ_i of the cloud along one of the three orthogonal trap axes $i \in \{x, y, z\}$ may be found from the equipartition theorem

$$\frac{1}{2}\kappa_i \sigma_i^2 = \frac{1}{2} k_{\mathrm{B}} T_i \ , \tag{4.5}$$

with κ_i the trap spring constant defined in eq. 4.4 and T_i the temperature of the cloud. In this regime the cloud radius does not depend on the number of atoms and the peak number density is determined by the cloud temperature

$$N_0 = \frac{\kappa^{3/2}\mathcal{N}}{2(2\pi)^{3/2}(k_{\mathrm{B}}T)^{3/2}} \ . \tag{4.6}$$

In the above, the fact that for a MOT $\kappa_x = \kappa_y = \kappa_z/2 = \kappa$ was used and the temperatures in all three dimensions were set equal $T_x = T_y = T_z = T$. Thus adding more atoms into the trap increases the peak density linearly. For clouds containing $\mathcal{N} \gtrsim 10^4$ two additional forces become important [131]. The first one is an extra confining force which arises due to intensity gradients in the trapping beams as they propagate through the cloud and are attenuated. This force becomes more important in traps formed by three retro-reflected laser beams. The second force was alluded to in the above discussion of the 3D MOT instabilities and arises due to photon rescattering. This force opposes both the trap and absorption forces and ultimately limits the attainable number density. In fact it was shown both theoretically and experimentally in [132] that the density of the cloud reaches a maximum value determined by the trap spring constant and laser intensity.

In this work the MOT operates far beyond the temperature-limited regime. Figure 4.9(a) shows a measurement of how the cloud size varies with atom number. These data are fitted to the following model

$$\sigma_i^{\mathrm{Rb}}(\mathcal{N}_{\mathrm{Rb}}) = \alpha_i \mathcal{N}_{\mathrm{Rb}}^{\gamma_i} \ , \tag{4.7}$$

with $i \in \{y, z\}$. The fit gives $\gamma_y = 0.35(2)$ (radial size) and $\gamma_z = 0.26(1)$ (axial size). Assuming that the cloud is radially symmetric the coefficient corresponding to the third orthogonal direction not visible to the imaging system is $\gamma_x = \gamma_y$. The number density is constant if $2\gamma_y + \gamma_z = 1$, decreases with $\mathcal{N}_{\mathrm{Rb}}$ if $2\gamma_y + \gamma_z < 1$ and increases when $2\gamma_y + \gamma_z > 1$. For this measurement $2\gamma_y + \gamma_z = 0.96(4)$ implying a constant peak number density of $5 \cdot 10^{10}$ cm^{-3} over the range explored here. These results are similar to the ones obtained in a more detailed experiment on the behaviour of large atom clouds in a MOT [133].

Figures 4.9(b)-(c) show the radial and axial cloud distributions respectively and fits to Gaussian distributions. These distributions correspond to a cloud containing the largest atom number used in the experiment and fit reasonably well to 1D Gaussian functions.

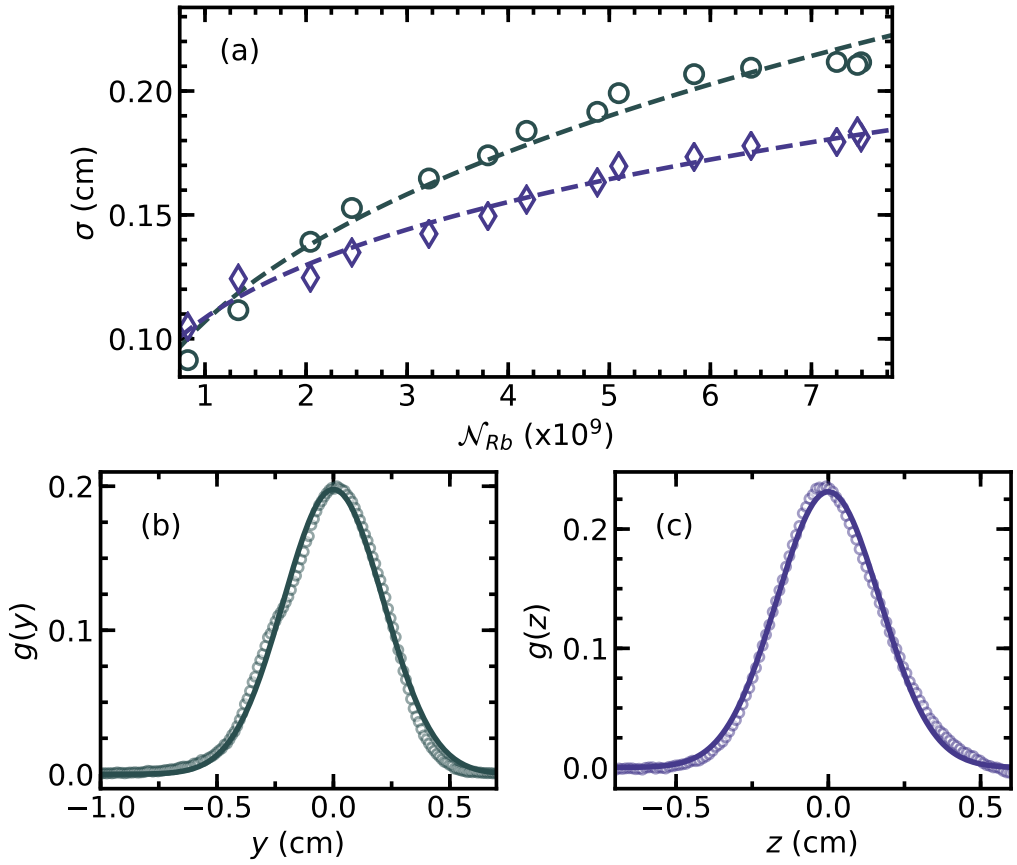

Figure 4.9: (a) Rb MOT size for different atom numbers along the radial (○) and axial (◊) directions. The dashed lines are fits to the power law model described in the main text. (b) and (c) show the integrated cross sections of the measured distributions along the radial and axial directions respectively. The solid lines are fits to Gaussian distributions.

4.2.8 Temperature of the Rb MOT

The temperature of atoms in a MOT determines the atom-molecule collision energy and thus is an important parameter to measure in relation to collision measurements described in chapter 5. Photon rescattering is also anticipated to affect the final cloud temperature and so this is investigated briefly in the experiment.

Figure 4.10 shows the temperature of the Rb MOT determined via ballistic expansion measurements of clouds containing different numbers of atoms. In these data T_{g} is the geometric mean temperature defined as $T_{\mathrm{g}} = T_{\mathrm{r}}^{2/3} T_{\mathrm{a}}^{1/3}$ with T_{r} and T_{a} the radial and axial temperatures respectively. The temperatures along the two orthogonal radial directions are assumed to be equal. The temperature of a smaller cloud with $\mathcal{N}_{\mathrm{Rb}} = 3 \cdot 10^7$ is 450 μK which is close to the Doppler temperature of $T_{\mathrm{D}} = 650$ μK for the cooling laser parameters used in this experiment. The temperature rises to around 1 mK for clouds containing $\mathcal{N}_{\mathrm{Rb}} > 3 \cdot 10^9$ atoms. The apparent dependence of the temperature on $\mathcal{N}_{Rb}$ may be due to a combination of trap light attenuation and multiple scattering effects. Larger clouds will have a higher optical depth thus attenuating the trap light more and

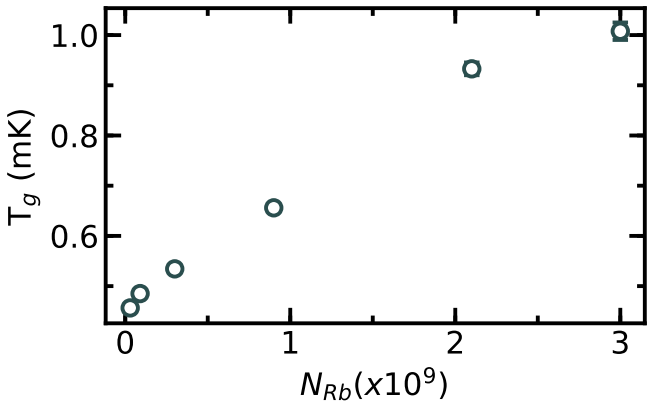

Figure 4.10: Temperatures of the Rb MOT containing different atom numbers. Error bars correspond to the standard error on the mean of 6 repeat measurements. Where not visible, they are smaller than the sizes of the point.

leading to variable cooling/heating rates across the cloud. In addition, the absorption of scattered photons by other atoms in the cloud may further increase the heating rate.

4.3 The CaF MOT

A beam of CaF molecules is produced in a He buffer gas source and is decelerated to below the capture velocity of a dual frequency MOT. The laser slowing scheme is described in detail in [119] and here only a brief description of the slowing sequence is given. The rest of this section is dedicated to describing some of the basic characteristics of the molecule MOT while more details may be found in [97, 91, 134, 135, 136].

4.3.1 Frequency chirped laser slowing

Molecules emerging from the buffer gas cell have a mean forward velocity of around $\bar{v}_{\mathrm{B}} = 160$ m/s which is well above the capture velocity of the MOT of around $v_{\mathrm{c}} \approx 13$ m/s [91]. The molecule beam is decelerated by applying resonant light $\mathcal{L}^{\mathrm{S}}_{00}$ (see figure 3.7) which is linearly polarized at a 45° angle relative to a uniform magnetic field of 5 G applied perpendicularly to the molecular beam. This destabilizes ground states which are dark to the slowing light [137] and thus increases the number of photons a molecule can scatter. In addition, a vibrational repumper beam propagates along the same direction and repumps molecules which decay into the $\nu = 1$ vibrational level. To account for the changing Doppler shift as the molecules are decelerated, the slowing laser frequency is chirped while the repumper light is spectrally broadened by about 300 MHz. The random walk of the molecule's momentum as it scatters photons leads to transverse heating which increases the beam divergence. The gain in transverse velocity is $v_{\mathrm{t}} = \sqrt{\mathcal{N}_{\mathrm{p}}/3}v_{\mathrm{r}}$, with $\mathcal{N}_{\mathrm{p}} \approx 10^4$ the number of photons a molecule scatters while it is being decelerated and

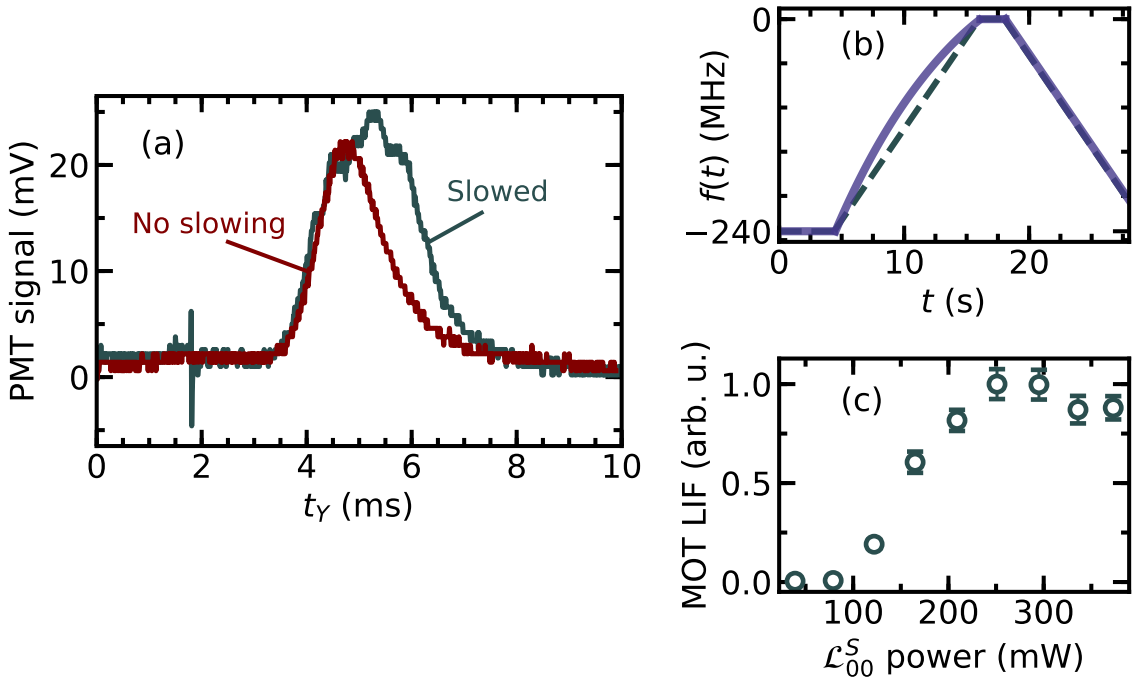

Figure 4.11: (a) ToF profiles of the molecular beam recorded 0.8 m downstream from the source with and without laser slowing. The signal in each case was averaged over 64 experiments. The molecules are produced inside the buffer gas source by laser ablation at $t = 0$. (b) The linear and exponential frequency chirp ramps. Zero frequency does not correspond to the slowing light being resonant with molecules at rest. (c) Signal in the MOT for variable $\mathcal{L}^S_{00}$ powers using an optimized exponential chirp.

$v_r = 1.27$ cm/s is the recoil velocity. To minimize this transverse heating, the $\mathcal{L}^S_{00}$ beam is focused towards the source and has a $1/e^2$ radius of roughly 3 mm at the exit aperture of the cell. The converging beam applies a small transverse scattering force component and reduces the divergence of the molecular beam.

A probe beam tuned to drive the A-X transition traverses perpendicular to the molecular beam 0.8 m downstream from the exit aperture of the buffer gas cell. Molecules passing through the probe beam scatter photons which are detected with a photomultiplier tube (PMT). Figure 4.11(a) shows example time of flight (ToF) profiles recorded with and without the slowing sequence applied. The effect of slowing manifests itself as an increase in the ToF amplitude at later arrival times. In addition, the total number of molecules traversing the probe region increases because of the small transverse scattering force applied by a converging $\mathcal{L}^S_{00}$ beam[3]. Although molecules have more than 0.5 m left to travel to the MOT region from where the ToF profiles are recorded, the effect of laser slowing is clearly visible and serves as a useful diagnostic when tuning the laser frequency on a daily basis.

[3]Note that the ToF signal was averaged over 64 experiments. Because the signal amplitude typically decays in time, it is not possible to make a direct comparison between the number of molecules in the detection region with and without the slowing applied.

Two different frequency ramps were explored and optimized using the number of molecules captured into the MOT as a figure of merit. The linear ramp, used in all prior work in our group, is shown in figure 4.11(b). The slowing light is switched on 2.4 ms after the ablation of the Ca rod and is kept on at a constant detuning for 2 ms. This initial hold time cools molecules longitudinally and slightly compresses [97] the velocity distribution. In practice it is found that when the holding time is varied by ± 2 ms it is simply enough to slightly change the initial laser frequency to produce the same number of molecules in the MOT. In fact, the holding time may be eliminated altogether without a significant change in the number of molecules captured by the MOT. This signifies that there exist many combinations of the slowing sequence parameters which lead to a similar number of molecules captured into the MOT. After the initial constant frequency hold, the frequency of the laser is ramped linearly to a new value over 11.6 ms and immediately switched off. The linearity of the frequency chirp is confirmed by coupling the slowing light into a very low finesse Fabry-Perot cavity with a wide transmission bandwidth. At the end of each frequency chirp the laser frequency is kept at a constant value for 2 ms before being chirped back to the initial value. This is to avoid sudden changes in frequency (especially changes in the sign of the applied chirp) which may damage the fibre amplifier due to back reflections. During the time it takes to chirp and bring back the frequency, the feedback to the laser from TCL is disabled.

Throughout this work an exponential frequency ramp, suggested by the Harvard group [138], was used instead and is shown alongside the linear ramp in figure 4.11(b). To generate the ramp, the exponential is approximated by a 4^{th} degree polynomial

$$f(t) = f_1 + f_2 \frac{8}{5}\left(\frac{t}{t_c} - \frac{1}{2}\frac{t^2}{t_c^2} + \frac{1}{6}\frac{t^3}{t_c^3} - \frac{1}{24}\frac{t^4}{t_c^4}\right) \ , \tag{4.8}$$

with f_2 the chirp amplitude, f_1 the start frequency, and t_c the duration which also sets the chirp rate. The parameters t_c and f_1 are scanned to optimize the number of molecules captured into the MOT while f_2 is kept constant. For t_c and f_1 the same as used for the linear chirp, the number of molecules captured into the MOT was reduced. Varying only f_1 led to an increase in the number of molecules captured into the MOT by $60 - 80$ % compared to a linear chirp.

To try to understand the reason for this dependence on the chirp parameters, the 1D trajectories of particles which scatter light at a rate given by eq. 2.52 are computed by integrating the equation of motion[4]. In the simulation a constant slowing light intensity is assumed with a saturation parameter of $s = 5$. Molecules are propagated for 40 ms and the slowing light is on only for the duration of the chirp. In the experiment molecules are decelerated over a distance of ~ 0.9 m. Figure 4.12(a) shows the simulated trajectories in phase space for a linear frequency chirp with f_1 set to be resonant with molecules at

[4]The deceleration force is modelled as $F = \hbar k R_s$ and since the simulation is constrained to 1D, the transversal heating due to spontaneous scattering is ignored.

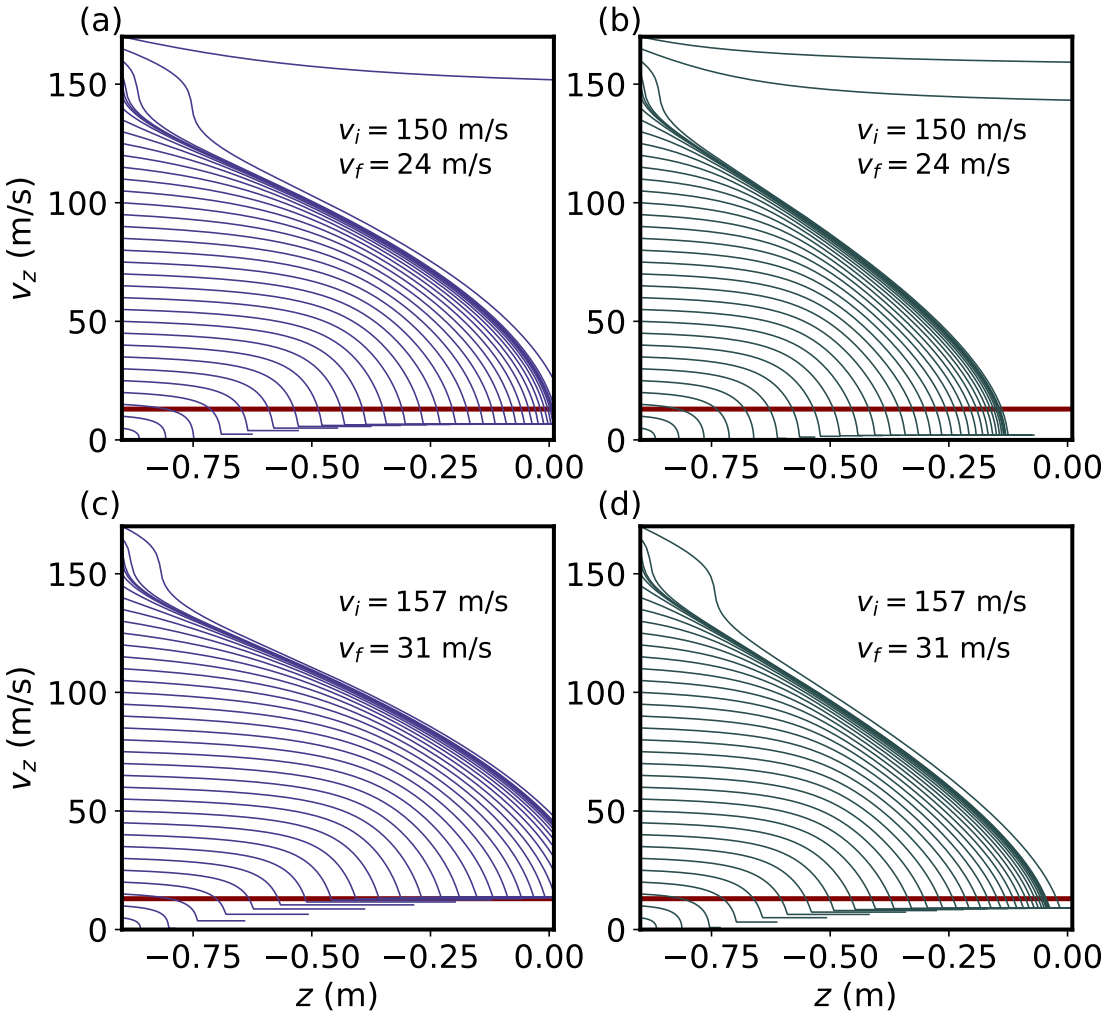

Figure 4.12: (a) and (c) show simulated trajectories of molecules which are decelerated using a linear frequency chirp. (b) and (d) show trajectories of molecules decelerated using an exponential frequency chirp. v_i and v_f are the initial and final molecule velocities corresponding to the initial and final laser frequencies. The red line indicates the capture velocity of the CaF MOT. $z = 0$ corresponds to the position of the MOT.

a velocity of 150 m/s, a ramp duration of $t_c = 13$ ms and a chirp rate which sets the final frequency to be resonant with molecules at a velocity of $v_f = 24$ ms. In (b) the parameters are kept the same but an exponential chirp is used instead. In this case, the molecules reach low velocity too far from the MOT. They will then take a long time to reach the MOT, and so will have spread too much in the transverse direction. In addition, faster molecules are not decelerated sufficiently. In figures 4.12(c) and (d) the slowing parameters are changed to $v_i = 157$ m/s and $v_f = 31$ ms for the linear and exponential frequency ramps respectively. In this case, the linear chirp protocol does not decelerate sufficiently while the exponential chirp protocol interacts with a wider class of velocities than in any of the other three cases. Although it is hard too draw general conclusions, these simulations agree qualitatively with the experimental observation that an exponential frequency chirp produces more slow molecules compared to a linear chirp.

Finally, figure 4.11(c) shows how the number of molecules captured into the MOT (proportional to the detected LIF) varies with $\mathcal{L}_{00}^{\mathrm{S}}$ power. Although the slowing performance seemingly saturates for powers above 250 mW, it is conceivable that at higher powers the optimal frequency ramp is different. Due to the complexity of this multi-parameter experimental sequence, in future campaigns attempting to optimize it, the use of an evolutionary algorithm [139, 140] could be explored.

4.3.2 Loading and optimization of the CaF MOT

The polarization and frequency scheme used to form the CaF MOT is shown in figure 4.13(a). Each of the four frequency components driving the $A - X$ transition has roughly the same optical power and a total $\mathcal{L}_{00}^{C}$ intensity of 1000 mW·cm^{-2} at the position of the MOT. The opposite polarization components which address the $F = 2$ and $F = 1$ hyperfine levels constitute the dual frequency scheme which provides with most of the confining force [141].

The molecule MOT is formed only when the $\mathcal{L}_{00}^{C}$, $\mathcal{L}_{00}^{S}$, $\mathcal{L}_{10}$, $\mathcal{L}_{21}$ laser frequencies are all tuned to within ± 10 MHz of their optimal values. The frequency of $\mathcal{L}_{32}$ is less sensitive and is always optimized last. In addition, the trap beams must be well aligned through the centre of the science chamber. Very small adjustments of the beam steering mirrors affect both the number of molecules and the cloud shape dramatically. The MOT is not particularly sensitive to the laser beam polarizations- changing the QWP angles by $\pm 10^{\circ}$ doest not affect the MOT noticeably.

Measurement of MOT loading

Figure 4.13(b) shows how the molecule MOT loads. In this experiment fluorescence images of the MOT are acquired using a 1 ms exposure time at variable times after the Ca rod is ablated. The MOT coils are turned on at $t_{\mathrm{Y}} = 0$ at an axial field gradient of 30 G/cm and kept on throughout the duration of the experimental sequence. An initial pulse of molecules arriving at the position of the intersecting trap beams around 5 ms after the ablation pulse is visible. The longitudinal velocities of most of these molecules are far above v_{c} and the trap light does not have sufficient time to turn around their trajectories. The signal recorded at times between $t_{\mathrm{Y}} = 10$ ms and $t_{\mathrm{Y}} = 20$ ms corresponds to the LIF from the stream of molecules which are still too fast to be captured by the MOT. At around $t_{\mathrm{Y}} = 20$ ms a visible cloud forms indicating the arrival of molecules with longitudinal velocities which are below v_{c}. The MOT continues to load up until $t_{\mathrm{Y}} = t_{\mathrm{L}} = 40$ ms when complete trap loading is assumed and further steps in the experimental sequence may proceed.

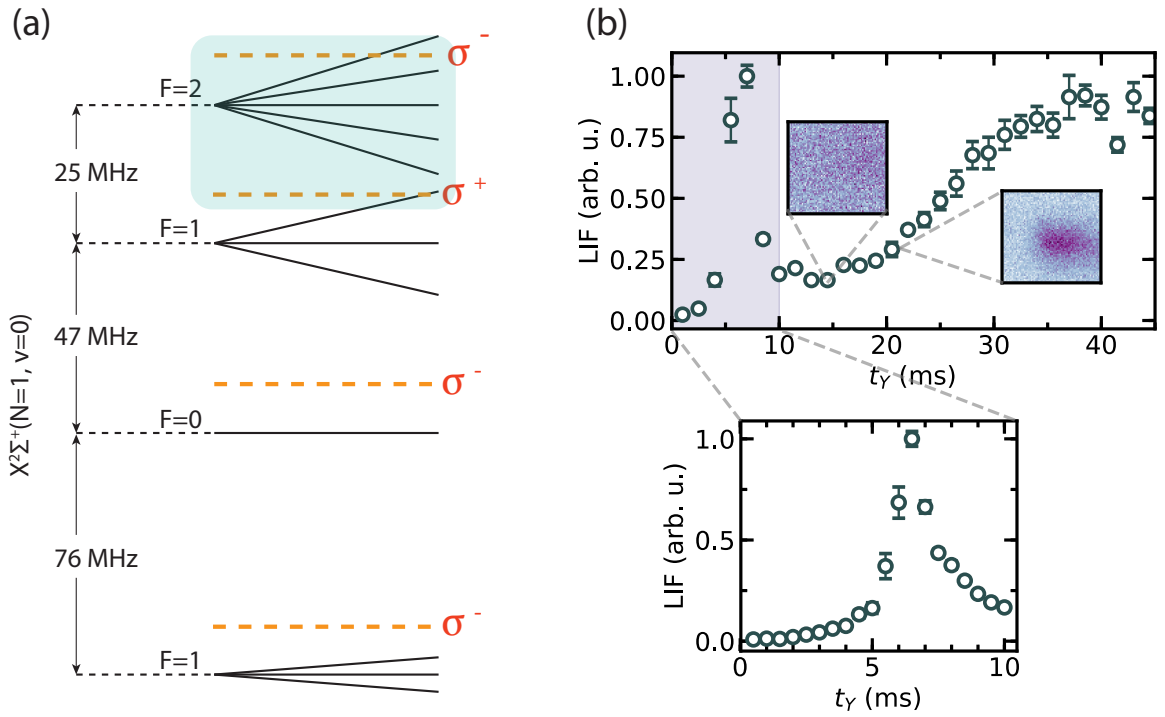

Figure 4.13: (a) Dual frequency MOT scheme with the polarizations of all four components used to address the ground state hyperfine structure indicated. (b) Loading of the CaF MOT: fluorescence images with an exposure time of 1 ms are acquired at variable times after the ablation of the Ca rod.

Optimal laser detuning and field gradient

With the vibrational repumpers tuned to their optimal frequencies the detuning Δ_{00} of $\mathcal{L}_{00}^{C}$ is scanned and the LIF in the MOT is measured with the CCD camera exposed for 10 ms at $t_{\mathrm{Y}} = 40$ ms. Due to the multiple frequencies and hyperfine transitions involved in making a MOT the definition of Δ_{00} is somewhat arbitrary. For the purposes of this measurement $\Delta_{00} = 0$ when the MOT is barely visible. Figure 4.14(a) shows how the LIF depends on Δ_{00}. The signal is maximized for $\Delta_{00} = -7$ MHz and this is the detuning at which the MOT is always loaded. The size of the cloud does not change for Δ_{00} in the range of -15 MHz to -5 MHz. The temperature of the cloud also does not vary for this range of detunings.

In figure 4.14(b) the radial field gradient b_{r} for the MOT loading phase is varied. The detected LIF is maximum for $b_{\mathrm{r}} = 15$ G/cm and begins to slowly fall for higher values. The scattering rate in the MOT is both a function of Δ_{00} and b_{r}, thus, the number of molecules is not directly proportional to the measured LIF. Nevertheless, since the signal is maximized and the cloud size begins to saturate using $b_{\mathrm{r}} = 15$ G/cm, this is the value used to load the molecule MOT throughout this work. Moreover, the current required to generate this gradient is at a value which does not cause significant heating and outgassing

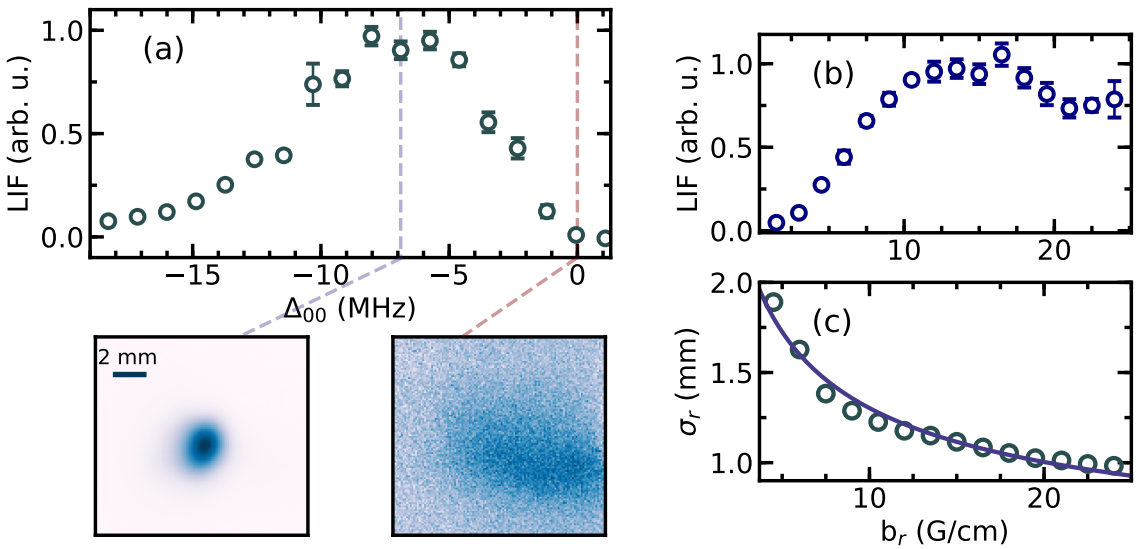

Figure 4.14: (a) The LIF detected in the MOT region as a function of the $\mathcal{L}_{00}$ laser detuning Δ_{00}. The lower two panels show fluorescence images of the trapped cloud for the optimal and critical values of Δ_{00}. (b) LIF in the MOT as a function of radial magnetic field gradient b_r. (c) The radial cloud size σ_r for different values of b_r with the solid line a fit to a $\sigma_\mathrm{r} \propto b_\mathrm{r}^{-1/2}$ model. For (b) and (c) $\Delta_{00} = -7$ MHz.

from the coil assembly over extended periods of operation. Figure 4.14(c) shows how the radial cloud size varies with b_r. These data fit reasonably well to the expected temperature limited behaviour where the size is $\sigma_\mathrm{r} \propto b_\mathrm{r}^{-1/2}$. The slight apparent deviation from this model may likely be explained by imperfect trap beam alignment and intensity imbalance both of which lead to a deformed trapping potential. Indeed, the axial cloud size for these data is very similar to the radial size while in the temperature limited regime the radial size should be $\sqrt{2}$ times larger. It is found that the cloud size and shape varies from one week to another thus for experiments where knowledge of the cloud shape is critical, measurements of it are performed on the same day.

4.3.3 Temperature of the CaF MOT

The temperature of the CaF MOT is measured by taking fluorescence pictures of the freely expanding cloud. The cloud is imaged by turning on the $\mathcal{L}_{00}^{C}$ light at full intensity at $\Delta_{00} = -7$ MHz for an exposure time of 1 ms. The first image is acquired after 1 ms of free expansion in order to ensure that the quadrupole field has decayed to negligible values such that turning on the imaging light does not apply a trapping force to the molecules. Systematic shifts in the measured cloud temperature due to a rather long exposure time were investigated in previous work [97]. It was found that the temperature of a 12 mK cloud is overestimated by 0.3(5) mK while the temperature of a 50 μK cloud is overestimated by only 0(3) μK.

Figure 4.15 shows the measured cloud temperatures as a function of the peak $\mathcal{L}_{00}^{C}$

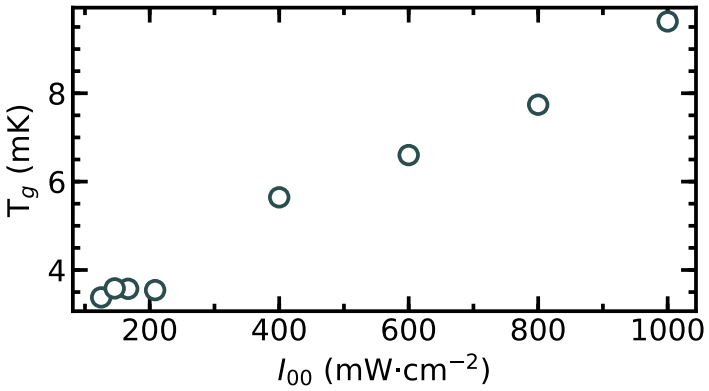

Figure 4.15: Temperature of the CaF MOT for different cooling light intensities. I_{00} is the total peak intensity of $\mathcal{L}_{00}$ light.

intensity. At a peak $\mathcal{L}_{00}^{C}$ intensity of 1000 mW·cm^{-2} the geometric mean temperature is around 9.5 mK. The Doppler temperature for the molecule MOT may be found by replacing the saturation parameter in eq. 2.49 with an effective saturation parameter defined in eq. 2.52. For $\Delta = -7$ MHz and $s = 20$ the Doppler temperature is $T_{\mathrm{D}} = 1.37$ mK which is almost 7 times smaller than the measured temperature. This indicates the existence of sub-Doppler heating mechanisms in the dual frequency MOT. Because the Doppler cooling and sub-Doppler heating rates have different dependencies on the laser intensities the final temperature may be controlled by changing the $\mathcal{L}_{00}^{C}$ intensity. Once the MOT is fully loaded the intensity is linearly ramped down to a new value over 5 ms and held at this value for another 2 ms before the molecules are released from the trap. Lowering the intensity by an order of magnitude reduces the temperature to 3.5 mK, still far above T_{D}.

The minimum temperature which may be obtained by lowering the light intensity is, again, sensitive to the trap beam alignment. Depending on the quality of this alignment it is possible to achieve temperatures as low as 1 mK by reducing the intensity by another factor of 5. If the alignment is not optimal, reducing intensity does not lower the temperature further but only reduces the trap depth. Thus the lifetime of molecules in the MOT under such circumstances becomes smaller- an undesirable effect for all experiments that follow. A final intensity of 100 mW·cm^{-2} is found to reproduce the temperature of the cloud from one month to the other and leads to a trap lifetime close to 200 ms.

5 | Collisions in a dual species MOT

After the successful demonstration of laser cooling, a natural starting point for experimental studies of cold atom-atom collisions was the MOT, where atoms could be confined with high densities and temperatures below 1 mK. These studies found that the rate of inelastic collisions is typically sensitive to both the trap light intensity and detuning. Three main mechanisms leading to inelastic loss of atoms out of the trap were identified: fine structure changing collisions (FCC), hyperfine structure changing collisions (HCC) and radiative escape (RE), which are briefly described below.

For FCC a pair of atoms which are both initially in the $^2S_{1/2}$ ground electronic state are transferred to a long range attractive molecular potential when one of the atoms in the colliding pair absorbs a photon. The pair of atoms now in the $^2S_{1/2}+^2P_{3/2}$ states[1] interact via the long range attractive potential[2] and may undergo a collision which changes the internal states to $^2S_{1/2} + ^2P_{1/2}$. In this process the two atoms gain kinetic energy equal to the separation between the fine-structure levels. This excess energy is distributed equally between the two atoms and may be much larger than the trap depth leading to the ejection of the pair out of the trap. The FCC process has been studied extensively both theoretically [142, 143] and in a wealth of different experiments [144, 145, 146]. Loss rate coefficients up to $\sim 10^{-10}$ cm$^3 \cdot$ s^{-1} were measured and were observed to depend strongly on the trap light intensity. In addition to the FCC process, after excitation the pair of atoms may accelerate towards each other before emitting a photon with an energy which is lower than the trap photon. The atoms gain kinetic energy equal to the difference between the absorbed and emitted photons. Provided this gain in energy is larger than the trap depth, both atoms are able to escape. This is the RE process and is commonly found to contribute strongly to trap loss. Finally, when the colliding atoms are both in the ground electronic state, the dominant inelastic process is typically HCC which involves a change in the hyperfine state of one of the colliding atoms. Because the

[1] Alkali metal atom MOT's are most commonly formed using the D_2 line thus the trap light excites the $^2P_{3/2}$ state.

[2] When the colliding atoms are of the same species the interaction potential has the $\sim \pm C_3/R^3$ form due to the resonant dipole-dipole interaction. The sign of the interaction is determined by the frequency of the excitation laser and it is negative (attractive) for red-detuned light and positive (repulsive) for blue-detuned light. Because atomic MOTs are typically formed using red-detuned light the interaction is attractive.

hyperfine splitting is smaller than the fine structure, loss due to the HCC process becomes dominant at lower trap beam intensities where the trap depth is greatly reduced. The loss processes described here may be controlled by the experimenter. For example, in [147] a blue detuned laser beam was used to excite ^{87}Rb atoms confined in a low intensity MOT to a repulsive C_3/R^3 molecular potential. In this case the two colliding atoms repel each other and never reach the required short range where a collision which changes the hyperfine level may occur. Similar methods are used today to enhance the loading of optical tweezer traps with single atoms [148].

In dual species atomic MOTs, which are more relevant for this work, similar processes were observed. In these traps the main difference is that an excited heteronuclear atom pair will interact via a much shorter range $\sim \pm C_6/R^6$ Van der Waals potential [149] compared to the long range dipole-dipole interaction potential of an excited homonuclear pair. The sign of the interaction is determined by which of the atoms in the colliding pair is excited by the trap light. When the atom with a higher (lower) transition frequency absorbs a photon the pair is transferred to a repulsive (attractive) molecular potential. Atoms interacting via the attractive potential may again undergo either an FCC or RE process and be lost out of the trap. Despite the weaker internuclear interaction, similar loss rate coefficients to those typically found in homonuclear systems were reported [149, 150]. Ground state collisions in dual species MOTs are also dominated by the HCC process and lead to trap loss when the trap light intensity is lowered.

More recently, in experiments with non-reactive ultracold molecules confined in an optical dipole trap, rapid two-body losses were observed [151, 65]. It was explained theoretically [152] and demonstrated experimentally [56] that the loss occurred due to excitation of short lived molecular complexes by the trap light. Because the dual species MOT uses several different wavelengths of light the presence of this type of process may not be excluded.

No experimental (or theoretical) studies of inelastic loss in a dual species MOT of molecules and atoms existed until this work. Nevertheless, all of the loss processes described above may in principle also occur in the molecule-atom MOT and serve as a useful guide in designing experiments to investigate this novel system. In addition, the more complicated internal structure of a molecule may give rise to new mechanisms of inelastic loss. For example, in a collision involving an excited CaF molecule and a ground state Rb atom, the molecule may relax to the negative parity state of the $J = 1/2$ level releasing $1.36 \times h$ GHz of energy which corresponds to a 4.3 m/s gain in the velocity of the CaF molecule. Although this is well below the capture velocity of the molecule MOT at full laser intensity, a molecule in the $J = 1/2, -$ state will decay to the $N = 0$ state which is not addressed by the trap lasers and will thus be lost from the trap. Other processes of inelastic loss may involve collisions between ground state molecules and atoms. Because the ground electronic state of CaF in the MOT is the first rotationally excited $N = 1$

level, a collision with an atom may transfer the molecule to $N = 0$ again leading to trap loss. Provided all of the internal energy of the molecule is transferred to the motional energy of only the CaF molecule it will correspond to a gain in velocity of 16.5 m/s- above the measured capture velocity of the molecule MOT.

The methods described in the previous two sections are applied to confine CaF molecules and Rb atoms in a MOT simultaneously. A rapid loss of molecules due to collisions with atoms is observed and the origins of this loss are investigated experimentally.

5.1 Experimental Sequence

The experimental sequence to load the dual species MOT and measure the trap lifetimes is illustrated in figure 5.1. At $t = 0$ the 2D MOT cooling light $\mathcal{L}_{Rb}^{2D}$ and the push beam $\mathcal{L}_{\mathrm{Rb}}^{\mathrm{P}}$ are turned on for a duration T_{Rb} to load a variable number of atoms $\mathcal{N}_{\mathrm{Rb}}$ into the trap. After a time T_{Rb} both $\mathcal{L}_{\mathrm{Rb}}^{\mathrm{2D}}$ and $\mathcal{L}_{\mathrm{Rb}}^{\mathrm{P}}$ are extinguished to interrupt the loading of the 3D MOT and the sequence to load molecules into the trap begins. A pulse of molecules is created in the buffer gas cell at T_{Rb} and the slowing light $\mathcal{L}_{00}^{\mathrm{S}}$, $\mathcal{L}_{10}^{\mathrm{S}}$ is pulsed on for 12 ms. For $T_{\mathrm{Rb}} > 1$ s the ablation laser is fired every 0.5 s to maintain a more uniform flux of molecules emerging from the source and reduce shot-to-shot fluctuations. It takes a time $T_{\mathrm{CaF}} = 40$ ms to fully load the trap with molecules after which the trap light intensity is linearly ramped down to 20% of its initial value over 4 ms to cool the molecules from an initial temperature of around 10 mK to roughly 3.5 mK.

With both species loaded into the trap, a burst of TTL pulses triggers a CCD camera to collect the LIF of CaF molecules. A 10 ms exposure time is used with each camera frame separated by 18 ms and in total 32 fluorescence images are recorded. This sequence of images is used to measure the trap loss rate Γ within a single experimental realization of the MOT. After the last camera image is acquired, the MOT coils are turned off together with the Rb trap light $\mathcal{L}_{\mathrm{Rb}}^{\mathrm{C}}$, $\mathcal{L}_{\mathrm{Rb}}^{\mathrm{R}}$ and the atoms are exposed to a 100 μs pulse of absorption imaging light $\mathcal{L}_{\mathrm{Rb}}^{\mathrm{P}}$.

The sequence to measure the loss rate of molecules in the absence of atoms is identical to the above except that the repump light $\mathcal{L}_{\mathrm{Rb}}^{\mathrm{R}}$ for both the 2D and 3D MOTs is turned off throughout to prevent atoms accumulating in the trap. This maintains the same experimental conditions for both the dual and single species trap loss measurements.

5.1.1 Measuring Loss Rates

In the absence of atoms, molecules are lost from the trap at a rate Γ_1. Provided that molecules collide with atoms inelastically, the natural loss rate will increase by an amount $\Gamma_{\text{Rb-CaF}}$ when atoms are introduced into the trap. For all experiments described here the spatial density of the molecule cloud is around 6 orders of magnitude smaller than

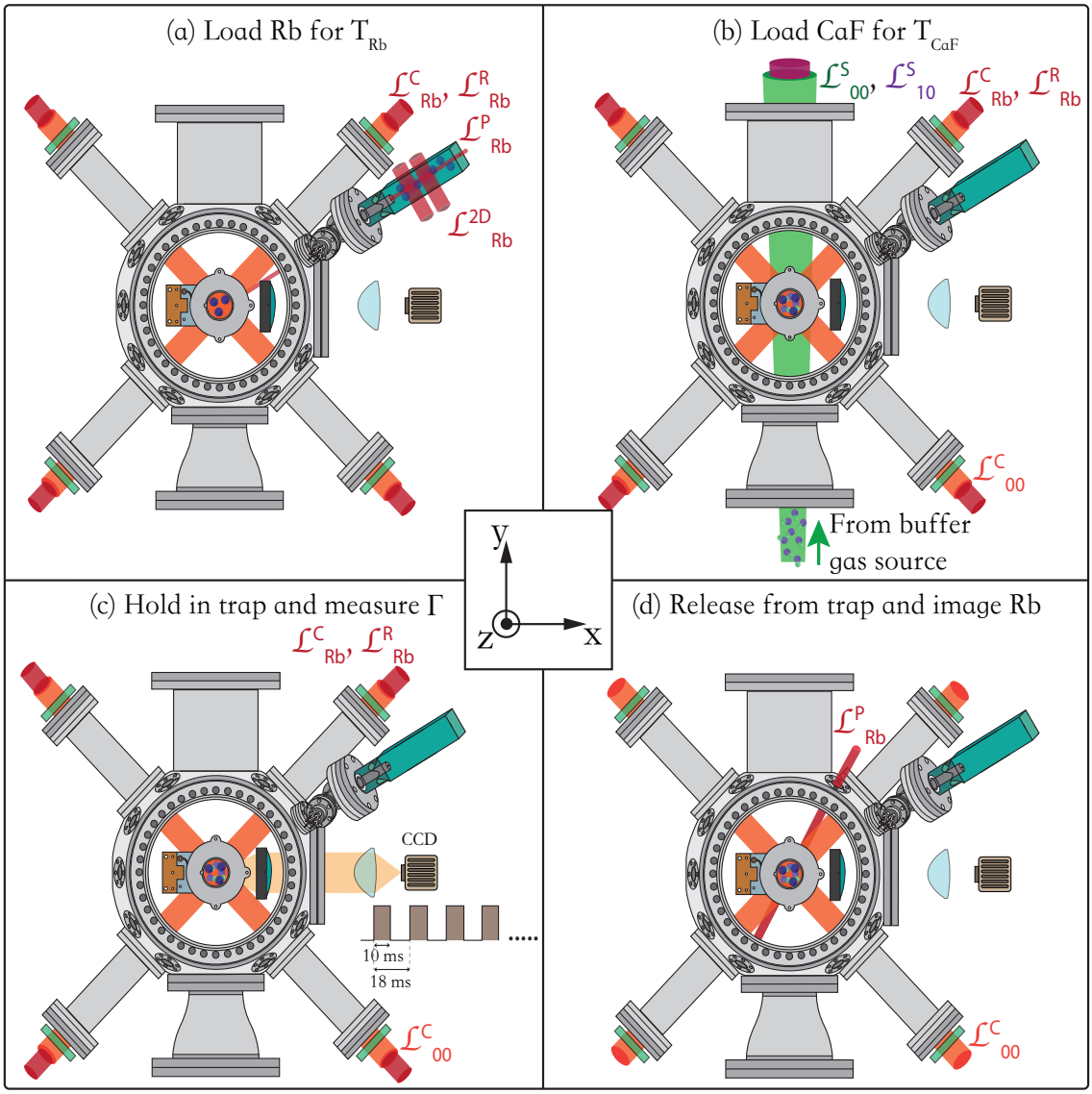

Figure 5.1: Experimental sequence to load the dual species MOT. A 2D MOT (a) of Rb is kept on for a variable time T_{Rb} to supply atoms to the 3D MOT. After a time T_{Rb} a pulse of molecules is created in a buffer gas cell and is laser slowed (b) to load them into the trap within a time T_{CaF}. Both species are held in the trap and a CCD camera records the molecule fluorescence (c) to measure the trap loss rate. At the end of the sequence the atom trap light and the MOT coils are turned off (d) to acquire an absorption image of the Rb cloud.

the density of the atom cloud, thus both molecule induced loss of atoms and molecule-molecule collisions may safely be ignored. In addition, the atom loss rate in the MOT is around 50 times smaller than Γ_1, so a constant atom density and cloud overlap over the duration of the measurements is assumed. With these considerations the loss of molecules from the dual species MOT is modelled using the rate equation

$$\frac{d\mathcal{N}_{\mathrm{CaF}}}{dt} = -\Gamma_1 \mathcal{N}_{\mathrm{CaF}} - \Gamma_{\text{Rb-CaF}} \mathcal{N}_{\mathrm{CaF}} \ , \tag{5.1}$$

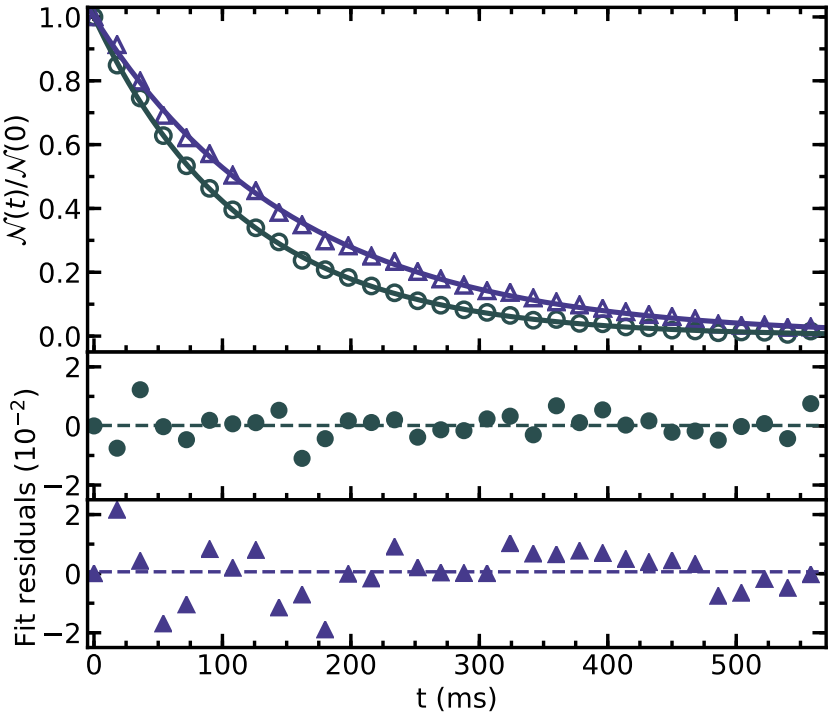

Figure 5.2: Decay of molecules in the single (△) and dual (○) species MOTs. The number of molecules in each image is normalized to the number detected at $t = 0$. Lines are fits of the single exponential decay model with the loss rate set as the only free parameter. The bottom two panels show the fitting residuals.

which has a single exponential decay solution

$$\mathcal{N}_{\mathrm{CaF}}(t) = \mathcal{N}_0 \exp(-t\Gamma_2) \ , \tag{5.2}$$

with the dual species loss rate given by

$$\Gamma_2 = \Gamma_1 + \Gamma_{\text{Rb-CaF}} \ . \tag{5.3}$$

The quantity of interest $\Gamma_{\text{Rb-CaF}}$ may thus be extracted from measurements of the single species Γ_1 and dual species Γ_2 loss rates. The single species loss Γ_1 is also modelled as a single exponential decay.

Example measurements of Γ_1 and Γ_2 are shown in figure 5.2. The fluorescence detected in each image is normalized to the signal detected in the first camera frame and the data is fit to the model of eq. 5.2 with $\mathcal{N}_0 = 1$. For this measurement the loss rates extracted from fits to the single exponential decay model are $\Gamma_1 = 6.39\ \mathrm{s}^{-1}$ and $\Gamma_2 = 8.6\ \mathrm{s}^{-1}$. The bottom two panels in the figure show the fit residuals while the dashed lines indicate their average. In both cases the fit residuals are randomly spread around the mean value which are very close to zero indicating a good fit to the model.

Each measurement of Γ_1 and Γ_2 is repeated 15 times and the mean values are used to obtain an estimate of $\Gamma_{\text{Rb-CaF}}$. The statistical uncertainties in both measurements are propagated to find the errors $\Delta(\Gamma_{\text{Rb-CaF}})$.

5.1.2 Natural loss

At the highest laser intensity used for the MOT, the natural loss rate of molecules exceeds $10\,\mathrm{s}^{-1}$. Because the cooling transition is rotationally closed, the only leak out of the cooling cycle comes from transitions to higher vibrational levels in the ground electronic state. In the experiment, vibrational levels $\nu > 3$ are not optically repumped. By solving rate equations with the Frank-Condon factors taken from [153], it is found that it takes 400 ms for 70 % of the molecules to decay to vibrational levels with $\nu > 3$. This corresponds to a natural loss rate of $2.5\ \mathrm{s}^{-1}$ and is considerably smaller than the measured values. Thus leakage to vibrational levels not addressed by the repump lasers is insufficient to explain the observed loss.

In general, molecular MOTs demonstrated thus far are relatively hot and exhibit weaker confinement compared to typical atomic MOTs. Because of these two reasons it was proposed in [123] that significant loss may occur due to hot molecules slowly boiling out of the shallow trap. This process is not conservative as the trapped molecules always interact with the cooling light which maintains the cloud at a constant temperature. Thus there is a constant fraction of molecules which have sufficient energy to overcome the trapping potential and escape the MOT. Assuming a harmonic trap of radius r_{MOT}, the loss rate corresponding to this process may be modelled [123] using the following equation

$$\Gamma = \frac{2\omega}{\pi} \exp\left(-\frac{m\omega^2 r_{\mathrm{MOT}}^2}{2k_{\mathrm{B}}T}\right) , \tag{5.4}$$

with ω and T the trap frequency and the molecule cloud temperature respectively. The trap frequency at an intensity of $1\ \mathrm{W}\cdot\mathrm{cm}^{-2}$ was previously measured [91] to be around 90 Hz. Taking r_{MOT} to be equal to the $1/e^2$ radius of the trap beams, the loss rate for a cloud at a temperature of 9.5 mK due to this process is negligible. Similar loss rates to those which are measured experimentally are reproduced when $r_{\mathrm{MOT}} \sim 5.5$ mm. Although quantitatively the agreement of this model with experimental observations is poor, it seems to explain the observed trend qualitatively- the trap lifetime tends to grow when the laser beam intensity is reduced. The molecular cloud temperature drops faster than the trap depth as the intensity is lowered, thus reducing the number of molecules which have sufficient energy to escape the trapping potential.

5.1.3 Background calibration

The model of eq. 5.2 is valid only for background subtracted data, so that when $t \to \infty$ the signal and thus the number of molecules detected $\mathcal{N}_{\mathrm{CaF}} \to 0$. In the experiment the dominant background is found to be the scatter of trapping light from the surrounding vacuum components and windows. For each trap loss measurement a set of 15 background images is recorded with the ablation laser turned off so that no molecules are captured into

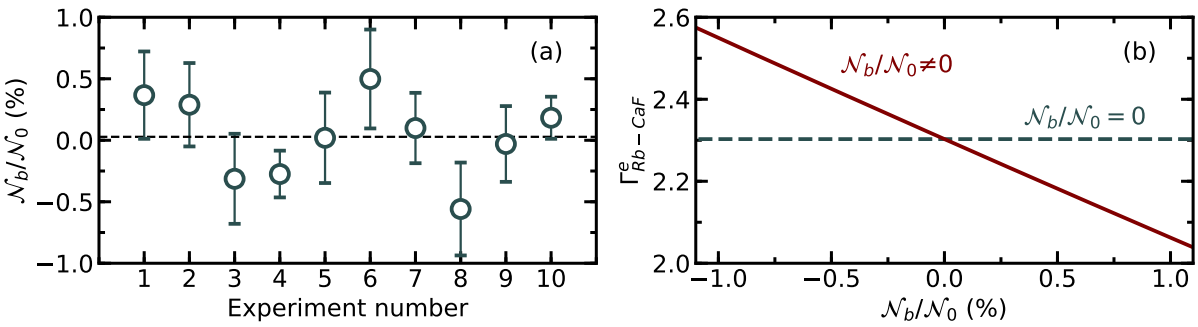

Figure 5.3: Effect of excess background on loss rate estimates. In (a) a set of 10 measurements of the dual species loss rate is fitted to an exponential decay model with an offset. The estimated offset values are expressed as percentages of the signal detected at $t = 0$, the error bars represent the standard errors and the dashed line is the mean of the 10 measurements. In (b) the effect of an excess background on the estimate of Γ_2 is modelled by introducing a non-zero offset (solid line). The dashed line corresponds to the estimate for a zero excess background.

the MOT but with all trap lasers kept on. The signal detected in these images is averaged to estimate the background and is then subtracted from the images corresponding to the trap loss measurements. To confirm that the correct background is subtracted an offset b is added to the model of eq. 5.2. This model is then used to fit to a set of 10 measurements of the trap loss. Figure 5.3(a) shows the estimates of the offset expressed as the percentage of background signal relative to the detected LIF from CaF at $t = 0$. Most estimates of excess background are consistent with zero indicating correct background calibration.

Careful calibration of the background is crucial to measurements described here as the dual and single species loss rates are similar: an incorrect estimate of either loss rate may have a large effect on the estimates of $\Gamma_{\text{Rb-CaF}}$. The effect of an excess background on the estimate of $\Gamma_{\text{Rb-CaF}}$ is modelled using the data in figure 5.2. A variable offset is added to the dual species data and a non-linear least squares fit performed using the model of eq.5.2, which has no offset. Figure 5.3(b) shows how the estimates vary with the amount of uncorrected background. It is found that an excess background which is only 1 % of the signal at $t = 0$ would change the estimate of $\Gamma_{\text{Rb-CaF}}$ by around 10 %. Comparing to the findings of (a), the shift in the estimates are less than 5 % and in most cases much smaller. The mean value corresponding to the data in (a) is 0.03 % which leads to a systematic shift in the estimate of $\Gamma_{\text{Rb-CaF}}$ of only 0.3 %.

These considerations originate from the first experiments on the dual species MOT. As the CCD camera to detect molecule fluorescence has a band-pass filter in front of it and attenuates light at 780 nm by at least 8 orders of magnitude (according to manufacturers specification) it was assumed that the same background image could be used for both dual and single species measurements. Background images were recorded always in the presence of Rb atoms and it was later discovered that a non-negligible amount of Rb

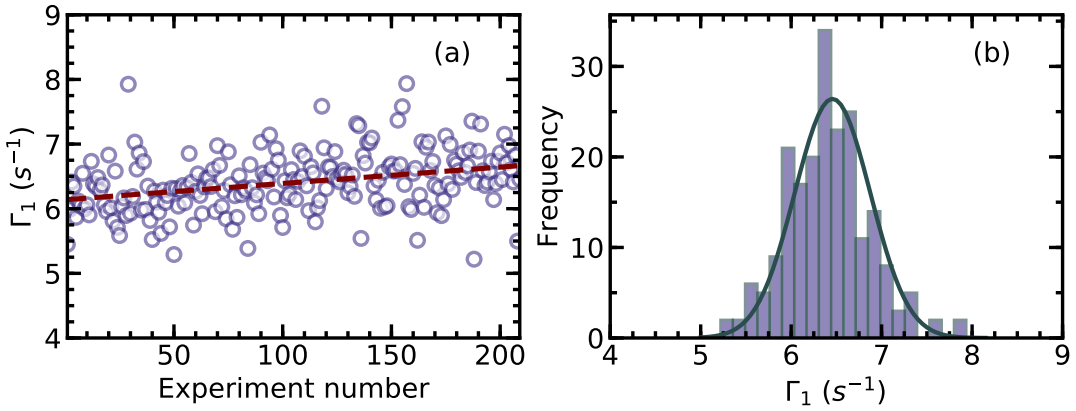

Figure 5.4: Statistics of the natural loss Γ_1 measurements over 210 realizations of the experiment. In (a) the estimates of Γ_1 obtained from each experiment are plotted. The dashed line is a linear fit to the data and gives a shift in the estimate by less than 5 %. (b) Shows how these measurements are distributed while the solid line corresponds to a fit to a normal distribution.

fluorescence was transmitted through the filter. This results in an incorrect background being systematically subtracted from single species measurements and leads to incorrect estimates of the loss rates. Fitting the data to a model that includes a background offset removes this systematic error but inflates the statistical uncertainties of the measurements of $\Gamma_{\mathrm{Rb-CaF}}$. For this reason, it is better to ensure that the correct background is subtracted and then fit to a model without a background. For all measurements described here, two measurements of the background are acquired, in the presence and absence of Rb atoms, and subtracted from the dual and single species loss measurements respectively.

5.1.4 Measurement statistics

A single experiment to measure a trap loss rate takes several minutes and is dominated by the time it takes to load Rb atoms into the MOT. To obtain an estimate of $\Gamma_{\mathrm{Rb\text{-}CaF}}$ takes around 2 minutes and the measurements are repeated multiple times under different experimental conditions.

Figure 5.4(a) shows estimates of the natural loss rate Γ_1 over 210 measurements. The shot-to-shot fluctuation remains roughly constant but the estimate shifts by 4.5(9) %. Although this shift is small, measurements of Γ_1 and Γ_2 are always interleaved so that the effect on Γ_1 from unexpected changes in experimental parameters is eliminated. Figure 5.4(b) shows how the data in (a) is distributed: as expected the distribution is slightly skewed due to the systematic shift in estimated values of Γ_1.

5.2 Measurement of the loss rate coefficient

To find the two-body loss rate coefficient, k_2, corresponding to the observed atom induced loss of molecules from the dual species MOT, the spatial overlaps and the density distributions of both clouds must be measured accurately. Due to limited optical access the molecule cloud may only be imaged in 2D, thus, displacement between the two clouds in the third direction cannot be obtained directly from fluorescence images. By measuring how Γ_2 varies with atom number and using several basic assumptions about the cloud shapes, it is possible to find this displacement empirically as well as the value for k_2.

Numerical estimate of cloud overlap

The measured loss rate is related to k_2 by

$$\Gamma_{\text{Rb-CaF}} = k_2 \mathcal{N}_{\text{Rb}} \mathcal{F} \ , \tag{5.5}$$

where $\mathcal{N}_{\text{Rb}}$ is the atom number and the overlap between the spatial distributions, $\mathcal{F}$, is given by

$$\mathcal{F} = \int f_{\text{Rb}}(\vec{r}) f_{\text{CaF}}(\vec{r}) \ d^3\vec{r} \ . \tag{5.6}$$

The spatial distributions $f_{\text{Rb}}(\vec{r})$, $f_{\text{CaF}}(\vec{r})$ are both normalized such that $\int f_{\text{Rb}}(\vec{r}) \ d^3\vec{r} = \int f_{\text{CaF}}(\vec{r}) \ d^3\vec{r} = 1$. Using fluorescence images of each cloud acquired with the same camera the overlap integral in 2D may be found directly by integrating over the product of the two images

$$\Upsilon^{2D} = \frac{1}{\Delta A} \sum_{j,k} \mathcal{P}^{\text{Rb}}_{j,k} \cdot \mathcal{P}^{\text{CaF}}_{j,k} \ , \tag{5.7}$$

where A is the camera pixel area and $\mathcal{P}^{\text{s}}_{j,k}$ is the normalized pixel count recorded in a fluorescence images of species s. The pixel area ΔA is adjusted for the magnification of the imaging system and $\mathcal{P}^{s}_{j,k}$ are given by

$$\mathcal{P}^{s}_{j,k} = \frac{p^{s}_{j,k}}{\sum_{l,m} p^{s}_{l,m}} \ , \tag{5.8}$$

with $p^{s}_{j,k}$ the raw counts recorded in pixel j,k.

To acquire fluorescence images of the CaF cloud, a band-pass filter centred around 606 nm is placed in front of the camera. With the camera in the same position, the 606 nm filter is replaced with a neutral density filter to acquire an image of the Rb cloud. Both clouds are assumed to be radially symmetric ($\sigma^s_x = \sigma^s_y$) and described well by 1D Gaussian spatial distributions along the blind direction, taken here as the $x-$axis. Thus the overlap integral may be approximated by

$$\mathcal{F} \approx \mathcal{F}_N = \Upsilon^{\text{2D}} \cdot \mathcal{G}^{\text{1D}}(\sigma^{\text{Rb}}_x, \sigma^{\text{CaF}}_x, \Delta_x) \ , \tag{5.9}$$

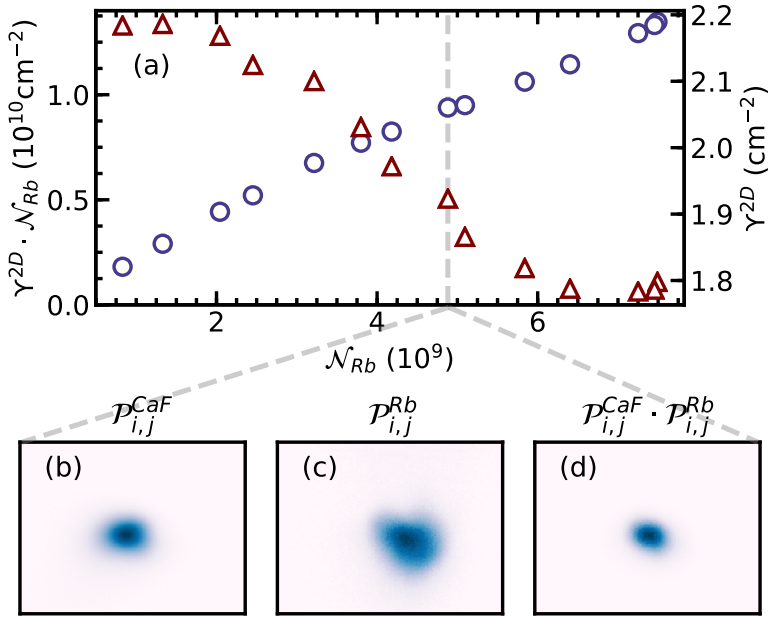

Figure 5.5: (a) Numerical estimates of the effective density overlap Υ^{2D} (△) for a variable number of atoms in the trap together with overlaps of the normalized spatial distributions (○). (b) The normalized CaF distribution; (c) the Rb distribution; (d) the resulting overlap. Both Rb and CaF distributions are obtained from fluorescence images as described in the main text.

with $\mathcal{G}^{1D}$ the overlap integral along the blind direction and Δ_x the unknown displacement between the cloud centres.

In the experiment, a variable number of atoms are loaded into the trap and the corresponding $\Gamma_{\text{Rb-CaF}}$ are measured. The numerical 2D and analytical 1D overlap integrals are calculated using the acquired fluorescence images for each $\mathcal{N}_{\text{Rb}}$. The model of eq. 5.5 is then fit to these data with k_2 and Δ_x set as free parameters. Figure 5.5 shows how the overlap integral Υ^{2D} varies with atom number loaded into the trap. The overlap between the normalized spatial distributions becomes smaller for clouds containing more atoms as the number density of the atom cloud remains roughly constant. On the other hand, the effective density overlap, $\Upsilon^{2D} \cdot \mathcal{N}_{\text{Rb}}$, increases as more atoms are added into the trap and leads to higher observed loss rates.

Analytical estimate of cloud overlap

Assuming that both the atom and molecule clouds are described by radially symmetric Gaussian distributions the overlap integral may be written as

$$\mathcal{F}_{\text{A}} = \frac{1}{(2\pi)^{3/2}} \prod_{i\in\{x,y,z\}} \frac{1}{\widetilde{\sigma}_i} \exp\left(-\frac{\Delta_i^2}{2\widetilde{\sigma}_i^2}\right) , \tag{5.10}$$

where $\widetilde{\sigma}_i^2 = \left(\sigma_i^{\text{Rb}}\right)^2 + \left(\sigma_i^{\text{CaF}}\right)^2$ and Δ_i are the displacements between the two cloud centres. In addition, the power law dependence of the atom cloud size on $\mathcal{N}_{\text{Rb}}$, given by eq. 4.7,

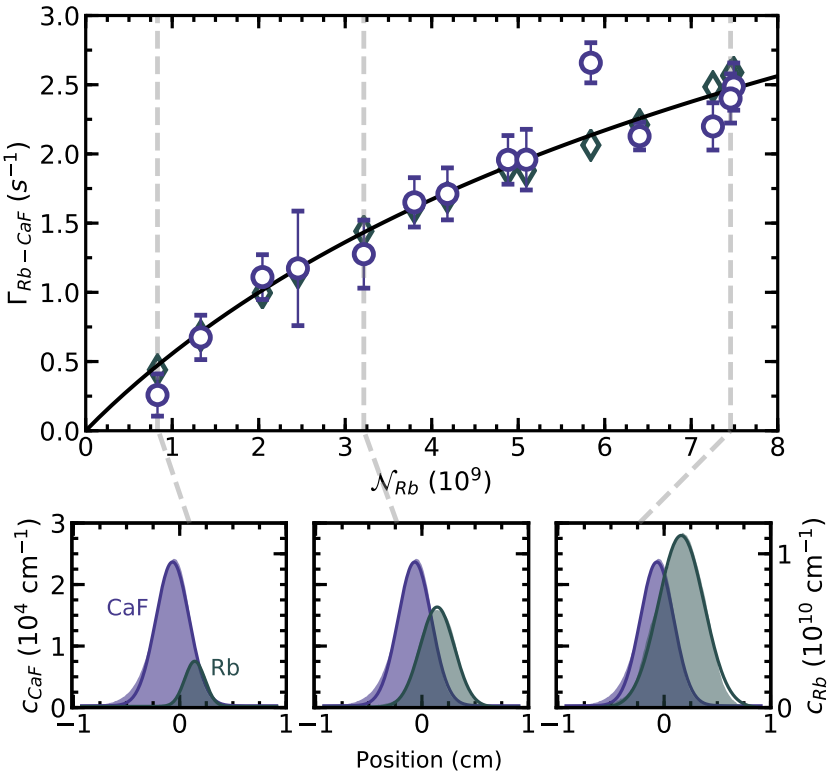

Figure 5.6: Atom induced loss rate of molecules (○) measured for a variable number of atoms in the trap. The diamonds represent the best fit of the numerical overlap model to this data. The black line is the best fit using the analytical overlap model. The lower three panels show the CaF and Rb spatial distributions integrated over x and z and demonstrate how the overlap along y varies with atom number.

may be used to express $\Gamma_{\text{Rb-CaF}}$ in terms of the atom number.

The relative cloud positions and widths are again extracted from the fluorescence images and radially symmetric spatial distributions are assumed. The value of k_2 is then extracted using the model of eq. 5.5 with the numerical overlap replaced by eq. 5.10. The analytical model is defined at all values of $\mathcal{N}_{\text{Rb}}$, whereas the numerical model is only defined at the values of $\mathcal{N}_{\text{Rb}}$ where measurements were made.

Values of k_2 using the numerical and analytical overlap estimates

Measured values of $\Gamma_{\text{Rb-CaF}}$ for variable $\mathcal{N}_{\text{Rb}}$ are shown in figure 5.6. Using the numerical overlap model only discrete values of the overlap integral may be obtained and the values which fit the data the best are represented by diamonds. The fit gives a loss rate coefficient $k_2 = 1.43 \pm 0.29 \cdot 10^{-10}$ cm^3/s and a displacement between the cloud centres along the blind direction $\Delta_x = 0.13 \pm 0.07$ cm. The displacement in the blind direction is similar to the measured radial displacement of 2 mm. Uncertainties on estimates of k_2 and Δ_x include the statistical measurement errors of $\Gamma_{\text{Rb-CaF}}$ and the uncertainties in the atom numbers. The shot-to-shot variation in the measured cloud overlaps is negligible and

there is no reason to believe that it varies significantly on the time scale of the experiment to measure $\Gamma_{\text{Rb-CaF}}$. To include the uncertainties in $\mathcal{N}_{Rb}$ and $\Gamma_{\text{Rb-CaF}}$ simultaneously, both values are sampled from the measured distributions and a fit to the model of eq. 5.5 performed several thousand times. The standard deviation of the estimated values of k_2 and Δ_x are taken as the uncertainty of the best estimates.

In addition, the data of figure 5.6 is used to extract k_2 using the analytical overlap model. The best fit is represented by the solid black line and the best estimates in this case are $k_2 = 1.29 \pm 0.21 \cdot 10^{-10}$ cm^3/s and $\Delta_x = 0.13 \pm 0.07$ cm. Both values are close to the ones found using the numerical overlap model. It seems reasonable to take the estimates obtained using the earlier approach to be more reliable as it better accounts for the spatial atom and molecule distributions.

5.3 Looking for loss channels

In the dual species MOT, atoms are in either the ground ($^2S_{1/2}$) or excited ($^2P_{3/2}$) states while the molecules are in either the ground ($^2\Sigma$) or excited ($^2\Pi_{1/2}$) states. The relative populations between all these levels depend on the trap light intensity and detuning and the observed loss of molecules may be due to inelastic collisions between atoms and molecules when they are in any combination of these states. In this section the value of k_2 is measured under varying experimental conditions in order to determine the dominant loss mechanisms.

5.3.1 Rb MOT light

To investigate whether light used to trap Rb atoms affects the loss rate coefficient, it is modulated between on and off cycles at a frequency of 10 kHz using an AOM. The modulation frequency is faster than the trap oscillation frequencies (roughly 1 kHz) but much slower than the rate at which atoms scatter the trap light (>1 MHz). Varying the modulation duty cycle thus has two effects: (i) the excited state fraction of atoms will change proportionally to the duty cycle and (ii) the average amount of time atoms and molecules spend in the presence of 780 nm light changes in proportion to the duty cycle. Effect (i) probes the dependence of k_2 on the relative population between excited and ground states while effect (ii) allows to investigate processes such as the potential formation of short lived molecular complexes.

The experiment proceeds in a similar way to as before: first around $3.8 \cdot 10^9$ atoms are loaded into the trap followed by the much faster sequence to load molecules. The Rb trap light is then modulated between on and off cycles with a duty cycle, $\eta_{\text{on}}^{\text{Rb}}$. The loss rate of molecules is measured during this modulation in the presence and absence of Rb atoms to find $\Gamma_{\text{Rb-CaF}}$. Lowering $\eta_{\text{on}}^{\text{Rb}}$ reduces the effective spring constant of the trap and thus

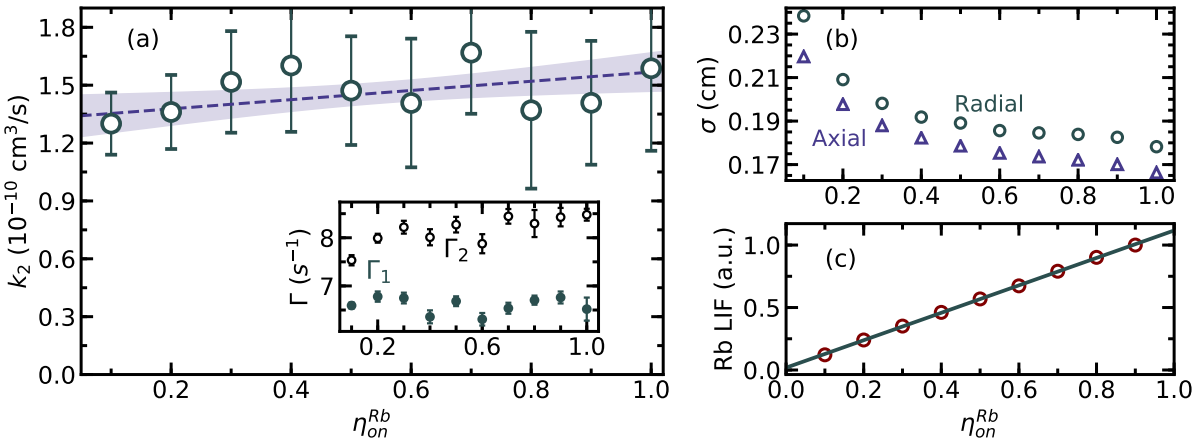

Figure 5.7: (a) Measured loss rate coefficient, k_2, versus the Rb trap light duty cycle, $\eta_{\rm on}^{\rm Rb}$. Error bars represent statistical measurement errors , dashed line is the best straight line fit, and the shaded regions are the 95% confidence bands. The inset shows how the natural (•) and dual species (○) loss rates vary with $\eta_{\rm on}^{\rm Rb}$. (b) The variation of the Rb cloud size with $\eta_{\rm On}^{\rm Rb}$ along the radial (○) and axial (△) directions. (c) The detected LIF from Rb atoms as a function of the Rb trap light duty cycle. The solid line is a linear model fit.

significantly increases the atom cloud size while the position is found to vary very little. For each value of the duty cycle, the fluorescence images together with the analytical model were used to determine the overlap integral. The displacement in the x-axis was fixed at 1.5 mm throughout. Since the position of the cloud in the other two dimensions hardly changes with the duty cycle, this approximation is reasonable. Figure 5.7(c) shows how the detected LIF from Rb atoms varies with $\eta_{\rm on}^{\rm Rb}$. A linear fit to these data gives a gradient of 1.1 which is in good agreement with the assumption that the excited state fraction is directly proportional to $\eta_{\rm on}^{\rm Rb}$. The number of atoms is again determined using absorption imaging and is found to not change over the entire range of $\eta_{\rm on}^{\rm Rb}$ values used in the experiment. Here and in the following experiments the analytical overlap model is used to extract the loss rate coefficient.

Figure 5.7(a) shows how k_2 varies with $\eta_{\rm on}^{\rm Rb}$. The dashed line is the best fit to a linear model which has a gradient of, $(2.4\pm3.0)\times10^{-11}$ cm^3/s, consistent with zero. Because the intercept of the linear fit is 9.5σ above zero, the hypothesis that the observed loss is due entirely to collisions with excited-state atoms can be rejected with very high confidence. The hypothesis that the presence of 780 nm light is responsible for the observed loss may be rejected at the same confidence level. If both ground and excited state atoms are involved in the inelastic process the loss rate coefficient may be written as

$$k_2 = k_2^{\rm e} f_{\rm e} + k_2^{\rm g}(1 - f_{\rm e}) = k_2^{g} + f_{\rm e}^{\rm max}\eta_{\rm on}^{\rm Rb}(k_2^{\rm e} - k_2^{\rm g}) \ , \tag{5.11}$$

where $k_2^{\rm g}$ and $k_2^{\rm e}$ are the loss rate coefficients due to collisions with ground and excited state atoms respectively. The excited state fraction of Rb is labelled as f_e, whose value for $\eta_{\rm e}^{\rm Rb} = 1$ is $f_{\rm e}^{\rm max}$. Using results of [154], the maximum excited state fraction of Rb

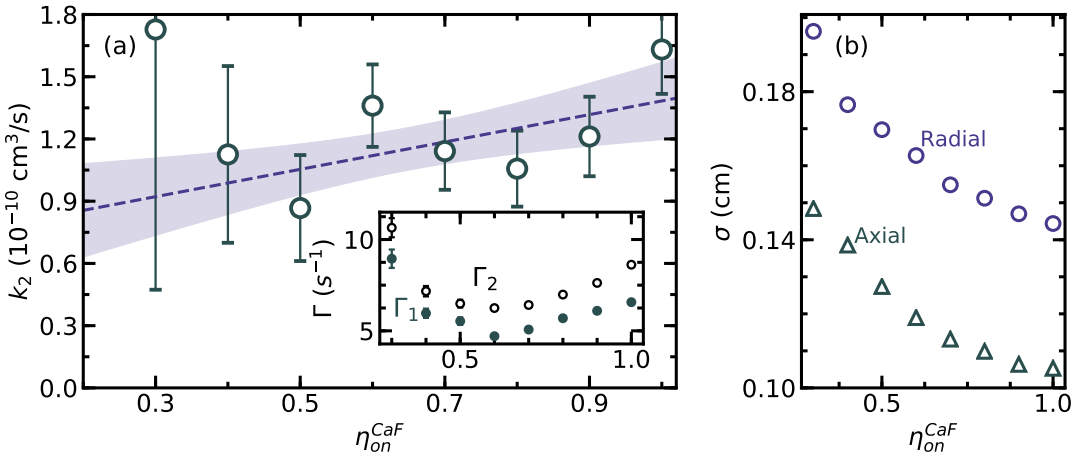

Figure 5.8: (a)Dependence of k_2 on the CaF trap light duty cycle, $\eta_{\text{on}}^{\text{CaF}}$. Error bars represent statistical loss rate measurement errors, dashed line is the best fit straight line, and the shaded regions are the 95% confidence bands. The inset shows how the natural (•) and dual species (○) loss rates vary with $\eta_{\text{on}}^{\text{CaF}}$. (b) The dependence of the CaF cloud size on $\eta_{\text{on}}^{\text{CaF}}$.

for the given trap parameters (detuning of -3Γ, intensity of 72.5 mW $\cdot$ cm^{-2}) is $f_{\text{e}}^{\text{max}} \backsimeq 0.15$. The loss rate coefficients are again obtained from a linear fit and are equal to $k_2^{\text{g}} = (1.33 \pm 0.14) \times 10^{-10}$ cm$^3 \cdot$ s^{-1} and $k_2^{\text{e}} = (2.9 \pm 1.9) \times 10^{-10}$ cm$^3 \cdot$ s^{-1}. Because $f_{\text{e}}^{\text{max}}$ is low and the loss rate coefficient is observed to vary slowly with $\eta_{\text{e}}^{\text{Rb}}$, the error on the estimate of k_2^{e} is large. Nevertheless, the measured value of k_2^{e} is consistent with the value of k_2^{g}, suggesting that the observed loss process occurs at a similar rate when atoms are excited to the $^2P_{3/2}$ level.

5.3.2 CaF MOT light (duty cycle)

Next, the CaF trap light is modulated also at a frequency of 10 kHz with a variable duty cycle, $\eta_{\text{on}}^{\text{CaF}}$, and the loss rate coefficients are measured. The Rb light is kept on continuously for these experiments. As shown in figure 5.8(b) the molecule cloud expands as the duty cycle is reduced due to a reduced effective spring constant. The values of k_2 at each duty cycle are determined using the same method as described in section 5.3.1 above. Figure 5.8(a) shows how k_2 varies with $\eta_{\text{on}}^{\text{CaF}}$. A linear model fit to these data gives a gradient of, $(7 \pm 5) \times 10^{-11}$ cm^3/s, which is consistent with zero. The best estimate of the intercept is $(0.76 \pm 0.38) \times 10^{-10}$ cm $\cdot$ s^{-1} and is above zero by 2σ, suggesting that the observed loss is not likely to be purely due to collisions with molecules in the excited ($^2\Pi_{1/2}$) state.

From the inset of figure 5.8(a), it is evident that the natural loss rate is reduced for lower values of $\eta_{\text{on}}^{\text{CaF}}$ but begins to grow again for $\eta_{\text{on}}^{\text{CaF}} < 0.6$. Lowering the amount of time the trap light is kept on reduces both the average scattering rate and the trap depth. A lower scattering rate leads to smaller loss but, as the temperature of the cloud does not

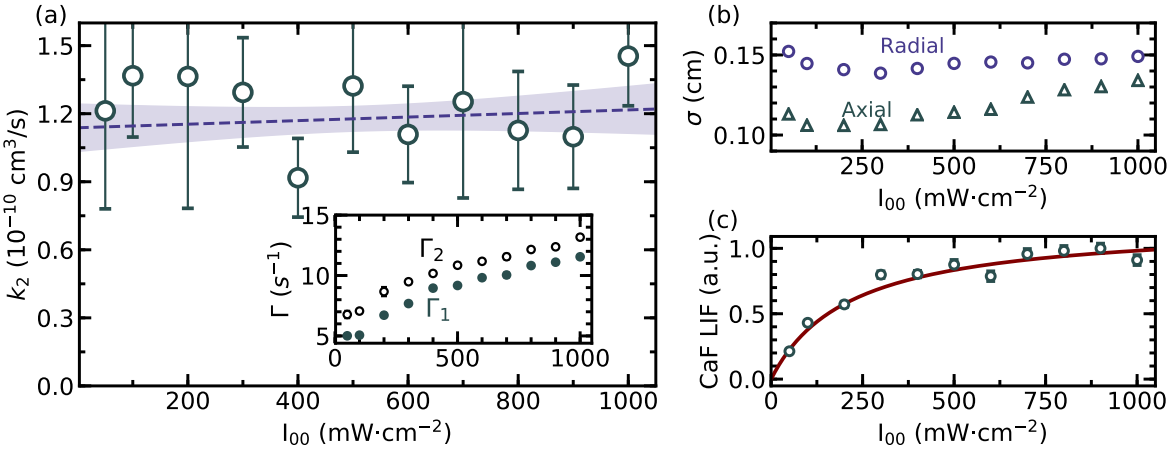

Figure 5.9: (a) Dependence of k_2 on the CaF trap light intensity. The dashed line is a fit to a linear model with the shaded region representing 95% confidence bands. The inset shows how the natural (•) and dual species (○) loss rates vary with light intensity. (b) The radial (○) and axial (△) molecule cloud size as a function of trap light intensity. (c) The LIF from CaF for different trap light intensities. The line is a fit to the effective scattering rate model described in the main text.

vary significantly with $\eta_{\text{on}}^{\text{CaF}}$, the reduced trap depth will enable more molecules to escape the trap. At $\eta_{\text{on}}^{\text{CaF}} = 20\%$, all molecules are lost from the trap within the first 20 ms or so. These observations are consistent with there being two loss channels, one that increases with scattering rate and another that increases as the trap depth is reduced. When the duty cycle is low the trap is shallow and the "boil off" dominates; when the duty cycle is high this effect is small but loss due to scattering into an unaddressed state dominates.

5.3.3 CaF MOT light (intensity)

To consolidate the findings from the experiment where the duty cycle of the CaF trap light is varied, an additional measurement was performed. After both species are loaded into the dual MOT, the molecule trap light is ramped down to a variable intensity and held at that value for the duration of the loss rate measurement. In all the experiments described above the $\mathcal{L}_{00}^{c}$ light was kept at an intensity of 200 mW $\cdot$ cm^{-2} and here both higher and lower values were explored. In figure 5.9(b) the variation of the molecule cloud size with light intensity is shown. The cloud becomes slightly smaller in both the radial and axial directions as the intensity is reduced to 200 mW $\cdot$ cm^{-2}, whereas begins to grow for lower intensities. For intensities down to 200 mW $\cdot$ cm^{-2} the temperature of the cloud drops, thus reducing its size. For lower intensities the temperature stops varying and the cloud becomes larger due to a reduced trap spring constant.

Figure 5.9(a) shows how k_2 varies with the trap light intensity. The values of k_2 for each trap beam peak intensity are computed using the same methods as above with the variation in cloud size and position as a function of $\mathcal{L}_{00}^{c}$ intensity taken into account.

A linear fit to these data gives a gradient of $(0.8 \pm 2.7) \times 10^{-14}$ cm$^5 \cdot$ s$^{-1} \cdot$ mW^{-1}, again indicating that the trap light does not affect the observed loss. The intercept is found to be equal to $(1.39 \pm 0.21) \times 10^{-10}$ cm $\cdot$ s^{-1}, which is above zero by 6.7σ. Thus the hypothesis that the observed loss is entirely due to the presence of 606 nm light may be rejected with high confidence. In addition, lowering the intensity significantly changes the excited state fraction of CaF. Figure 5.9(c) shows the LIF detected in the first camera frame as a function of intensity. The detected LIF is directly proportional to the scattering rate which determines the fraction of molecles in the excited electronic state. The excited state fraction for this experiment thus dropped by around a factor of 5 for these measurements when reducing the trap light intensity from 1000 mW $\cdot$ cm^{-2} to 50 mW $\cdot$ cm^{-2}. Because no significant variation in k_2 with intensity is observed, the results of this experiment agree with the conclusions of section 5.3.2.

The solid line in figure 5.9(c) is a fit to the model of eq. 2.52. The fit gives $I_{\mathrm{s,eff}} = 73(5)$ mW $\cdot$ cm^{-2}, which is 46 % larger than the expected value (see section 2.2.5) of $\frac{72}{7} I_{\mathrm{s}} = 50$ mW $\cdot$ cm^{-2}. Because the frequency detuning is somewhat poorly defined relative to the multi-level structure of CaF, this discrepancy is reasonable.

5.4 Discussion

For the measurements described above, the effective temperature of the relative motion is 2.4 mK. At this temperature, the results of the single-channel model have almost no dependence on the scattering phase shift δ^{S}, because the shape resonances corresponding to the different partial waves are washed out by thermal averaging. The loss rate can be approximated as

$$k_2(T) = \frac{4y}{(1+y)^2} k_2^{\max}(T) \ , \tag{5.12}$$

with y the loss rate parameter defined in section 2.3.3. The thermally averaged universal loss rate coefficient $k_2^{\max}(T)$ depends only on the reduced mass $\mu = (m_{\mathrm{Rb}} m_{\mathrm{CaF}})/(m_{\mathrm{Rb}} + m_{\mathrm{CaF}})$ and the asymptotic interaction potential $-C_6/R^6$. In this system, the universal loss rate coefficient is estimated to be equal to $k_2^{\max} = 1.32 \times 10^{-10}$ cm^{-3} and is in agreement with the experimentally measured value of $k_2 = (1.43 \pm 0.29) \times 10^{-10}$ cm^{-3}. In addition, the measurement results in the MOT constrain the loss rate parameter to be $y > 0.46$. This corresponds to a probability $P > 0.86$ that each time the pair reaches short range a molecule will be lost from the trap. The loss rate parameter y is expected to be independent of energy, so this constraint should apply to collisions at ultracold temperatures. As will be discussed in detail in the following chapter, collisions between molecules in the ground electronic $N = 1$ state and ground state atoms lead to loss which is close to the universal rate. When the molecules are in $N = 0$ the loss is highly suppressed. Because molecules are in the $N = 1$ state in the MOT and the measured

loss rate coefficient is consistent with $k_2^{\max}$, rotation-changing collisions are sufficient to explain the experimental observations. Contributions from collisions with excited state molecules or atoms, or light induced processes may not be ruled out, although they are insufficient to explain the experimental results.

At a temperature obtained in the experiments described here, a total of 4 to 7 partial waves may contribute to the inelastic scattering process. In this regime, the universal loss may be approximated by the Langevin capture model [105]. In this model, all classical particle trajectories with energies higher than the centrifugal barrier are assumed to result in loss. For an asymptotic potential $-C_6R^{-6}$, the Langevin model gives a loss rate [155]

$$k_2^{\max}(T) = 2^{11/6}\,\Gamma(2/3)\left(\frac{\pi}{\mu}\right)^{1/2} C_6^{1/3}(k_{\mathrm{B}}T)^{1/6}\,, \tag{5.13}$$

where $\Gamma(z)$ is the gamma function. For Rb+CaF at a temperature of 2.4 mK, the universal loss rate evaluates to $k_2^{\max} = 1.34 \times 10^{-10}$ cm $\cdot$ s^{-1}, which is in very good agreement both with the measured value and the quantum-mechanical universal rate. The $T^{1/6}$ temperature scaling in the Langevin model remains valid down to temperatures of around $\sim E_6/k_{\mathrm{B}}$ [105][3], where $E_6 = \hbar^3/\sqrt{8\mu^3 C_6}$, which is 124 μK for the Rb+CaF system. The measurement results in the mK and μK regimes will be compared in the next chapter.

In the MOT, molecules in all hyperfine states of the $N = 1$ rotational level are trapped. The maximum energy released for a molecule relaxing from the $F = 2$ to $F = 1^-$ hyperfine level is roughly 7 mK in temperature units. This corresponds to a gain in velocity of 1.4 m/s which is below the capture velocity of the MOT. In a collision which involves a relaxation of the atoms hyperfine state, a molecule would emerge with a velocity of 7.4 m/s. This is close to the capture velocity of the MOT, thus lowering the trap depth by reducing the duty cycle could lead to an increased loss rate. However, as argued above, rotational relaxation causes loss that is already at the universal limit. In this limit, adding an additional collisional loss mechanism, no matter how strong, does not increase the loss rate. The same argument applies to the RE process, but not to processes involving excited-state atoms and/or molecules since they form distinct populations with their own distinct values of the universal loss rate.

The results presented here are important for designing future experimental protocols to transfer both species into a conservative trap where collisional cooling may be performed. The high loss rate of molecules observed in the dual species MOT will limit the achievable number densities in a conservative trap, especially when the two cloud centres are better overlapped and the size is compressed using a compressed-MOT [156] or DARK SPOT MOT [157, 158]. To circumvent this limitation, the molecules could be loaded into the trap first. As will be shown in the next chapter, the atom induced loss

[3]In the non-universal case when the loss rate parameter $y << 1$, the $T^{1/6}$ temperature scaling can break down even at temperatures well above E_6/k_{B}.

rate of molecules prepared in $N = 0$ is highly suppressed. Thus, losses can be avoided by preparing molecules in a conservative trap and in the ground rotational state, before introducing the atoms.

6 | Collisions in a magnetic quadrupole trap

Sympathetic cooling of molecules using an ultracold gas of atoms must proceed in the absence of near resonant trap light, which usually limits the lowest achievable temperatures. Such cooling was for the first time demonstrated only very recently [159], when ^{23}Na^{6}Li molecules where shown to thermalize with an ultracold gas of ^{23}Na atoms, both confined in a 1D optical lattice. In addition, the authors were able to perform evaporation of the Na atoms to lower the temperature of both the atoms and the molecules to 220 nK and obtain a molecular phase space density of $2 \cdot 10^{-2}$. Contrary to theory predictions, sympathetic cooling turned out to be surprisingly efficient in this system, with an elastic to inelastic collision rate ratio of 62(12). Inelastic losses due to the presence of trap light or due to chemical reactions were not found to limit the collisional cooling process. Other molecular species are not so fortunate [160, 56] and require additional care to prevent losses due to trap light induced processes or chemical reaction processes. Thus a natural trap to perform collisional cooling is the magnetic trap where all laser light may be extinguished. In this trap the inelastic collisional processes are limited to spin-changing collisions as the molecules may not be confined in their lowest ground state. Such spin-changing collisional processes are expected to have a relatively small cross section [161]. If this is considerably smaller than the elastic cross section, sympathetic cooling in the magnetic trap becomes feasible.

In this work CaF molecules and Rb atoms are transferred to a magnetic quadrupole trap. To investigate the feasibility of sympathetic cooling, inelastic processes are studied first. In addition to these studies being of practical importance, it also contributes to the currently scarce available experimental work where atom-molecule collisions [162, 163, 164, 165] at ultracold temperatures were studied.

This chapter details the experimental sequence used to prepare the atoms and molecules in the magnetic trap. Quantum state dependent loss of molecules out of the trap due to inelastic collisions with atoms are observed and the loss rate coefficients are measured. Experimental findings are compared to theory predictions.

6.1 Dynamics in the magnetic trap

First, the working principle of the magnetic trap is reviewed and the dynamics of trapped particles are described using numerical trajectory simulations. A particle with a magnetic moment $\vec{\mu}$ will experience a force in a spatially varying magnetic field $\vec{B}(x, y, z)$ given by

$$\vec{F}(x, y, z) = -\nabla(\vec{\mu} \cdot \vec{B}(x, y, z)) \ . \tag{6.1}$$

For a magnetic moment pointing along the direction of the local magnetic field the particle will be pulled towards the direction of decreasing magnetic field. When the magnetic moment is anti-aligned with the magnetic field it will experience a force towards regions of higher field. It is thus possible to spatially confine particles using a magnetic field with a local minimum. Both Rb and CaF have an unpaired electron in the ground electronic state, thus making it possible to trap both particles magnetically.

In the magnetic trap, trapped particles precess around the pointing direction of the local magnetic field. Initially particles are spin-polarized along a bias field of 200 mG but the direction of the field in the trap is not uniform in space. Thus it is important to consider whether the orientation of the particle spin will be able to adiabatically follow the changing direction of the magnetic field as the trap is turned on. The relevant time-scales to compare here are the Larmor precession period in the applied bias field with the time it takes for the trap to turn on. The Larmor period is given by $\frac{4\pi m_e}{eB}$ and is equal to 3.6 μs for both Rb and CaF prepared in spin-stretched states for a bias field strength of 200 mG- much faster than the time it takes to switch on the trap.

The most basic configuration which produces a spatially varying magnetic field with a local minimum is the magnetic quadrupole, also used to make the MOT. Close to the field zero the magnetic quadrupole field may be approximated by

$$\vec{B}(x, y, z) = b_z \left(\frac{x\hat{e}_x}{2} + \frac{y\hat{e}_y}{2} - z\hat{e}_z \right) \ , \tag{6.2}$$

with b_z the field gradient along the axis of the anti-Helmholtz coils, which is here chosen as the $z-$axis. The motion of a particle of mass m prepared in a spin state with total angular momentum projection m_F moving in a quadrupole field is described by the following equations of motion

$$\ddot{x} = -\frac{\mu_B g_F M_F b_z}{4m} \frac{x}{\sqrt{\frac{x^2}{4} + \frac{y^2}{4} + z^2}} \ , \tag{6.3}$$

$$\ddot{y} = -\frac{\mu_B g_F M_F b_z}{4m} \frac{y}{\sqrt{\frac{x^2}{4} + \frac{y^2}{4} + z^2}} \ , \tag{6.4}$$

$$\ddot{z} = -\frac{\mu_B g_F M_F b_z}{m} \frac{z}{\sqrt{\frac{x^2}{4} + \frac{y^2}{4} + z^2}} - g \ . \tag{6.5}$$

Here μ_B and g_F are the Bohr magneton and Lande g-factor respectively, and the approximation that the Zeeman shift is linear in the magnetic field was used. In this case, this is a

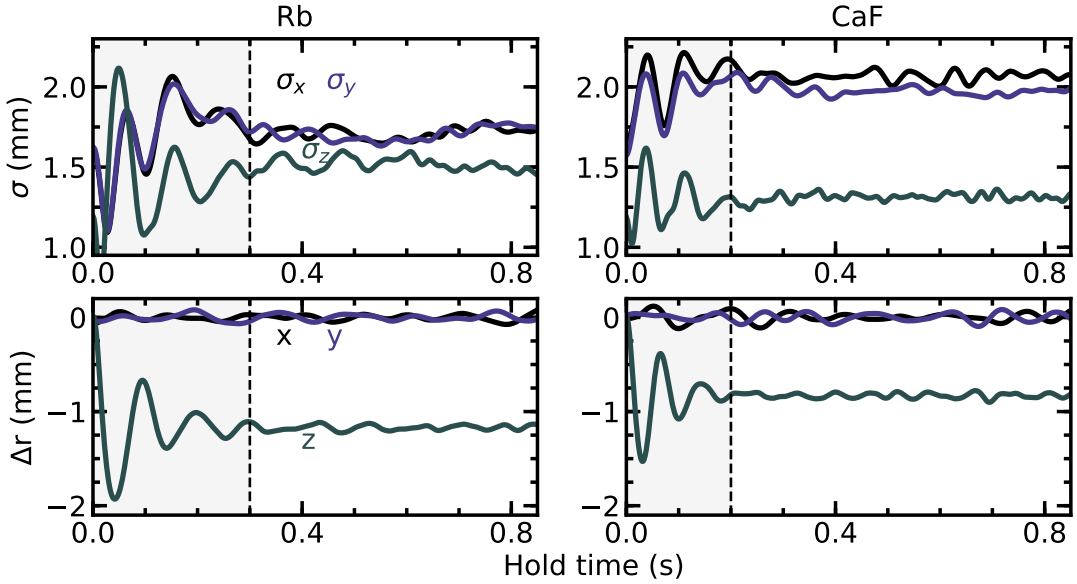

Figure 6.1: Numerically simulated dynamics of a gas loaded into a magnetic quadrupole trap. The top row shows how the cloud sizes of Rb and CaF vary for the first 0.85 s after turning on the trap. The bottom row shows the transient motion of the cloud centres. The dashed lines indicate roughly the time it takes for the dynamics of both gases to reach a steady state.

good approximation when the Zeeman shift is small compared to the hyperfine structure. The gravitational force, mg, exerted on the particle along the $z-$axis is also included. In the following, these equations are solved numerically for a gas of particles loaded into the magnetic trap with variable initial conditions.

6.1.1 Macroscopic properties of a gas in a magnetic trap

The dynamics of a gas in a magnetic quadrupole field are simulated by randomly drawing particles from a thermal distribution and propagating their trajectories using eqs. 6.3-6.5. The initial position of a particle in the gas is drawn from a normal distribution with width σ_i and mean displacement from the trap centre d_i, where $i \in \{x, y, z\}$. The initial particle velocity is drawn from a thermal distribution with a given characteristic temperature. For a given set of initial parameters, the trajectories of $5 \cdot 10^3$ particles are simulated to approximate the macroscopic properties of a bulk gas. The size of the cloud at any given time is given by the standard deviation of the particle positions while the trap centre is given by the mean position. To extract the temperature, the velocity distribution after a fixed hold time in the magnetic trap is fitted to a thermal distribution.

Figure 6.1 shows the transient dynamics of clouds of Rb and CaF loaded into a magnetic trap with $b_z = 0.3$ T/m. Both particles are assumed to be in the spin stretched states with magnetic moments of $1\mu_B$. The initial geometric temperature of the atom and molecule gases are 40 μK and 100 μK respectively. Because of the lower mass of CaF it

will be accelerated more than Rb and the individual trajectories of the particles will be dephased faster. It takes roughly 300 ms for the size and position of the Rb gas to reach a steady state while the CaF cloud settles within 200 ms. Due to the gravitational sag the spatial distributions of the clouds along gravity become asymmetric and their centres of mass are shifted below the trap centre. The shift is approximately proportional to the mass of the particle thus the Rb cloud sags more than the CaF cloud. The widths of both clouds are smaller along the axial direction because the magnetic field gradient is two times larger than along the radial direction.

One curiosity of the magnetic quadrupole trap is that even in the absence of collisions or other dissipative processes the dynamics of the gas reaches a steady state. For example, the centre of mass of a gas of atoms loaded into a harmonic trap[1] with an initial displacement from the trap centre would oscillate indefinitely without a means to dissipate the extra potential energy. In contrast, the dynamics of a gas displaced from the field zero in a quadrupole field will reach a steady state within hundreds of ms. The anharmonicity of the magnetic quadrupole potential dephases the trajectories of individual particles and pushes the bulk gas towards a quasi-thermal equilibrium.

Magnetic field gradient (sudden ramp)

The force experienced by a particle in the magnetic trap is proportional to the magnetic field gradient. It is thus interesting to investigate to what extent the gas may be compressed by simply increasing the field gradient. Assuming the cloud in the magnetic trap has a thermal distribution and neglecting the gravitational sag it follows from the equipartition theorem that the size of the cloud is $\sigma_z \propto T/\mathrm{b}_z$. Increasing the field gradient changes the momentum distribution of the particles in a non-trivial way as the trajectories along along the radial (x, y) and axial (z) direction are coupled. The numerical simulation of particles trajectories is thus useful for understanding how both the cloud width and temperature change as a function of b_z.

Figure 6.2(a-b) shows how the size and temperature of the CaF cloud vary with the magnetic field gradient. In the simulation, the magnetic field is switched on instantly at $t = 0$. The initial cloud dimensions are 1.6 mm and 1.2 mm along the radial and axial directions, similar to the size obtained in the experiment. According to the results of the simulation the size ceases to decrease above axial gradients of 1 T/m. Fitting these simulation data to a power law model $\sigma = \sigma_0 + h b_z^{\gamma}$ gives $\gamma_\mathrm{a} = -1.3$, $h_\mathrm{a} = 0.016$ for the axial direction and $\gamma_\mathrm{r} = -1.68$, $h_\mathrm{r} = 0.0064$ for the radial direction. As the gradient is increased the temperature continues to rise due to the additional magnetic potential energy added to each molecule and limits further compression. The temperature increases two times faster along the axial direction as the gradient along this direction is two times

[1] This could be an Ioffe-Pritchard magnetic trap or an optical dipole trap.

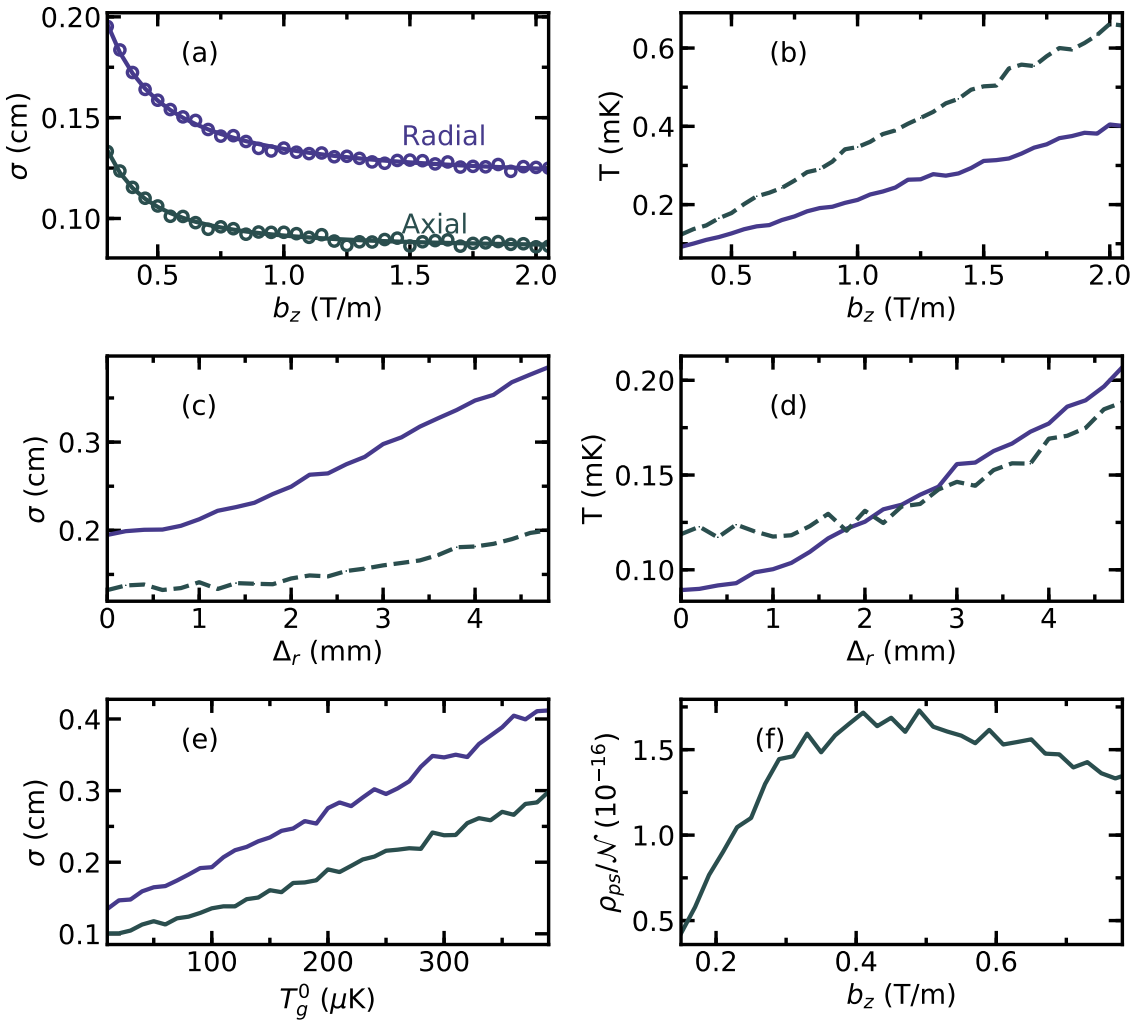

Figure 6.2: Numerical simulation of the cloud (a) size and (b) temperature as a function of the axial magnetic field gradient. The initial axial cloud temperature is 120 μK, the radial is 90 μK. In (a) the solid lines are fits to a power law model described in the main text. (c) and (d) the cloud size and temperature as a function of initial displacement from the trap centre along the radial direction. (e) Cloud size in the MQT as a function of the initial geometric mean temperature at a field gradient of 0.3 T/m. (f) The phase space density as a function of the field gradient.

higher. For experiments described in this work a 0.3 T/m gradient is used thus there is scope to substantially reduce the size of the cloud. Unfortunately, the electrical current required to achieve higher gradients in the present experimental setup causes too much ohmic heating of the coil assembly and thus an increase in background pressure. In the future, the magnetic quadrupole field provided by the in-vacuum coils may be combined with a quadrupole field from a set of external coils and a gradient close to 1 T/m should be attainable.

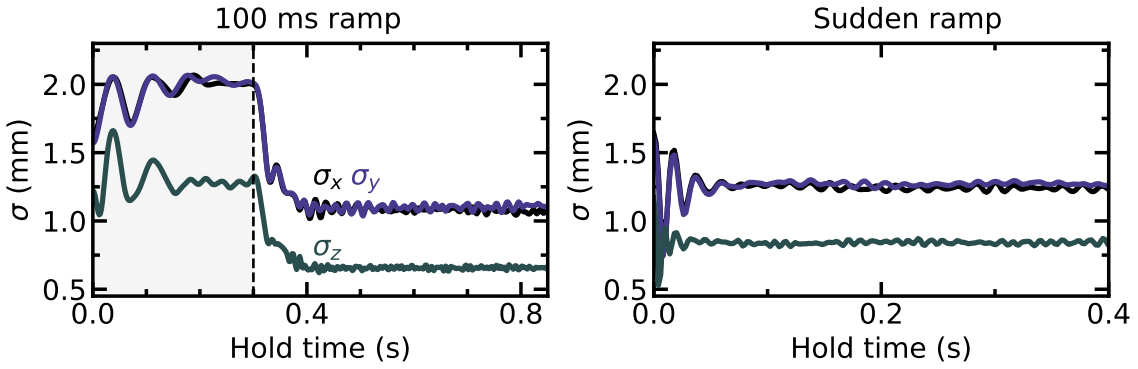

Figure 6.3: Numerical simulation of cloud compression in the magnetic trap. The size of the molecular cloud is plotted as a function of hold time in the trap using a linear 100 ms ramp (left) and a sudden ramp (right) to a final axial magneic field gradient of 2 T/m. The ramp starts at $t = 0.3$ ms from an initial field gradient of 0.3 T/m.

Magnetic field gradient (slow ramp)

Increasing the magnetic field strength gradually rather than suddenly jumping it to the final value has a different effect on the dynamics of the trapped cloud. Figure 6.3 shows how the size of the molecule cloud changes with time when the field is suddenly ramped up to 0.3 T/m at $t = 0$ followed by a 100 ms linear ramp at $t = 0.3$ s up to an axial gradient of 2 T/m. Using a linear ramp gives a cloud which is $\sim 30\%$ smaller along the axial direction and $\sim 10\%$ smaller radially compared to the size obtained when the field is suddenly jumped to the final value. This suggests that even in the anharmonic quadrupole trap the cloud may be compressed adiabatically to some extent.

Initial cloud displacement and temperature

A molecule cloud displaced from the trap centre will reach a steady state size and temperature within ~ 200 ms. Figures 6.2(c-d) show how the size and temperature of the cloud vary with initial radial displacement from the magnetic field zero. The additional magnetic potential energy added to the molecules leads to a larger cloud size and increases the temperature. Even though the initial displacement is along the radial direction, the axial dimension is also affected because the equations of motion in a magnetic quadrupole trap are coupled in both dimensions.

Figure 6.2(e) shows how the size of the cloud varies with the initial geometric temperature, T_g^0. The size scales roughly linearly with T_g^0. Thus another route to increase the number density in the trap is to load a colder cloud. At a temperature of 5 μK the cloud size in the radial direction would be reduced to ~ 0.13 cm, which corresponds to an increase in number density by a factor of three. This temperature has been demonstrated experimentally for laser cooled CaF molecules [98, 166].

The results of these simulations compare very well with measured properties of the

CaF cloud loaded into the magnetic trap. The simulation predicts that a cloud with radial and axial dimensions of 1.6 mm and 1.2 mm displaced from the trap centre by 2 mm will expand to 2.3 mm along the radial direction once loaded into the trap. This is indeed observed in the experiment. The cloud temperature predicted by the simulation for these initial conditions is around 130 μK while in the experiment a temperature of 175(37) μK is measured.

Phase space density

Finally, it is interesting to look at how the phase space density of the gas varies with the magnetic field gradient. The phase space density of a gas at temperature T and density $N = \mathcal{N}/((2\pi)^{3/2}\sigma_x\sigma_y\sigma_z)$ is given by

$$\rho_{\mathrm{ps}} = N\left(\frac{2\pi\hbar^2}{mk_{\mathrm{B}}T}\right)^{3/2} . \tag{6.6}$$

For a Bose condensed gas $\rho_{\mathrm{ps}} > 1$. From the equipartition theorem, the magnetic field gradient for which the phase space density of the cloud is matched with the phase space acceptance of the quadrupole trap is $b_z^{\mathrm{o}} = \frac{3}{2^{1/3}}k_{\mathrm{B}}T_{\mathrm{g}}/\sigma_{\mathrm{g}}\mu_{\mathrm{B}}$, with T_{g} and σ_{g} the geometric mean temperature and size of the cloud respectively. For the initial parameters of the cloud in the simulation, $b_z^{\mathrm{o}} = 0.22$ T/m. Figure 6.2(f) shows how ρ_{ps} changes with the loading gradient. At a field of around 0.45 T/m the phase space density is maximized, which is a factor of two larger than predicted using the equipartition theorem. Because the motion in a quadrupole trap is coupled in all three dimensions, the use of geometric mean quantities may not give the correct estimates. In addition, the gravitational potential energy was excluded from the above. The optimum $\rho_{\mathrm{ps}}/\mathcal{N} \simeq 1.7 \cdot 10^{-16}$ in the trap is about ~ 30 % lower than the initial phase space density.

6.1.2 Spatial distribution in a magnetic trap

A particle confined in a magnetic quadrupole trap has potential energy

$$U(x,y,z) = \mu b_z\sqrt{\frac{x^2+y^2}{4}+z^2} + mgz , \tag{6.7}$$

where $\mu = g_F M_F \mu_{\mathrm{B}}$ and the gravitational potential energy is also included. Using the equipartition theorem, the corresponding density distribution of a cloud in thermal equilibrium is

$$N(x,y,z) = \mathcal{N}_0\frac{(\beta\mu b_z)^3}{32\pi}\exp\left(-\beta\mu b_z\left(\sqrt{\frac{x^2+y^2}{4}+z^2}+mgz\right)\right) , \tag{6.8}$$

where $\beta = 1/k_{\mathrm{B}}T$ and $\mathcal{N}_0$ is the total particle number. Integrating along the radial directions, x and y, gives the axial distribution

$$g(z) = \frac{(\gamma^2-1)^2}{4z_0}\left(1+\frac{|z|}{z_0}\right)\exp\left(-\frac{|z|+\gamma z}{z_0}\right) , \tag{6.9}$$

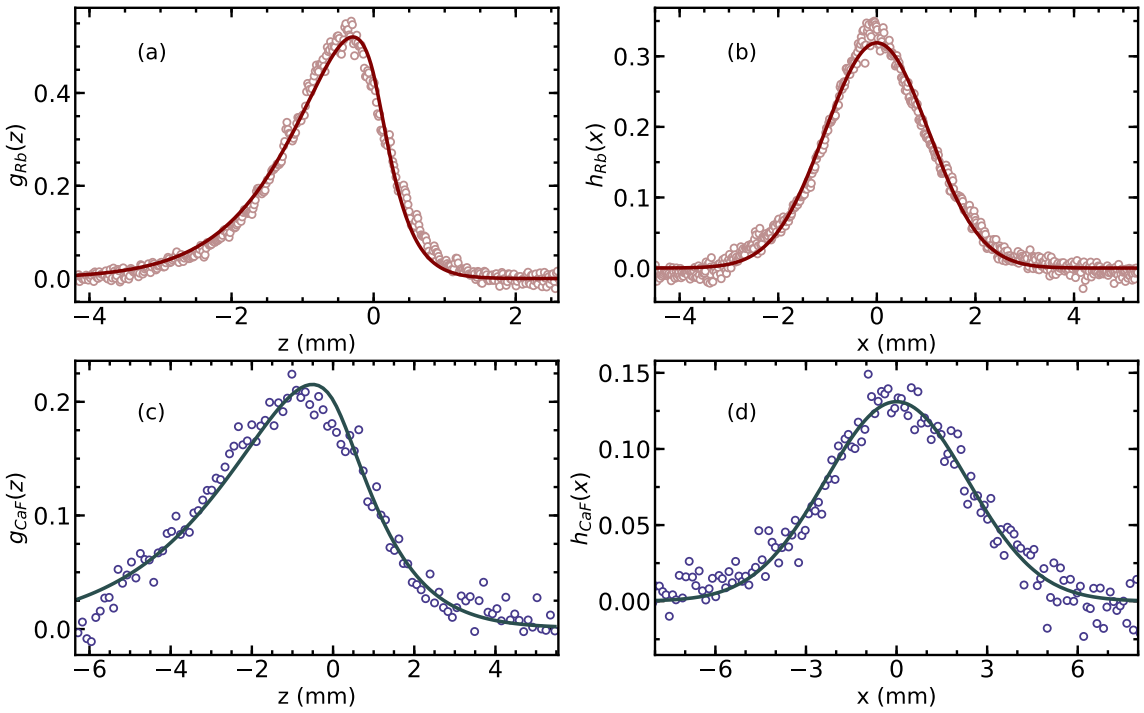

Figure 6.4: Measured spatial distributions of molecules and atoms in the magnetic quadrupole trap. (a,c) Axial distributions for (a) Rb and (c) CaF, integrated over the radial direction. (b,d) Radial distributions for (b) Rb and (d) CaF, integrated over the axial direction. The solid lines are fits to the axial and radial distributions described in the main text.

with $\gamma = mg/\mu b_z$ and $z_0 = k_B T/\mu b_z$. There is no analytical expression for the radial spatial distribution but it is found that a Gaussian distribution, $h(x)$, fits well the experimentally measured distributions. The 3D distributions are thus modelled as $f_s(x, y, z) = h_s(x)h_s(y)g_s(z)$, with $s \in \{\mathrm{Rb}, \mathrm{Ca}F\}$. Figure 6.4 shows the measured Rb and CaF distributions, together with fits to $g(z)$ and $h(x)$. Both species were held in the trap for 300 ms, then released and imaged in free space.

The overlap integral between the two distributions is then given by

$$\int f_{\mathrm{Rb}}(\vec{r}) f_{\mathrm{CaF}}(\vec{r})\, d^3\vec{r} = \frac{A_{\mathrm{Rb}}^2 A_{\mathrm{CaF}}^2 \left(C^2 \left(4\bar{z_0}^2 - 3z_{0,\mathrm{Rb}} z_{0,\mathrm{CaF}}\right) - 4\bar{z_0}^2 \left(4\bar{z_0}^2 + z_{0,\mathrm{Rb}} z_{0,\mathrm{CaF}}\right)\right)}{4\pi \left(\sigma_{\mathrm{Rb}}^2 + \sigma_{\mathrm{CaF}}^2\right) \left(2\bar{z_0} + C\right)^3 \left(D_{\mathrm{CaF}} z_{0,\mathrm{Rb}} + D_{\mathrm{Rb}} z_{0,\mathrm{CaF}}\right)^3}\,, \tag{6.10}$$

with the various constants defined as

$$A_s = \gamma_s^2 - 1\,, \tag{6.11}$$

$$D_s = \gamma_s - 1\,, \tag{6.12}$$

$$C = \gamma_{\mathrm{Rb}} z_{0,\mathrm{CaF}} + \gamma_{\mathrm{CaF}} z_{0,\mathrm{Rb}}\,, \tag{6.13}$$

$$\bar{z_0} = \frac{1}{2}\left(z_{0,\mathrm{Rb}} + z_{0,\mathrm{CaF}}\right)\,. \tag{6.14}$$

This analytical expression for the overlap integral is used to find the effective density and accounts for the differential gravitational sag between the two species in a natural way.

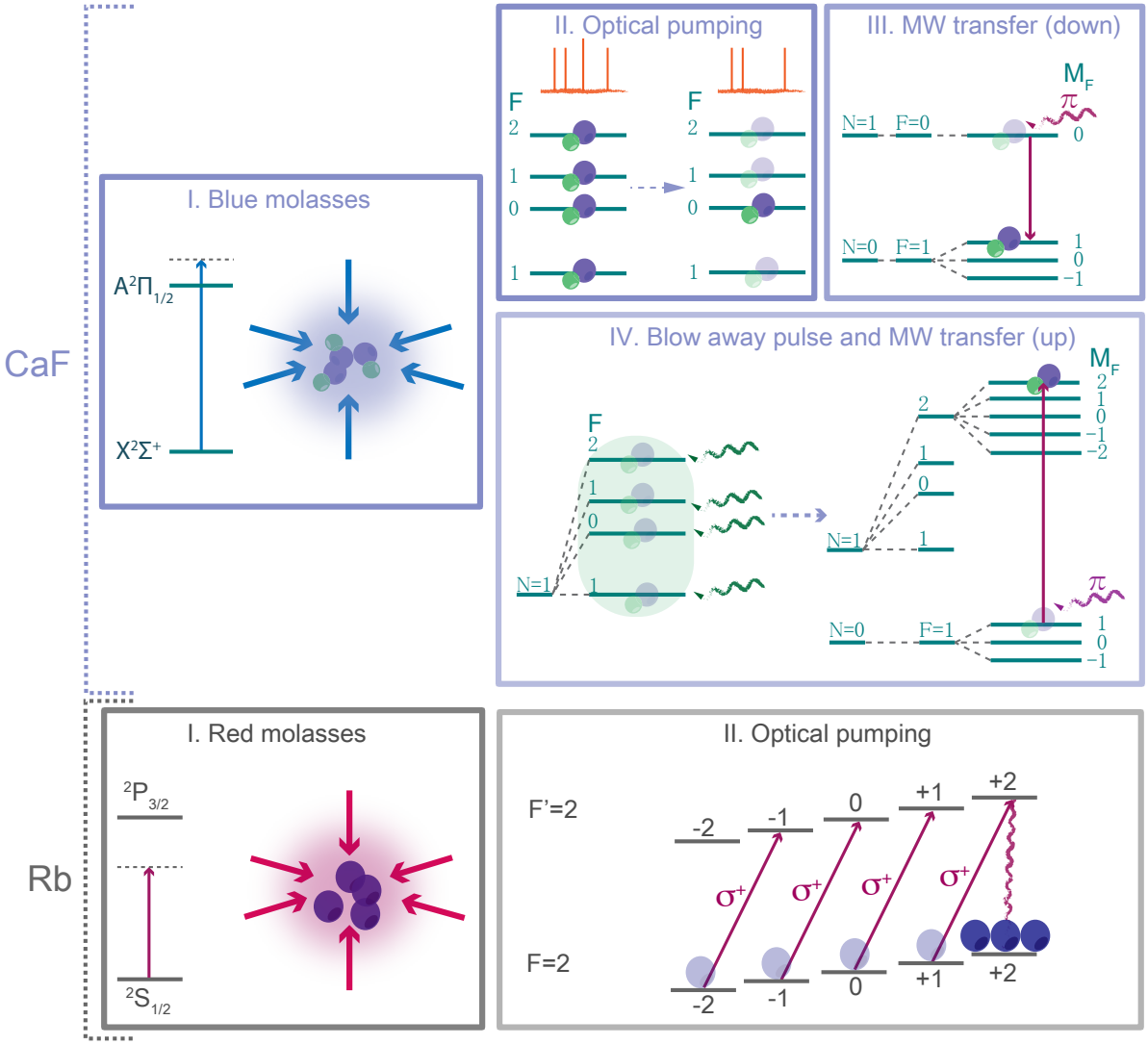

Figure 6.5: Preparing molecules and atoms for the magnetic trap. Molecules are cooled in a blue-detuned optical molasses while atoms are cooled in a red-detuned molasses. The quantum state of the molecule is prepared using a sequence of optical pumping and microwave transfer steps while atoms are pumped into the spin-stretched state just before turning the magnetic trap on.

6.2 Preparing molecules and atoms for magnetic trap

After loading the dual species MOT, molecules and atoms are cooled in an optical molasses and are prepared in magnetically trappable quantum states. Figure 6.5 illustrates these steps. Molecules are cooled in a blue detuned molasses for 12 ms[2], while atoms are cooled in a red-detuned molasses. Then, the molecules are optically pumped into the $|N = 1, F = 0, M_F = 0\rangle$ state followed by microwave transfer to the magnetically trappable $|N = 0, F = 1, M_F = +1\rangle$ state. Remaining molecules in the $N = 1$ state are blown

[2]It takes around 1 ms for the molecules to reach their final temperature in the blue molasses but they are held longer to allow the magnetic field due to induced Eddy currents after switching off the MOT coils to decay to the 1 mG level. This is important for the subsequent microwave transfer steps.

away using resonant light which drives the B-X transition. In the meantime, atoms are optically pumped into the spin stretched $|F = 2, M_F = +2\rangle$ state. At this point the magnetic trap may be turned on or an additional MW pulse may be applied to transfer molecules to either the $|N = 1, F = 2, M_F = +2\rangle$ or $|N = 1, F = 1, M_F = +1\rangle$ states, which are both magnetically trappable. When molecules are trapped in $N = 0$, a second MW pulse is necessary to bring the population back to $N = 1$ for recapturing into the MOT and imaging. The time the magnetic trap is turned on coincides with the end of the state preparation steps for both CaF and Rb. The rest of this section describes each of these steps in detail.

6.2.1 Blue-detuned molasses for molecules

Typical magnetic trap depths are on the order of a few mK, which is also the temperature of molecules in the dual species MOT. To load a large fraction of these molecules into the magnetic trap, the temperature must thus be lowered. The temperature of molecules is reduced by cooling them in a blue-detuned optical molasses prior to the quantum state preparation steps.

By lowering the $\mathcal{L}_{00}$ intensity in the MOT molecules cool to roughly 3 mK. Because the cooling light drives type-II transitions, a red detuning leads to sub-Doppler heating of molecules with low velocities, preventing further reduction in temperature. The situation is reversed for blue-detuned light: in this case the slower molecules become cooled while the faster ones are heated by Doppler forces.

After cooling in the red-detuned MOT, the cloud is released from the trap and the laser frequency is jumped up by an amount Δ_{BM}. The light is switched off during this jump for 1 ms to allow the AOM drive frequency to settle to the new value. The capture velocity of the blue-detuned molasses is higher for larger cooling light intensities and is in theory [167] on the order of several m/s. Using a sufficiently high laser intensity most molecules released from the MOT will thus experience the sub-Doppler cooling forces. To investigate how the temperature varies with laser intensity, the following experimental sequence is applied. After jumping the laser detuning, the molecules are held in the blue molasses at full intensity for a duration of 2 ms. The intensity is then ramped down to a new value over 2 ms and held at that value for 9 ms. The cloud is then released from the molasses and allowed to expand. Figure 6.6(a) shows a ballistic expansion measurement of a cloud released from a blue molasses which is optimized to give the lowest temperature. The external lab field is zeroed using a set of 3 Helmholtz coils for this and the following measurements. Molecules are imaged after a variable free expansion time by exposing them to the cooling light at full intensity using the MOT detuning. The geometric mean temperature of this cloud is found to be 53(3) μK.

In figure 6.6(b) the laser frequency is jumped up by a variable amount Δ_{BM} from the

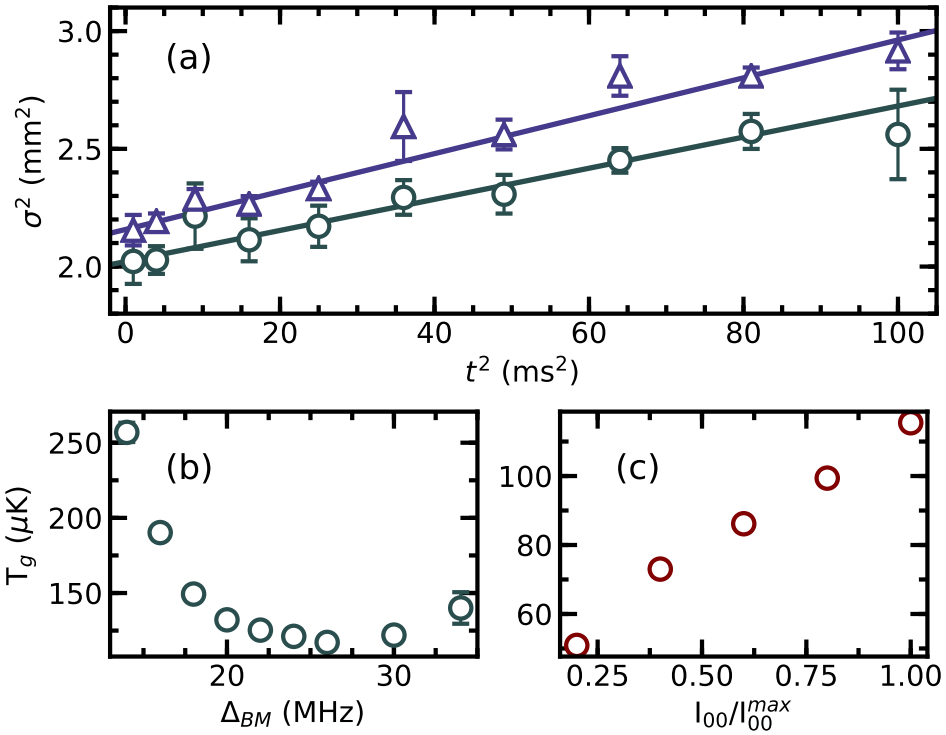

Figure 6.6: Cooling CaF in the blue-detuned molasses. (a) Ballistic expansion of the cloud released from the molasses along the radial (△) and axial (○) directions. The laser parameters are chosen to give the smallest cloud temperature in this measurement. A fit to a linear model gives radial and axial temperatures of 57(3) μK and 47(6) μK respectively. (b) The geometric mean temperature of the cloud for different laser frequencies at full intensity. Δ_{BM} is the amount by which the frequency is jumped upwards from the optimal MOT frequency. (c) The geometric mean temperature as a function of the total blue molasses intensity with $\Delta_{\mathrm{BM}} = 26$ MHz and $\mathrm{I}_{00}^{max} = 800$ mW·cm^{-2}.

optimal MOT frequency. The measurement is done using full $\mathcal{L}_{00}$ intensity for the blue molasses and shows a minimum in the geometric mean temperature at around $\Delta_{\mathrm{BM}} = 26$ MHz. Lowering the intensity of $\mathcal{L}_{00}$ should cool the molecules further because heating due to spontaneous scattering and sub-Doppler effects are reduced. Figure 6.6(c) shows how the temperature varies with laser intensity. Indeed, the molecules cool down further and the minimum temperature is reached at an intensity of 150 mW·cm^{-2} at the cost of losing a substantial number of molecules. Measurements of temperature using lower intensity cooling light are difficult because of the rather mysterious sharp drop in signal.

Loss of molecules in the blue molasses

Figure 6.7(a) shows how the number of molecules remaining after cooling in the blue molasses varies with the cooling laser intensity. A sharp drop in the number of molecules occurs for intensities lower than $0.1\mathrm{I}_{00}^{max}$ and 80 % are lost after holding in a molasses at an intensity of $0.2\mathrm{I}_{00}^{max}$. Because the capture velocity of the molasses is reduced at lower

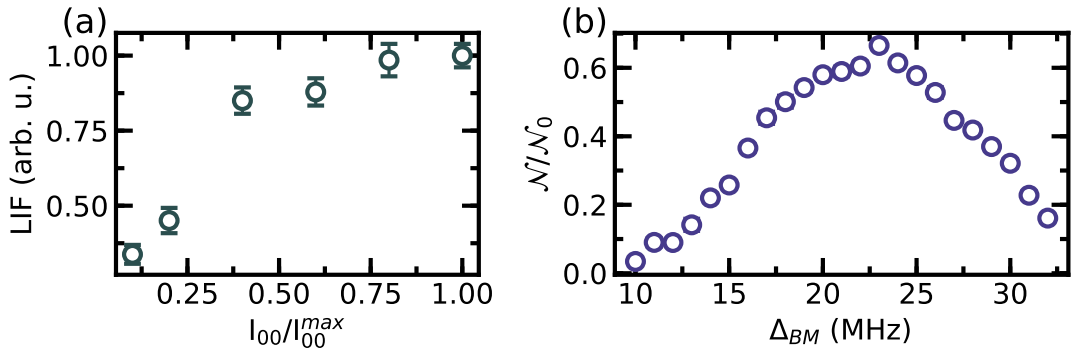

Figure 6.7: Loss of molecules in the blue-detuned molasses. (a) The LIF collected from molecules after 1 ms of free expansion for various molasses intensities. (b) Fraction of molecules recaptured into the MOT after the blue molasses as a function of the laser frequency used to cool the cloud.

intensities it is reasonable to expect that the faster molecules simply do not have sufficient time to cool and are lost. To investigate this, the laser intensity is ramped down more slowly or gradually stepped down. In both cases the observed loss in molecule number is similar.

Figure 6.7(b) shows how the fraction of molecules recaptured into the MOT varies with Δ_{BM}. The loss is minimized at laser detunings which also cool the cloud to the lowest temperatures. Still, only 60 % of the molecules remain. Given the experimental sequence length to lower the temperature of the cloud is 30 ms, the cloud lifetime which would be consistent with the observed loss is only 60 ms. The lifetime of the MOT at full intensity is above 80 ms while at $0.2\mathrm{I}_{00}^{max}$ it is around 150 ms. Although the lifetime of the molecules in the blue molasses was not measured explicitly, it is reasonable to conclude that it is significantly smaller than in the MOT.

It was noticed on several occasions that the temperature obtained after cooling in the molasses is particularly sensitive to the laser beam alignment. Similarly, the loss out of the molasses may be sensitive to alignment and more so at lower cooling light intensities. The present optical setup makes it extremely challenging to ensure good intensity balance between the counter-propagating beams. Provided that in the future lasers with higher output power will be available, it will be possible to make a trap using 3 independent laser beams and have much better control over the intensity balance.

Because a temperature of 100 μK is low enough to load the cloud into the magnetic trap and no signal may be spared, for measurements described in the rest of this work a blue molasses at full intensity is used.

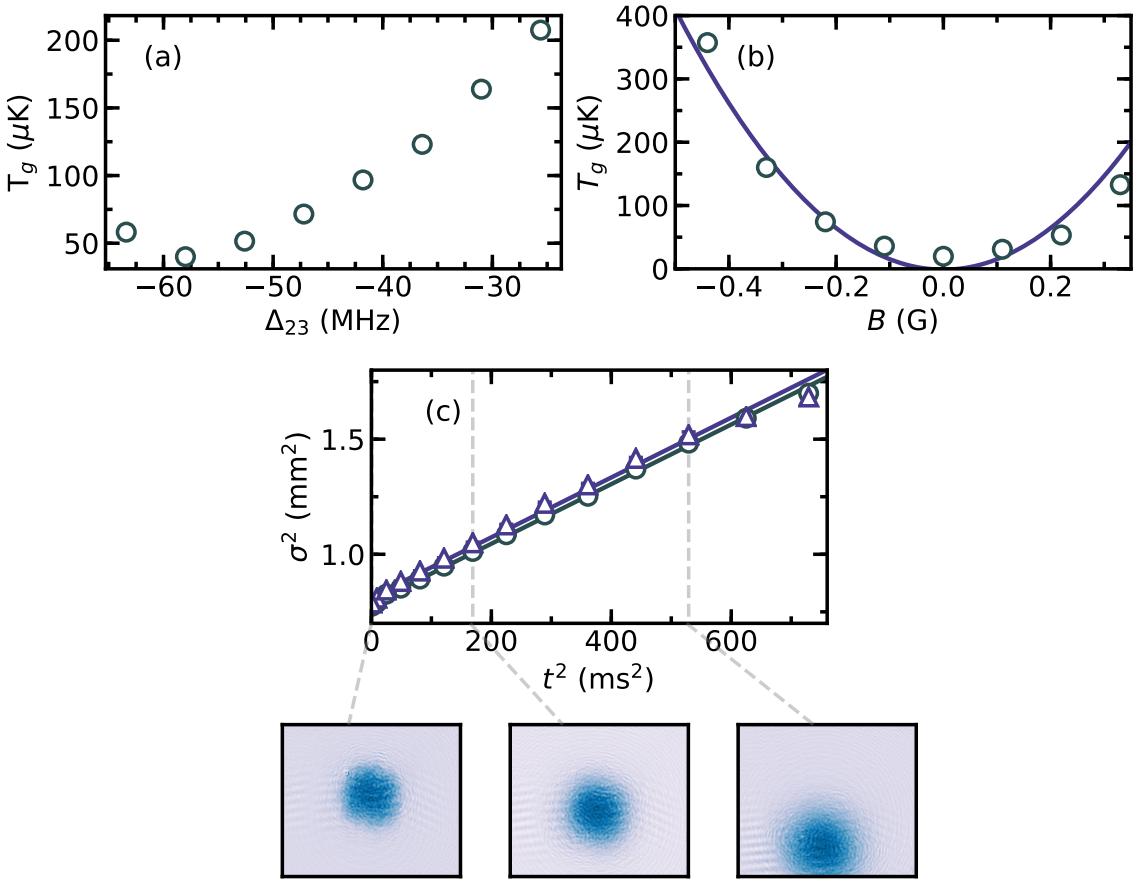

Figure 6.8: (a) Rb cloud temperature as a function of the cooling laser end frequency detuning. (b) Temperature dependence on magnetic field applied along the $z-$axis with the line a fit to the quadratic model described in the main text. (c) Ballistic expansion of the coldest cloud along the radial (△) and axial (○) directions, which was cooled in an optical molasses at zero magnetic field. The bottom three images are absorption images of the cloud after various expansion times, indicated by the dashed lines.

6.2.2 Red-detuned molasses for atoms

After switching off the MOT the detuning of Rb cooling light is linearly ramped down further to the red over 10 ms. Figure 6.8(a) shows how the temperature of the Rb cloud varies as a function of the final frequency detuning. As discussed in section 2.2.4, the temperature of the cloud is reduced for a larger detuning due to a reduction of the spontaneous scattering rate. In addition to ramping down the frequency detuning, the cooling light intensity is ramped down by an order of magnitude to further reduce heating due to spontaneous scattering. The lowest temperature is obtained using a laser detuning of 60 MHz and is equal to 40(1) μK.

The red molasses was optimized in the presence of a 200 mG applied bias field used for the subsequent quantum state preparation steps. This field is applied along the $y-$axis. Zeroing the field at the position of the atoms allows to reach even colder temperatures. Figure 6.8(b) shows how the temperature varies with magnetic field. In this experiment

the field components along x and y are cancelled while the z component is varied using shim coils. The presence of a magnetic field leads to Larmor precession of the atomic state. If the precession period, $T = h/\mu_B B$, is comparable to the time $t = \lambda/v$ it takes for an atom with velocity v to move along one period λ of the polarization gradient,[3] then sub-Doppler cooling will become ineffective. The mean velocity for which sub-Doppler cooling becomes inefficient then amounts to $v \approx \mu_B B\lambda/h$ and is equivalent to a temperature of $T \approx \frac{m}{3k_B}\left(\frac{\mu_B \lambda B}{h}\right)^2$. Based on these considerations, the temperature of the cloud will be a quadratic function of the magnetic field, with a coefficient of about 4200 $\mu\mathrm{K}\cdot\mathrm{G}^{-2}$. The data of figure 6.8(b) are fit to $T = aB^2$ and gives $a = 1650$ $\mu\mathrm{K}\cdot\mathrm{G}^{-2}$ as the temperature sensitivity to the magnetic field. In practice, it is found that the sensitivity to the magnetic field also depends on the direction of the field. This is about 2.5 times smaller than the rough estimate made above. The lowest measured temperature of $T = 13.6(1)$ μK coincides with the stray fields being cancelled in all three dimensions. Figure 6.8(c) shows the ballistic expansion measurement corresponding to this ultracold cloud together with absorption images at three different free expansion times.

6.3 Sate preparation of CaF

Following the blue molasses step, molecules are distributed over all of the 12 Zeeman sub-levels in the $\nu = 0$ and $\nu = 1$ vibrational states. The first step to purify the sample of molecules is to optically pump them into the $|N = 1, F = 0, M_F = 0\rangle$ state. The $\mathcal{L}_{00}^{\mathrm{C}}$ light is reduced to around 1 % of the initial value and the RF power to the EOM which generates the frequency sidebands is increased to extinguish the carrier. The carrier addresses the $F = 0$ hyperfine component thus the absence of it forces most molecules to be rapidly pumped into the $F = 0$ state. It is found that it takes less than 100 μs for the population in $F = 0$ to reach a steady state. The efficiency of optical pumping is found using microwave (MW) spectroscopy as described in the following section.

6.3.1 Microwave spectroscopy of CaF

Transitions between the $N = 1$ and $N = 0$ states are driven using a MW source. The output of a MW synthesizer (*Gigatronics* 7100) is passed to a frequency doubler (*Pasternack* PE8603) via a fast switch (*Analog Devices* HMC641ALC4) and the signal is coupled to free space via a microwave horn (*Pasternack* PE9853/SF-15 15), positioned in front of

[3] In the molasses the counter-propagating beams have opposite circular polarizations. When the counter-propagating beams have the same intensity, the superposition of all 6 beams leads to a polarization gradient which is linear everywhere but rotates with a period of λ. In the more general case, for non-equal intensities, the polarization is elliptical and has the same ellipticity everywhere but also rotates with a period of λ.

a vacuum view port. The polarization of the MW field at the position of the molecule cloud is poorly defined and it is found that all, $\Delta M_F = 0, \pm 1$, transitions may be driven.

The fraction of molecules remaining in the $N = 1$ state after a MW pulse[4] is measured by recapturing them into the MOT and recording the LIF in the usual way. The number of molecules recaptured into the MOT after the MW pulse, $\mathcal{N}$, divided by the number of molecules captured into the MOT at the beginning of the experimental sequence, $\mathcal{N}_0$, is the fraction remaining. Normalizing the signal in such a way largely eliminates shot-to-shot fluctuations in the flux of molecules produced in the buffer gas source. Each image has an exposure time of 10 ms and this measurement method is used throughout the rest of this chapter.

Single pulse spectroscopy

First, the $|N = 1, F = 0, M_F = 0\rangle \rightarrow |N = 0, F = 1, M_F = 0\rangle$ transition is driven, which is insensitive to the magnetic field at the position of molecules. Figure 6.9(a) shows the number of molecules recaptured into the MOT as a function of MW frequency after a π-pulse. The measured line shape may be modelled using eq. 2.32. Setting the Rabi frequency to $\Omega = \pi/t_\pi$, the number of molecules recaptured into the MOT may be written as

$$\frac{\mathcal{N}(\omega - \omega_0, A_0, A)}{\mathcal{N}_0} = A_0 + \frac{A}{1 + \frac{(\omega-\omega_0)^2 t_\pi^2}{\pi^2}} \sin^2 \left(\frac{\left(\frac{\pi^2}{t_\pi^2} + (\omega - \omega_0)^2 \right)^{1/2} t_\pi}{2} \right) , \qquad (6.15)$$

where t_π is the duration of a π-pulse, A_0 is the fraction of molecules remaining when no microwaves are present and A is an amplitude. Setting $t_\pi = 70$ μs and fitting the model above to the data of figure 6.9(a) gives $A_0 = 0.54$, which is consistent with the combined loss of molecules due to the MOT lifetime and the observed losses in the blue molasses. The optical pumping efficiency may then be found by comparing A_0 with the number recaptured using resonant microwaves. It is found that the optical pumping efficiency is at least 50 %, assuming that the efficiency of the MW pulse is 100 %. The efficiency is limited by off-resonant scattering and imperfect extinction of the carrier which addresses the target $F = 0$ state. The duration of the π-pulse implies that the microwave power in the relevant field polarization is 256 nW $\cdot$ cm^{-2}.

Next, the magnetically sensitive $|N = 1, F = 0, M_F = 0\rangle \rightarrow |N = 0, F = 1, M_F = +1\rangle$ MW transition is driven. To reduce the sensitivity to stray magnetic fields this transition is driven with a somewhat shorter MW pulse of $t_\pi = 50$ μs, which leads to a broader line width. Figure 6.9(b) shows the measured line shape of this transition. Evidently, this pulse is less efficient than the one which drives the magnetically insensitive transition

[4] Only molecules which are in the $N = 1$ state are resonant with the trap light while molecules in the $N = 0$ state are > 20 GHz off-resonance and do not contribute to the detected LIF signal.

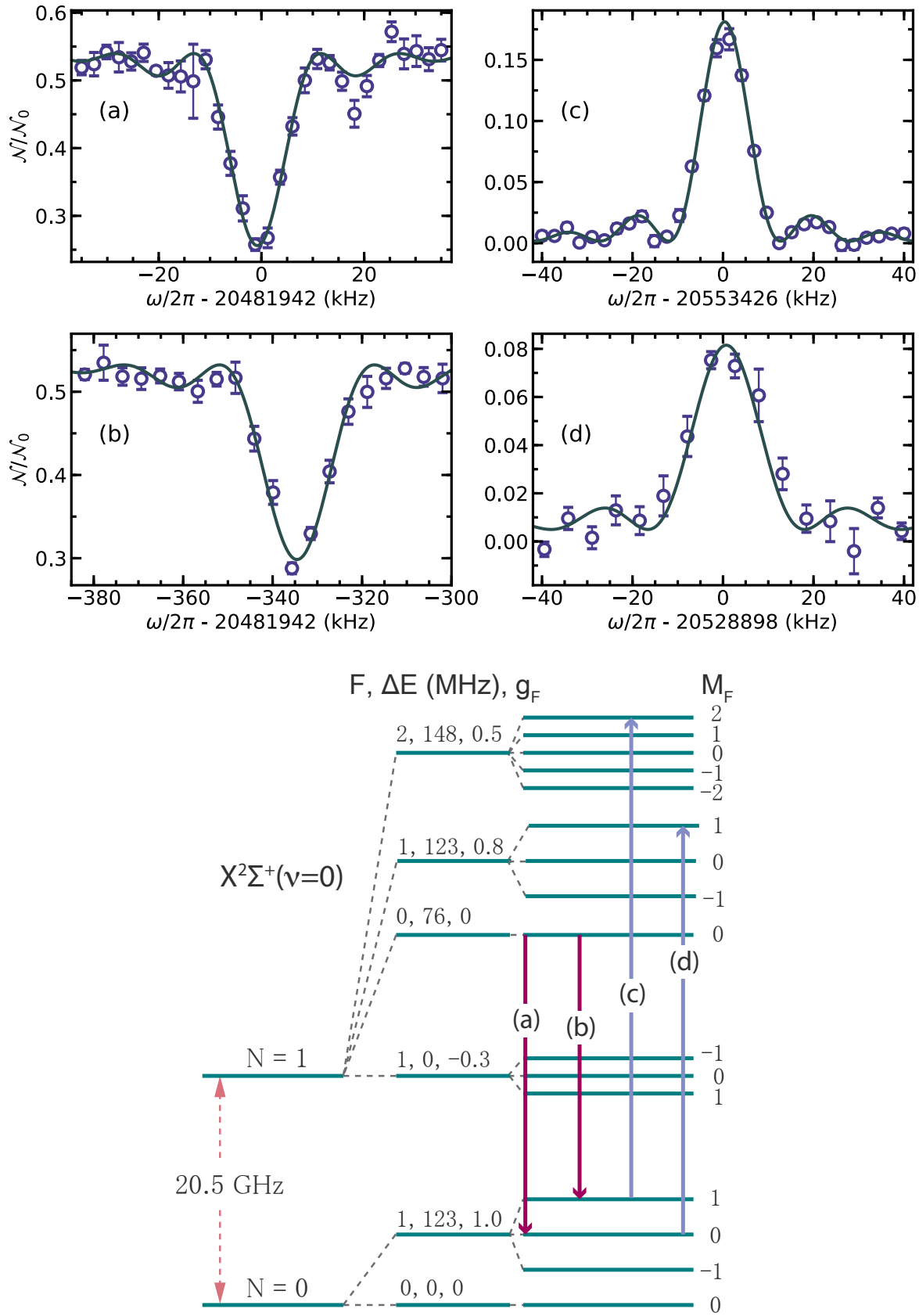

Figure 6.9: Microwave transitions between the $N = 1$ and $N = 0$ rotational levels. (a,b) Depletion of molecules in the $|N = 1, F = 0, M_F = 0\rangle$ state as a function of microwave frequency. (c,d) Driving the population back into the $N = 1$ state. Solid lines are fits to the Rabi lineshape described in the main text. The diagram below shows the detailed hyperfine structure of the $N = 1$ and $N = 0$ states and indicates which transitions are driven. Each point is an average over at least 7 experiment runs.

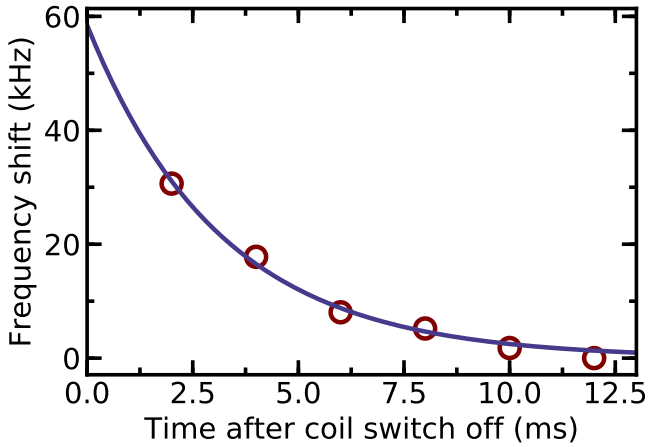

Figure 6.10: Decay of stray magnetic fields measured using microwave spectroscopy. The shift in the transition resonance frequency is plotted as a function of the time after switching off the MOT coils. Solid line is a fit to an exponential decay model.

and produces a line shape which is slightly broadened for the given pulse length. The magnetic field at the position of molecules is inferred from the shift in resonance frequency and is equal to 240 mG in this case. To check whether the magnetic field due to induced Eddy currents after switching off the MOT coils has decayed to sufficiently small values, the MW line shape is measured at different delay times after switching off the coils. In figure 6.10 the positions of the depletion dips relative to the position of the dip recorded 12 ms after the coils are switched off are plotted against the delay time. Between 10 ms and 12 ms the dip moves by 1.8 kHz, which corresponds to a change in magnetic field of only 1.3 mG. An exponential fit to these data gives a $1/e$ decay time of 3.1 ms.

Two pulse spectroscopy

Following the first MW pulse, a substantial number of molecules remain in the $N = 1$ rotational level, some of which are also magnetically trappable. To purify this sample, the remaining molecules are pushed away by turning on the B-X light for 3 ms. The MW pulse tuned to drive the $|N = 0, F = 1, M_F = +1\rangle \rightarrow |N = 1, F = 2, M_F = +2\rangle$ transition is applied immediately after, in free space. This transition is magnetically insensitive[5] and may be driven while the molecules are magnetically trapped. Figure 6.9(c) shows the fraction of molecules recaptured into the MOT following the second MW pulse of a $t_\pi = 70$ μs duration as a function of the MW field frequency. The baseline is consistent with zero, indicating that molecules remaining in $N = 1$ after the first pulse are all removed with the B-X light. The maximum fraction of molecules driven up to the $N = 1$ state is $\mathcal{N}/\mathcal{N}_0 = 0.18$, which implies a second MW pulse efficiency of 72 %. It is found

[5]The magnetic field sensitivity of this transition was previously measured in our group and was found to be $\Delta\mu/h = -104(4)$ Hz $\cdot$ G^{-1} [168].

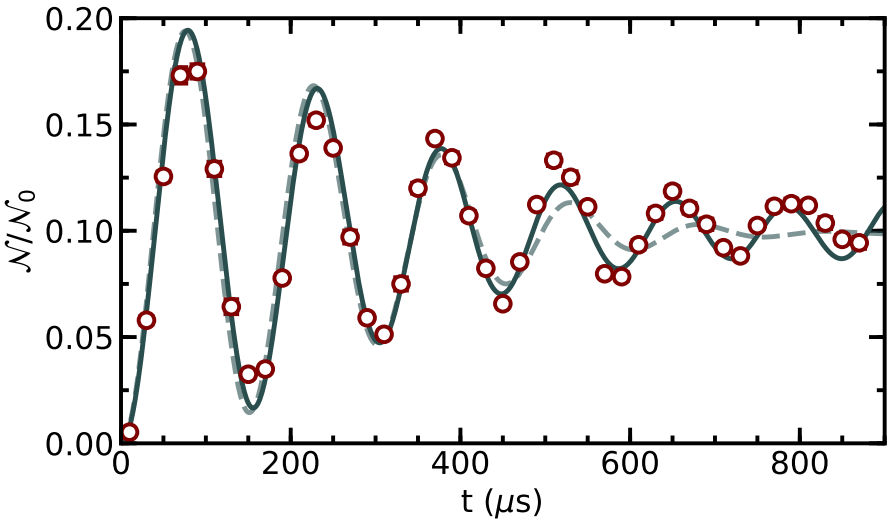

Figure 6.11: Rabi flopping on the $|0,1,+1\rangle \longleftrightarrow |1,2,+2\rangle$ transition. The dashed line is a fit to the model described in the main text. The solid line is a fit to a model which also takes into account the expansion and motion of the cloud during the microwave pulse.

that this transition may also be driven with similar efficiency while the magnetic trap is turned on at an axial field gradient of $b_z = 30$ G/cm.

Figure 6.11 shows Rabi flops on the $|0,1,+1\rangle \longleftrightarrow |1,2,+2\rangle$ transition. The oscillations have a coherence time of roughly 500 μs and are limited primarily by microwave field gradients. Reflections of the MW field from the chamber walls set up a standing wave with a period of $\lambda/2 \approx 7.3$ mm, which is comparable to the size of the molecule cloud. Molecules in different parts of the spatial distribution will thus experience different Rabi frequencies. To take this into account, the Rabi oscillations are averaged over a Gaussian spread of Rabi frequencies and the data are fit to the following model

$$\frac{\mathcal{N}(t, A_0, A, \Delta\Omega, \Omega)}{\mathcal{N}_0} = A_0 + \frac{1}{\sqrt{2\pi}\Delta\Omega} \int_{-\infty}^{+\infty} A\rho_{11}(t,\Omega) \exp\left(-\frac{(\Omega-\Omega_0)^2}{2(\Delta\Omega)^2}\right) d\Omega \ , \quad (6.16)$$

where $\Delta\Omega$ is the spread in Rabi frequencies. The fit is improved when a linear time dependence is added to Ω_0 and a quadratic time dependence is added to $\Delta\Omega$. The former accounts for motion of the cloud centre during the MW pulse while the later accounts for the cloud expansion. The cloud may be moving after being released from the blue molasses if the molasses beam intensities are not perfectly balanced while the expansion is due to the finite cloud temperature of ~ 100 μK. Fits using both models give $\Delta\Omega/\Omega_0 \approx 0.1$, which is reasonable considering that the cloud radius is around ~ 1.5 mm. On the other hand, the best fit parameter which accounts for the cloud expansion is equivalent to a fractional change in the frequency spread of $\Delta\Omega'/\Delta\Omega \approx 0.33$ for a $t = 800$ μs pulse. This is far greater than the fractional change due to the ballistic expansion of a 100 μK cloud within this time and suggests the presence of other mechanisms of decoherence at longer MW pulse durations.

Finally, the population may also be transferred to the $|N = 1, F = 1, M_F = +1\rangle$ state following the first MW pulse, which transfers the population to $|N = 0, F = 1, M_F = 0\rangle$. Figure 6.9(d) shows the measured line shape corresponding to the transition between the two states. This transition is magnetically sensitive and leads to a substantially smaller MW pulse efficiency.

6.4 State preparation of Rb

After cooling in the red-detuned molasses, Rb atoms are distributed over the five Zeeman sub-levels in the $F = 2$ state. Provided the state distribution is uniform, only 20 % of these atoms will be captured by the magnetic trap when the axial field gradient is $b_z = 30$ G/cm. To prepare more atoms in the $|F = 2, M_F = +2\rangle$ state, they are optically pumped using a laser beam which is tuned to drive the $F = 2 \rightarrow F' = 2$ transition. The optical pumping beam is combined with the molecule slowing light on a dichroic mirror and propagates along the same direction. It has an intensity of $\sim 0.5 I_s$. A magnetic field of 200 mG applied along the direction of propagation sets the quantization axis. The beam is σ^+ polarized using a combination of $\lambda/4$ and $\lambda/2$ wave plates. This provides full control of the polarization and compensation of the additional phase retardation imparted by the dichroic mirror in transmission. The polarization is analysed using a polarimeter just before the beam enters the vacuum chamber to confirm that it has σ^+ polarization. Provided the beam indeed drives only σ^+ transitions, the atoms will reach the $|F = 2, M_F = +2\rangle$ state after scattering a few photons on average. This state is dark to the pumping light thus photon scattering ceases once it is reached. It is important to note here that optical pumping on this transition must be done in the presence of repumping light since atoms excited to the $F' = 2$ state may spontaneously decay directly to $F = 1$. In the experiment, the repump light used for the MOT is kept on during the time it takes to optically pump the atoms.

Optical pumping time

To estimate the optical pumping efficiency, the number of atoms captured into the magnetic trap is measured following the optical pumping pulse. The efficiency is defined here as the number of atoms in the magnetic trap, $\mathcal{N}_{\mathrm{MQT}}$, divided by the number of atoms in the MOT, $\mathcal{N}_{\mathrm{MOT}}$. To measure $\mathcal{N}_{\mathrm{MQT}}$, the atoms are held in the trap for 300 ms before being released and exposed to the absorption imaging beam.

Figure 6.12(a) shows the optical pumping efficiency, η_{OP}, as a function of pumping duration. Without optical pumping, less than 10 % of atoms are captured into the magnetic trap. This suggests that following cooling in the optical molasses atoms are not equally distributed over the five Zeeman levels. An exponential model fit to these

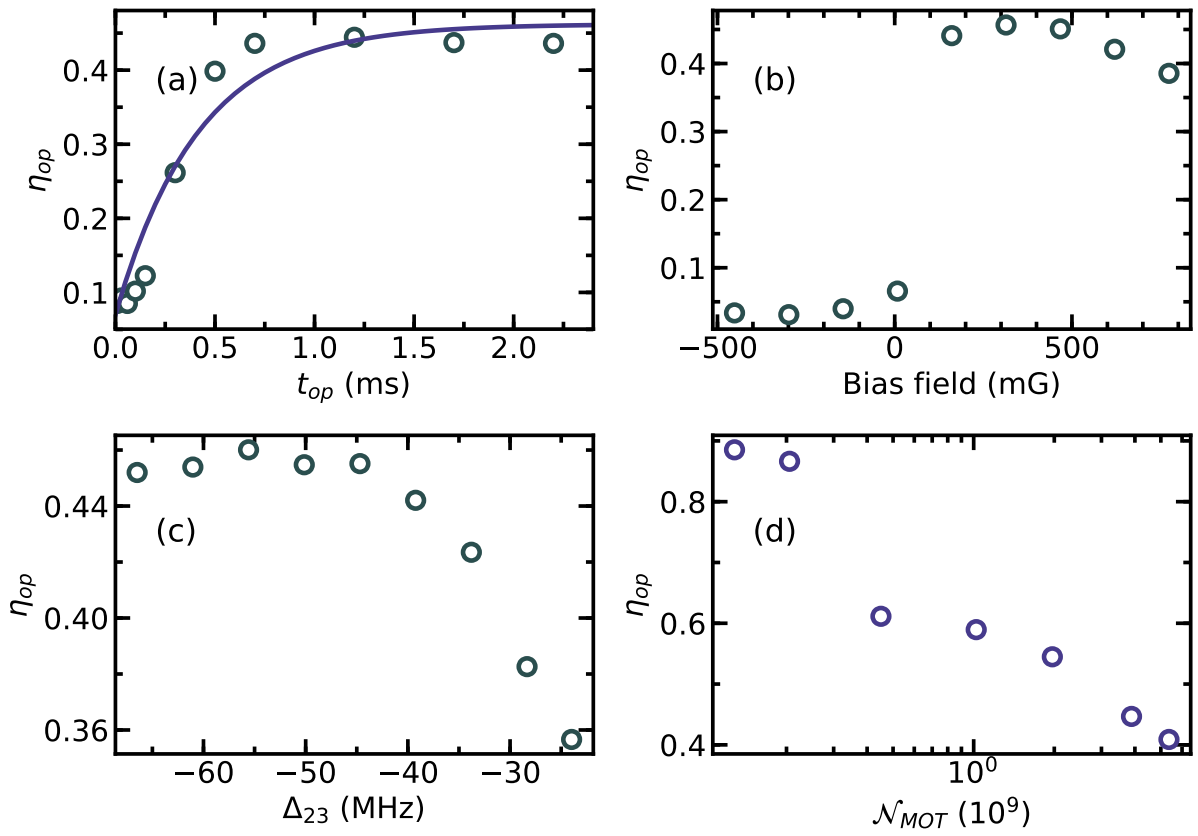

Figure 6.12: Optical pumping of Rb atoms. (a) Optical pumping efficiency, $\eta_{\rm op} = \mathcal{N}_{\rm MQT}/\mathcal{N}_{\rm MQT}$, as a function of pumping time. Solid line is a fit to an exponential mode. (b) $\eta_{\rm op}$ as a function of the magnitude of a magnetic field applied along the optical pumping beam direction. (c) $\eta_{\rm op}$ as a function of the final cooling light frequency detuning in the optical molasses. (d) $\eta_{\rm op}$ for different initial atom numbers loaded into the MOT. In (a-c) the MOT was loaded with $3 \cdot 10^9$ atoms.

data gives a pumping time of 0.42 ms. The average scattering cross section for atoms distributed equally over the five levels is $\frac{2}{5}\sigma_0$. Since after scattering a photon, an atom may decay to the $F = 1$ state with equal probability the cross section is reduced to $\sim \frac{1}{5}\sigma_0$. Thus, during the observed optical pumping time, atoms will scatter several thousand photons from an optical pumping beam which has an intensity of $0.5 I_{\rm s}$. This is clearly many more than are required for an atom to reach the dark $|F = 2, M_F = +2\rangle$ state. The slow optical pumping time scale is attributed to the large optical thickness of the cloud, which leads to photon rescattering. Because each rescattered photon has a random polarization, even an atom which ends up in the dark state may be depolarized while the optical pumping light is still present. Reducing the pump beam intensity by an order of magnitude gives the same $\eta_{\rm op}$ using a very similar pumping duration.

Direction and magnitude of bias field for optical pumping

Figure 6.12(b) shows how η_{OP} changes as the magnitude of the quantization field is varied. The fields along the other two dimensions are cancelled using the calibrated values from MW spectroscopy. For negative values of the field, σ^- transitions are driven which pump the atoms into the untrappable $|F = 2, M_F = -2\rangle$ state and reduce the number of atoms captured into the trap to 3.5 %. When the field crosses zero and is positive, atoms are pumped into the $|F = 2, M_F = +2\rangle$ state. In the experiment a bias field of 200 mG is used.

Trap depth and initial temperature of the cloud

The magnetic trap potential reaches its maximum value at a radial distance of $\Delta r = 2.2$ cm. For an atom in the $|2, 2\rangle$ state, the trap depth, in temperature units, is approximately $\mu_{\mathrm{B}} b_r \Delta r/k = 1.5$ mK. Any atoms remaining in the $|F = 2, M_F = +1\rangle$ state after the optical pumping pulse are not trapped because the axial magnetic field gradient does not provide a sufficient force to levitate them against gravity.

Figure 6.12(c) shows how η_{op} depends on the temperature of the cloud before the trap is turned on. The range of final cooling light detunings for the molasses corresponds to a range of temperatures from 40 μK to 210 μK (see section 6.2.2). As the temperature of the cloud is reduced, the pumping efficiency changes from $\eta_{\mathrm{op}} = 0.36$ to $\eta_{\mathrm{op}} = 0.45$. For the range of temperatures explored here, the mean velocity of atoms is below the trap depth. Because optical pumping heats the atoms, starting with a lower temperature increases the number of photon scattering events required to push the atoms above the capture velocity of the trap and hence increases η_{op}.

Pumping efficiency versus atom number

Figure 6.12(d) confirms the hypothesis that photon rescattering limits the achievable η_{op}. As the number of atoms in the MOT is increased so is the optical depth. It thus becomes harder to pump more atoms into the dark state due to the depolarizing effect of photon rescattering. For an atom number of $\sim 10^8$, the efficiency increases to $\eta_{\mathrm{op}} = 0.88$.

It is worth mentioning another useful method for preparing atoms for the magnetic trap, which could be used in future experiments. By simply turning off the repump light close to the end of the optical molasses phase, most atoms will decay to the $F = 1$ state due to off-resonant scattering. Around 1/3 of these atoms should accumulate in the $|F = 1, M_F = -1\rangle$ state, which is magnetically trappable. If in addition atoms are transferred to a DARK SPOT MOT [157] before loading the magnetic trap, the number density of the cloud may be increased substantially. On the other hand, the magnetic moment of the $|F = 1, M_F = -1\rangle$ state is two times smaller and thus a two times larger

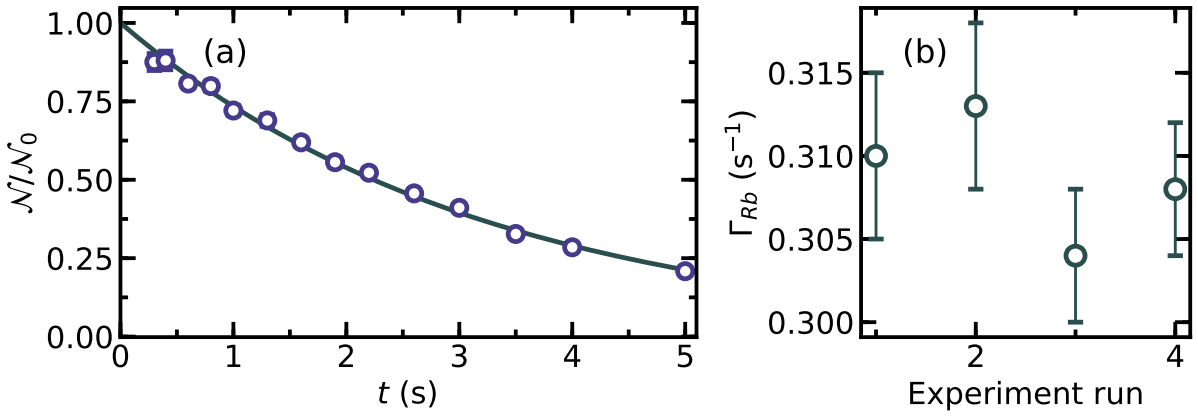

Figure 6.13: (a) Natural loss rate of Rb in the magnetic trap. Line is a fit to single exponential decay model. Each point is an average over 5 experiment runs and error bars are the standard errors of the mean values. (b) Four measurements of Γ_{Rb} over 40 minutes. The error bars correspond to the fitting errors.

field gradient should be used to obtain the same cloud properties as when trapping atom which are prepared in the $|F = 2, M_F = +2\rangle$ state.

6.5 Loss rate measurements

With the tools for controlling the quantum states of molecules and atoms at hand, state selective inelastic collisions in the trap may be studied. Because the atom density greatly exceeds that of the molecules, only atom-induced losses of molecules from the trap could be investigated in this work. The experimental method is the same as used for studying collisions in the dual species MOT: the trap loss rate of CaF is measured in the presence and absence of atoms, then the two are compared to extract the Rb induced loss rate of CaF. Measuring the spatial distributions of each cloud determines the density overlap and the loss rate coefficient.

To measure a molecule loss curve in the presence of Rb atoms, the molecules are held in the trap for a variable time and then recaptured back into the MOT. The LIF from the MOT is collected for 10 ms to measure the number of molecules remaining, $\mathcal{N}_{\mathrm{CaF}}(t)$. The signal is normalized to the number of molecules initially captured into the MOT to get the fraction of molecules remaining, $r_{\mathrm{CaF}}(t) = \mathcal{N}_{\mathrm{CaF}}(t)/\mathcal{N}_{\mathrm{CaF}}^{\mathrm{MOT}}$. After an image to measure $\mathcal{N}_{\mathrm{CaF}}(t)$ is acquired, the quadrupole field is switched off and an absorption image of the atom cloud is acquired 1 ms later. Figure 6.13(a) shows an example measurement of how the atom number decays in the trap. The loss is attributed to collisions with background gas and the data fit well to a single exponential decay model. In this case the measured loss rate[6] is $\Gamma_{\mathrm{Rb}} = 0.310(5)$ s^{-1}. The background pressure and its variation with time may

[6]It is worth noting here that loss rates below $\Gamma_{\mathrm{Rb}} = 0.1$ s^{-1} were measured earlier in this apparatus. The loss has increased due to loss of UHV due to several power outages in the lab, following which the

be affected by the He gas flow originating from the source chamber and the outgassing from the MOT coils. In figure 6.13(b) the results of four measurements of Γ_{Rb} are shown. These measurements were carried out over a total time of ~ 40 minutes and indicate no significant variation in Γ_{Rb}. Thus it may be assumed that the contributions from He gas and potential outgassing from the MOT coils to the background pressure do not vary over time and thus do not affect the measurements. In addition, no change in the background pressure is registered by the ion gauge throughout these measurements.

6.5.1 Loss rate without atoms

Molecules are lost from the magnetic trap due to various different contributions which are discussed and quantified below.

Loss due to vibrational and rotational excitations

In addition to loss due to collisions with background gas particles, the molecules are lost due to vibrational excitation by thermal radiation. The thermal radiation energy density spectrum may be modelled using the blackbody radiation spectrum at temperature T. The loss rate due to thermal excitation [169, 170] from $\nu = 0$ to $\nu = 1$ is given by

$$\Gamma_{\mathrm{vib}} = \frac{\omega_{01}^3 d_{01}^2}{3\pi\epsilon_0 \hbar c^3} \frac{1}{e^{\frac{\hbar\omega_{01}}{k_{\mathrm{B}}T}} - 1} \,, \tag{6.17}$$

where ω_{01} is the spacing between the first two vibrational levels and

$$d_{01} = \sqrt{\frac{\hbar}{2m_r\omega_{01}}} \left[\frac{d\mu}{dR}\right]_{R=R_e} \,, \tag{6.18}$$

is the transition dipole moment expressed in terms of the gradient of the dipole moment evaluated at the equilibrium nuclear separation and the reduced mass m_r. Using the value from [170] for the gradient of the dipole moment for CaF, the loss rate is $\Gamma_{\mathrm{vib}} = 0.21\ \mathrm{s}^{-1}$ at a temperature of $T = 293$ K. A similar loss rate was measured experimentally when the background pressure in this apparatus was below $5 \cdot 10^{-10}$ mbar. The loss rate increases by ~ 40 % when the surrounding surface temperature is increased by 100 K. It is also noted here that loss due to rotational excitation by thermal radiation is negligible [170].

Loss due to Majorana transitions

Atoms or molecules passing through regions of space where the magnetic field is close to zero may undergo a spin flip (Majorana) transition and thus be lost from the trap. These transitions become important when the Larmor precession frequency becomes similar or lower than the rate of change of the field direction [171]. For atoms moving with velocity,

vacuum system was not baked again and thus the background pressure was ~ 3 times higher.

v, the width of the region where loss occurs is $\sim (v\hbar/\mu_B b)^{1/2}$. The loss rate is proportional to the rate at which atoms enter this volume and is given by

$$\Gamma_{\text{Majorana}} = a \left(\frac{\mu_B b}{k_B T} \right)^2 \frac{\hbar}{m} , \tag{6.19}$$

where a is a proportionality constant and b is the magnetic field gradient. For ^{87}Rb atoms the measured constant of proportionality $a = 0.9$ [172]. For atoms at a temperature of $T = 70$ μK trapped using a field gradient of 0.3 T/m, the loss rate is $5.4 \cdot 10^{-3}$ s^{-1} and is thus negligible compared to loss due to collisions with background gas particles. At a temperature of 10 μK the loss rate rises dramatically to 0.27 s^{-1} and spin flip transitions dominate the overall loss. Taking $a = 1$, the loss rate of CaF molecule at a temperature of $T = 170$ μK is only $1.5 \cdot 10^{-3}$ s^{-1}.

6.5.2 Loss rate with atoms

In the presence of atoms, the loss of molecules out of the trap is described by the following rate equation

$$\dot{r}_{\text{CaF}}(t) = -\left(\Gamma^0_{\text{CaF}} + \Gamma_{\text{Rb-CaF}} e^{-\Gamma_{\text{Rb}} t}\right) r_{\text{CaF}}(t) , \tag{6.20}$$

where $r_{\text{CaF}}(t) = N_{\text{CaF}}(t)/N^{\text{MOT}}_{\text{CaF}}$ is the fraction of molecules, $N_{\text{CaF}}(t)$, remaining in the trap, both in the presence and absence of atoms, normalized to the number of molecules, $N^{\text{MOT}}_{\text{CaF}}$, initially captured into the MOT. Division by $N^{\text{MOT}}_{\text{CaF}}$ makes the measurement immune to shot-to-shot fluctuation in the number of molecules captured into the MOT. Γ^0_{CaF} is the measured loss rate of molecules in the absence of atoms and $\Gamma_{\text{Rb-CaF}}$ is the atom-induced loss rate of molecules at $t = 0$. The exponential factor takes into account the decay in atom number, which occurs on the same timescale as the natural loss of molecules, Γ^0_{CaF}. The differential equation above has the solution

$$r_{\text{CaF}}(t) = r_{\text{CaF}}(0) \exp\left(-\Gamma^0_{\text{CaF}} t - \frac{\Gamma_{\text{Rb-CaF}}}{\Gamma_{\text{Rb}}} \left(1 - e^{-\Gamma_{\text{Rb}} t}\right) \right) . \tag{6.21}$$

Figure 6.14 shows example measurements of the loss rate of molecules in the absence and presence of atoms. In the absence of atoms the data fit well to a single exponential decay model with an estimated loss rate of $\Gamma^0_{\text{CaF}} = 0.35(1)$ s^{-1}. Using experimental estimates of Γ^0_{CaF} and Γ_{Rb}, the dual species data is fit to the model of eq. 6.21 with $r_{\text{CaF}}(0)$ and $\Gamma_{\text{Rb-CaF}}$ set as free parameters. For these data, at $t = 0$ there are $\mathcal{N}_{\text{Rb}} = 1.5 \cdot 10^9$ atoms at a peak density of $n_{\text{Rb}} = 5(1) \cdot 10^{10}$ cm^{-3} and the measured atom induced loss rate is $\Gamma_{\text{Rb-CaF}} = 0.368(38)$ s^{-1}. The statistical measurement uncertainties in the natural trap loss rates Γ_{Rb} and Γ^0_{CaF} are not taken into account here. A method which includes these uncertainties is described below.

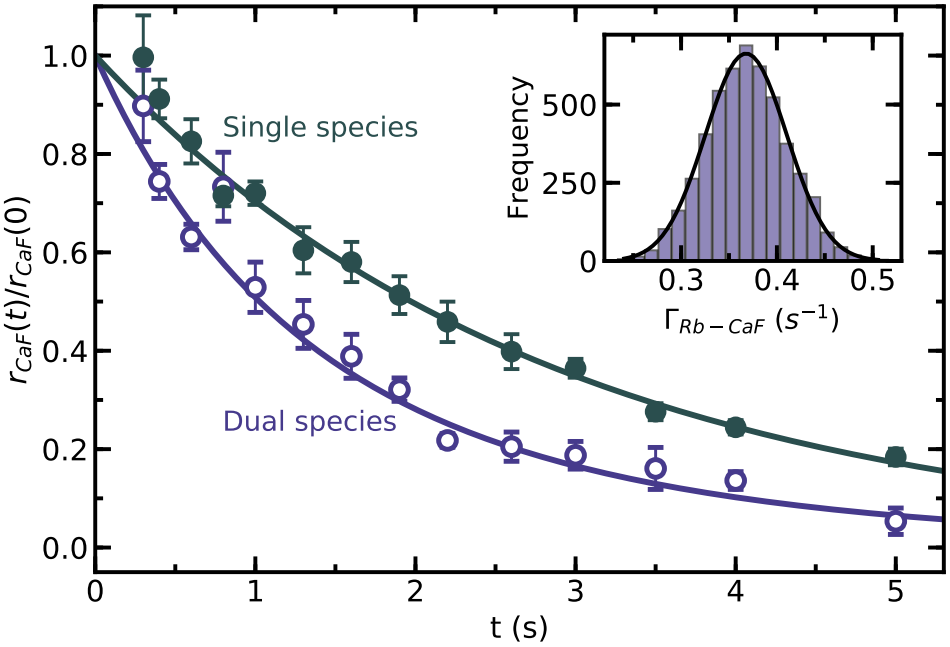

Figure 6.14: Loss of molecules prepared in the $|1, 2, +2\rangle$ state from the magnetic trap in the presence (○) and absence (●) of Rb atoms. The single species decay is modelled by a single exponential, while the dual species decay follows a double exponential decay model described in the main text. Each point is an average over 6 experiment runs and the error bars are the standard errors on the mean. The histogram shows the statistics of the re-sampling method used to estimate $\Gamma_{\text{Rb-CaF}}$ and the solid line is a fit to a normal distribution.

Estimating $\Gamma_{\text{Rb-CaF}}$ and the associated uncertainty

The values for Γ^0_{CaF} and Γ_{Rb} are measured separately and have their own associated statistical uncertainties. To account for these uncertainties a re-sampling technique is used. Values of $r_{\text{CaF}}(t)$ are drawn from the set of measured values randomly with replacement at each hold time t. For each of these random sets of values, Γ^0_{CaF} and Γ_{Rb} are drawn repeatedly from their measured distributions and the re-sampled data is then fit to the model of eq. 6.21. Repeating this procedure several thousand times gives a distribution of $\Gamma_{\text{Rb-CaF}}$ values. The distribution of estimates is shown in the inset of figure 6.14 together with a fit to a normal distribution. The mean and width of this distribution are the best estimate and the associated uncertainty, which for the data of figure 6.14 are $\Gamma_{\text{Rb-CaF}} = 0.368(44)$ s^{-1}. This method gives values for $\Gamma_{\text{Rb-CaF}}$ which are very similar to the ones obtained from a single fit to the measurements but lead to a slightly larger uncertainty since both measurement uncertainties in Γ^0_{CaF} and Γ_{Rb} are included. Because these uncertainties are small, they have a marginal effect.

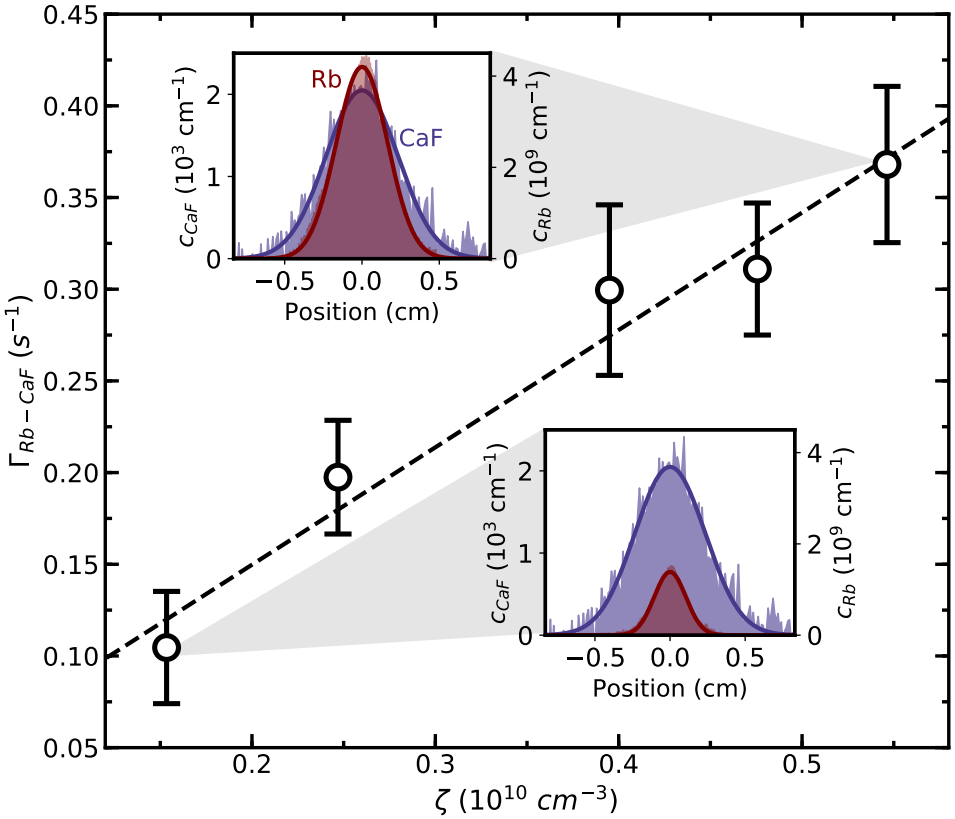

Figure 6.15: Atom-induced loss rate of molecules prepared in the $|1,2,+2\rangle$ state in the magnetic trap as a function of effective atom density. The line is a fit to a linear model. Insets show radial density distributions, $c_s = \int \mathcal{N}_s f_s(x,y,z)\, dydz$, of atoms and molecules for small and large values of the effective atom density, ζ.

6.5.3 Determining the loss rate coefficient

The loss rate coefficient k_2 corresponding to the observed atom-induced loss process is related to the measured $\Gamma_{\text{Rb-CaF}}$ by $\Gamma_{\text{Rb-CaF}} = k_2\zeta$, with

$$\zeta = \mathcal{N}_{\text{Rb}}(0) \int f_{\text{Rb}}(\vec{r}) f_{\text{CaF}}(\vec{r})\; d^3\vec{r}\,, \tag{6.22}$$

an effective density of Rb which accounts for the spatial overlap between the two clouds. To obtain ζ in the experiment, the number density of atoms in the trap is inferred from an absorption image (see section 3.8) while the spatial distribution of molecules is measured by releasing the cloud from the trap and acquiring a fluorescence image (see section 3.7.1) using an exposure time of 1 ms. Because the MOT coils are turned off for this measurement and there is no trapping force, the estimate of the size is affected negligibly even when using this rather long exposure time. For molecules in the $|1,2,+2\rangle$ state the measured cloud size in the radial direction is 2.30(7) mm, which is in excellent agreement with the result of numerical trajectory simulations described in the beginning of this chapter.

The loss rate measurement of CaF is repeated for a set of 5 different Rb atom numbers loaded into the trap. The natural trap loss measurement is also repeated multiple times, in a random order and is found to vary negligibly. As $\mathcal{N}_{\text{Rb}}$ is increased, the effective

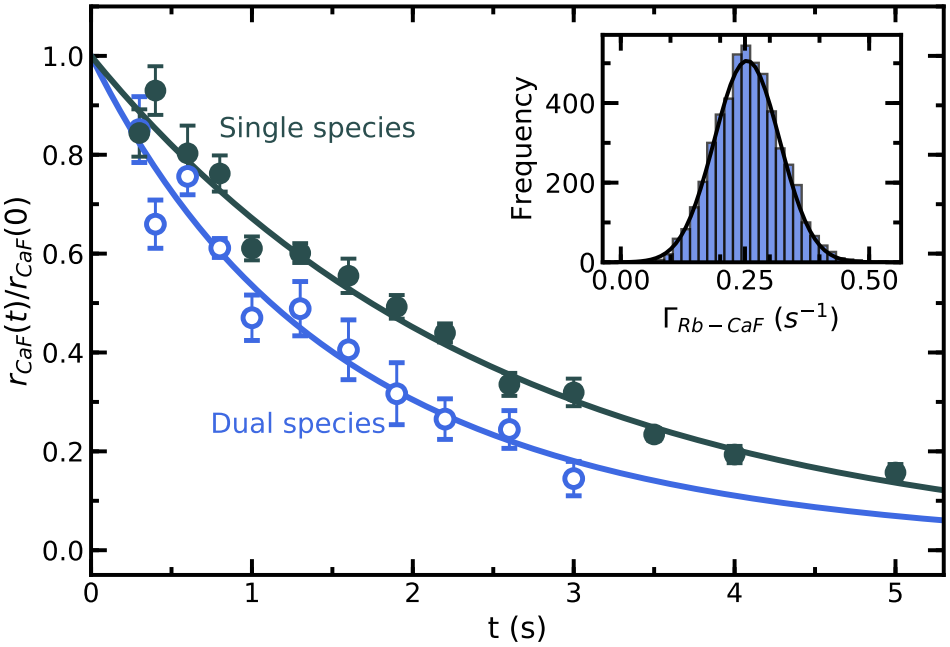

Figure 6.16: Loss of molecules prepared in the $|1,1,+1\rangle$ state from the magnetic trap in the presence (○) and absence (●) of Rb atoms. The inset shows how estimates of $\Gamma_{\text{Rb-CaF}}$ are distributed using the re-sampling method.

density, ζ, grows and so does the observed atom-induced loss rate. Figure 6.15 shows how the measured $\Gamma_{\text{Rb-CaF}}$ changes as ζ is increased, for molecules prepared in the $|1,2,+2\rangle$ state. A linear model fit to these data gives a gradient of $k_2 = (6.6 \pm 1.5) \times 10^{-11}$ cm$^3 \cdot$s^{-1}. The uncertainty in the above value takes into account the uncertainties in atom number and the size of both clouds[7]. The insets in the figure show how the overlap between the two clouds in the radial dimension changes as more atoms are added into the trap.

Loss of molecules in the $|1,1,+1\rangle$ state

The above measurements were performed with both molecules and atoms prepared in spin-stretched states, which is an arrangement that often suppresses inelastic loss [159, 47]. In addition to these measurements, the loss rate coefficient is also measured when molecules are prepared in the $|1,1,+1\rangle$ state, which is not a spin-stretched state. Figure 6.16 shows the single and dual species loss measurements for molecules in this state. The g factor is 20 % smaller for this state thus for the same magnetic field gradient the cloud is found to be slightly larger. The loss rate coefficient in this case is measured to be $k_2 = (5.7 \pm 1.8) \times 10^{-11}$ cm$^3 \cdot$ s^{-1}, similar to the value measured for molecules in the $|1,2,+2\rangle$ state. This indicates that there is no strong dependence of the observed loss on

[7]To take into account the uncertainties in atom number and measured cloud dimensions, the linear model fit to the data is performed many times with randomly drawn values of the parameters required to calculate ζ from their measured distributions. The mean and width of the distribution of k_2 estimates are then taken to be as the best estimate and error respectively.

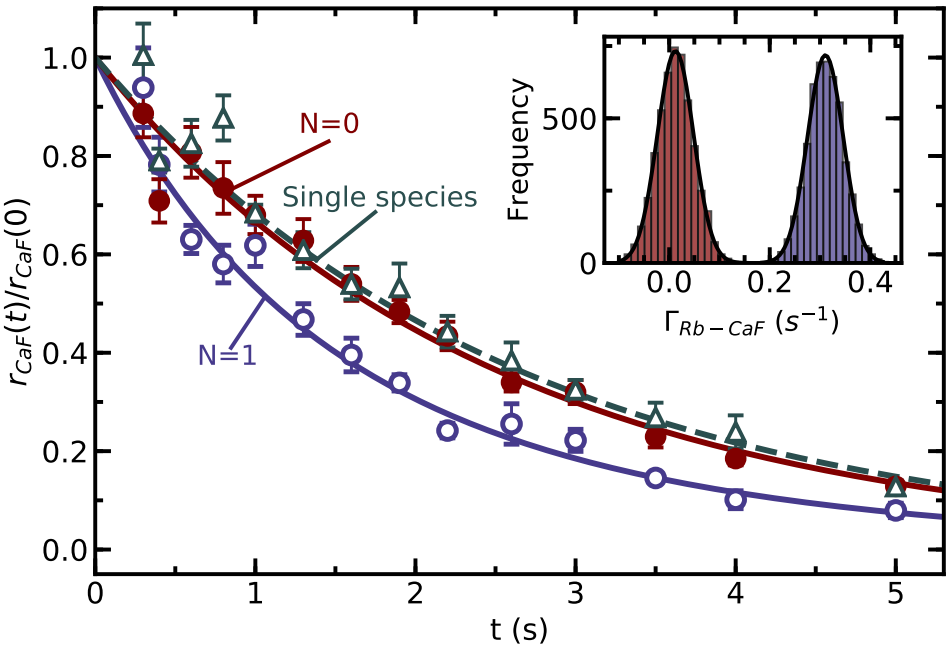

Figure 6.17: Loss of molecules from the magnetic trap for molecules in the $|1,2,+2\rangle$ state ($\circ$) and the $|0,1,+1\rangle$ state ($\bullet$). Solid lines are fits to eq. 6.21 using the re-sampling method. Also shown is the decay of molecules in the $|0,1,+1\rangle$ state in the absence of atoms ($\triangle$). Inset shows the estimate distribution of $\Gamma_{\text{Rb-CaF}}$ for the $N=0$ and $N=1$ measurements.

either the hyperfine or Zeeman levels.

6.5.4 Suppression of loss for molecules in $N = 1$

Finally, the loss measurements were repeated with molecules prepared in the ground rotational $|0,1,+1\rangle$ state, which is the only magnetically trappable state in $N=0$. Here the only available loss channel is spin changing collisions. Figure 6.17 compares the measured loss for molecules prepared in $N=1$ and $N=0$, in the presence of $1.2\cdot10^9$ atoms. For these data the estimated loss rate is $\Gamma_{\text{Rb-CaF}} = 0.30(5)$ s^{-1} for molecules in $|1,2,+2\rangle$ and is reduced to $\Gamma_{\text{Rb-CaF}} = 0.013(36)$ s^{-1} when molecules are in the $|0,1,+1\rangle$ state. The loss rate coefficient is estimated from an average of four such measurements and is found to be $k_2 = (-0.05 \pm 2.9)\times10^{-12}$ cm$^3\cdot$s^{-1}. This result is consistent with zero loss and gives an upper bound on the loss rate coefficient $k_2 < 5.8\times10^{-11}$ cm$^3\cdot$s^{-1} at the 95 % confidence level. This upper bound is an order of magnitude smaller than the measured value of k_2 when molecules are in the $N=1$ state.

6.5.5 Discussion and comparing results with theory

The experimental observations above suggest that the loss is due to inelastic atom-molecule collisions where the rotational level of the molecule is changed. Such collisions result in loss for two reasons: (i) only molecules which are in the $N=1$ state are re-

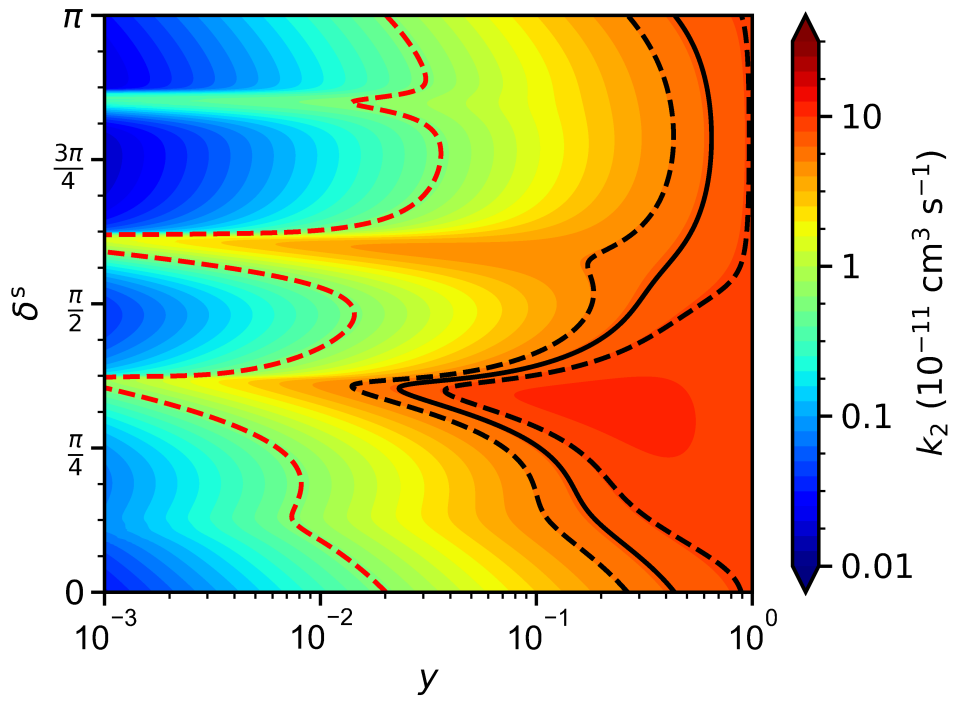

Figure 6.18: Thermally averaged loss rate coefficient obtained using the single-channel model plotted as a function of the parameters y and δ^{S}. The experimentally measured value of k_2 and its associated uncertainty for molecules in the $|1,2,+2\rangle$ state are shown by black lines. The upper 95 % confidence bound on the value of k_2 for molecules in $|0,1,+1\rangle$ is shown by the red dashed line.

captured into the MOT and thus detected; (ii) the collision is exothermic by 1 K, which releases an amount of energy many times larger than the trap depth of ~ 1.5 mK.

The single-channel loss model described in section 2.3.3 is used to calculate the loss-rate coefficient as a function of the parameters y and δ^{S}. These and the following measurements are performed with Rb atoms at a temperature of $T_{\mathrm{Rb}} = 70(1)$ μK and the molecules at $T_{\mathrm{CaF}} = 175(35)$ μK. The temperatures of each cloud are inferred from a separate ballistic expansion measurement. Because the relative motion energy is finite, the computed loss rate coefficients are thermally averaged as

$$k_2(T) = \int_0^\infty \frac{2}{\sqrt{\pi}} k_2(E) x^{1/2} \exp(-x)\, dx \ , \tag{6.23}$$

where $x = E/k_{\mathrm{B}}T$. Figure 6.18 shows how the calculated[8] k_2 varies with y and δ^S at a temperature $T = 133$ μK. The measured value of k_2 for molecules in $|1,2,+2\rangle$ and the associated uncertainty are indicated by black lines. The upper limit on the measured k_2 for molecules in $|0,1,+1\rangle$ is indicated by the red dashed line. Due to the rather high temperature, the calculated values of k_2 show strong peaks around $\delta^{\mathrm{S}} = 3\pi/8$ and $5\pi/8$ and a weaker peak around $7\pi/8$; these correspond to contributions from the $p-$, $d-$ and

[8]These calculations were done by our theory collaborators Matthew Frye and Jeremy Hutson.

$f-$waves respectively. The peak at $\delta^{\mathrm{S}} = \pi/8$, which corresponds to $s-$wave scattering and is very prominent at lower temperatures [173], is relatively weak here due to increased transmission past the long rate potential and thermal averaging.

At this temperature, the universal loss rate ($y = 1$) for molecules in $N = 1$ is equal to $k_2^{\mathrm{Univ}}(T) = 8.2 \times 10^{-11}$ cm^{-3}s^{-1}. It is above but consistent with the experimentally measured value of $k_2 = (6.6 \pm 1.5) \times 10^{-11}$ cm$^3 \cdot$s^{-1}. The most likely range of parameters have $y > 0.4$ although values of y as small as 0.03 are not ruled out if δ^S happens to be at a resonance. The spin state of the colliding molecules is found to have little or no influence on the experimentally measured loss rate. In addition, the molecular complex lifetime due to sticky collisions is estimated as 60 ps using the expression from [174], which is too short to cause loss due to excitation by a resonant photon or collisions with a third body. It is thus safe to conclude that the observed loss is dominated by rotation-changing collisions. The measured loss for molecules in $N = 0$ is consistent with loss parameters in the range $y < 0.04$.

The experimentally measured value of k_2 for molecules in the $N = 1$ state in the magnetic trap is a factor of 2.17(66) smaller than the rate coefficient measured in the MOT, where the relative motion temperature was at 2.4 mK. This is consistent with the $T^{1/6}$ temperature scaling obtained using the Langevin model (see section 5.4).

These results are promising for the future prospects of collisional cooling. The natural next step is thus to investigate elastic atom-molecule collisions. At the time the experiments described here were performed, the available molecule number was too low to enable a systematic investigation of thermalization in these mixtures. The next two chapters describe how the number of molecules was increased and present the preliminary results of thermalization measurements.

In future experiments it would also be interesting to investigate inelastic collisions when atoms are prepared in the non spin-stretched $|F = 1, M_F = +1\rangle$ state. As mentioned above, in this setting high loss rates were observed in other experiments [159]. The atoms and molecules may be loaded into optical tweezers, where collisions at the single particle level may be studied [57]. The trapped mixtures may also be used to form ultracold triatomic molecules either via photoassociation or magnetoassociation [165].

7 | Transverse cooling of the molecular beam

The transverse divergence of the molecular beam greatly limits the available flux of slow molecules that reaches the capture volume of a 3D MOT. There are several proposed methods to increase the collimation of a laser decelerated buffer gas beam though no successful experimental realizations have been reported yet. One may be able to use either a 1D or 2D MOT [175, 176] which both confines and cools the molecules although the rather high temperatures obtained in a molecular MOT may quickly limit the degree of collimation. A promising proposal which was conceived and is still pursued in our group [177] is to use a magnetic field to guide molecules and optical pumping to remove kinetic energy and thus decelerate. Transverse cooling- yet another obvious method to collimate a molecular beam was already successfully demonstrated in one or two dimensions [178, 175, 176] but has never been shown to substantially increase the flux of molecules which are available to be captured into a MOT. In our group earlier attempts to reduce the divergence of the CaF beam by transverse cooling in 1D also proved fruitless. Because each gain in the number of molecules opens doors to potential new experiments, this topic was revisited in this work.

In this chapter experiments on transverse cooling of a beam of CaF molecules are presented. Transverse cooling both in 1D and 2D is investigated. Although this is still very much work in progress, cooling the molecular beam in 2D increased the number of molecules captured into the MOT by a factor of ~ 3 after optimizing all available experimental parameters. As this work was done towards the very end of my research and for the sole purpose of increasing the signal to enable systematic temperature measurements of the cloud in the magnetic trap, the complete understanding of the observations presented here is postponed to future work.

7.1 Cooling in 1D

For the transverse cooling experiments described here a new 5 W laser system from *Azurlight Systems* operating at a wavelength of 531 nm was installed. First, transverse cooling was attempted in 1D. Figure 7.1(a) shows the experimental setup used to cool the

molecular beam along the x-axis. The cooling light is tuned to drive the B-X transition and the frequency of the laser beam is modulated with an EOM which is driven at 72 MHz. The 1st order sidebands with roughly equal amplitudes to that of the carrier address primarily the $F = 2$ and $F = 1^-$ ground hyperfine levels[1] when the carrier is tuned to address $F = 0$. The transverse cooling beam is delivered to the experiment using a single mode optical fibre and collimated to a $1/e^2$ diameter of 3.7 mm. It is then expanded along the direction of the molecular beam propagation using a pair of cylindrical lenses with focal lengths of $f_1 = 30$ mm and $f_2 = 300$ mm. The beam enters the chamber 170 mm away from the exit aperture of the buffer gas cell and propagates along the x-axis. The entrance viewport is circular and has a diameter of 32 mm. After passing the beamline, the transverse cooling light is retro-reflected by a silver mirror placed at the opposite end of the chamber. To repump molecules from the $\nu = 1$ vibrational level, the frequency broadened $\mathcal{L}_{10}$ laser beam used to repump the laser slowed molecules is kept on. The slowing beam itself is blocked for all experiments described in this section.

Molecules are detected at two different regions by collecting their light induced fluorescence. The first camera (CCD1) is positioned perpendicularly to the transverse cooling viewport and collects the cooling light scattered from the molecules. This is used as a diagnostic of the laser frequency relative to the hyperfine transitions on the B-X line. The second detection region (CCD2) is in the science chamber and here the MOT beams at 606 nm are used to image the molecular beam. In particular, the $\mathcal{L}_{00}^{C}$ laser frequency is tuned so that the vertical beams along the $x-$axis are resonant with the molecules that reach the chamber. The two pairs of horizontal MOT beams are at a 45 $^\circ$ angle to the molecular beam and for molecules travelling at a velocity of 150 m/s are Doppler shifted out of resonance by $\pm$175 MHz. The MOT beam contains all the usual vibrational repump components and is apertured down to a diameter of a few mm.

In figures 7.1(b) and (c) the ToF profiles recorded using CCD1 and CCD2 are shown. An exposure time of 1 ms is used to detect molecules with CCD1 while the exposure time for CCD2 is set to 5 ms. Thus in both cases the real ToF profiles are convolved with a rectangular pulse which has a width comparable to that of the molecular pulse. It is worth noting here that the laser slowing light used to decelerate molecules and load them into the MOT is switched on at $t_Y = 2.4$ ms. In experiments where the effect of transverse cooling on the number of molecules loaded into the MOT is investigated this ensures that the laser slowing light does not interact with the molecules while they traverse the transverse cooling region. For the results presented in the remainder of this section CCD2 is triggered at $t_Y = 5$ ms and is exposed for 5 ms to record an image of the molecular beam.

[1]Note that for the B-X transition the hyperfine structure of the excited level is resolved. In particular, the $F = 1^- \rightarrow F' = 0$ transition is resolved. The $F = 1^+ \rightarrow F' = 0$ and $F = 2 \rightarrow F' = 1$ transitions differ only by 5 MHz and are thus not resolved.

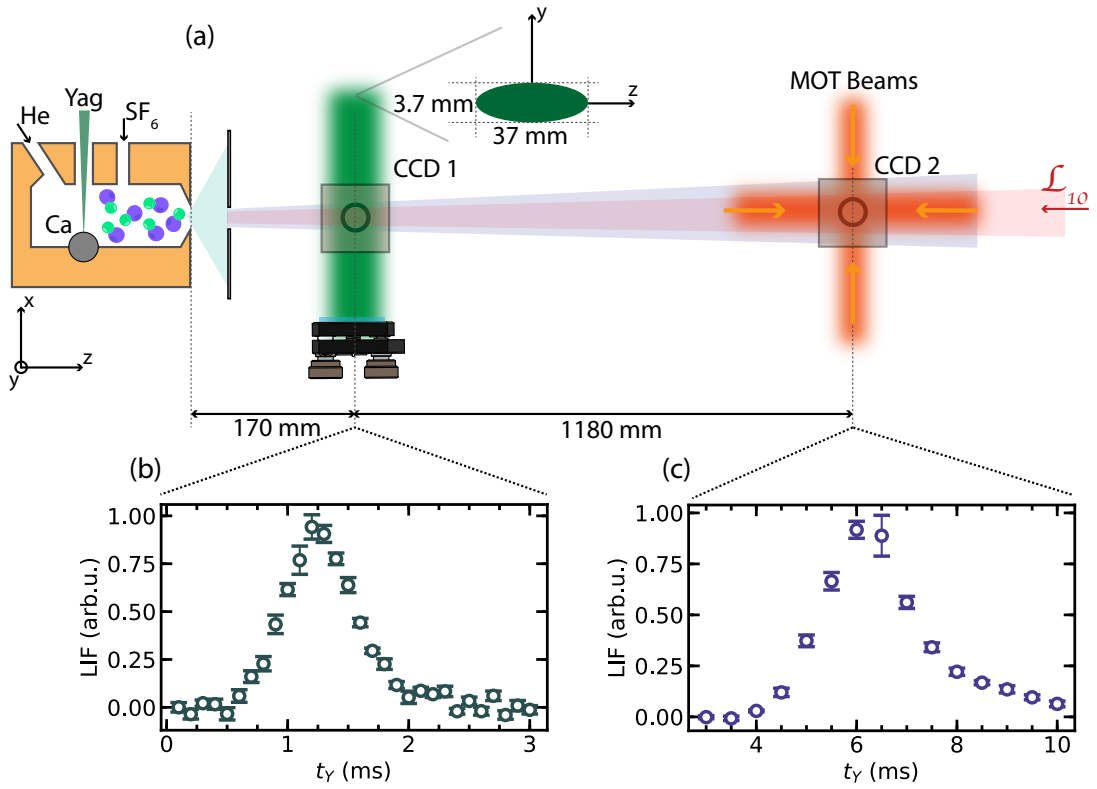

Figure 7.1: (a) Experimental setup for transverse cooling of the molecular beam in 1D. Molecules produced in the buffer gas source travel for $\sim$ 170 mm before they reach the transverse cooling region. The transverse cooling beam has an elliptical shape. It passes the molecular beam along the x-axis and is retro-reflected by a mirror placed on the opposite end of the chamber. CCD1 is used to detect the fluorescence induced by the transverse cooling light. CCD2 is used to image the molecular beam in the science chamber using the vertical 3D MOT beam as a probe. Note: the MOT beams drawn along the $z-$axis make an angle of 45° with the z and y axes and do not contribute to the signal due to the Doppler shift. Molecules which leak to $\nu = 1$ are repumped using the frequency broadened $\mathcal{L}_{10}$ light. (b) The detected LIF by CCD1 a time t_Y after the ablation pulse using the transverse cooling beam tuned to be resonant with molecules as a probe. (c) The detected LIF by CCD2 in the MOT chamber with the transverse cooling light switched off and using the vertical MOT beams as a probe.

7.1.1 Evidence of cooling in 1D

The transverse cooling laser frequency is scanned and fluorescence images of the molecular beam with CCD2 are recorded. For these measurements, the transverse cooling beam had a peak intensity[2] of 250 mW $\cdot$ cm^{-2}. The light was linearly polarized relative to the

[2]This was the maximum power the optical fibre used to deliver the light to the experiment could handle.

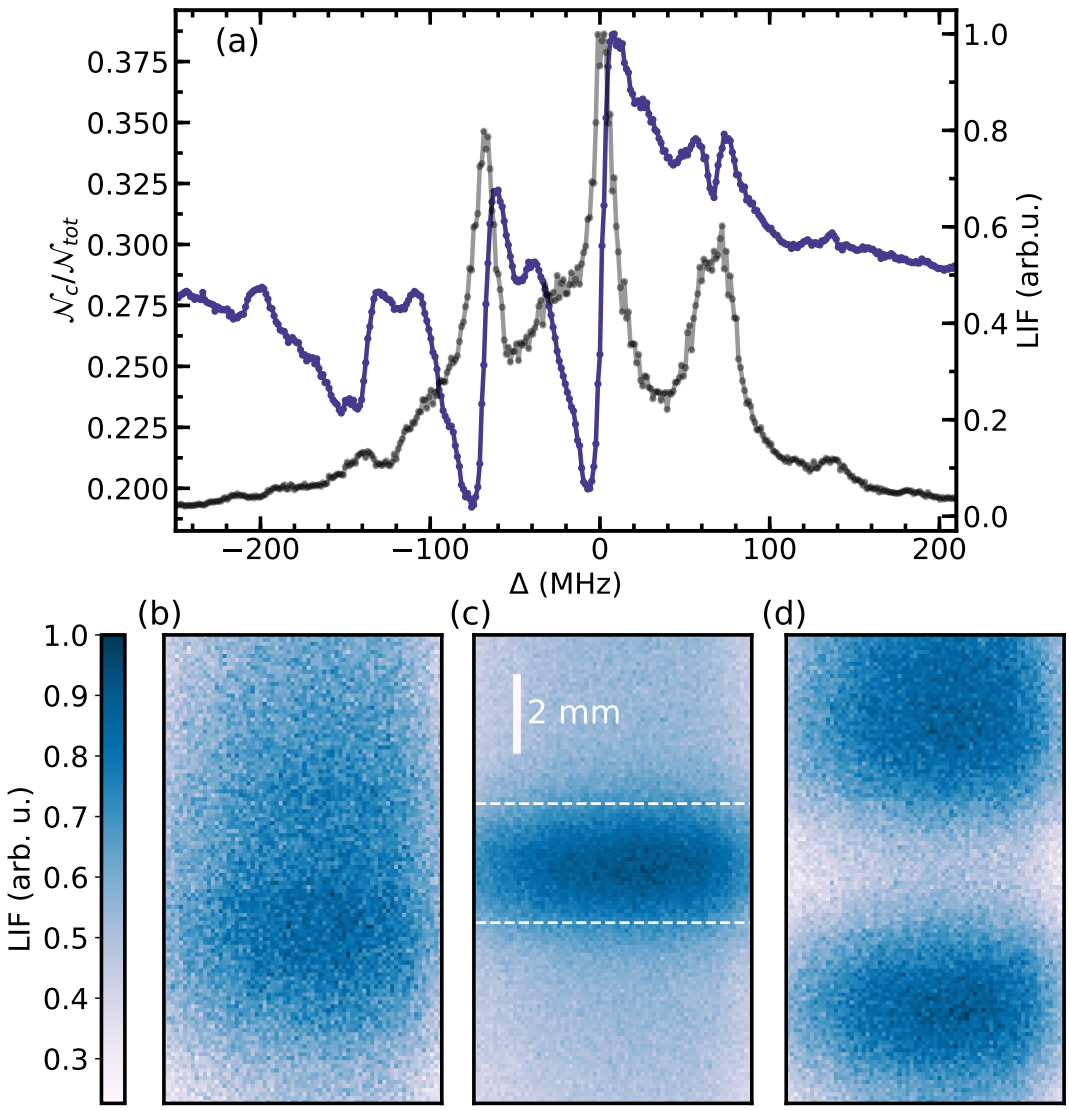

Figure 7.2: Evidence of cooling of the molecular beam in 1D. (a) Blue trace: number of molecules detected with CCD2 in a central region of 3.1×12.4 mm^2 size normalized to the total number of molecules as a function of the transverse cooling laser frequency. Black trace: LIF detected with CCD1. $\Delta = 0$ is defined as the laser frequency for which the fluorescence detected with CCD1 is maximum. Each data point is the average of 6 experiments. Error bars are not included. (b) Image of the molecular beam cross section acquired with CCD2 when the transverse cooling light is blocked. (c) and (d): images of the beam when transverse cooling is applied using $\Delta = 7$ MHz and $\Delta = -7$ MHz respectively.

direction of propagation of the molecular beam[3]. In figure 7.2(a) the number of molecules detected with CCD2 in a central region of size 3.1×12.4 mm^2, normalized to the total number of molecules, is plotted as a function of the cooling laser detuning. This figure of merit quantifies the effect of transverse cooling on the transverse spatial distribution

[3]The stray magnetic field at the position of the interaction region along the direction of the molecular beam was later measured to be ~ 200 mG.

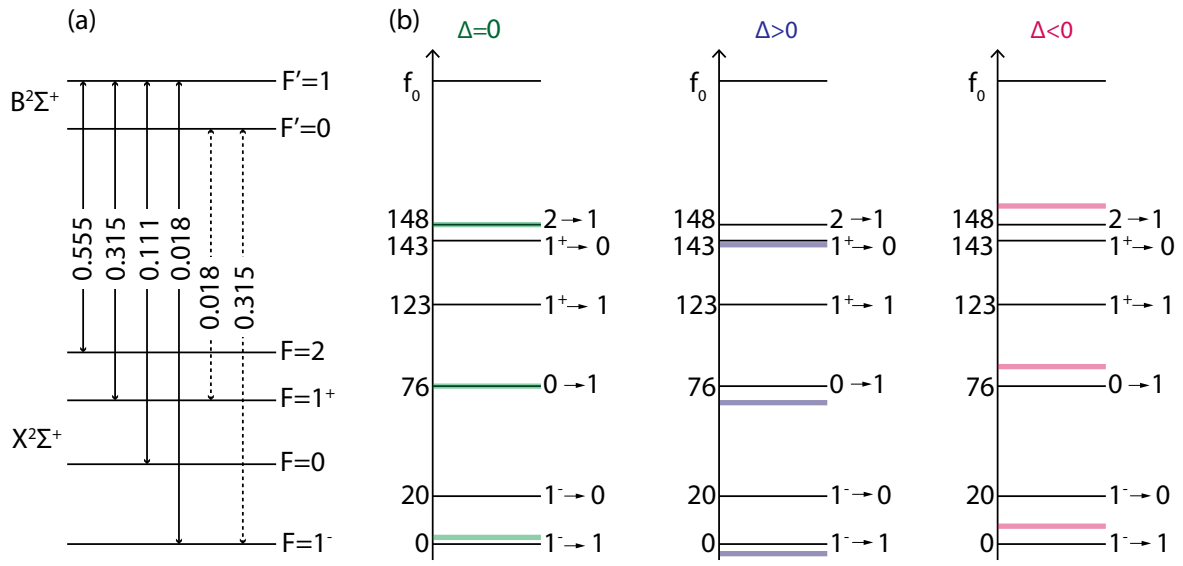

Figure 7.3: (a) Energy level diagram relevant for transverse cooling. The numbers indicate the relative transition strengths. (b) Laser cooling frequencies relative to the frequencies of allowed transitions for $\Delta = 0$, $\Delta > 0$, $\Delta < 0$. Not to scale.

of the molecular beam and eliminates the effect of longer term drifts and fluctuations in the flux of molecules produced by the buffer gas source. Here $\Delta = 0$ is defined as the laser detuning for which the LIF detected with CCD1 is maximum. The signal detected by CCD1 is shown in the same figure by the black points.

Two prominent dispersive features appear in figure 7.2(a) when the laser frequency is tuned around $\Delta = 0$ MHz and $\Delta = -70$ MHz. To aid in orienting between the relative laser and transition frequencies, figure 7.3(a) shows the allowed transitions while (b) shows the positions of the laser frequencies when $\Delta = 0$, $\Delta > 0$ and $\Delta < 0$. The fluorescence image of the beam for $\Delta = 7$ MHz is shown in figure 7.2(c): the transversally slow molecules are collimated by the cooling light while the faster ones are heated out from the beam. This is a feature of simultaneous Sisyphus cooling and Doppler heating. Molecules which have sufficiently low transverse velocities are damped by the blue-detuned light while molecules above the capture velocity of this blue-detuned molasses are heated. Because the polarization of the retro-reflected cooling beam is the same as that of the incoming beam, there are no polarization gradients. In this case, there is a gradient in the light intensity and the molecules are likely cooled by the magnetically assisted Sisyphus mechanism which was first demonstrated for SrF molecules [178] and subsequently demonstrated for several other species, e.g. YbF [179]. Because at the time of these experiments no control over the magnetic field at the position of the molecules was available, the dependence on the magnetic field was not investigated systematically.

The situation is reversed when $\Delta = -7$ MHz. In this case, the Sisyphus mechanism heats transversally slow molecules while Doppler cooling collimates the faster ones. Fig-

ure 7.2(d) shows an image of the beam at this laser frequency: molecules are removed from the central part of the beam with more molecules present on either side[4]. For reference, figure 7.2(b) shows an image of the molecular beam when the cooling light is blocked.

To measure the transverse temperature of the beam it needs to be imaged at two different locations along the direction of its propagation. By measuring the amount by which the collimated feature expands during the time it takes the beam to travel between the two detection regions, the temperature may be inferred [179]. This measurement was not attempted here.

7.1.2 Effect on number of molecules in the MOT

Figure 7.4(a) shows cross sections of the fluorescence images recorded with CCD2 when the cooling laser detuning is $\Delta = 7$ MHz and $\Delta = -7$ MHz. The total signal detected when the cooling light is blue-detuned turns out to be 20 % lower than when the light is detuned to the red. In figure 7.4(b) the cross sections without the cooling applied and with the cooling light detuned to the blue are compared. The total signal detected without cooling is 11 % higher than with cooling, but the cooling clearly increases the number of molecules in the central region.

Next, the effect of 1D transverse cooling on the number of molecules loaded into the MOT is investigated. The detuning of $\mathcal{L}^C_{00}$ is set to optimize the MOT loading and laser slowing is applied to the molecular beam. The transverse cooling light frequency is set to $\Delta = 7$ MHz. It is found that when transverse cooling is applied[5], the number of molecules captured into the MOT is consistently reduced by ~ 20 %. This result is not unexpected when compared with the findings of figure 7.4(b). The total flux of molecules through the detection region is reduced when the beam is cooled transversally. Molecules are redistributed spatially, with an enhancement in signal only over a short range away from the molecular beam axis. The MOT beams have a $1/e^2$ radius of 8.2 mm, which is much larger than the width of the feature in figure 7.4(b). Thus the molecules which are cooled transversally may reach the capture volume of the MOT even when cooling is not applied. On the other hand, because the transversally faster molecules are heated, the total effect is to slightly reduce the number of molecules which arrive within the capture volume of the MOT.

[4]Because the performance of the molecular source degrades with time, the images of the molecular beam shown in the figure are normalized to the maximum pixel values in each individual image.

[5]Here, only a detuning of $\Delta = 7$ MHz was investigated systematically. No obvious improvement in the MOT number was observed while scanning the frequency by ± 20 MHz

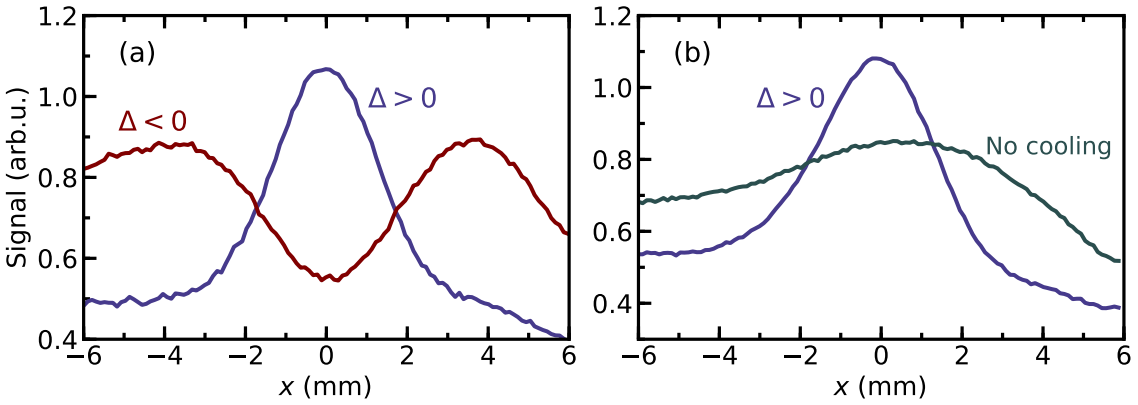

Figure 7.4: Molecular beam cross sections for different transverse cooling laser frequency detunings integrated along the z-axis. (a) Integrated cross sections of the molecular beam for a red and blue frequency detuning. (b) Cross sections of the beam with blue detuned laser cooling light and with the cooling light blocked.

7.2 Cooling in 2D

Because no positive effect on the number of molecules captured into the MOT was observed after the application of transverse cooling in 1D, the setup was extend to 2D. Applying cooling in both dimensions increases the capture velocity of the blue-detuned molasses and rather unsurprisingly increases the brightness of the molecular beam compared to cooling just in 1D as was recently demonstrated for YbF molecules [180].

To implement 2D transverse cooling, several changes to the previous setup were made. The diagnostic CCD1 camera had to be removed. The transverse cooling beam was made slightly wider along the shorter axis by expanding it[6] to a waist diameter of 5.3 mm. The size of the beam along the longer axis was reduced to 31.8 mm compared to the 1D cooling setup described earlier. The cooling light was delivered to the experiment with an optical fibre that has a higher input power threshold and was wrapped through the beamline chamber to recycle optical power. Referring back to figure 7.1(a), the light was first passed along the x-axis, then along y and retro-reflected onto itself. Several different frequency sideband structures were investigated as will be described below. For these experiments, a pair of coils which produce a magnetic field along the z-axis were installed to apply a field of up to several Gauss along the propagation direction of the molecular beam.

7.2.1 Increasing number of molecules captured into the MOT

Since the laser lock set points drift from one month to another, the cooling laser was calibrated once more relative to the allowed transitions for the experiments that follow.

[6] In fact, the same beam size as for cooling in 1D was also tested but with visibly worse results as will be briefly described later in this section.

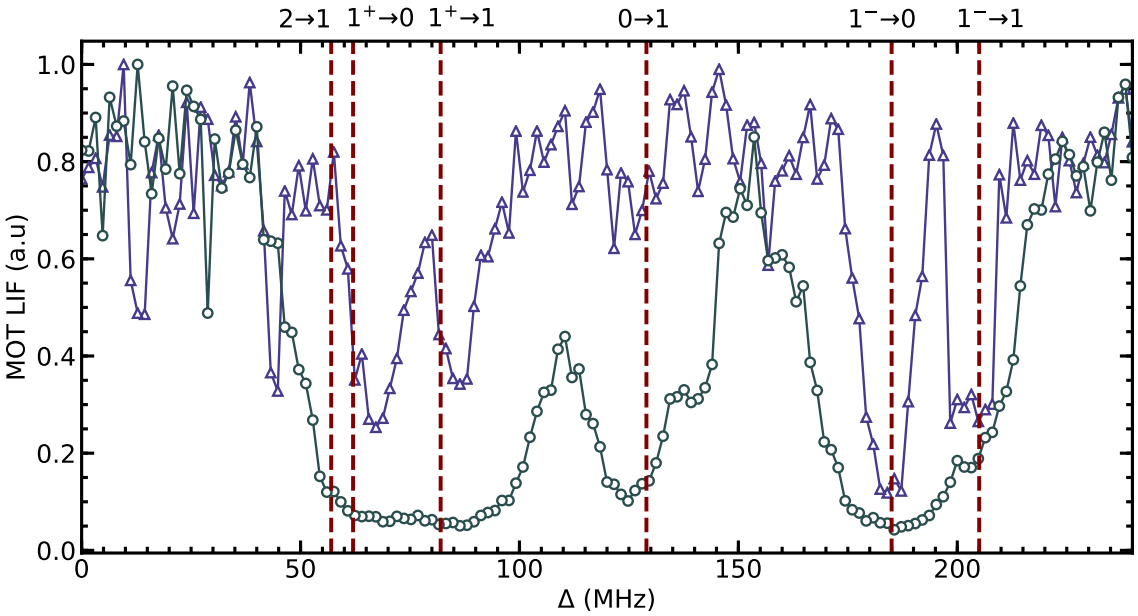

Figure 7.5: Calibration of the transverse cooling laser frequency by pushing molecules out of the MOT. The MOT is pushed using only a single frequency component with an intensity of 8.2 $\mathrm{mW \cdot cm^{-2}}$ (△) and 80 $\mathrm{mW \cdot cm^{-2}}$ (○). The red dashed lines indicate rough estimates of the laser detuning Δ corresponding to the 5 allowed transitions ($F \rightarrow F'$).

To do this, some of the cooling light was picked off before being modulated with an EOM and coupled into the science chamber to interact with molecules trapped in the MOT. The laser beam is passed through the molecules in only one direction, so pushes them out of the MOT when resonant with one of the hyperfine components of the transition. Figure 7.5 shows the LIF from the MOT as a function of the cooling laser frequency using beams with peak intensities of 8.2 $\mathrm{mW \cdot cm^{-2}}$ and 80 $\mathrm{mW \cdot cm^{-2}}$. The dips in signal at different laser frequencies correspond to the different transitions between the ground and excited hyperfine levels[7]. The red dashed lines indicate these transitions and are roughly matched with the observed dips in the MOT LIF[8]. Here $\Delta = 0$ is defined as simply the initial laser frequency and has no particular meaning relative to the hyperfine structure.

To see the effects of 2D transverse cooling on the molecular beam directly, it is required to image the beam head on. Because the viewport on the opposite end of the beamline is too far from the centre of the science chamber to collect enough light, the number of molecules loaded into the MOT was used as a figure of merit. For these experiments, a measurement of the number of molecules captured into the MOT with transverse cooling applied $\mathcal{N}_\mathrm{C}$ was each time followed by a measurement of the number captured with the

[7]The estimates of the laser frequency relative to the allowed transitions should be taken with a pinch of salt here as the light is applied in the presence of a quadrupole magnetic field and all of the MOT light. The presence of a magnetic field shifts the transition frequencies due to the Zeeman effect while the MOT light dresses the ground electronic states and may significantly shift the resonance frequencies.

[8]In hindsight, a better method of calibrating the laser frequency would be to push molecules released from the MOT when both the cooling light and magnetic field are switched off.

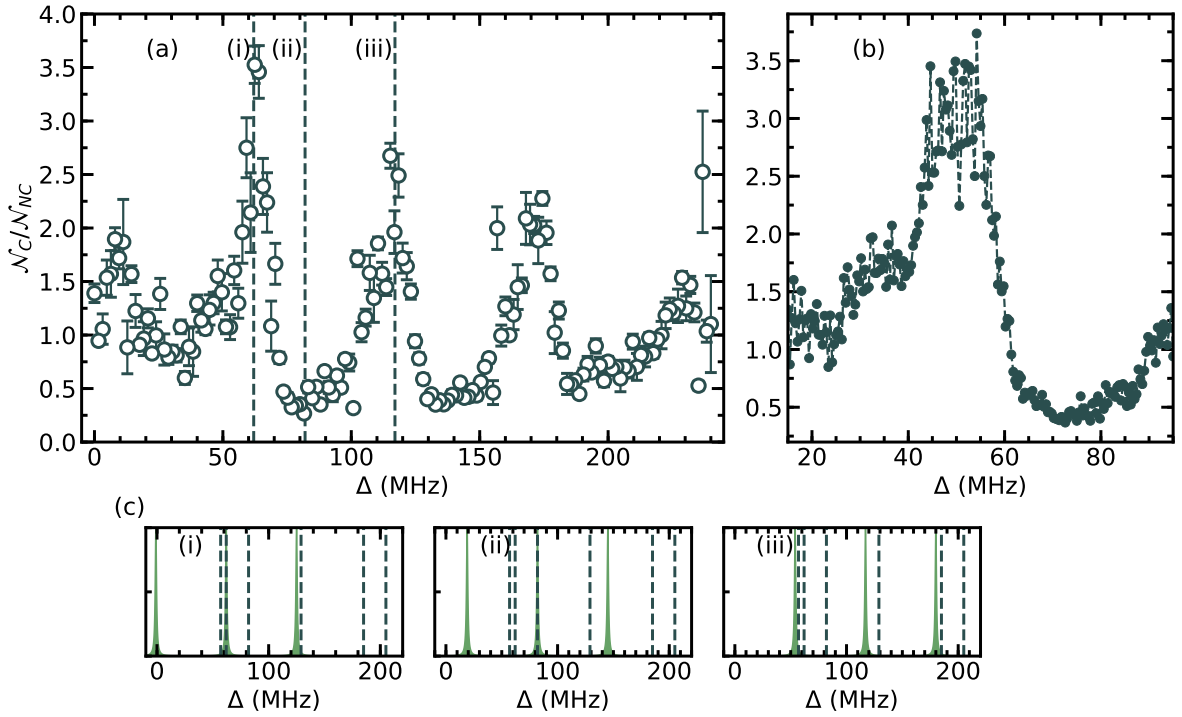

Figure 7.6: (a) Effect of 2D transverse cooling on the number of molecules captured into the MOT as a function of the cooling laser frequency. The number of molecules in the MOT $\mathcal{N}_{\mathrm{C}}$ with transverse cooling applied is normalized to the number of molecules captured $\mathcal{N}_{\mathrm{NC}}$ with no transverse cooling. Points are averages of 6 experiment runs and error bars are the standard errors on the mean values. (b) Finer laser frequency scan around the left most largest feature. (c) The cooling light frequency structures relative to the allowed transitions for a set of three different laser detunings indicated by dashed lines in (a).

cooling light blocked $\mathcal{N}_{\mathrm{NC}}$ using a mechanical shutter.

Figure 7.6(a) shows how $\mathcal{N}_{\mathrm{C}}/\mathcal{N}_{\mathrm{NC}}$ varies with the laser frequency using three frequency components of equal intensity (total peak intensity of 350 $\mathrm{mW \cdot cm^{-2}}$) and separated by 63 MHz. The number of molecules in the MOT is increased at three different laser detunings separated by $55 - 60$ MHz. To the right of each of these features, the number of molecules is reduced. This observation hints that the molecular beam is collimated using red-detuned light and thus a Doppler cooling process while for blue-detuned light Sisyphus cooling heats out molecules which would otherwise be within the capture volume of the MOT. The panels in figure 7.6(c) show the estimated positions of the three laser cooling frequency components relative to the allowed transitions. In configuration (i) the MOT number is enhanced the most. Interestingly, there is no laser frequency close to the $1^- \rightarrow 1$ transition which should lead to rapid optical pumping into the $F = 1^-$ state and thus produce no cooling force. A possible explanation to why this is not the case could be that the modulator produces a non-zero 2nd order frequency sideband which has sufficient intensity to prevent optical pumping. In configuration (ii) there are two frequency components which are closer to being blue detuned from the $1^+ \rightarrow 1$ and $0 \rightarrow 1$

transitions. In configuration (iii) all three components are red detuned though at this laser frequency the MOT number enhancement is somewhat lower.

7.2.2 Dependence on various parameters

The frequency structure, size and intensity of the transverse cooling beam are varied to further investigate the cooling process which is responsible for the observed gain in number of molecules captured into the MOT.

Intensity of cooling beam

For a Sisyphus cooling mechanism the capture velocity of the molecular beam is expected to continue to increase as the cooling light intensity is increased. On the other hand, because Doppler cooling relies on scattering as many photons as possible, its effect on the collimation of the molecular beam is expected to saturate for sufficiently high laser intensity. Figure 7.7(a) shows how $\mathcal{N}_C/\mathcal{N}_{NC}$ varies with the intensity of the cooling light[9] when the laser frequency is set to $\Delta = 60$ MHz. The beam is linearly polarized at $\phi = 45°$ relative to a 1 G magnetic field applied along the direction of the molecular beam propagation. At an intensity of ~ 150 mW $\cdot$ cm^{-2} the effect begins to saturate, which is another indication that Doppler cooling is likely to be responsible for the observed enhancement in the MOT number.

Polarization of cooling beam

Figure 7.7(b) shows how $\mathcal{N}_C/\mathcal{N}_{NC}$ changes with the orientation of the cooling beam polarization relative to the applied magnetic field, which points along z. The effectiveness of transverse cooling is reduced substantially as the polarization is made perpendicular to the applied magnetic field. This suggests that a magnetic field and a linearly polarized beam at an angle to this field are required to prevent optical pumping into dark states which limits the number of photons that may be scattered. No strong dependence is observed on the magnetic field amplitude, but a broad optimum is found near 1.5 G (figure 7.7(c)).

Different frequency structures

The experiments described above were also repeated using a set of two different frequency sideband structures for the cooling light. The EOM resonant circuit was retuned to frequencies of 79 MHz and 72 MHz. In each case, the amplitudes of the 1st order sidebands were made equal, as before. Using both of these arrangements increased the number of

[9] The total peak intensity is 4 times the value indicated on the graph as the same beam is recycled for each pass through the chamber.

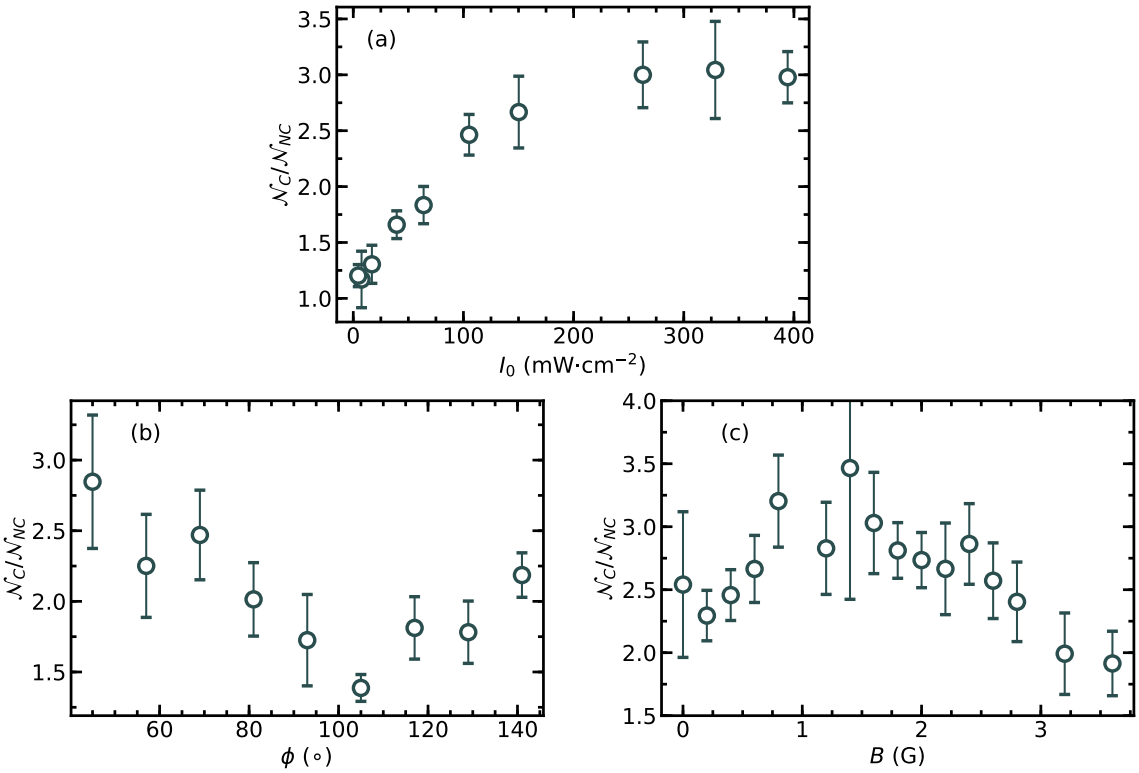

Figure 7.7: (a) MOT number enhancement as a function of the transverse cooling beam intensity with laser frequency set to $\Delta = 60$ MHz and a magnetic field of 1 G. (b) and (c) MOT number enhancement for varying polarization orientation, relative to the applied magnetic field, and magnetic field amplitude respectively. At $B = 0$ there is a residual magnetic field of several hundred mG.

molecules in the MOT at three different cooling laser frequencies but by somewhat lesser amounts and at different laser frequencies.

Size of cooling beam

Reducing the diameter of the cooling beam along the short axis from 5.3 mm to 3.7 mm made the transverse cooling a factor of ~ 2 less effective. This is most likely because of the reduced cooling volume. Since the MOT beams have a diameter of around 16 mm, increasing the transverse cooling beam width may further enhance the number of molecules captured into the MOT.

7.3 Conclusions and future improvements

Transverse cooling of the CaF beam was demonstrated both in 1D and 2D. The beam was collimated in 1D using blue detuned light although it did not lead to an increase in the flux of molecules arriving within the capture volume of the MOT. By extending the setup to cool in two dimensions, a factor of 3.5 improvement in the MOT number was

observed. Although the exact process responsible for this improvement is still somewhat uncertain, the experiments performed so far suggest that the beam was collimated by Doppler cooling.

If Doppler cooling is indeed responsible for the observed enhancement, further gains may be obtained by simply extending the cooling region to increase the number of photon scattering events. A new vacuum chamber with rectangular windows of size 30×120 mm was designed and is currently being built in the workshop and will be integrated into the experiment in the nearest future. To extend the total cooling length, a multipass configuration will be used, similar to the one described in [180]. With this configuration, the cooling beam may be expanded more along the direction perpendicular to the molecular beam and thus increase the total cooling volume. In addition, full magnetic field control at the position of the molecules will be implemented to investigate both Doppler and sub-Doppler cooling mechanisms in a more systematic way.

8 | Towards sympathetic cooling

The improvements to the experiment described so far increased the number of molecules in the magnetic trap so that temperature measurements could be made without requiring too much averaging. In this chapter a new optical pumping scheme, which was implemented in the experiment to pump molecules directly into the spin stretched state is also presented. The first systematic temperature measurements of the molecule cloud in the presence of a colder atom cloud are discussed. Although no thermalization was observed at the effective density used, the measurement places an upper bound on the elastic scattering cross-section. The chapter concludes with a discussion of near term future improvements to the experiment which should enable collisional cooling of molecules either in a magnetic or optical dipole trap.

8.1 Two-frequency optical pumping of CaF

The optical pumping scheme used in the experiments described above relied on eliminating the frequency component of light which addresses the target state. This scheme can only pump into the $|F = 0, M_F = 0\rangle$ state, which is not magnetically trappable. Although a microwave transition from this state to a magnetically trappable state can be driven, this transition is highly sensitive to background magnetic fields which broaden the transition and drift from one day to the next. Instead, an optical pumping scheme which relies on the polarization of light to select the target state may be used. This scheme was first demonstrated for laser cooled SrF molecules [118], which have a similar internal structure to CaF. The scheme is illustrated in figure 8.1(a): a pair of beams propagate at right angles and have σ^+ and π polarizations relative to the direction of an applied magnetic field of 200 mG. The frequency component tuned closer to the $F = 1^-$ state propagates perpendicular to the applied field and drives π transitions while the component tuned closer to the $F = 2$ level propagates along the applied field and drives σ^+ transitions. Here the $B^2\Sigma^+ - X^2\Sigma^+$ electronic transition is used. The only state which is dark to the two beams is $|2, +2\rangle$ and thus is the state molecules are optically pumped into. This is very conveniently a magnetically trappable state and connects to the $|N = 0, F = 1, M_F = +1\rangle$ state through a magnetically insensitive microwave transition. The scheme is very sensitive to the purity of polarization- any component remaining in $\sigma-$ will drive the molecules out

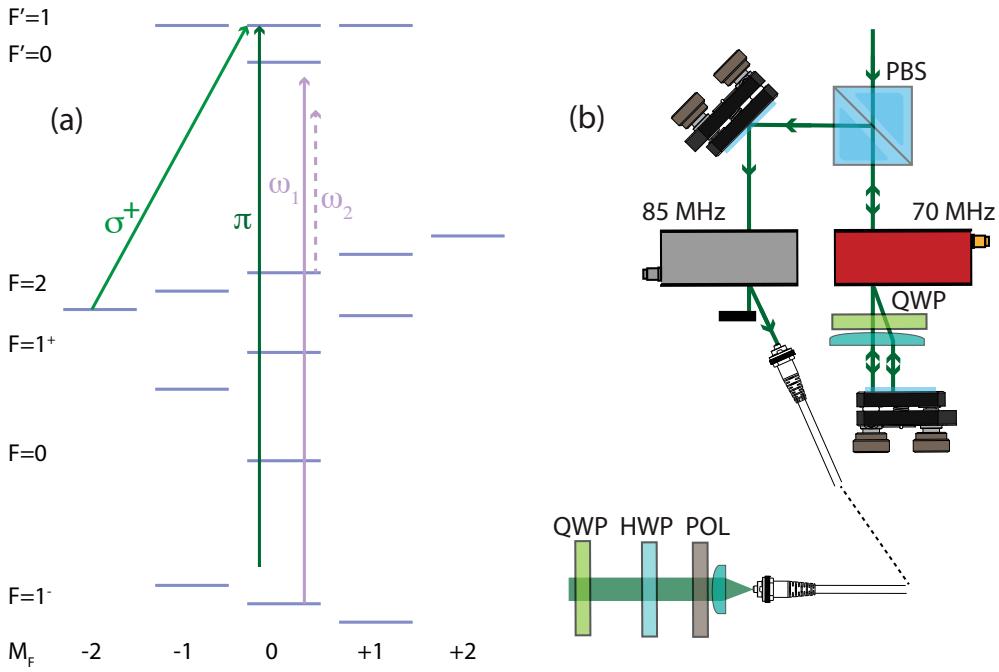

Figure 8.1: (a) Two-frequency optical pumping scheme of CaF. In the first version of this scheme, indicated by green arrows, two beams with σ^+ and π polarizations propagate at right angles relative to an applied magnetic field. In the second version, indicated by pink arrows, both frequency components have the same elliptical polarization and propagate along the same direction. (b) Optical setup used to realize the second version of the two-frequency optical pumping scheme.

of the target state and limit the optical pumping efficiency.

Finding the required optical access for coupling two optical pumping beams into the science chamber with near perfect polarizations proved challenging. Instead, a slightly different arrangement was used. The two frequency components were both polarized elliptically and made to propagate along the same direction. Provided the elliptical polarization is chosen such that it has no component which drives σ^- transitions, the population should end up in the target $|2, +2\rangle$ state. Figure 8.1(b) shows a schematic of the optical setup used to create the required frequencies and polarization. The beam passes an AOM driven at 70 MHz and both the -1$^{\text{st}}$ and 0$^{\text{th}}$ orders are reflected and combined into a single beam for the 2$^{\text{nd}}$ pass. The frequency difference is then $\omega_1 - \omega_2 = 2\pi \times 140$ MHz. An additional AOM is used as a fast switch to control the duration of the optical pumping pulse. The beam is delivered to the experiment with a single mode PM fibre and collimated to a waist radius of 2.5 mm. It then passes a linear polarizer which fixes the input polarization. A combination of a HWP and QWP is used to set the polarization of the optical pumping beam. Both wave plates are mounted in motorized rotation mounts so that an automatic scan of angles may be performed to optimize the optical pumping efficiency.

Calculations using optical Bloch equations show that, when perfect, this scheme can

pump all molecules into the target state. The calculations also show that by choosing the power of the lower frequency (ω_2) beam to be much less than the power of the higher frequency (ω_1) component allows for some imperfection in the chosen polarization. In the experiment $P_{\omega_1}/P_{\omega_2} \approx 10$ while the total power is 7 mW. The optical pumping parameters are optimized by measuring the number of molecules captured into the magnetic trap following the optical pumping pulse. A grid and differential evolution search are performed to find the optimal wave plate angles, which produces the largest sample of molecules in the magnetic trap. Both algorithms give the same final result.

Figure 8.2(a) shows the fraction of molecules captured into the trap as a function of the optical pumping duration. The efficiency is measured relative to the number of molecules captured into the MOT. It is noted here that this method of measurement does not allow to directly infer the fraction of molecules pumped into the target state as there are two other states which are magnetically trappable. This issue will be addressed later. In the first measurement, the optical pumping beam was passed through the chamber once. The $1/e$ pumping time in this case is found to be 91(5) μs and a maximum of 47.9(6) % of molecules are captured into the trap. In another iteration of the experiment the optical pumping beam was retro-reflected. The $1/e$ pumping time in this case was found to be 89(4) μs and a maximum of 53.5(7) % of molecules where captured into the trap. The higher optical pumping efficiency using a retro-reflected beam may be explained by imperfect polarization which increases the number of photons a molecule must scatter to reach the target state, and therefore increases the push the molecules receive from the optical pumping light. By retro-reflecting the pumping beam this push may be reduced.

Figure 8.2(b) shows the optical pumping efficiency as a function of the common two frequency detuning. Zero detuning corresponds to the ω_1 component being near resonant with the $F = 1^- \rightarrow F' = 1$ transition. When the detuning is close to 25 MHz the number of molecules in the target state is reduced dramatically. The origin of this dip is currently under investigation.

Due to the lifetime of the MOT and losses when transferring to the molasses, the fraction of molecules remaining just before the optical pumping pulse is applied was ~ 60 % for the above measurements. Taking into account the loss of molecules during the 300 ms hold time in the magnetic trap, the results suggest that the efficiency of optical pumping to a magnetically trappable state is close to unity. As alluded to above, this does not necessarily mean that the optical pumping efficiency is perfect since molecules in the $|1, +1\rangle$ and $|2, +1\rangle$ states are also captured by the magnetic trap. To investigate the efficiency further, a microwave pulse which drives the $|1, 2, +2\rangle \rightarrow |0, 1, +1\rangle$ transition is applied. For these measurements the molecules are not captured into the magnetic trap but simply recaptured into the MOT following the microwave pulse. Figure 8.2(c) shows the measured line shape using a 50 μs long pulse and (d) shows the resonant Rabi flops corresponding to this transition. From the Rabi flopping data it is evident

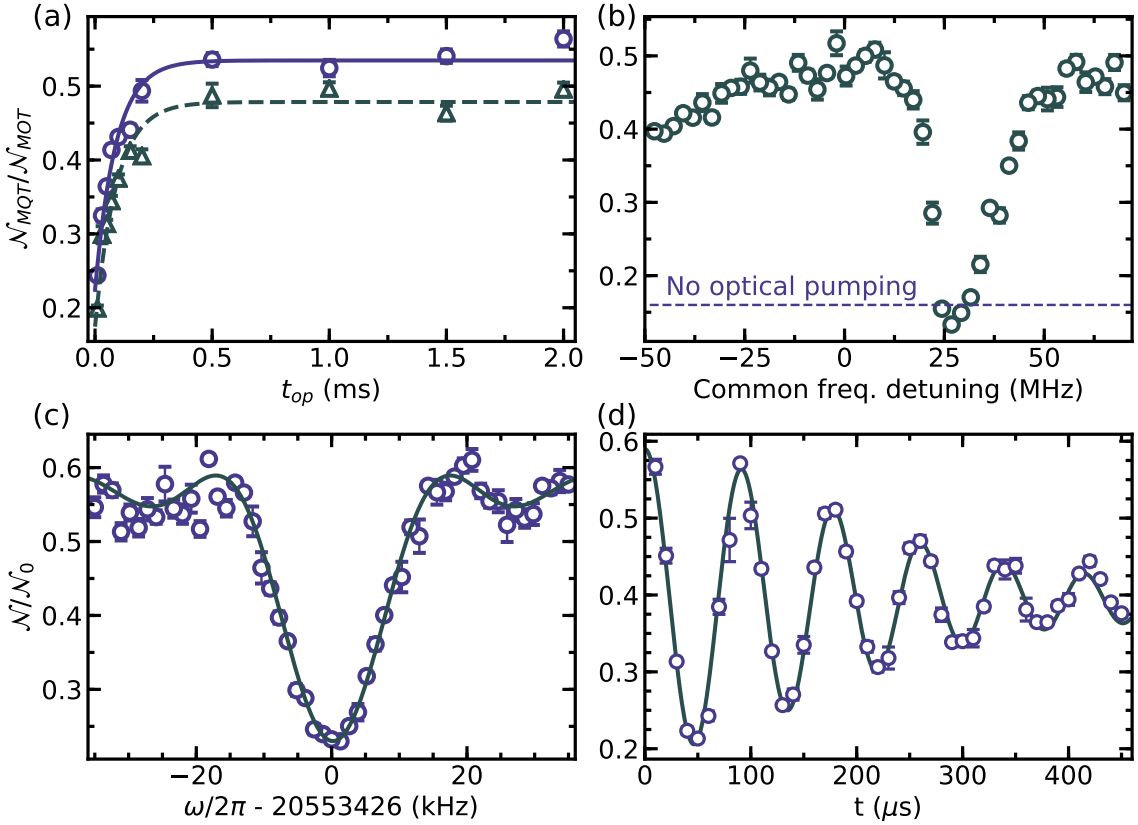

Figure 8.2: (a) Fraction of molecules captured into the magnetic trap as a function of optical pumping duration using a single-pass (△) and retro-reflected (○) beams. (b) Pumping efficiency versus common two-frequency detuning. Zero detuning corresponds to the ω_1 component being near resonant with $F = 1^- \rightarrow F' = 1$. (c) and (d) microwave line shape and Rabi flops corresponding to the $|1, 2, +2\rangle \rightarrow |0, 1, +1\rangle$ transition driven following the optical pumping pulse. Here molecules are recaptured into the MOT following the microwave pulse.

that a π microwave pulse has an efficiency very close to 100 %. This pulse transfers ~ 70 % of the molecules into $N = 0$ and thus sets an upper limit on the optical pumping efficiency. Because the $|1, 2, -2\rangle \rightarrow |0, 1, -1\rangle$ transition may also be driven by this pulse, the efficiency may be slightly smaller.

The two-frequency optical pumping scheme has increased the fraction of molecules transferred to the magnetic trap, shortened the state preparation sequence, and eliminated the need to drive a magnetically sensitive microwave transition. After two microwave pulses on the $|1, 2, +2\rangle \longleftrightarrow |0, 1, +1\rangle$ transition, with a blow away pulse in between, the number of molecules captured back into the MOT was ~ 40 % of the initial number of molecules in the MOT. This is double the number of molecules available compared to using the state preparation scheme of section 6.3 and substantially improved the signal to noise ratio.

8.2 Temperature measurements in the magnetic trap

The experimental sequence to prepare dual species mixtures in the magnetic trap for thermalization measurements is the one described in chapter 6. The only difference is the optical pumping scheme. Due to the high observed loss rate of molecules in the $N = 1$ state, the measurements presented here were performed with molecules in the ground rotational state. As usual, the temperature of the molecule cloud is inferred from a ballistic expansion measurement. For each expansion and trap hold time, the images are integrated over 4 experimental realizations. Figure 8.3 shows an example of a ballistic expansion measurement of a molecule cloud released from the magnetic trap after a 0.6 s hold duration in the presence of a Rb cloud at 90(2) μK temperature. Each point corresponds to 5 repetitions of the cloud size measurement for a given hold duration. The widths are estimated by fitting 2D Gaussian distributions to the integrated images. The error in the size becomes larger for longer expansion times due to a decreasing signal to noise ratio as the cloud expands. For this measurement, the radial temperature is estimated as $T_{\mathrm{r}} = 210(31)$ μK and the axial temperature is $T_{\mathrm{a}} = 196(20)$ μK.

Next, measurements of the molecule cloud temperature are repeated after holding both species in the trap for a variable duration. The rate of change in the temperature difference $\Delta T = T_{\mathrm{CaF}} - T_{\mathrm{Rb}}$ between the two species may be modelled using the following equation [159]

$$\frac{d(\Delta T)}{dt} = -\frac{\beta}{3}(\Delta T)\zeta\sigma_{\mathrm{el}}v_{\mathrm{rel}} \ , \tag{8.1}$$

where ζ is the effective density and σ_{el} is the elastic scattering cross-section for the colliding molecule-atom pair. The mean relative velocity v_{rel} depends on the temperatures T_{Rb} and T_{CaF} of each species and is given by

$$v_{\mathrm{rel}} = \sqrt{\frac{8k_{\mathrm{B}}}{\pi}\left(\frac{T_{\mathrm{Rb}}}{m_{\mathrm{Rb}}} + \frac{T_{\mathrm{CaF}}}{m_{\mathrm{CaF}}}\right)} \ . \tag{8.2}$$

For $T_{\mathrm{Rb}} = 90$ μK and $T_{\mathrm{CaF}} = 200$ μK the relative velocity is $v_{\mathrm{rel}} = 31$ cm/s. It requires $3/\beta$ collisions per particle on average for the mixture to thermalize, where

$$\beta = \frac{4m_{\mathrm{Rb}}m_{\mathrm{CaF}}}{(m_{\mathrm{Rb}} + m_{\mathrm{CaF}})^2} \ . \tag{8.3}$$

For a mixture of hotter molecules and colder atoms it will thus require ~ 3.1 collisions on average for the molecule temperature to equilibrate. For a high rate of thermalization equation 8.1 must be integrated numerically as the relative particle velocity will be a function of the changing cloud temperature[1]. Here a single exponential decay model is used to fit to the experimental data. Because the number of Rb atoms is overwhelmingly

[1]Note also that the effective density ζ is in general time dependent due to finite life times of each species in the trap. In addition, provided the temperature of the cloud changes significantly, more molecules will congregate closer to the trap centre.

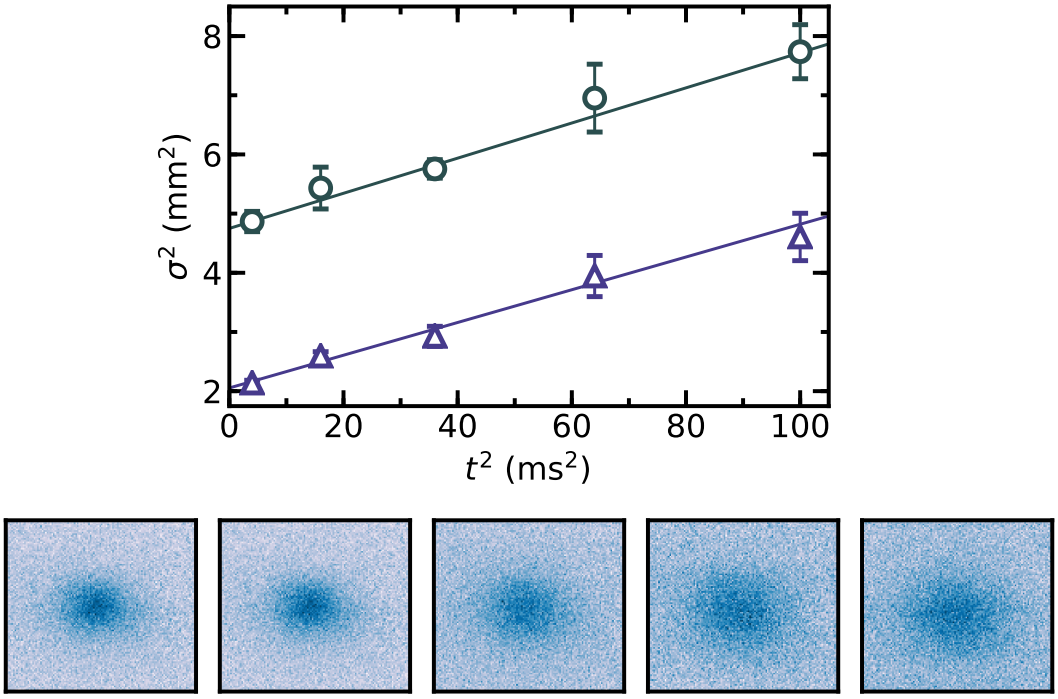

Figure 8.3: Ballistic expansion of a molecule cloud released from the magnetic quadrupole trap along the radial (○) and axial (△) directions. Error bars: standard errors on the mean values estimated from 5 measurements. The bottom panels show fluorescence images of the cloud (from shortest to longest expansion times), which where integrated over four experimental realizations.

larger than the number of molecules, the atom cloud temperature T_{Rb} is constant and the temperature of the molecule cloud will change as

$$T_{\mathrm{CaF}}(t) = (T^0_{\mathrm{CaF}} - T_{\mathrm{Rb}}) \exp(-\Gamma_{\mathrm{th}} t) + T_{\mathrm{Rb}} \ , \tag{8.4}$$

where T^0_{CaF} is the initial temperature and Γ_{th} is the thermalization rate. If the decaying number density of atoms in the trap is taken into account the solution becomes

$$T_{\mathrm{CaF}}(t) = (T^0_{\mathrm{CaF}} - T_{\mathrm{Rb}}) \exp\left(\frac{\Gamma_{\mathrm{th}}}{\Gamma_{\mathrm{Rb}}}\left(e^{-\Gamma_{\mathrm{Rb}} t} - 1\right)\right) + T_{\mathrm{Rb}} \ , \tag{8.5}$$

with Γ_{Rb} the decay rate of atoms.

Figure 8.4 shows temperatures of the molecule cloud in the presence of atoms for variable trap hold durations. These data are fit to the exponential model of eq. 8.5 with the final temperature fixed to $T_{\mathrm{Rb}} = 90\ \mu$K and the atom decay rate $\Gamma_{\mathrm{Rb}} = 0.305(5)\ \mathrm{s}^{-1}$ while T_0 and Γ_{th} are set as free parameters. The fit gives $\Gamma_{\mathrm{th}} = -0.16(21)\ \mathrm{s}^{-1}$, where only the errors in temperature estimates are included. The thermalization and elastic collision rates are related by $\Gamma_{\mathrm{el}} \approx \frac{3}{\beta}\Gamma_{\mathrm{th}}$ and the elastic cross-section is thus given by $\sigma_{\mathrm{el}} = \frac{3}{\beta}\Gamma_{\mathrm{th}}/\zeta v_{\mathrm{rel}}$. For the measurement above $\zeta = (4.0 \pm 0.4) \times 10^9\ \mathrm{cm}^{-3}$ and the value for the elastic cross-section has an upper bound of $1.3 \times 10^{-11}\ \mathrm{cm}^2$ at the 95 % confidence level. It is worth noting here that because of the somewhat high relative motion temperature

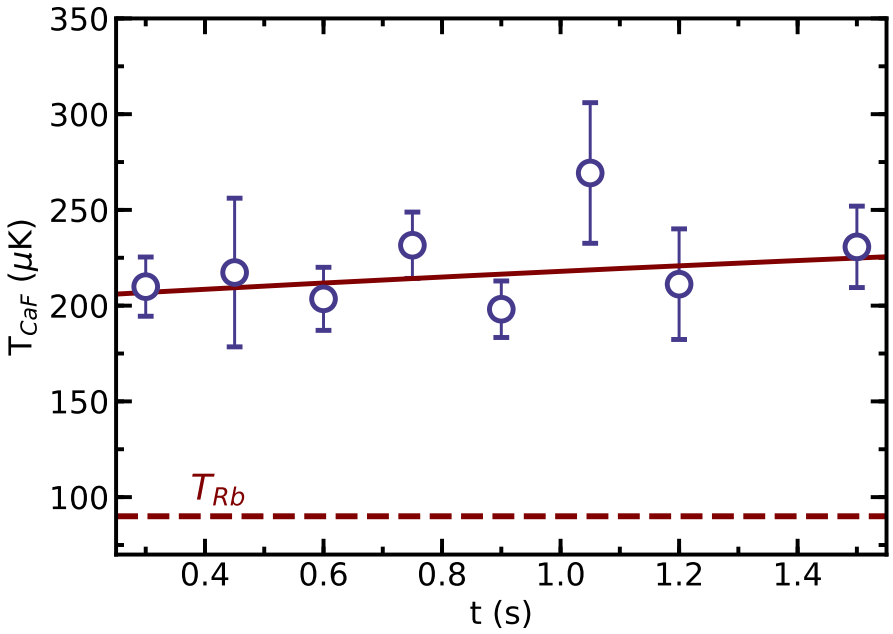

Figure 8.4: Temperature of the molecule cloud as a function of the time it is held in the magnetic trap in the presence of Rb atoms. Each data point corresponds to the best estimates of temperature and the error bars correspond to the fitting errors. The solid line is a fit to the thermalization model described in the main text, which accounts for the decaying atom number density in the trap. The dashed line indicates the temperature of the atoms.

higher order partial waves contribute to the scattering process and in general σ_{el} depends on the temperature. A well known example of strong σ_{el} dependence on the collision energy in ultracold atomic gases is ^{85}Rb [181, 182] for which σ_{el} decreases by some three orders of magnitude in the temperature range of 10 nK $-$ 350 μK.

Earlier theoretical work [106] estimated a typical elastic cross-section of $\sigma_{\text{el}} \approx 2.5 \times 10^{-12}$ cm^2 for the Rb-CaF system at the temperature obtained in the experiment[2]. This value is well below the estimated upper bound from the temperature measurements. It is interesting to compare these results to the elastic scattering measurements in the NaLi-Na system [159]. In that experiment the temperature was sufficiently low so that mostly $s-$wave scattering was important and the authors estimated a cross-section of $\sigma_{\text{el}} = (2.5 \pm 0.5) \times 10^{-11}$ cm^2. This result is particularly favourable for using Na atoms to evaporatively cool NaLi molecules.

[2]Values of σ_{el} were calculated using a range of different scattering lengths and for the value quoted here an s-wave scattering length of $a = +1.5\bar{a}$ was used, where the mean scattering length $\bar{a}$ was defined in section 2.3.1

8.2.1 Future improvements

The measurements described in the previous section do not provide sufficient information to accurately estimate the ratio between elastic and inelastic collision rates. The main technical difficulty in observing thermalization is the currently attainable effective density ζ, which is primarily limited[3] by the rather large size of the molecule cloud in the magnetic trap. In this final section some of the pathways open to increase ζ are explored. Assuming an elastic cross section $\sigma_{\mathrm{el}} = 2 \cdot 10^{-12}$ cm^{-2}, a tenfold increase in ζ is required to achieve thermalization rates of a second.

Increasing the effective density in the magnetic trap

As discussed in section 6.1.1, the molecule density in the magnetic trap is limited by the initial cloud temperature and a displacement from the trap centre. The temperature may in principal be reduced to 5 μK using the single frequency molasses cooling method described in [98] although in this case the temperature of the molecules would be similar to that of the co-trapped atoms. Assuming the cloud is initially of the same size as in the measurements described thus far, the numerical trajectory simulations suggest that reducing the temperature to 5 μK would lead to a cloud size of $\{\sigma_{\mathrm{r}}, \sigma_{\mathrm{a}}\} = \{1.3, 1.0\}$ mm when the trap is loaded at the usual axial gradient of 30 G/cm. This corresponds to an increase in ζ by a factor of ~ 2.5 compared to all previous measurements. The initial size of the cloud may be reduced in a compressed MOT (CMOT)[4]. For an initial circular cloud of 0.9 mm radius and a temperature of 5 μK, the simulations give a cloud size in the magnetic trap of $\{\sigma_{\mathrm{r}}, \sigma_{\mathrm{a}}\} = \{0.8, 0.7\}$ mm at a temperature of $T_{\mathrm{g}} = 55$ μK. This corresponds to nearly a fourfold increase in ζ although the temperature becomes smaller or very close to the atom temperature obtained in the experiment making it more challenging to observe thermalization. Instead, by increasing the trap loading gradient to 100 G/cm and compressing in the CMOT, a $T_{\mathrm{g}} = 100$ μK cloud will have a size of $\{\sigma_{\mathrm{r}}, \sigma_{\mathrm{a}}\} = \{0.9, 0.68\}$ mm once loaded into the magnetic trap. At this point it becomes beneficial to also decrease the atom cloud size. Reducing it by a factor of 2 in all three dimensions would lead to a tenfold overall gain in ζ. As already mentioned several times before in this work, such gains in atom density may be obtained by using a DARK SPOT MOT and preparing atoms in the $|F = 1, M_F = -1\rangle$ state for confinement in the magnetic trap.

[3] Since the molecule cloud is substantially larger than the atom cloud, increasing the atom number density increases the effective density marginally.

[4] A CMOT for molecules was investigated in this work and the size of the cloud was reduced to ~ 0.9 mm along both dimensions at the cost of a substantial loss in molecule number. Because the size of the cloud in the magnetic trap was limited by its temperature, the compressed MOT was not used.

Loading an optical dipole trap

The optical dipole trap [183] typically provides much tighter confinement and is a popular trap for ultracold collision experiments. It relies on the optical dipole force and in its simplest form consists of a single tightly focused laser beam with a Gaussian intensity profile, tuned far away from an atomic or molecular resonance. For temperatures much lower than the depth of the trapping potential, the particles accumulate close to the intensity maximum and undergo simple harmonic motion with radial frequency $\omega_\mathrm{r} = \sqrt{4U_0/mw_0^2}$ and axial frequency $\omega_\mathrm{a} = \sqrt{2}\omega_\mathrm{r}/kw_0$. The trap depth $U_0 = \alpha P/\pi c\epsilon_0 w_0^2$ depends on the polarizability α and the waist radius w_0 of the trapping beam. Using a 30 W beam at $\lambda = 1064$ nm focused down to $w_0 = 40$ μm, the trap frequencies[5] for CaF are $\omega_\mathrm{r} = 2\pi \times 2$ kHz and $\omega_\mathrm{a} = 2\pi \times 12$ Hz. For Rb atoms the trap frequencies[6] are $\omega_\mathrm{r} = 2\pi \times 4$ kHz and $\omega_\mathrm{a} = 2\pi \times 24$ Hz. The cloud size in the trap is given by $\sigma_i = (k_\mathrm{B}T_i/m\omega_i^2)^{1/2}$, where $i \in \{r, a\}$ and is many times smaller along the radial direction because the light intensity gradient is much larger than along the direction of the trapping beam. Neglecting the gravitational sag, loading such a trap with $T_\mathrm{Rb} = 40$ μK and $T_\mathrm{CaF} = 100$ μK would lead to a spatial density overlap of $\zeta/\mathcal{N}_\mathrm{Rb} = 3.8 \cdot 10^5$ cm^{-3}. Even when only 1 % of the atoms initially loaded into the MOT are transferred into the optical dipole trap, the effective density $\zeta > 10^{12}$ cm^{-3}, which is far greater than what could be achieved in the magnetic trap with the considerations above. In addition, combining two dipole trap beams which intersect at a shallow angle would increase the confinement along the weak trap axis and increase the density even further.

[5] The trap frequencies are calculated using results from [100] and rescaled to match the different trap beam parameters.

[6] The polarizability value for ^{87}Rb at 1064 nm is taken from [184].

9 | Conclusions

In this work the first laser-cooled mixtures of atoms and molecules were prepared and confined in magneto-optical and magnetic quadrupole traps. Inelastic atom-molecule collisions were studied both experimentally and theoretically and the conditions under which sympathetic cooling of molecules should be feasible were identified. In particular, an inelastic atom-induced loss rate coefficient of $k_2 = (1.43 \pm 0.29) \times 10^{-10}$ cm$^3 \cdot$ s^{-1} was measured in the dual species MOT. Although high, the typical time-scale of subsequent experimental steps to prepare molecules in a single quantum state in the ground rotational level are fast so that this loss is tolerable. When molecules occupy the $N = 0$ state, the loss rate coefficient is at least an order of magnitude smaller and in the magnetic quadrupole trap was measured to change from $k_2 = (6.6 \pm 1.5) \times 10^{-11}$ cm$^3 \cdot$ s^{-1}, for $N = 1$, to $k_2 = (-0.05 \pm 2.9) \times 10^{-12}$ cm$^3 \cdot$ s^{-1}, when the molecular sample is prepared in $N = 0$.

With several realistic near term improvements to the existing apparatus, the density overlap between the two species may be improved substantially which will allow to explore elastic atom-molecule collisions in the magnetic trap. Successful implementation of transverse laser cooling of the molecular beam and a new optical pumping protocol, described in the previous chapter, enhanced the number of molecules in the magnetic trap by a factor of 7-8 compared to the available number in experiments described in chapters 5 and 6. These improvements enabled the first proof of principle thermalization measurement. Although no evidence of thermalization was discovered, an upper bound of 1.3×10^{-11} cm^2 at the 95 % confidence level was placed on the scattering cross-section.

In addition, the existing apparatus is capable of accommodating an optical dipole trap or a 1D optical lattice. The enormous increase in the number density of both the molecular and atomic samples provided by the optical trap will lead to many exciting new experiments.

Finally, findings from these studies will feed into the design of future experiments aiming to produce a quantum degenerate gas of strongly interacting polar molecules.

A | Geometric ray tracing

Geometric ray tracing is a useful tool for investigating the imaging performance of a particular imaging system. Although many commercial software packages to perform numerical ray tracing exist it is useful and reasonably simple to set up a custom ray tracer from first principles to gain access to a larger variety of optical system characteristics that one would like to investigate in greater depth. In particular, one of the main goals was to determine the light collection efficiency of the CaF imaging system. Here a derivation, without going into too much algebraic detail, of the relevant equations for geometric ray tracing are presented.

To find the trajectory of an optical ray traversing an optical system two key ingredients are required: finding the intersection points of rays with spherical or planar surfaces (surfaces described using conic sections are not considered here) and determining how the direction of an incident ray is modified by these surfaces. The direction of an optical ray will change either due to refraction or reflection and equations describing each process are derived below.

Ray-surface intercepts

First, consider a spherical surface (figure A.1) with radius of curvature R centred at position z_c on the optical axis (defined as the z-axis). The intersection point of an optical ray originating from a point described by a position vector $\vec{p_0}$ along the direction $\hat{k}$ may be expressed as

$$\vec{p} = \vec{p_0} + \lambda \hat{k} \tag{A.1}$$

The problem of finding the intersection point given the pair of vectors $\vec{p_0}$ and $\hat{k_0}$ is reduced to simply finding the value λ for which the (x, y, z) components of $\vec{p}$ all lie on the spherical surface described by

$$x^2 + y^2 + (z - z_c)^2 = R^2 \tag{A.2}$$

Defining an origin vector $\vec{o} = [0, 0, z - z_c]$ the solution for λ may be written in compact vector form

$$\lambda = -(\vec{p_0} - \vec{o}) \cdot \hat{k_0} \pm \sqrt{[(\vec{p_0} - \vec{o}) \cdot \hat{k}]^2 - |\vec{p_0} - \vec{o}|^2 + R^2} \tag{A.3}$$

There are 3 scenarios to consider. If the square root in eq. A.3 is negative then there are no solutions to the posed problem and the ray does not have an intercept with the

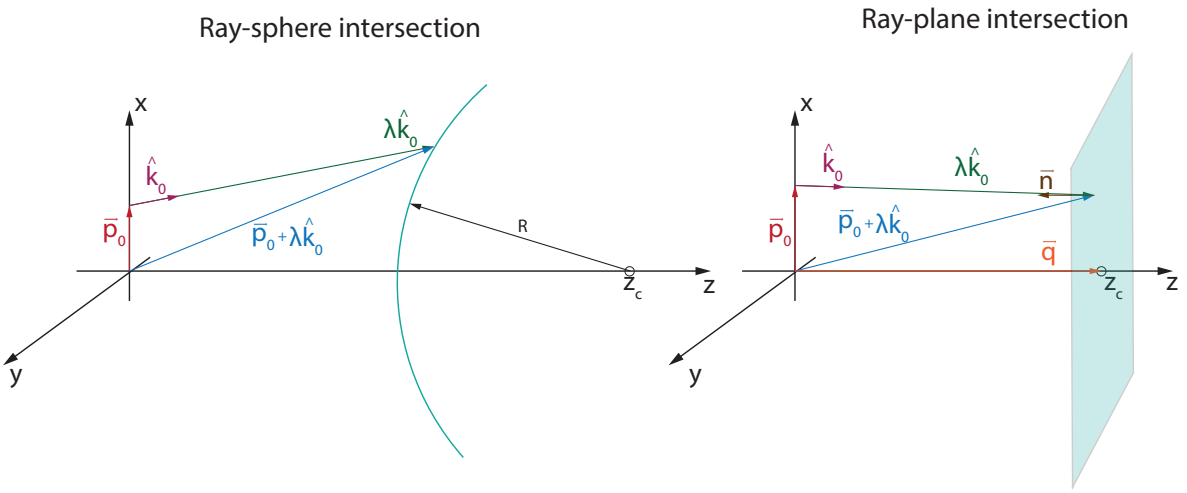

Figure A.1: Graphical representation of the vectors (defined in the text) used to calculate optical ray intercepts with a spherical (left) and planar (right) surfaces.

specified surface, if it is equal to zero there is only one intercept point and if it is greater than zero there are two intersection points. The correct point is chosen by considering the radius of curvature of the surface. For positive R the smaller λ of the pair is selected and for negative R the larger λ is retained.

To find the intersection point with a planar surface consider the equation describing a 3-D plane

$$\hat{n} \cdot (\vec{p} - \vec{o}) = 0 \tag{A.4}$$

The vectors $\vec{p}$ and $\vec{o}$ are defined identically as above and define two points lying in the same plane on the z-axis at position z_c. The dot product of the difference of these two vectors with the unit normal vector $\hat{n}$ thus must be equal to zero as the two vectors are always orthogonal if they describe a planar surface in 3-D.

Substituting the definition of $\vec{p}$ into the above equation leads to the following solution for the coefficient λ that determines the intersection point

$$\lambda = \frac{\hat{n} \cdot (\vec{o} - \vec{p_0})}{\hat{k_0} \cdot \hat{n}} \tag{A.5}$$

Having found the intercept points with spherical and planar surfaces all that is left to do is find how the ray direction vectors are modified due to refraction and reflection.

Snell's Law in vector form

Consider a ray incident on an arbitrary surface with an angle θ_0 relative to a unit normal vector pointing towards the direction of the incoming ray. The incoming ray (figure A.2) propagates in a medium with refractive index n_1 and is refracted by a surface which

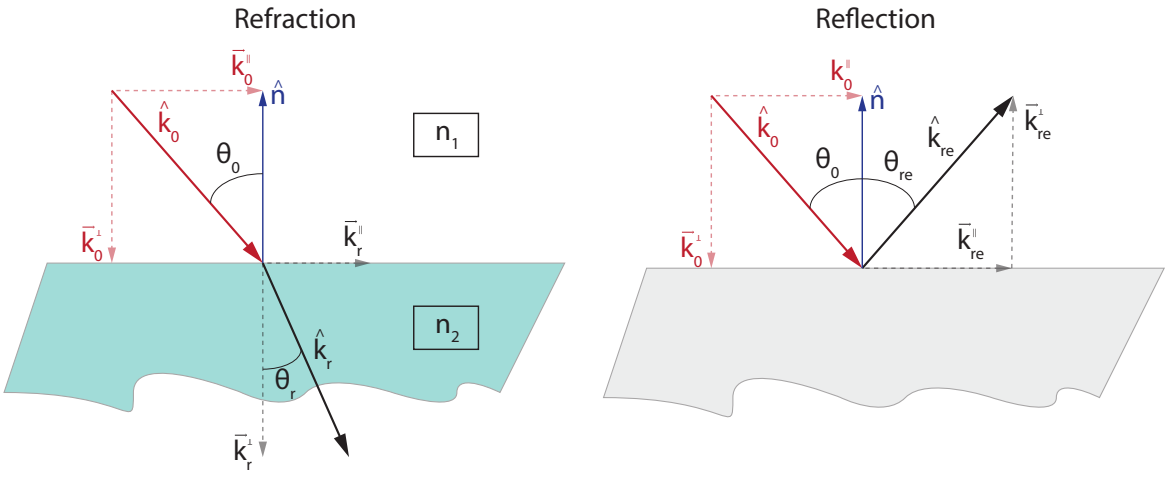

Figure A.2: Refraction and reflection of optical rays. The graphs define the relative vectors used in the text to derive Snell's Law in vector form and the change in the ray direction due to specular reflection.

separates a medium with refractive index n_2. The angle θ_r of the refracted ray is found from Snell's Law

$$n_1 \sin(\theta_0) = n_2 \sin(\theta_r) \tag{A.6}$$

The unit vector $\hat{k_0}$ describing the incident ray is changed to $\hat{k_r}$ upon refraction by the separating boundary. The vector $\hat{k_r}$ is decomposed into a superposition of two vectors: one parallel to the surface ($\vec{k}_0^{\parallel}$) and the other orthogonal ($\vec{k}_0^{\perp}$)

$$\hat{k_r} = \vec{k}_0^{\parallel} + \vec{k}_0^{\perp} \tag{A.7}$$

Similarly the incident vector $\hat{k_0}$ is decomposed into the sum of vectors $\vec{k}_r^{\parallel}$ and $\vec{k}_r^{\perp}$. Since $|\hat{k}_0| = 1$ and $|\hat{k}_r| = 1$ the angles θ_0 and θ_r are simply given by

$$\begin{aligned} \sin(\theta_0) &= |\vec{k}_0^{\parallel}| \\ \sin(\theta_r) &= |\vec{k}_r^{\parallel}| \end{aligned} \tag{A.8}$$

Using Snell's Law and the fact that the vectors $\vec{k}_0^{\parallel}$ and $\vec{k}_r^{\parallel}$ both point in the same direction the parallel component of the refracted vector may be written as

$$\vec{k}_r^{\parallel} = \frac{n_1}{n_2}(\hat{k}_0 + \cos\theta_0 \hat{n}) \tag{A.9}$$

The magnitude of the perpendicular component is found using Pythagoras theorem and since it points in a direction opposite to the unit normal vector it is given by

$$\vec{k}_r^{\perp} = -\hat{n}\sqrt{1 - |\vec{k}_r^{\parallel}|^2} \tag{A.10}$$

Using eqs. A.6 and A.8 this may be expressed more conveniently in terms of known quantities

$$\vec{k}_r^{\perp} = -\hat{n}\sqrt{1 - \frac{n_1^2}{n_2^2}[1 - \cos^2(\theta_0)]} \tag{A.11}$$

Using the fact that $\cos\theta_0 = -\hat{n}\cdot\hat{k_0}$ the final expression for the refracted vector may be written compactly as

$$\hat{k_r} = \frac{n_1}{n_2}\hat{k_0} - \left\{\frac{n_1}{n_2}\hat{n}\cdot\hat{k_0} - \sqrt{1 - \frac{n_1^2}{n_2^2}[1-(\hat{n}\cdot\hat{k_0})^2]}\right\}\hat{n} \tag{A.12}$$

The above equation gives the direction of the refracted ray given the incident ray direction relative to the unit surface normal vector. This equation is general and suitable to model refraction by any surface provided that $\hat{n}$ may be determined.

Reflection

For specular reflections the angle of incidence is equal to the angle of reflection. As before, the incoming and outgoing ray directions are defined relative to the surface normal. A similar procedure to the one above is used to find the reflected ray vector $\hat{k}_{re}$. From figure A.2 it is easy to see that the two orthogonal components of the incident and reflected rays are related in the following way

$$\begin{aligned}\vec{k}_0^{\parallel} &= \vec{k}_{re}^{\parallel}\\ \vec{k}_0^{\perp} &= -\vec{k}_{re}^{\perp}\end{aligned} \tag{A.13}$$

The reflected ray may now be written as

$$\hat{k}_{re} = \hat{k_0} - 2\vec{k}_0^{\perp} \tag{A.14}$$

The perpendicular component is equal to

$$\vec{k}_0^{\perp} = (\hat{k_0}\cdot\hat{n})\hat{n} \tag{A.15}$$

And finally the reflected ray direction vector may be written as

$$\hat{k}_{re} = \hat{k_0} - 2(\hat{k_0}\cdot\hat{n})\hat{n} \tag{A.16}$$

As before the outgoing ray direction is expressed as a function of the incoming ray and its direction relative to the surface normal.

B | Design of a new buffer gas cell

Molecular MOTs with the largest number of molecules have been reported by the Harvard and JILA groups. Both groups have reported numbers exceeding 10^5 molecules in their traps [99, 124], which is roughly an order of magnitude higher than the number trapped using the apparatus described in this work[1]. These differences may arise due to several reasons including the design of the buffer gas source. Motivated to increase the flux of molecules a new buffer gas cell was designed (and already machined though not tested) based on our findings and those of other groups.

The design of the new cell is shown in figure B.1. The dimensions of this cell were kept very similar to the original cell used in this work so that it stayed compatible with the cryostat and vacuum chamber assembly. The design has two key new features introduced. It was found by chance on several occasions that a Ca target in contact with the cell walls would produce a slower molecular beam and lead to an increase in the number of molecules captured into the MOT. For this reason the new cell has a fixed target in the shape of a 15 mm diameter cylinder glued to a copper plate which attaches to the side of the cell. In the old design a new surface area on the target was exposed to the ablation laser by turning the target using a rotary vacuum feedthrough. In this new design the cell is entirely thermally decoupled from components at ambient room temperature while the diameter of the snorkel via which the ablation laser pulse enters the cell is made sufficiently wide such that any spot on the Ca target may be exposed. Both groups also seem to use fixed targets in their cells. The second difference is the method of delivering the He gas into the cell. Both JILA and Harvard found that a flow of He along the propagation direction of the molecular beam works best. In addition, a diffuser plate sandwiched between the He inlet and the cell itself, prevents the stream of gas from directly reaching the Ca target. The JILA group in particular have reported that a diffuser plate substantially improves the flux of molecules at lower forward velocities.

The new cell has the same inner diameter bore and length as the original one. Extension pieces of different lengths and exit apertures with different diameters were also machined and may easily be swapped to test which arrangement works best. Because these are tedious tasks it has never been experimented with before, especially using the number of molecules in the MOT as a figure of merit.

[1] With transverse cooling of the molecular beam this difference was reduced to a factor of ~ 3.

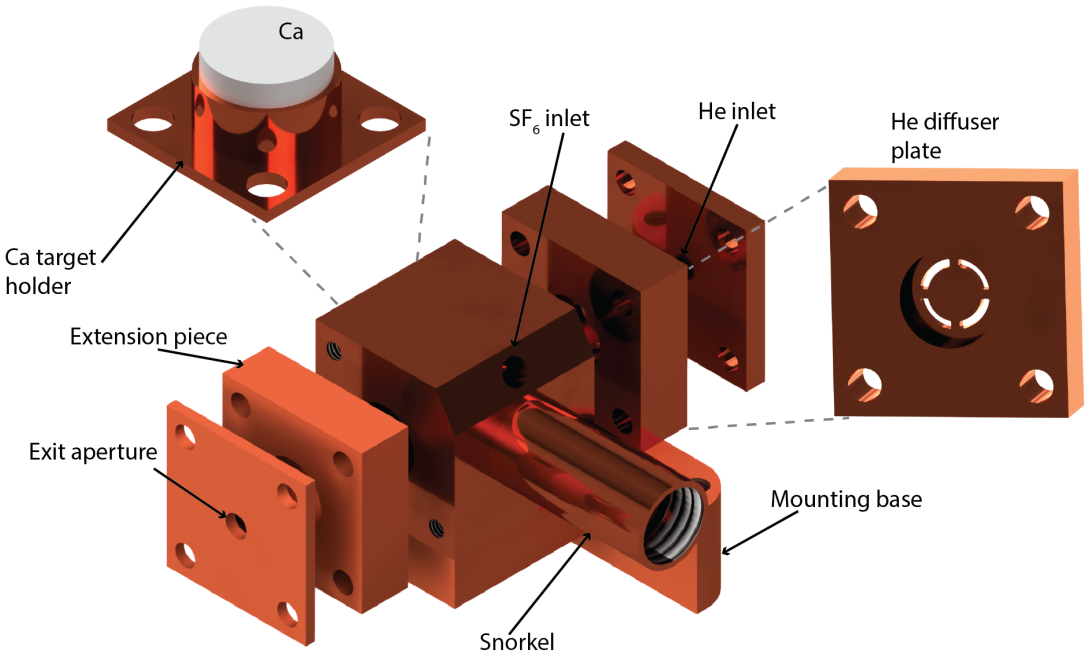

Figure B.1: Design of a new buffer gas cell.

Other observations

The JILA group have reported the use of a Y_2O_3 powder to dramatically increase the number of molecules exiting their buffer gas cell. By coating the inner walls of the cell with just the correct amount of powder the peak signal was enhanced by a factor of 4. Although the reasons for this observed enhancement are unclear[2] it would be interesting to coat the cell walls with a CaF_2 powder.

It was found on multiple occasions that depositing a new layer of coconut charcoal would very substantially improve the MOT number and the longer term stability of the source. This suggests that in the current setup there may not be sufficient pumping of He gas especially in the vicinity of the exit aperture where the rate of collisions with emerging CaF molecules is high. Although the current source chamber and cryostat assembly would not accommodate larger sorb shields it should be possible to add additional fins coated with charcoal to the top lid of the radiation shield.

Several experiments working with buffer gas cooled hydroxides [185] have found that electronically exciting the metal atoms with laser light substantially increases the yield of molecules. No such experiments have been reported for molecules containing a fluorine atom. It would thus be interesting to excite the Ca atoms produced in the buffer gas cell to the $^3P_1$ state using light at 657 nm and search for an effect on the reaction yield.

[2] A speculative guess is that the powder coating reduces the reaction rate of molecules with the cell walls and thus allows to extract a larger number of molecules into the beam.

Bibliography

[1] Arthur Ashkin. Trapping of atoms by resonance radiation pressure. *Physical Review Letters*, 40(12):729, 1978.

[2] Alan L Migdall, John V Prodan, William D Phillips, Thomas H Bergeman, and Harold J Metcalf. First observation of magnetically trapped neutral atoms. *Physical Review Letters*, 54(24):2596, 1985.

[3] EL Raab, M Prentiss, Alex Cable, Steven Chu, and David E Pritchard. Trapping of neutral sodium atoms with radiation pressure. *Physical Review Letters*, 59(23):2631, 1987.

[4] Nicolas Schlosser, Georges Reymond, Igor Protsenko, and Philippe Grangier. Sub-poissonian loading of single atoms in a microscopic dipole trap. *Nature*, 411(6841):1024–1027, 2001.

[5] Mike H Anderson, Jason R Ensher, Michael R Matthews, Carl E Wieman, and Eric A Cornell. Observation of Bose-Einstein condensation in a dilute atomic vapor. *Science*, pages 198–201, 1995.

[6] Kendall B Davis, M-O Mewes, Michael R Andrews, Nicolaas J van Druten, Dallin S Durfee, DM Kurn, and Wolfgang Ketterle. Bose-Einstein condensation in a gas of sodium atoms. *Physical Review Letters*, 75(22):3969, 1995.

[7] Brian DeMarco and Deborah S Jin. Onset of Fermi degeneracy in a trapped atomic gas. *Science*, 285(5434):1703–1706, 1999.

[8] SR Granade, ME Gehm, KM O'Hara, and JEl Thomas. All-optical production of a degenerate Fermi gas. *Physical Review Letters*, 88(12):120405, 2002.

[9] Mikhail D Lukin, Michael Fleischhauer, Robin Cote, LM Duan, Dieter Jaksch, J Ignacio Cirac, and Peter Zoller. Dipole blockade and quantum information processing in mesoscopic atomic ensembles. *Physical Review Letters*, 87(3):037901, 2001.

[10] Henning Labuhn, Daniel Barredo, Sylvain Ravets, Sylvain De Léséleuc, Tommaso Macrì, Thierry Lahaye, and Antoine Browaeys. Tunable two-dimensional arrays of

single Rydberg atoms for realizing quantum Ising models. *Nature*, 534(7609):667–670, 2016.

[11] Nathan Hinkley, Jeff A Sherman, Nathaniel B Phillips, Macro Schioppo, Nathan D Lemke, Kyle Beloy, Marco Pizzocaro, Christopher W Oates, and Andrew D Ludlow. An atomic clock with 10^{-18} instability. *Science*, 341(6151):1215–1218, 2013.

[12] Andrew D Ludlow, Martin M Boyd, Jun Ye, Ekkehard Peik, and Piet O Schmidt. Optical atomic clocks. *Reviews of Modern Physics*, 87(2):637, 2015.

[13] Dylan O Sabulsky, Indranil Dutta, EA Hinds, Benjamin Elder, Clare Burrage, and Edmund J Copeland. Experiment to detect dark energy forces using atom interferometry. *Physical Review Letters*, 123(6):061102, 2019.

[14] Savas Dimopoulos, Peter W Graham, Jason M Hogan, Mark A Kasevich, and Surjeet Rajendran. Gravitational wave detection with atom interferometry. *Physics Letters B*, 678(1):37–40, 2009.

[15] Immanuel Bloch, Jean Dalibard, and Wilhelm Zwerger. Many-body physics with ultracold gases. *Reviews of Modern Physics*, 80(3):885, 2008.

[16] Markus Greiner, Olaf Mandel, Tilman Esslinger, Theodor W Hänsch, and Immanuel Bloch. Quantum phase transition from a superfluid to a Mott insulator in a gas of ultracold atoms. *Nature*, 415(6867):39–44, 2002.

[17] Russell A Hart, Pedro M Duarte, Tsung-Lin Yang, Xinxing Liu, Thereza Paiva, Ehsan Khatami, Richard T Scalettar, Nandini Trivedi, David A Huse, and Randall G Hulet. Observation of antiferromagnetic correlations in the Hubbard model with ultracold atoms. *Nature*, 519(7542):211–214, 2015.

[18] Masao Ogata and Hidetoshi Fukuyama. The t-J model for the oxide high-T_c superconductors. *Reports on Progress in Physics*, 71(3):036501, 2008.

[19] Axel Griesmaier, Jörg Werner, Sven Hensler, Jürgen Stuhler, and Tilman Pfau. Bose-Einstein condensation of chromium. *Physical Review Letters*, 94(16):160401, 2005.

[20] Mingwu Lu, Nathaniel Q Burdick, Seo Ho Youn, and Benjamin L Lev. Strongly dipolar Bose-Einstein condensate of dysprosium. *Physical Review Letters*, 107(19):190401, 2011.

[21] K Aikawa, A Frisch, M Mark, S Baier, A Rietzler, R Grimm, and F Ferlaino. Bose-Einstein condensation of erbium. *Physical Review Letters*, 108(21):210401, 2012.

[22] Simon Baier, Manfred J Mark, Daniel Petter, Kiyotaka Aikawa, Lauriane Chomaz, Zi Cai, M Baranov, P Zoller, and F Ferlaino. Extended Bose-Hubbard models with ultracold magnetic atoms. *Science*, 352(6282):201–205, 2016.

[23] Tatjana Wilk, A Gaëtan, C Evellin, J Wolters, Y Miroshnychenko, P Grangier and A Browaeys. Entanglement of two individual neutral atoms using Rydberg blockade. *Physical Review Letters*, 104(1):010502, 2010.

[24] Hannes Bernien, Sylvain Schwartz, Alexander Keesling, Harry Levine, Ahmed Omran, Hannes Pichler, Soonwon Choi, Alexander S Zibrov, Manuel Endres, Markus Greiner, et al. Probing many-body dynamics on a 51-atom quantum simulator. *Nature*, 551(7682):579–584, 2017.

[25] Antoine Browaeys and Thierry Lahaye. Many-body physics with individually controlled Rydberg atoms. *Nature Physics*, 16(2):132–142, 2020.

[26] Bo Yan, Steven A Moses, Bryce Gadway, Jacob P Covey, Kaden RA Hazzard, Ana Maria Rey, Deborah S Jin, and Jun Ye. Observation of dipolar spin-exchange interactions with lattice-confined polar molecules. *Nature*, 501(7468):521–525, 2013.

[27] Kaden RA Hazzard, Bryce Gadway, Michael Foss-Feig, Bo Yan, Steven A Moses, Jacob P Covey, Norman Y Yao, Mikhail D Lukin, Jun Ye, Deborah S Jin, et al. Many-body dynamics of dipolar molecules in an optical lattice. *Physical Review Letters*, 113(19):195302, 2014.

[28] Alexey V Gorshkov, Salvatore R Manmana, Gang Chen, Eugene Demler, Mikhail D Lukin, and Ana Maria Rey. Quantum magnetism with polar alkali-metal dimers. *Physical Review A*, 84(3):033619, 2011.

[29] GR Stewart. Superconductivity in iron compounds. *Reviews of Modern Physics*, 83(4):1589, 2011.

[30] Andrea Micheli, GK Brennen, and Peter Zoller. A toolbox for lattice-spin models with polar molecules. *Nature Physics*, 2(5):341–347, 2006.

[31] David DeMille. Quantum computation with trapped polar molecules. *Physical Review Letters*, 88(6):067901, 2002.

[32] Michael Hughes, Matthew D Frye, Rahul Sawant, Gaurav Bhole, Jonathan A Jones, Simon L Cornish, MR Tarbutt, Jeremy M Hutson, Dieter Jaksch, and Jordi Mur-Petit. Robust entangling gate for polar molecules using magnetic and microwave fields. *Physical Review A*, 101(6):062308, 2020.

[33] André, Axel and DeMille, David and Doyle, John M and Lukin, Mikhail D and Maxwell, St Ex and Rabl, Peter and Schoelkopf, Robert J and Zoller, Peter. A coherent all-electrical interface between polar molecules and mesoscopic superconducting resonators. *Nature Physics*, 2(9):636–642, 2006.

[34] Victor V Albert, Jacob P Covey, and John Preskill. Robust encoding of a qubit in a molecule. *Physical Review X*, 10(3):031050, 2020.

[35] Sara L Campbell, RB Hutson, GE Marti, A Goban, N Darkwah Oppong, RL McNally, L Sonderhouse, JM Robinson, W Zhang, BJ Bloom, et al. A Fermi-degenerate three-dimensional optical lattice clock. *Science*, 358(6359):90–94, 2017.

[36] L Badurina, E Bentine, Diego Blas, K Bongs, D Bortoletto, T Bowcock, K Bridges, W Bowden, O Buchmueller, C Burrage, et al. AION: an atom interferometer observatory and network. *Journal of Cosmology and Astroparticle Physics*, 2020(05):011, 2020.

[37] B Canuel, A Bertoldi, L Amand, E Pozzo Di Borgo, T Chantrait, C Danquigny, M Dovale Álvarez, B Fang, Andreas Freise, R Geiger, et al. Exploring gravity with the MIGA large scale atom interferometer. *Scientific Reports*, 8(1):1–23, 2018.

[38] Jun Kobayashi, Atsushi Ogino, and Shin Inouye. Measurement of the variation of electron-to-proton mass ratio using ultracold molecules produced from laser-cooled atoms. *Nature Communications*, 10(1):1–5, 2019.

[39] SS Kondov, C-H Lee, KH Leung, C Liedl, I Majewska, R Moszynski, and T Zelevinsky. Molecular lattice clock with long vibrational coherence. *Nature Physics*, 15(11):1118–1122, 2019.

[40] Peter W Graham and Surjeet Rajendran. Axion dark matter detection with cold molecules. *Physical Review D*, 84(5):055013, 2011.

[41] Vitaly Andreev and NR Hutzler. Improved limit on the electric dipole moment of the electron. *Nature*, 562(7727):355–360, 2018.

[42] William B Cairncross, Daniel N Gresh, Matt Grau, Kevin C Cossel, Tanya S Roussy, Yiqi Ni, Yan Zhou, Jun Ye, and Eric A Cornell. Precision measurement of the electron's electric dipole moment using trapped molecular ions. *Physical Review Letters*, 119(15):153001, 2017.

[43] JJ Hudson, BE Sauer, MR Tarbutt, and EA Hinds. Measurement of the electron electric dipole moment using YbF molecules. *Physical review letters*, 89(2):023003, 2002.

[44] Noah Fitch, Jongseok Lim, Ed A Hinds, Ben E Sauer, and Mike R Tarbutt. Methods for measuring the electron's electric dipole moment using ultracold YbF molecules. *Quantum Science and Technology*, 2020.

[45] DM Neumark, AM Wodtke, GN Robinson, CC Hayden, K Shobatake, RK Sparks, TP Schafer, and YT Lee. Molecular beam studies of the F+ D_2 and F+ HD reactions. *The Journal of chemical physics*, 82(7):3067–3077, 1985.

[46] Ayelet Klein, Yuval Shagam, Wojciech Skomorowski, Piotr S Żuchowski, Mariusz Pawlak, Liesbeth MC Janssen, Nimrod Moiseyev, Sebastiaan YT van de Meerakker, Ad van der Avoird, Christiane P Koch, et al. Directly probing anisotropy in atom–molecule collisions through quantum scattering resonances. *Nature Physics*, 13(1):35–38, 2017.

[47] Matthew T Hummon, Timur V Tscherbul, Jacek Kłos, Hsin-I Lu, Edem Tsikata, Wesley C Campbell, Alexander Dalgarno, and John M Doyle. Cold N + NH collisions in a magnetic trap. *Physical Review Letters*, 106(5):053201, 2011.

[48] M-G Hu, Yu Liu, David D Grimes, Y-W Lin, Andrei H Gheorghe, Romain Vexiau, Nadia Bouloufa-Maafa, Olivier Dulieu, Till Rosenband, and K-K Ni. Direct observation of bimolecular reactions of ultracold KRb molecules. *Science*, 366(6469):1111–1115, 2019.

[49] John L Bohn, Ana Maria Rey, and Jun Ye. Cold molecules: Progress in quantum engineering of chemistry and quantum matter. *Science*, 357(6355):1002–1010, 2017.

[50] N Balakrishnan and A Dalgarno. Chemistry at ultracold temperatures. *Chemical Physics Letters*, 341(5-6):652–656, 2001.

[51] S Ospelkaus, K-K Ni, D Wang, MHG De Miranda, B Neyenhuis, 1 G Quéméner, PS Julienne, JL Bohn, DS Jin, and J Ye. Quantum-state controlled chemical reactions of ultracold potassium-rubidium molecules. *Science*, 327(5967):853–857, 2010.

[52] K-K Ni, S Ospelkaus, D Wang, G Quéméner, Brian Neyenhuis, MHG De Miranda, JL Bohn, Jun Ye, and DS Jin. Dipolar collisions of polar molecules in the quantum regime. *Nature*, 464(7293):1324–1328, 2010.

[53] Kyle Matsuda, Luigi De Marco, Jun-Ru Li, William G Tobias, Giacomo Valtolina, Goulven Quéméner, and Jun Ye. Resonant collisional shielding of reactive molecules using electric fields. *Science*, 370(6522):1324–1327, 2020.

[54] Loïc Anderegg, Sean Burchesky, Yicheng Bao, Scarlett S Yu, Tijs Karman, Eunmi Chae, Kang-Kuen Ni, Wolfgang Ketterle, and John M Doyle. Observation of microwave shielding of ultracold molecules. *arXiv preprint arXiv:2102.04365*, 2021.

[55] Luigi De Marco, Giacomo Valtolina, Kyle Matsuda, William G Tobias, Jacob P Covey, and Jun Ye. A degenerate Fermi gas of polar molecules. *Science*, 363(6429):853–856, 2019.

[56] Philip D Gregory, Jacob A Blackmore, Sarah L Bromley, and Simon L Cornish. Loss of Ultracold $^{87}Rb^{133}Cs$ Molecules via Optical Excitation of Long-Lived Two-Body Collision Complexes. *Physical Review Letters*, 124(16):163402, 2020.

[57] Lawrence W Cheuk, Loïc Anderegg, Yicheng Bao, Sean Burchesky, S Yu Scarlett, Wolfgang Ketterle, Kang-Kuen Ni, and John M Doyle. Observation of collisions between two ultracold ground-state CaF molecules. *Physical Review Letters*, 125(4):043401, 2020.

[58] Daniel K Hoffmann, Thomas Paintner, Wolfgang Limmer, Dmitry S Petrov, and Johannes Hecker Denschlag. Reaction kinetics of ultracold molecule-molecule collisions. *Nature Communications*, 9(1):1–6, 2018.

[59] MHG De Miranda, A Chotia, Brian Neyenhuis, D Wang, G Quéméner, Silke Ospelkaus, JL Bohn, Jun Ye, and DS Jin. Controlling the quantum stereodynamics of ultracold bimolecular reactions. *Nature Physics*, 7(6):502–507, 2011.

[60] Ph Courteille, RS Freeland, DJ Heinzen, FA Van Abeelen, and BJ Verhaar. Observation of a Feshbach resonance in cold atom scattering. *Physical Review Letters*, 81(1):69, 1998.

[61] Nikolay V Vitanov, Andon A Rangelov, Bruce W Shore, and Klaas Bergmann. Stimulated Raman adiabatic passage in physics, chemistry, and beyond. *Reviews of Modern Physics*, 89(1):015006, 2017.

[62] Peter K Molony, Philip D Gregory, Zhonghua Ji, Bo Lu, Michael P Köppinger, C Ruth Le Sueur, Caroline L Blackley, Jeremy M Hutson, and Simon L Cornish. Creation of ultracold $^{87}Rb^{133}Cs$ molecules in the rovibrational ground state. *Physical review letters*, 113(25):255301, 2014.

[63] Timur M Rvachov, Hyungmok Son, Ariel T Sommer, Sepehr Ebadi, Juliana J Park, Martin W Zwierlein, Wolfgang Ketterle, and Alan O Jamison. Long-lived ultracold molecules with electric and magnetic dipole moments. *Physical Review Letters*, 119(14):143001, 2017.

[64] Mingyang Guo, Bing Zhu, Bo Lu, Xin Ye, Fudong Wang, Romain Vexiau, Nadia Bouloufa-Maafa, Goulven Quéméner, Olivier Dulieu, and Dajun Wang. Creation of an ultracold gas of ground-state dipolar $^{23}Na^{87}Rb$ molecules. *Physical Review Letters*, 116(20):205303, 2016.

[65] Jee Woo Park, Sebastian A Will, and Martin W Zwierlein. Ultracold dipolar gas of fermionic $^{23}Na^{40}K$ molecules in their absolute ground state. *Physical Review Letters*, 114(20):205302, 2015.

[66] Lukas Reichsöllner, Andreas Schindewolf, Tetsu Takekoshi, Rudolf Grimm, and Hanns-Christoph Nägerl. Quantum engineering of a low-entropy gas of heteronuclear bosonic molecules in an optical lattice. *Physical Review Letters*, 118(7):073201, 2017.

[67] Mayle, Michael and Quéméner, Goulven and Ruzic, Brandon P and Bohn, John L. Scattering of ultracold molecules in the highly resonant regime. *Physical Review A*, 87(1):012709, 2013.

[68] Alexander Guttridge, Stephen A Hopkins, Matthew D Frye, John J McFerran, Jeremy M Hutson, and Simon L Cornish. Production of ultracold Cs* Yb molecules by photoassociation. *Physical Review A*, 97(6):063414, 2018.

[69] Alexander Guttridge, Matthew D Frye, BC Yang, Jeremy M Hutson, and Simon L Cornish. Two-photon photoassociation spectroscopy of CsYb: Ground-state interaction potential and interspecies scattering lengths. *Physical Review A*, 98(2):022707, 2018.

[70] Andrew J Kerman, Jeremy M Sage, Sunil Sainis, Thomas Bergeman, and David DeMille. Production of Ultracold, Polar RbCs* Molecules via Photoassociation. *Physical Review Letters*, 92(3):033004, 2004.

[71] K Aikawa, D Akamatsu, M Hayashi, K Oasa, J Kobayashi, P Naidon, T Kishimoto, M Ueda, and S Inouye. Coherent transfer of photoassociated molecules into the rovibrational ground state. *Physical Review Letters*, 105(20):203001, 2010.

[72] J Deiglmayr, A Grochola, M Repp, K Mörtlbauer, C Glück, J Lange, O Dulieu, R Wester, and M Weidemüller. Formation of ultracold polar molecules in the rovibrational ground state. *Physical Review Letters*, 101(13):133004, 2008.

[73] LR Liu, JD Hood, Yichao Yu, JT Zhang, NR Hutzler, Till Rosenband, and K-K Ni. Building one molecule from a reservoir of two atoms. *Science*, 360(6391):900–903, 2018.

[74] Alon B Henson, Sasha Gersten, Yuval Shagam, Julia Narevicius, and Edvardas Narevicius. Observation of resonances in Penning ionization reactions at sub-kelvin temperatures in merged beams. *Science*, 338(6104):234–238, 2012.

[75] Nandini Mukherjee and Richard N Zare. Stark-induced adiabatic Raman passage for preparing polarized molecules. *The Journal of Chemical Physics*, 135(2):024201, 2011.

[76] Jonathan D Weinstein, Robert DeCarvalho, Thierry Guillet, Bretislav Friedrich, and John M Doyle. Magnetic trapping of calcium monohydride molecules at millikelvin temperatures. *Nature*, 395(6698):148–150, 1998.

[77] Nicholas R Hutzler, Hsin-I Lu, and John M Doyle. The buffer gas beam: An intense, cold, and slow source for atoms and molecules. *Chemical Reviews*, 112(9):4803–4827, 2012.

[78] Hendrick L Bethlem, Giel Berden, and Gerard Meijer. Decelerating neutral dipolar molecules. *Physical Review Letters*, 83(8):1558, 1999.

[79] Yair Segev, Martin Pitzer, Michael Karpov, Nitzan Akerman, Julia Narevicius, and Edvardas Narevicius. Collisions between cold molecules in a superconducting magnetic trap. *Nature*, 572(7768):189–193, 2019.

[80] MD Di Rosa. Laser-cooling molecules. *The European Physical Journal D-Atomic, Molecular, Optical and Plasma Physics*, 31(2):395–402, 2004.

[81] Immanuel Bloch, Markus Greiner, Olaf Mandel, Theodor W Hänsch, and Tilman Esslinger. Sympathetic cooling of ^{85}Rb and ^{87}Rb. *Physical Review A*, 64(2):021402, 2001.

[82] Andrew G Truscott, Kevin E Strecker, William I McAlexander, Guthrie B Partridge, and Randall G Hulet. Observation of Fermi pressure in a gas of trapped atoms. *Science*, 291(5513):2570–2572, 2001.

[83] William D Phillips and Harold Metcalf. Laser deceleration of an atomic beam. *Physical Review Letters*, 48(9):596, 1982.

[84] Steven Chu, Leo Hollberg, John E Bjorkholm, Alex Cable, and Arthur Ashkin. Three-dimensional viscous confinement and cooling of atoms by resonance radiation pressure. *Physical Review Letters*, 55(1):48, 1985.

[85] Takeshi Kuwamoto, Kazuhito Honda, Yoshiro Takahashi, and Tsutomu Yabuzaki. Magneto-optical trapping of yb atoms using an intercombination transition. *Physical Review A*, 60(2):R745, 1999.

[86] Jabez J McClelland and James L Hanssen. Laser cooling without repumping: a magneto-optical trap for erbium atoms. *Physical Review Letters*, 96(14):143005, 2006.

[87] Mingwu Lu, Seo Ho Youn, and Benjamin L Lev. Trapping ultracold dysprosium: A highly magnetic gas for dipolar physics. *Physical Review Letters*, 104(6):063001, 2010.

[88] Daniel A Steck. Rubidium 87 D line data, 2001.

[89] Leonid A Kaledin, Jonathan C Bloch, Michael C McCarthy, and Robert W Field. Analysis and deperturbation of the $A^2\Pi$ and $B^2\Sigma^+$ states of CaF. *Journal of Molecular Spectroscopy*, 197(2):289–296, 1999.

[90] Benjamin K Stuhl, Brian C Sawyer, Dajun Wang, and Jun Ye. Magneto-optical trap for polar molecules. *Physical Review Letters*, 101(24):243002, 2008.

[91] H. J. Williams, S. Truppe, M. Hambach, L. Caldwell, N. J. Fitch, E. A. Hinds, B. E. Sauer, and M. R. Tarbutt. Characteristics of a magneto-optical trap of molecules. *New Journal of Physics*, 19:113035, 2017.

[92] Christopher J Foot et al. *Atomic physics*, volume 7. Oxford University Press, 2005.

[93] Paul D Lett, Richard N Watts, Christoph I Westbrook, William D Phillips, Phillip L Gould, and Harold J Metcalf. Observation of atoms laser cooled below the Doppler limit. *Physical Review Letters*, 61(2):169, 1988.

[94] Jean Dalibard and Claude Cohen-Tannoudji. Laser cooling below the Doppler limit by polarization gradients: simple theoretical models. *JOSA B*, 6(11):2023–2045, 1989.

[95] DJ Berkeland and MG Boshier. Destabilization of dark states and optical spectroscopy in Zeeman-degenerate atomic systems. *Physical Review A*, 65(3):033413, 2002.

[96] Matthias Weidemüller, Tilman Esslinger, Maxim A Ol'shanii, Andreas Hemmerich, and Theodor W Hänsch. A novel scheme for efficient cooling below the photon recoil limit. *EPL (Europhysics Letters)*, 27(2):109, 1994.

[97] S Truppe, HJ Williams, M Hambach, L Caldwell, NJ Fitch, EA Hinds, BE Sauer, and MR Tarbutt. Molecules cooled below the Doppler limit. *Nature Physics*, 13(12):1173–1176, 2017.

[98] L Caldwell, JA Devlin, HJ Williams, NJ Fitch, EA Hinds, BE Sauer, and MR Tarbutt. Deep laser cooling and efficient magnetic compression of molecules. *Physical review letters*, 123(3):033202, 2019.

[99] Shiqian Ding, Yewei Wu, Ian A Finneran, Justin J Burau, and Jun Ye. Sub-Doppler Cooling and Compressed Trapping of YO Molecules at μK Temperatures. *Physical Review X*, 10(2):021049, 2020.

[100] Loïc Anderegg, Benjamin L Augenbraun, Yicheng Bao, Sean Burchesky, Lawrence W Cheuk, Wolfgang Ketterle, and John M Doyle. Laser cooling of optically trapped molecules. *Nature Physics*, 14(9):890–893, 2018.

[101] B Sheehy, SQ Shang, P Van Der Straten, S Hatamian, and H Metcalf. Magnetic-field-induced laser cooling below the doppler limit. *Physical Review Letters*, 64(8):858, 1990.

[102] Olivier Emile, Robin Kaiser, Christoph Gerz, Hartmut Wallis, Alain Aspect, and Claude Cohen-Tannoudji. Magnetically assisted Sisyphus effect. *Journal de Physique II*, 3(12):1709–1733, 1993.

[103] MR Tarbutt, BE Sauer, JJ Hudson, and EA Hinds. Design for a fountain of YbF molecules to measure the electron's electric dipole moment. *New Journal of Physics*, 15(5):053034, 2013.

[104] Charles S Adams and Ifan G Hughes. *Optics f2f: from Fourier to Fresnel*, pages 214–216. Oxford University Press, USA, 2018.

[105] Matthew D Frye, Paul S Julienne, and Jeremy M Hutson. Cold atomic and molecular collisions: approaching the universal loss regime. *New Journal of Physics*, 17(4):045019, 2015.

[106] Jongseok Lim, Matthew D Frye, Jeremy M Hutson, and MR Tarbutt. Modeling sympathetic cooling of molecules by ultracold atoms. *Physical Review A*, 92(5):053419, 2015.

[107] Jean Dalibard. Collisional dynamics of ultra-cold atomic gases. In *Proceedings of the International School of Physics-Enrico Fermi*, volume 321, page 14, 1999.

[108] Alexander Guttridge. *Photoassociation of Ultracold CsYb Molecules and Determination of Interspecies Scattering Lengths*. PhD thesis, Durham University, 2018.

[109] GF Gribakin and VV Flambaum. Calculation of the scattering length in atomic collisions using the semiclassical approximation. *Physical Review A*, 48(1):546, 1993.

[110] Jeremy M Hutson. Coupled channel methods for solving the bound-state Schrödinger equation. *Computer Physics Communications*, 84(1-3):1–18, 1994.

[111] Stephen R Langhoff, Charles W Bauschlicher Jr, and Harry Partridge. Theoretical dissociation energies for the alkali and alkaline-earth monofluorides and monochlorides. *The Journal of Chemical Physics*, 84(3):1687–1695, 1986.

[112] Geetha Gopakumar, Minori Abe, Masahiko Hada, and Masatoshi Kajita. Dipole polarizability of alkali-metal (Na, K, Rb)- alkaline-earth-metal (Ca, Sr) polar molecules: Prospects for alignment. *The Journal of chemical physics*, 140(22):224303, 2014.

[113] Zbigniew Idziaszek and Paul S Julienne. Universal rate constants for reactive collisions of ultracold molecules. *Physical Review Letters*, 104(11):113202, 2010.

[114] HJ Williams, L Caldwell, NJ Fitch, S Truppe, J Rodewald, EA Hinds, BE Sauer, and MR Tarbutt. Magnetic trapping and coherent control of laser-cooled molecules. *Physical Review Letters*, 120(16):163201, 2018.

[115] Schoser, J and Batär, A and Löw, R and Schweikhard, V and Grabowski, A and Ovchinnikov, Yu B and Pfau, T. Intense source of cold Rb atoms from a pure two-dimensional magneto-optical trap. *Physical Review A*, 66(2):023410, 2002.

[116] K Dieckmann, RJC Spreeuw, M Weidemüller, and JTM Walraven. Two-dimensional magneto-optical trap as a source of slow atoms. *Physical Review A*, 58(5):3891, 1998.

[117] Tim Kovachy, Jason M Hogan, Alex Sugarbaker, Susannah M Dickerson, Christine A Donnelly, Chris Overstreet, and Mark A Kasevich. Matter wave lensing to picokelvin temperatures. *Physical Review Letters*, 114(14):143004, 2015.

[118] DJ McCarron, MH Steinecker, Y Zhu, and D DeMille. Magnetic trapping of an ultracold gas of polar molecules. *Physical Review Letters*, 121(1):013202, 2018.

[119] S Truppe, HJ Williams, NJ Fitch, M Hambach, TE Wall, EA Hinds, BE Sauer, and MR Tarbutt. An intense, cold, velocity-controlled molecular beam by frequency-chirped laser slowing. *New Journal of Physics*, 19(2):022001, 2017.

[120] S Truppe, M Hambach, SM Skoff, NE Bulleid, JS Bumby, RJ Hendricks, EA Hinds, BE Sauer, and MR Tarbutt. A buffer gas beam source for short, intense and slow molecular pulses. *Journal of Modern Optics*, 65(5-6):648–656, 2018.

[121] Albert G Tobin, Douglas W Sedgley, Thomas H Batzer, and Wayne R Call. Evaluation of charcoal sorbents for helium cryopumping in fusion reactors. *Journal of Vacuum Science & Technology A: Vacuum, Surfaces, and Films*, 5(1):101–105, 1987.

[122] Charles S Adams and Ifan G Hughes. *Optics f2f: from Fourier to Fresnel*, pages 27–28. Oxford University Press, USA, 2018.

[123] JF Barry, DJ McCarron, EB Norrgard, MH Steinecker, and D DeMille. Magneto-optical trapping of a diatomic molecule. *Nature*, 512(7514):286–289, 2014.

[124] Loïc Anderegg, Benjamin L Augenbraun, Eunmi Chae, Boerge Hemmerling, Nicholas R Hutzler, Aakash Ravi, Alejandra Collopy, Jun Ye, Wolfgang Ketterle, and John M Doyle. Radio frequency magneto-optical trapping of CaF with high density. *Physical Review Letters*, 119(10):103201, 2017.

[125] Alejandra L Collopy, Shiqian Ding, Yewei Wu, Ian A Finneran, Loïc Anderegg, Benjamin L Augenbraun, John M Doyle, and Jun Ye. 3D magneto-optical trap of yttrium monoxide. *Physical Review Letters*, 121(21):213201, 2018.

[126] L. Baum, N. B. Vilas, C. Hallas, B. L. Augenbraun, S. Raval, D. Mitra, and J. M. Doyle. 1D magneto-optical trap of polyatomic molecules. *Physical Review Letters*, 124:133201, 2020.

[127] EB Norrgard, DJ McCarron, MH Steinecker, MR Tarbutt, and D DeMille. Submillikelvin dipolar molecules in a radio-frequency magneto-optical trap. *Physical Review Letters*, 116(6):063004, 2016.

[128] Jimmy Stammers. *An atom interferometer for measuring horizontal accelerations*. PhD thesis, Imperial College London, 2018.

[129] Guillaume Labeyrie, Franck Michaud, and Robin Kaiser. Self-sustained oscillations in a large magneto-optical trap. *Physical Review Letters*, 96(2):023003, 2006.

[130] Marius Gaudesius, Robin Kaiser, Guillaume Labeyrie, Y-C Zhang, and Thomas Pohl. Instability threshold in a large balanced magneto-optical trap. *Physical Review A*, 101(5):053626, 2020.

[131] CG Townsend, NH Edwards, CJ Cooper, KP Zetie, CJ Foot, AM Steane, P Szriftgiser, H Perrin, and J Dalibard. Phase-space density in the magneto-optical trap. *Physical Review A*, 52(2):1423, 1995.

[132] Thad Walker, David Sesko, and Carl Wieman. Collective behavior of optically trapped neutral atoms. *Physical Review Letters*, 64(4):408, 1990.

[133] Abdoulaye Camara, Robin Kaiser, and Guillaume Labeyrie. Scaling behavior of a very large magneto-optical trap. *Physical Review A*, 90(6):063404, 2014.

[134] Hannah J. Williams. *Producing, trapping and controlling ultracold CaF molecules*. PhD thesis, Imperial College London, 2018.

[135] Moritz Hambach. *Development of a magneto-optical trap for CaF molecules*. PhD thesis, Imperial College London, 2017.

[136] Luke Caldwell. *Deep laser cooling and coherent control of molecules*. PhD thesis, Imperial College London, 2020.

[137] ES Shuman, JF Barry, DR Glenn, and D DeMille. Radiative force from optical cycling on a diatomic molecule. *Physical Review Letters*, 103(22):223001, 2009.

[138] Loïc Anderegg. *Ultracold molecules in optical arrays: from laser cooling to molecular collisions*. PhD thesis, Harvard University, 2019.

[139] Wolfgang Rohringer, Robert Buecker, Stephanie Manz, Thomas Betz, Ch Koller, Martin Goebel, Aurelien Perrin, Joerg Schmiedmayer, and Thorsten Schumm. Stochastic optimization of a cold atom experiment using a genetic algorithm. *Applied Physics Letters*, 93(26):264101, 2008.

[140] Tobias Lausch, Michael Hohmann, Farina Kindermann, Daniel Mayer, Felix Schmidt, and Artur Widera. Optimizing quantum gas production by an evolutionary algorithm. *Applied Physics B*, 122(5):112, 2016.

[141] MR Tarbutt and TC Steimle. Modeling magneto-optical trapping of caf molecules. *Physical Review A*, 92(5):053401, 2015.

[142] Alan Gallagher and David E Pritchard. Exoergic collisions of cold Na*-Na. *Physical Review Letters*, 63(9):957, 1989.

[143] Paul S Julienne and Jacques Vigué. Cold collisions of ground-and excited-state alkali-metal atoms. *Physical Review A*, 44(7):4464, 1991.

[144] LG Marcassa, GD Telles, SR Muniz, and VS Bagnato. Collisional losses in a K-Rb cold mixture. *Physical Review A*, 63(1):013413, 2000.

[145] D Sesko, T Walker, C Monroe, A Gallagher, and C Wieman. Collisional losses from a light-force atom trap. *Physical Review Letters*, 63(9):961, 1989.

[146] Christopher D Wallace, Timothy P Dinneen, Kit-Yan N Tan, Timothy T Grove, and Phillip L Gould. Isotopic difference in trap loss collisions of laser cooled rubidium atoms. *Physical Review Letters*, 69(6):897, 1992.

[147] V Sanchez-Villicana, SD Gensemer, KYN Tan, A Kumarakrishnan, TP Dinneen, W Süptitz, and PL Gould. Suppression of ultracold ground-state hyperfine-changing collisions with laser light. *Physical Review Letters*, 74(23):4619, 1995.

[148] MO Brown, T Thiele, C Kiehl, T-W Hsu, and CA Regal. Gray-molasses optical-tweezer loading: controlling collisions for scaling atom-array assembly. *Physical Review X*, 9(1):011057, 2019.

[149] Schlöder, U and Engler, H and Schünemann, U and Grimm, R and Weidemüller, M. Cold inelastic collisions between lithium and cesium in a two-species magneto-optical trap. *The European Physical Journal D-Atomic, Molecular, Optical and Plasma Physics*, 7(3):331–340, 1999.

[150] GD Telles, W Garcia, LG Marcassa, VS Bagnato, Donatella Ciampini, M Fazzi, JH Müller, D Wilkowski, and Ennio Arimondo. Trap loss in a two-species Rb-Cs magneto-optical trap. *Physical Review A*, 63(3):033406, 2001.

[151] Mingyang Guo, Xin Ye, Junyu He, Maykel L González-Martínez, Romain Vexiau, Goulven Quéméner, and Dajun Wang. Dipolar collisions of ultracold ground-state bosonic molecules. *Physical Review X*, 8(4):041044, 2018.

[152] Arthur Christianen, Martin W Zwierlein, Gerrit C Groenenboom, and Tijs Karman. Photoinduced two-body loss of ultracold molecules. *Physical Review Letters*, 123(12):123402, 2019.

[153] Valentina Zhelyazkova. *Laser cooling of CaF molecules*. PhD thesis, Imperial College London, 2018.

[154] MH Shah, HA Camp, ML Trachy, G Veshapidze, MA Gearba, and BD DePaola. Model-independent measurement of the excited fraction in a magneto-optical trap. *Physical Review A*, 75(5):053418, 2007.

[155] Antonio Fernández-Ramos, James A Miller, Stephen J Klippenstein, and Donald G Truhlar. Modeling the kinetics of bimolecular reactions. *Chemical Reviews*, 106(11):4518–4584, 2006.

[156] Wolfgang Petrich, Michael H Anderson, Jason R Ensher, and Eric A Cornell. Behavior of atoms in a compressed magneto-optical trap. *JOSA B*, 11(8):1332–1335, 1994.

[157] Wolfgang Ketterle, Kendall B Davis, Michael A Joffe, Alex Martin, and David E Pritchard. High densities of cold atoms in a dark spontaneous-force optical trap. *Physical Review Letters*, 70(15):2253, 1993.

[158] N Radwell, G Walker, and S Franke-Arnold. Cold-atom densities of more than 10 12 cm- 3 in a holographically shaped dark spontaneous-force optical trap. *Physical Review A*, 88(4):043409, 2013.

[159] Hyungmok Son, Juliana J Park, Wolfgang Ketterle, and Alan O Jamison. Collisional cooling of ultracold molecules. *Nature*, 580(7802):197–200, 2020.

[160] Giacomo Valtolina, Kyle Matsuda, William G Tobias, Jun-Ru Li, Luigi De Marco, and Jun Ye. Dipolar evaporation of reactive molecules to below the Fermi temperature. *Nature*, 588(7837):239–243, 2020.

[161] RV Krems, A Dalgarno, N Balakrishnan, and GC Groenenboom. Spin-flipping transitions in $^2\Sigma$ molecules induced by collisions with structureless atoms. *Physical Review A*, 67(6):060703, 2003.

[162] Nassim Zahzam, Thibault Vogt, Marcel Mudrich, Daniel Comparat, and Pierre Pillet. Atom-molecule collisions in an optically trapped gas. *Physical Review Letters*, 96(2):023202, 2006.

[163] Peter Staanum, Stephan D Kraft, Jörg Lange, Roland Wester, and Matthias Weidemüller. Experimental investigation of ultracold atom-molecule collisions. *Physical Review Letters*, 96(2):023201, 2006.

[164] Eric R Hudson, Nathan B Gilfoy, Svetlana Kotochigova, Jeremy M Sage, and David DeMille. Inelastic collisions of ultracold heteronuclear molecules in an optical trap. *Physical Review Letters*, 100(20):203201, 2008.

[165] Huan Yang, De-Chao Zhang, Lan Liu, Ya-Xiong Liu, Jue Nan, Bo Zhao, and Jian-Wei Pan. Observation of magnetically tunable Feshbach resonances in ultracold $^{23}Na^{40}K + ^{40}K$ collisions. *Science*, 363(6424):261–264, 2019.

[166] Lawrence W Cheuk, Loïc Anderegg, Benjamin L Augenbraun, Yicheng Bao, Sean Burchesky, Wolfgang Ketterle, and John M Doyle. Λ-enhanced imaging of molecules in an optical trap. *Physical Review Letters*, 121(8):083201, 2018.

[167] JA Devlin and MR Tarbutt. Three-dimensional doppler, polarization-gradient, and magneto-optical forces for atoms and molecules with dark states. *New Journal of Physics*, 18(12):123017, 2016.

[168] L Caldwell, HJ Williams, NJ Fitch, J Aldegunde, Jeremy M Hutson, BE Sauer, and MR Tarbutt. Long rotational coherence times of molecules in a magnetic trap. *Physical Review Letters*, 124(6):063001, 2020.

[169] Nicolas Vanhaecke and Olivier Dulieu. Precision measurements with polar molecules: the role of the black body radiation. *Molecular Physics*, 105(11-12):1723–1731, 2007.

[170] Stefan Yoshi Buhmann, MR Tarbutt, Stefan Scheel, and EA Hinds. Surface-induced heating of cold polar molecules. *Physical Review A*, 78(5):052901, 2008.

[171] Wolfgang Petrich, Michael H Anderson, Jason R Ensher, and Eric A Cornell. Stable, tightly confining magnetic trap for evaporative cooling of neutral atoms. *Physical Review Letters*, 74(17):3352, 1995.

[172] Y-J Lin, Abigail R Perry, Robert L Compton, Ian B Spielman, and James V Porto. Rapid production of ^{87}Rb Bose-Einstein condensates in a combined magnetic and optical potential. *Physical Review A*, 79(6):063631, 2009.

[173] Philip D Gregory, Matthew D Frye, Jacob A Blackmore, Elizabeth M Bridge, Rahul Sawant, Jeremy M Hutson, and Simon L Cornish. Sticky collisions of ultracold RbCs molecules. *Nature Communications*, 10(1):1–7, 2019.

[174] Arthur Christianen, Tijs Karman, and Gerrit C Groenenboom. Quasiclassical method for calculating the density of states of ultracold collision complexes. *Physical Review A*, 100(3):032708, 2019.

[175] Matthew T Hummon, Mark Yeo, Benjamin K Stuhl, Alejandra L Collopy, Yong Xia, and Jun Ye. 2D magneto-optical trapping of diatomic molecules. *Physical Review Letters*, 110(14):143001, 2013.

[176] Eunmi Chae, Loic Anderegg, Benjamin L Augenbraun, Aakash Ravi, Boerge Hemmerling, Nicholas R Hutzler, Alejandra L Collopy, Jun Ye, Wolfgang Ketterle, and John M Doyle. One-dimensional magneto-optical compression of a cold CaF molecular beam. *New Journal of Physics*, 19(3):033035, 2017.

[177] NJ Fitch and MR Tarbutt. Principles and design of a Zeeman-Sisyphus decelerator for molecular beams. *ChemPhysChem*, 17(22):3609, 2016.

[178] Edward S Shuman, John F Barry, and David DeMille. Laser cooling of a diatomic molecule. *Nature*, 467(7317):820–823, 2010.

[179] J Lim, JR Almond, MA Trigatzis, JA Devlin, NJ Fitch, BE Sauer, MR Tarbutt, and EA Hinds. Laser cooled YbF molecules for measuring the electron's electric dipole moment. *Physical Review Letters*, 120(12):123201, 2018.

[180] X Alauze, J Lim, MA Trigatzis, S Swarbrick, NJ Fitch, BE Sauer, and MR Tarbutt. An ultracold molecular beam for testing fundamental physics. *arXiv preprint arXiv:2104.06194*, 2021.

[181] Simon L Cornish, Neil R Claussen, Jacob L Roberts, Eric A Cornell, and Carl E Wieman. Stable ^{85}Rb Bose-Einstein condensates with widely tunable interactions. *Physical Review Letters*, 85(9):1795, 2000.

[182] EGM Van Kempen, SJJMF Kokkelmans, DJ Heinzen, and BJ Verhaar. Interisotope determination of ultracold rubidium interactions from three high-precision experiments. *Physical Review Letters*, 88(9):093201, 2002.

[183] Rudolf Grimm, Matthias Weidemüller, and Yurii B Ovchinnikov. Optical dipole traps for neutral atoms. *Advances in atomic, molecular, and optical physics*, 42:95–170, 2000.

[184] MS Safronova, Bindiya Arora, and Charles W Clark. Frequency-dependent polarizabilities of alkali-metal atoms from ultraviolet through infrared spectral regions. *Physical Review A*, 73(2):022505, 2006.

[185] Arian Jadbabaie, Nickolas H Pilgram, Jacek Kłos, Svetlana Kotochigova, and Nicholas R Hutzler. Enhanced molecular yield from a cryogenic buffer gas beam source via excited state chemistry. *New Journal of Physics*, 22(2):022002, 2020.